Fabrication, Assembly, and Electrical Characterisation of Gold Nanowires

by

Joseph Boote

Submitted in accordance with the requirements for the degree of Doctor of Philosophy

The University of Leeds

School of Physics and Astronomy

September 2005

The candidate confirms that the work submitted is his own and that appropriate credit has been given where reference has been made to the work of others.

Acknowledgements

I would like to thank my supervisor Professor Stephen Evans, for the original thought behind this project, regular support, and insight throughout the work presented in this thesis.

There are several other individuals that have made notable contributions to the development of this work, or the results presented in this thesis.
Professor Haoli Zhang's advice during the early stages of this project was invaluable when fabricating the first nanowires. His assistance was also gratefully received during when he provided electrodes enabling the dielectrophoretic assembly of nanowires.
Dr Simon Connell provided considerable assistance in all aspects of AFM characterisation. His initial training for my use of the AFM provided the first observations of porous alumina, and his continued interest was the driving force behind the AFM manipulation of nanowires on electrodes.
Discussions with Dr Kevin Critchley have proved invaluable, in all areas of this work. His direct contributions have been in XPS (training) and SAMs. In addition, he has developed the Omicron 4-probe STM for electrical measurements of isolated nanowires.
The TEM images in this thesis were collected by Dr Andy Brown, and John Harrington has provided assistance during SEM characterisation of samples.
I am indebted to all these people, without which this work would not have been possible.

Many additional past and present members of the Molecular and Nanoscale physics group have also assisted me during my PhD. Their contributions have varied from useful discussions, training, advice, and welcome distractions. Of particular note in this respect are Lucy Holt, Dr Nicola Cant, Dr Ed Cheadle, Khizar Sheikh, Pete Barber, Katherine Byrne and Neal Crampton amongst many others. In addition, I would like to thank the technicians for their expertise and craftsmanship.

On a more personal note, I would like to thank my family for continued encouragement and support. My partner, Charlotte Lister has provided friendship and understanding at times when I have needed it most.

The award of scholarship from The University of Leeds and additional funding derived from a partial CASE award from ICI are gratefully acknowledged.

Abstract

The work presented in this thesis has concerned the synthesis, manipulation and characterisation of gold nanowires.

Porous alumina membranes have been electrochemically fabricated as templates for the deposition of gold nanowires. They consist of a thick oxide membrane, shown to be perforated by a high density array of isolated cylindrical pores, with a narrow size distribution. In addition, nanowires have been fabricated in commercially available porous alumina, and polycarbonate track-etched filtration membranes. Gold has been deposited by electrochemical and electroless techniques from a variety of solutions.

A range of non-covalent interactions have been used to direct the aggregation of nanowires in solution, or assembly of nanowires on surfaces. These include hydrophobic interactions, surface wettability, hydrogen bonding, carboxylate salt formation, electrostatic interactions between charged surfactants, and biotin binding. Of particular interest is the ability to control both the placement and orientation of nanowires onto surfaces. These conditions have been best satisfied by the deposition of nanowires from solution onto surfaces patterned with alternating hydrophilic and hydrophobic stripes. Nanowires are located on the hydrophilic regions of the surface, aligned parallel to the patterned surface.

The use of alternating electric fields to manipulate particles in solution is labelled dielectrophoresis. Considerable control over the assembly of nanowires is afforded by adjusting the assembly parameters. These conditions have been modelled, and investigated experimentally, to determine the optimum assembly conditions consistent with positioning a single nanowire across the electrode gap. After assembly, single nanowires displayed an Ohmic response with 35 Ω resistance values predominantly due to contact resistance between the electrode and nanowire. By optimising the assembly and cleaning procedures the contribution of contact resistance to measured resistance has been reduced below values reported elsewhere in the literature.

Table of Contents

List of Figures

List of Tables

Publications

Dielectrophoretic Manipulation and Electrical Characterisation of Gold Nanowires, Boote, J.J.; Evans, S.D.; *Nanotechnology* **2005**, 16, 1500-1505

Surfactant Mediated Assembly of Gold Nanowires on Surfaces, Boote, J.J.; Critchley, K.; Evans, S.D.; *submitted to the Journal of Experimental Nanoscience.*

Chapter 1: Introduction

The word nanotechnology has come to span a wide variety of disciplines, where the only discernable similarity is that they concern systems where 1 or more dimension is within the range 1 – 1000 nm. This may include nano-structured materials, instrumentation that allows nanoscale observations, and biological or chemical systems. The birthplace of this discipline can be traced directly to the 1959 lecture by Feynman "There's Plenty of Room at the Bottom".[1] Here, Feynman discussed the benefits that would arise from the miniaturisation of current technologies. Although imaginative, his suggestions were only bound by practical rather than fundamental constraints. He discussed a range of topics which initiated new research into computers and electronics, information storage, instrumentation, and single-atom manipulation. As Feynman commented, the largest single barrier to this field was instrumentation that allowed observation at the nanoscale. Although electron microscopy had already been invented, its development together with a host of other analytical techniques, including scanning tunnelling microscopy[2] and atomic force microscopy[3], has allowed the rapid advance of this field in more recent years. The most accurate realisation of Feynman's suggestions was the manipulation of individual atoms, famously achieved by Eigler *et al*[4] at IBM with an STM, figure 1.1.

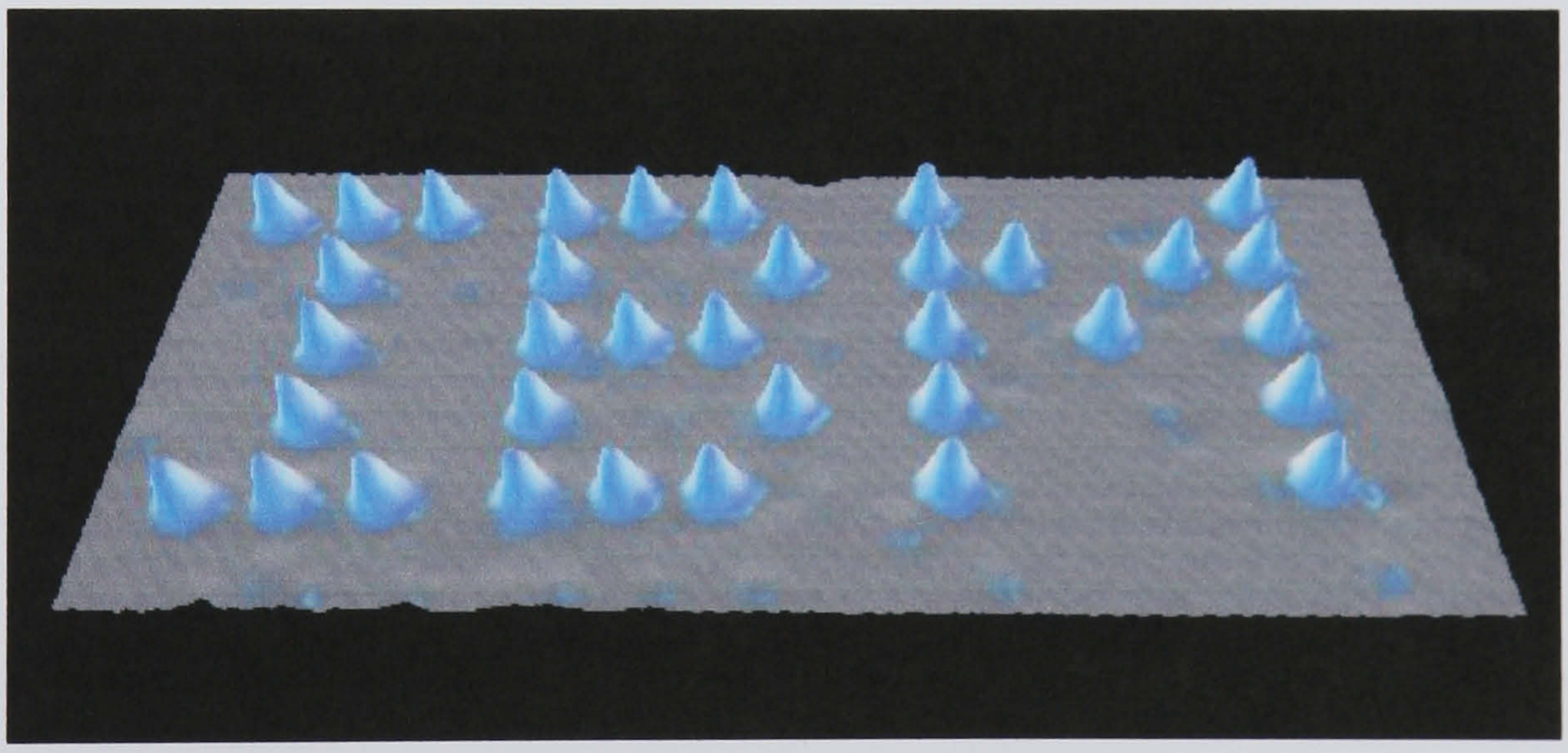

Figure 1.1. STM image of xenon atoms on nickel (100) after manipulation of individual xenon atoms with an STM tip to form the characters IBM.[4]

Around this period, the field of electronics was undergoing significant advances, like the development of solid state devices. Most notable amongst these was the transistor, which superseded valve technology and brought increased reliability, and durability, at a scale an order of magnitude smaller. In the years immediately following Feynman's lecture, advances in electronics were tracked by Moore[5]. He showed that the density of

components on a microchip had increased exponentially, and more importantly predicted that this trend would continue. Remarkably, this relationship has held to the present day, primarily due to advancement of lithographic techniques and silicon based integrated circuitry. Moore's statement has come to become something of a benchmark, known as Moore's Law. However, it is widely anticipated that in order for Moore's law to hold in the future there will need to be a paradigm shift in the nature of computing devices.

Feynman's lecture was strongly biased towards the direct manipulation of components into devices, although he also suggested that nano-devices may self-replicate, or act as nano-factories for a yet smaller range of devices. This approach is now labelled the 'top-down' procedure, where components or materials are directly manipulated to construct architecture and devices. Lithographic techniques used for the commercial fabrication of integrated circuitry are typical of this approach. However, difficulties increase with every reduction in scale, and this technique is highly intensive. Future miniaturization of integrated circuitry with top-down fabrication techniques is limited by experimental barriers that are, as yet, unresolved. The alternative route, the 'bottom-up' approach, exploits self-assembly such that component parts spontaneously assemble into functional arrangements, without the individual manipulation of each component. The promise of bottom-up techniques is reduced complexity and cost. However, these techniques rely upon nano-components that can be encouraged to interact in specific ways to cause their assembly into functional arrangements. Such systems routinely operate in biological and chemical systems.

1.1: Nanoparticles

Nanoparticles were first synthesised for use as pigment. In 1685 Andreas Cassius published a procedure for producing purple pigment by the reduction of gold salt, called Purple of Cassius. However, it was Sir Humphrey Davy and Faraday who first theorised about origin of the pigmentation and nature of colloidal gold.[6] Many interesting phenomenon occur with the reduction in scale of metallic particles. The mobility of electrons in the conduction band is confined, decreasing their mean free path. Consequently both the optical and electronic properties of nanoparticles are changed from those of the bulk metal. In addition, conductivity through particles becomes a quantum effect, where the population of electrons on any isolated particle is limited by their low total capacitance. Similarly, the increase in surface area to volume greatly enhances any

catalytic activity. Recently, research into gold nanoparticles has increased following the synthesis route developed by Brust *et al.*[7]

In addition to the development of nanoparticles, the pursuit of nanowires has seen significant activity in recent years. Carbon nanotubes[8] have received considerable attention, however there are a wide variety of techniques available to produce other one dimensional structures. Nanowires may be fabricated by a variety of techniques, of which several of the most common are outlined below:

- In a similar process to the surfactant controlled fabrication of nanoparticles[7], reduction of salt in the presence of certain surfactants may also be used to generate metallic nanowires.[9] Gold salt is reduced in the presence of a mixed cationic surfactant solution, it is thought that a dynamic micelle systems acts as a template for the growth of nanowires.
- Template fabrication of nanowires describes a process whereby gold is deposited either into, or onto, a physical template that defines the size and shape of the deposited material. Nanowires were first fabricated in porous membranes[10], but the technique has since been extended to the deposition of gold on DNA[11] and in micelle structures mentioned above.
- The Vapour-Liquid-Solid (VLS) growth procedure requires that material is deposited from a vapour phase to a liquid-solid interface. Commonly a solid substrate is coated with metal nanoparticles, and heated until these nanoparticles melt. These metal particles alloy with the material from the substrate or vapour phase, until the composition of the alloy is at equilibrium. When more growth material is supplied at this temperature, the alloyed particle becomes supersaturated, and excess species deposit below nanoparticle resulting in one-dimensional growth. The metal particle is not consumed during growth and acts as a catalyst.[12, 13]
- The epitaxial deposition of metals on substrates tends initially to grow as dislocation-free islands. It has been found that these islands may form long thin nanowires, which allows better elastic relaxation of the island's stress.[14] Alternatively, deposited material may collect at step-edges on the substrate surface producing nanowires.[15]
- Finally, nanowires have been seen to form directly between electrodes upon the application of high field conditions.[16, 17]

In recognition of the barriers faced by lithographic circuit fabrication, there has been considerable effort to construct devices from molecules[18, 19], carbon nanotubes[20-22], and nanowires[23-25]. The formation of nanowires by template deposition into porous membranes allows the greatest control over the structure of the nanowire. They may be fabricated from a variety of materials[26-28], or combinations thereof[29].

1.2: Nanoparticle Assembly

To fabricate functional devices from nanoscale components, assembly routes must be developed that are capable of constructing specific arrangements of components. For example, one of the goals is to assemble an interconnected high density array of elements[23, 30, 31]. Such arrays could form the basis of logic or memory circuits, and other integrated nanosystems such as chemical / biological sensors[32, 33] or photonic devices[34]. The development of a viable bottom-up procedures to construct nano-scale circuitry requires not only the development of assembly techniques, but may also include aspects of surface patterning[30, 35, 36], alternative circuit architectures[23, 37, 38], and molecular electronics[18, 19, 38-40]. Discussed below is a summary of some of the techniques used for nanoparticle assembly presented in the literature.

The first demonstrations of nanoparticle self-assembly on surfaces used colloidal particles. Brust *et al*[41] showed that networks of gold nanoparticles could be self-organised into 3-D structures via attachment between organic dithiols surfactants at their surface. Subsequent research has lead to a diverse range of assembly techniques[42] that have been split into four key mechanisms, for the descriptive purposes of this thesis:

- Fluidic Assembly – interactions between the surface, solvent or colloid direct assembly. Nanoparticles may be driven together whilst suspended in solution by the evaporation of solvent[43-45]. Alternatively upon evaporation of the solvent nanopartices may become trapped at certain positions within a template or on a surface[46, 47]. Finally, assembly may be due to rearrangement at nanoparticles at a fluid-interface to adopt the highest packing density[48, 49], as in Langmuir-Blodgett assembly.
- Chemical Assembly – chemical interactions can assemble specific arrangements of functional components. This technique is most notably applied to molecules during the formation of self-assembled monolayers.[50] However, when applied to colloidal particles some chemical functionality must be present at their surface to co-ordinate their assembly. Nanoparticle assembly has been demonstrated with

both covalent[51-54] and non-covalent binding interactions[55, 56]. Recently there has been considerable work on biochemical interactions which potentially add further selectivity. Interactions are due to the presence of biological components such as DNA[57], or avidin / streptavidin[58, 59].

- Electrostatic Assembly - electrostatic interactions between charged components drive their assembly. These interactions may be interactions between identical polar molecules, or attractive and repulsive between oppositely charged and like charged particles respectively. Certain chemical groups may be charged at specific solvent conditions, and these have been used to functionalise colloids to control their deposition depending upon solvent conditions.[60-63]
- Field Mediated Assembly - where interactions between the components and an external field are used to define their assembly. Both external magnetic[64] and electric[65] fields have been used to assemble colloids onto surfaces.

The assembly of non-spherical particles has allowed more complex arrangements and structures to be created.[66] However, complications are also introduced when manipulating anisotropic components, including the requirement to control both their placement and orientation. The directed assembly of carbon nanotubes has received considerable attention. Adding chemical functionality to carbon nanotubes is difficult, and consequently there a few examples of chemical assembly, although some success has been achieved with DNA binding processes.[67, 68] Dielectrophoresis is the movement of dielectric particles in a fluid, with different dielectric properties, under the influence of an alternating field. The field not only directs the motion of the particle, but aligns anisotropic particles. Consequently, this is an ideal tool for the assembly of one-dimensional structures such as carbon nanotubes.[69, 70] Carbon nanotubes have also been assembled by fluidic processes[71, 72], electrostatic forces[73, 74], and magnetic fields[75]. The quantity of research undertaken on carbon nanotubes dwarfs that conducted on the assembly of metallic nanowires. However, there are specific examples of nanowire assembly in all the categories defined above. Langmuir-Blodgett techniques have been used to form liquid crystalline assemblies of nanowires both at fluid interfaces and on surfaces.[76, 77] Furthermore, by varying the nanowire concentration transitions may be induced between the isotropic, nematic and semetic phases has been observed.[78] In comparison to carbon nanotubes, gold nanowires may be easily functionalised with chemical groups. Dujardin *et al* have shown the specific organization of gold nanorods into anisotropic 3-D aggregates after DNA hybridisation.[79] Similarly Mbindyo *et al* have

demonstrated this binding process is capable of binding nanowires to complementary surfaces.[80] By functionalising the nanowires with charged surfactants, the assembly of nanowires can be controlled by tailoring the solvent pH.[81, 82] Finally, dielectrophoresis has also been applied to metallic nanowires to control their deposition either onto electrodes[83, 84], and to create integrated arrays[85]. Nanowire assembly under the influence of an external applied field is considered directed assembly, whilst interactions based between functional particles and surfaces are labelled (for the purposes of this work) self-assembly.

1.3: Electrical Characterisation of Nano-Components

The components used for the self-assembly of circuitry must in some way be addressed to determine their electrical behaviour. However, the manipulation of these components between electrodes, and the contact made once in place, presents some challenges to their characterisation. For example, one of the largest problems associated with electrical characterisation of molecules is their interface at the electrodes.[86] One solution to address molecular elements would be to embed them within metallic nanowires, and then assemble these between electrodes.[84] Indeed, nanowires provide ideal hosts to a variety of devices in addition to providing interconnect leads, and may be used as hosts for more complex devices.[24, 84]

However, addressing nanowires to determine their electrical properties is not without its own problems. A variety of techniques have been used to provide contacts for the characterisation of these elements. Initially, nanowires were deposited at random on a surface, and electrodes were overlaid by either electron beam lithography[87] or focused ion-beam induced deposition[84, 88]. Alternatively, they could be addressed directly with a conducting AFM tip, either within the template membrane or on surfaces[89]. AFM has also been used to manipulate individual nanowires directly between electrodes[90]. Although the in-situ fabrication of nanowires between electrodes is possible[91], this technique does not extend to more complex nanowire devices. Currently, the preferred solution is to assembly nanowires between electrodes with dielectrophoresis.[92]

1.4: Summary of Work and Description of Thesis

During the course of the work presented in this thesis, research has been focused towards developing expertise for the fabrication of gold nanowires, controlling their self-assembly on surfaces, and characterising their electrical behaviour.

Chapter 2 introduces the theoretical background to the techniques important for the fabrication, assembly and electrical characterisation of nanowires. During this discussion, specific techniques that have been used during the course of this work are highlighted, along with the experimental requirements for their application. Finally, the range of instrumentation used for characterisation throughout this thesis is presented. The scientific basis of these techniques, and comments that aid the understanding of their application, is also included.

The results and discussion surrounding the fabrication of gold nanowires is presented in chapter 3. Nanowires have been generated by template deposition. Both the templates themselves and the range of nanowire growth procedures used are documented. Following this, a complete characterisation of the gold nanowires is presented. In addition, the various chemical operations that have been performed during the creation and manipulation of gold nanowires are presented. These include techniques to expose or remove nanowires from templates, and the techniques used to modify the surface properties of these nanowires with thiol surfactants. Finally, a chemical analysis of surfactant coated nanowires is presented.

Chapter 4 explores the potential of surfactant based interactions to direct the assembly of gold nanowires. To successfully self-assemble nanowires into functional circuit architectures, the assembly procedure must control both the location and orientation of components on surfaces. Here, we assess the potential for surfactant interactions to direct both the placement and orientation of gold nanowires onto surfaces. The driving force for assembly arises from competition between nanowire-surface, nanowire-fluid and fluid-surface interactions. The mechanisms are summarised below, and fully documented in chapter 2.

- Interactions between hydrophobic functionalised nanowires in aqueous solutions.
- Nanowire assembly from solution onto patterned hydrophilic / hydrophobic surfaces.
- Chemical attachment of nanowires to surfaces by hydrogen bonding.
- Chemical attachment of nanowires to surfaces by carboxylate salt formation.
- Attachment of biotinylated nanowires to active streptavidin surfaces.
- Aggregation of biotinylated nanowires in solution after the introduction of streptavidin.

- The assembly of charged nanowires onto charged surfaces due to electrostatic interactions.
- Aggregation of charged nanowires in solution.

Results concerning the dielectrophoretic assembly and electrical characterisation of nanowires are presented in chapter 5. The dielectrophoretic force is modelled, based upon the interaction between an alternating applied field and the induced dipole moment of gold nanowires in solution. These results are compared with experimental exploration of the variable-space available during dielectrophoretic assembly, to determine the optimum assembly conditions. Once assembled the transport properties of these nanowires are measured.

1.5: References

1. Feynman, R.P., Engineering and Science, 1960. **23**(Feb): p. 22-36.
2. Binning, G.; Rohrer, H.; Gerber, C., et al., Physical Review Letters, 1982. **49**(1): p. 57-61.
3. Binnig, G.; Quate, C.F.; Gerber, C., Physical Review Letters, 1986. **56**(9): p. 930-933.
4. Eigler, D.M.; Schweizer, E.K., Nature, 1990. **344**(6266): p. 524-526.
5. Moore, G.E., Electronics, 1965. **38**(8): p. 114-117.
6. Faraday, M., Philosophical Transactions of the Royal Society of London, 1857. **147**: p. 145-181.
7. Brust, M.; Walker, M.; Bethell, D., et al., Journal of the Chemical Society-Chemical Communications, 1994(7): p. 801-802.
8. Iijima, S., Nature, 1991. **354**(6348): p. 56-58.
9. Chang, S.S.; Shih, C.W.; Chen, C.D., et al., Langmuir, 1999. **15**(3): p. 701-709.
10. Martin, C.R., Chemistry of Materials, 1996. **8**(8): p. 1739-1746.
11. Braun, E.; Eichen, Y.; Sivan, U., et al., Nature, 1998. **391**(6669): p. 775-778.
12. Givargizov, E.I., Journal of Crystal Growth, 1975. **31**(DEC): p. 20-30.
13. Givargiz.Ei; Sheftal, N.N., Journal of Crystal Growth, 1971. **9**(1): p. 326-&.
14. Tersoff, J.; Tromp, R.M., Physical Review Letters, 1993. **70**(18): p. 2782-2785.
15. Himpsel, F.J.; Jung, T.; Ortega, J.E., Surface Review and Letters, 1997. **4**(2): p. 371-380.
16. Cheng, C.D.; Gonela, R.K.; Gu, Q., et al., Nano Letters, 2005. **5**(1): p. 175-178.
17. Curtis, C.L.; Ritchie, J.E.; Sailor, M.J., Science, 1993. **262**(5142): p. 2014-2016.
18. Collier, C.P.; Wong, E.W.; Belohradsky, M., et al., Science, 1999. **285**(5426): p. 391-394.
19. Reed, M.A.; Zhou, C.; Muller, C.J., et al., Science, 1997. **278**(5336): p. 252-254.

20. Javey, A.; Guo, J.; Wang, Q., et al., Nature, 2003. **424**(6949): p. 654-657.

21. Derycke, V.; Martel, R.; Appenzeller, J., et al., Nano Letters, 2001. **1**(9): p. 453-456.

22. Rueckes, T.; Kim, K.; Joselevich, E., et al., Science, 2000. **289**(5476): p. 94-97.

23. Zhong, Z.H.; Wang, D.L.; Cui, Y., et al., Science, 2003. **302**(5649): p. 1377-1379.

24. Kovtyukhova, N.I.; Mallouk, T.E., Chemistry-a European Journal, 2002. **8**(19): p. 4355-4363.

25. Lieber, C.M., Solid State Communications, 1998. **107**(11): p. 607-616.

26. Piraux, L.; Dubois, S.; Duvail, J.L., et al., Journal of Materials Research, 1999. **14**(7): p. 3042 - 3050.

27. Yi, G.; Schwarzacher, W., APPLIED PHYSICS LETTERS, 1999. **74**(12): p. 1746 - 1748.

28. Yin, A.J.; Li, J.; Jian, W., et al., Applied Physics Letters, 2001. **79**(7): p. 1039-1041.

29. Piraux, L.; Dubois, S.; Duvail, J.L., et al., Journal of Magnetism and Magnetic Materials, 1997. **175**(1-2): p. 127-136.

30. Cai, L.T.; Skulason, H.; Kushmerick, J.G., et al., Journal of Physical Chemistry B, 2004. **108**(9): p. 2827-2832.

31. Melosh, N.A.; Boukai, A.; Diana, F., et al., Science, 2003. **300**(5616): p. 112-115.

32. Jin, S.; Whang, D.M.; McAlpine, M.C., et al., Nano Letters, 2004. **4**(5): p. 915-919.

33. Evans, S.D.; Johnson, S.R.; Cheng, Y.L.L., et al., Journal of Materials Chemistry, 2000. **10**(1): p. 183-188.

34. Dodabalapur, A.; Someya, T.; Crone, B., et al., Abstracts of Papers of the American Chemical Society, 2002. **223**: p. 019-PMSE.

35. Dodabalapur, A., Solid State Communications, 1997. **102**(2-3): p. 259-267.

36. Wouters, D.; Schubert, U.S., Angewandte Chemie-International Edition, 2004. **43**(19): p. 2480-2495.

37. Xia, Y.N.; Whitesides, G.M., Angewandte Chemie-International Edition, 1998. **37**(5): p. 551-575.

38. Heath, J.R.; Kuekes, P.J.; Snider, G.S., et al., Science, 1998. **280**(5370): p. 1716-1721.

39. Stan, M.R.; Franzon, P.D.; Goldstein, S.C., et al., Proceedings of the Ieee, 2003. **91**(11): p. 1940-1957.

40. Zehe, A.; Martinez, J.G.R., Journal of Molecular Structure-Theochem, 2004. **709**(1-3): p. 215-222.

41. Ball, P., Nature, 2000. **406**(6792): p. 118-120.

42. Brust, M.; Bethell, D.; Schiffrin, D.J., et al., Advanced Materials, 1995. **7**(9): p. 795-&.

43. Shipway, A.N.; Katz, E.; Willner, I., Chemphyschem, 2000. **1**(1): p. 18-52.

44. Ye, Y.H.; Mayer, T.S.; Khoo, I.C., et al., Journal of Materials Chemistry, 2002. **12**(12): p. 3637-3639.

45. Connolly, S.; Fullam, S.; Korgel, B., et al., Journal of the American Chemical Society, 1998. **120**(12): p. 2969-2970.

46. Harfenist, S.A.; Wang, Z.L.; Alvarez, M.M., et al., Journal of Physical Chemistry, 1996. **100**(33): p. 13904-13910.

47. Cui, Y.; Bjork, M.T.; Liddle, J.A., et al., Nano Letters, 2004. **4**(6): p. 1093-1098.

48. Xia, Y.N.; Yin, Y.D.; Lu, Y., et al., Advanced Functional Materials, 2003. **13**(12): p. 907-918.

49. Lin, Y.; Boker, A.; Skaff, H., et al., Langmuir, 2005. **21**(1): p. 191-194.

50. Pieranski, P., Physical Review Letters, 1980. **45**(7): p. 569-572.

51. Hare, E.F.; Shafrin, E.G.; Zisman, W.A., Journal of Physical Chemistry, 1954. **58**(3): p. 236-239.

52. Liu, S.T.; Maoz, R.; Schmid, G., et al., Nano Letters, 2002. **2**(10): p. 1055-1060.

53. Colvin, V.L.; Goldstein, A.N.; Alivisatos, A.P., Journal of the American Chemical Society, 1992. **114**(13): p. 5221-5230.

54. Grabar, K.C.; Smith, P.C.; Musick, M.D., et al., Journal of the American Chemical Society, 1996. **118**(5): p. 1148-1153.

55. Bandyopadhyay, K.; Patil, V.; Vijayamohanan, K., et al., Langmuir, 1997. **13**(20): p. 5244-5248.

56. Boal, A.K.; Ilhan, F.; DeRouchey, J.E., et al., Nature, 2000. **404**(6779): p. 746-748.

57. Collier, C.P.; Vossmeyer, T.; Heath, J.R., Annual Review of Physical Chemistry, 1998. **49**: p. 371-404.

58. Demers, L.M.; Park, S.J.; Taton, T.A., et al., Angewandte Chemie-International Edition, 2001. **40**(16): p. 3071-3073.

59. Fleming, M.S.; Mandal, T.K.; Walt, D.R., Chemistry of Materials, 2001. **13**(6): p. 2210-2216.

60. Mann, S.; Shenton, W.; Li, M., et al., Advanced Materials, 2000. **12**(2): p. 147-150.

61. Ling, X.; Zhu, X.; Zhang, J., et al., Journal of Physical Chemistry B, 2005. **109**(7): p. 2657-2665.

62. Mendes, P.M.; Preece, J.A., Current Opinion in Colloid & Interface Science, 2004. **9**(3-4): p. 236-248.

63. Liu, S.T.; Maoz, R.; Sagiv, J., Nano Letters, 2004. **4**(5): p. 845-851.

64. Li, Q.G.; Zheng, J.W.; Liu, Z.F., Langmuir, 2003. **19**(1): p. 166-171.

65. Lee, H.; Purdon, A.M.; Chu, V., et al., Nano Letters, 2004. **4**(5): p. 995-998.

66. Hayward, R.C.; Saville, D.A.; Aksay, I.A., Nature, 2000. **404**(6773): p. 56-59.

67. Whitesides, G.M.; Boncheva, M., Proceedings of the National Academy of Sciences of the United States of America, 2002. **99**(8): p. 4769-4774.

68. Li, S.N.; He, P.G.; Dong, J.H., et al., Journal of the American Chemical Society, 2005. **127**(1): p. 14-15.

69. Xin, H.J.; Woolley, A.T., Journal of the American Chemical Society, 2003. **125**(29): p. 8710-8711.

70. Chen, X.Q.; Saito, T.; Yamada, H., et al., Applied Physics Letters, 2001. **78**(23): p. 3714-3716.

71. Chung, J.Y.; Lee, K.H.; Lee, J.H., et al., Langmuir, 2004. **20**(8): p. 3011-3017.

72. Lay, M.D.; Novak, J.P.; Snow, E.S., Nano Letters, 2004. **4**(4): p. 603-606.

73. Dierking, I.; Scalia, G.; Morales, P., et al., Advanced Materials, 2004. **16**(11): p. 865-869.

74. Rao, S.G.; Huang, L.; Setyawan, W., et al., Nature, 2003. **425**(6953): p. 36-37.

75. Liu, J.; Casavant, M.J.; Cox, M., et al., Chemical Physics Letters, 1999. **303**(1-2): p. 125-129.

76. Long, D.P.; Lazorcik, J.L.; Shashidhar, R., Advanced Materials, 2004. **16**(9-10): p. 814-+.

77. Jana, N.R.; Gearheart, L.A.; Obare, S.O., et al., Journal of Materials Chemistry, 2002. **12**(10): p. 2909-2912.

78. Yang, P.D.; Kim, F., Chemphyschem, 2002. **3**(6): p. 503-+.

79. Kim, F.; Kwan, S.; Akana, J., et al., Journal of the American Chemical Society, 2001. **123**(18): p. 4360-4361.

80. Dujardin, E.; Hsin, L.B.; Wang, C.R.C., et al., Chemical Communications, 2001(14): p. 1264-1265.

81. Mbindyo, J.K.N.; Reiss, B.D.; Martin, B.R., et al., Advanced Materials, 2001. **13**(4): p. 249-+.

82. Orendorff, C.J.; Hankins, P.L.; Murphy, C.J., Langmuir, 2005. **21**(5): p. 2022-2026.

83. Martin, B.R.; St Angelo, S.K.; Mallouk, T.E., Advanced Functional Materials, 2002. **12**(11-12): p. 759-765.

84. Smith, P.A.; Nordquist, C.D.; Jackson, T.N., et al., Applied Physics Letters, 2000. **77**(9): p. 1399-1401.

85. Duan, X.F.; Huang, Y.; Cui, Y., et al., Nature, 2001. **409**(6816): p. 66-69.

86. Mantooth, B.A.; Weiss, P.S., Proceedings of the Ieee, 2003. **91**(11): p. 1785-1802.

87. Huang, Y.; Duan, X.F.; Wei, Q.Q., et al., Science, 2001. **291**(5504): p. 630-633.

88. Lin, J.F.; Bird, J.P.; He, Z., et al., Applied Physics Letters, 2004. **85**(2): p. 281-283.

89. Durkan, C.; Welland, M.E., Critical Reviews in Solid State and Materials Sciences, 2000. **25**(1): p. 1-28.

90. Hertel, T.; Martel, R.; Avouris, P., Journal of Physical Chemistry B, 1998. **102**(6): p. 910-915.

91. Oon, C.H.; Thong, J.T.L., Nanotechnology, 2004. **15**(5): p. 687-691.

92. Pohl, H.A., Journal of Applied Physics, 1951. **22**(7): p. 869-871.

Chapter 2: Background, Theory and Experimental Techniques

This chapter introduces the background for the techniques important to the fabrication, assembly, and electrical characterisation of gold nanowires. The specific relevance and theoretical basis of certain key techniques is discussed in further detail. This information is used to introduce the experimental procedures and instrumentation used during the work presented in this thesis.

2.1: Structure and Electronic Properties of Gold

Gold is a soft yellow metal. It is chemically inert, and unaffected by air, water, alkalis and acids, with the exception of aqua regia. It is a good thermal and electrical conductor and has excellent reflective properties to both light and infrared. It has a face centered cubic crystalline structure where the cubic cell has length of 407.32 pm. Within this structure the closest gold-gold separation is 288.4 pm. It has an electrical resistivity of 2.2×10^{-8} Ωm and a melting point of 1337 K.[1]

2.2: Nanowire Fabrication

From the various nanowire fabrication techniques discussed in chapter 1, only template deposition has been used during the course of this work. The technique affords a high degree of control over the final shape, structure and functionality of fabricated nanowires. The template deposition technique is discussed in greater detail below.

2.2.1 Template deposition

Template deposition describes a process where thin fibrils of a desired material are synthesised within the voids of a porous host[2]. It is a versatile technique capable of producing complex structures from a variety of materials, but typically within the confines of a porous template. Deposition into template materials has been used to form magnetic[2], non-magnetic[2] and superconducting[3] nanowires, carbon[4] and conductive polymer[2] nanotubes, and many more complex structures.

The shape and structure of fabricated nanowires / nanostructures is defined by both the template geometry and the growth conditions. Many porous materials and zeolites provide suitable structures for template deposition of nanowires. At the larger end of the

scale, track-etched polycarbonate membranes and porous alumina are the two most commonly used materials. Huczko[5] has summarised many other potential zeolites below this scale suitable for template deposition, including aluminophosphate, aluminosilicate and porous silicon. Template materials used during the course of this work are described below.

2.2.1.1 Porous Alumina

The formation of porous alumina by anodising aluminium has been widely studied to protect and decorate the surface of aluminium, and to make inorganic membranes. When aluminium is anodised in neutral or basic solutions (pH>5), a corrosion resistant, flat, non-porous barrier film is produced.[6] However, at specific electrochemical conditions and in the presence of polyprotic acids a thick porous oxide layer is generated.[7] The porous oxide originates from the valve effect that causes some metal surfaces to act as diodes or rectifiers when an oxide layer is formed. The transport of certain ionic components across the oxide layer, that enable the chemical process at the metal-oxide and oxide-electrolyte interfaces, is limited by the structure of the oxide layer itself. Among the valve metals, pores are known to form in anodised Al, Si[8] and Ge[9].

Porous alumina is characterised by cylindrical pores of uniform diameter, perpendicular to the plane of the film. Whilst pores are open at the oxide surface, an oxide barrier layer closes each pore at its base and attaches the membrane to the aluminium substrate. The structural geometry is directly controlled by the anodising conditions. Pore diameters can be varied from ~5 nm[5] to several hundred nanometers[10, 11] with remarkable uniformity, and may be self-organised in a close-packed hexagonal array. Porous alumina membranes possess excellent mechanical, thermal, and optical properties, offer good corrosion resistance and can be exposed to both organic, and inorganic solutions[12]. These properties make porous alumina an ideal host material for template fabrication.

The frequently cited structure of porous alumina, Figure 2.1, depicts uniform cylindrical pores packed in a hexagonal cellular arrangement. Many contributory processes must be considered before the theoretical basis for porous alumina film formation can be understood.

Figure 2.1. Schematic representation of hexagonally ordered pores in anodic alumina

2.2.1.1.1 Formation of Porous Alumina

Throughout the growth of porous alumina two factors dominate; dissolution at the oxide-electrolyte interface, and oxide formation at the metal-oxide interface. During steady state growth the processes at each interface must be balanced such that the barrier oxide thickness remains constant. Alumina is considerably, but not entirely, ionic, so that its dissolution requires the breaking of Al-O bonds. Dissolution is enhanced by any process that weakens these bonds in the oxide, such as hydrogen bonding or the presence of an electric field, and the temperature dependence of the reaction rate. Whilst dissolution is dependent on the local field and chemical reaction kinetics, the growth rate is regulated by ionic transport across the oxide barrier layer, the current, Figure 2.2.[13]

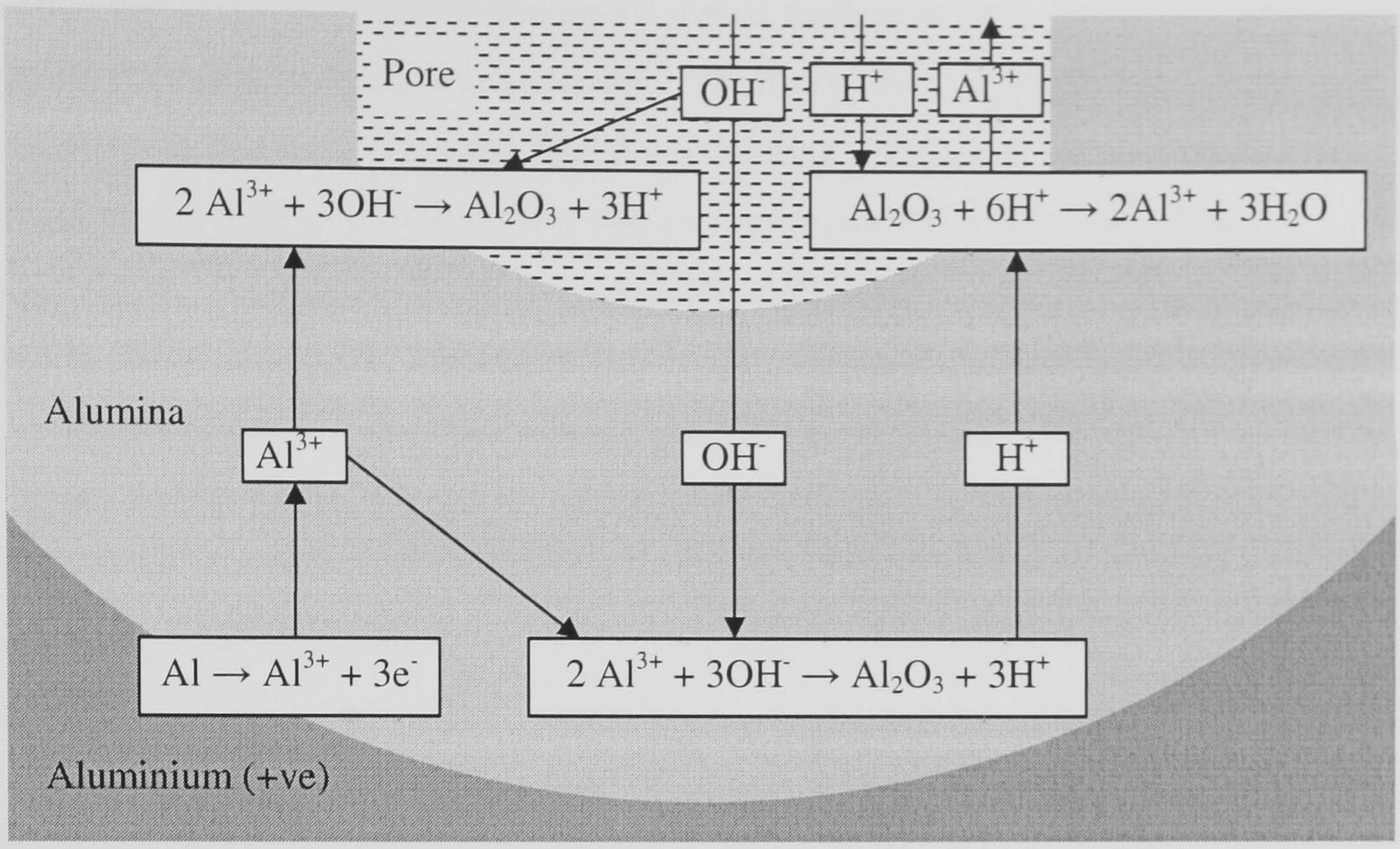

Figure 2.2. Oxide formation and dissolution at the metal-oxide and oxide-electrolyte interfaces[13]

Aluminium-oxygen bonds are effectively polarised upon the application of an electric field. At the oxide-electrolyte interface Al^{3+} ions are ejected into the solution and OH^- or O^{2-} ions are pulled into the oxide.[12] Under high field conditions, water molecules attracted to the alumina surface will also be polarised, with the negatively charged oxygen next to the surface. Hydrogen bonding between the hydrogen atoms of the water molecule and the oxygen atoms of the acid oxyanions is possible. Consequently, the O-H bond of the water molecule is weakened resulting in an OH^- or O^{2-} ion. At higher fields the discharge of the larger acid anion may become more competitive, and any such anions incorporated into the film modify the structure and properties of the oxide.[14] Aluminium is anodised more successfully in electrolytes that contain divalent or trivalent acid anions, which replace water molecules assembled at the alumina surface under the influence of an electric field. In addition such acids can form more than one anion by removal of successive protons from the acid molecule, equation 2.1 and 2.2.

Equation 2.1 $H_3PO_4 \rightarrow H^+ + H_2PO_4^- \rightarrow H^+ + HPO_4^{2-} \rightarrow H^+ + PO^{3-}_4$

Equation 2.2 $H_2SO_4 \rightarrow H^+ + HSO_4^- \rightarrow H^+ + SO_4^{2-}$

Chemical dissolution of the oxide, and consequently oxide growth, is also dependent on the electrolyte bath temperature[15]. The local temperature at pore bases can be increased by two factors; heat generated by exothermic chemical dissolution of the oxide, and Joule

heating due to electrical power dissipation across the barrier layer. It has been predicted that the later effect is the more significant.[16] Similarly, electrolyte pH affects the rate of dissolution. It has also been suggested the electrolyte pH drops at the pore bases, increasing the solubility of the oxide; this is an autocatalytic mechanism of pit propagation.[15] Vigorous stirring of the electrolyte has been shown to affect the current passed, and consequently, the growth rate[17]. Stirring does not affect the electrolyte at the base of pores; rather, it exchanges the bulk electrolyte at the pore-mouths. The exchange of species between the bulk electrolyte and pore bottoms is a diffusion-controlled process. As pore depth increases, the concentration gradient driving diffusion is reduced. It is the state of the electrolyte at the pore base that determines the chemical conditions for pore growth.[17]

2.2.1.1.2 Barrier Layer Chemical Composition.

Ionic transport, controlling oxidation at the metal-oxide interface, is highly dependent on the composition of the barrier layer. Transmission electron microscopy has shown that the barrier layer is not homogenous, but has a duplex structure containing microcrystallites of largely anhydrous alumina and intercrystallite regions containing molecular water, hydroxyl groups and the acid anions[18-20]. Alumina formed at the metal-oxide interface is anhydrous, but Al^{3+}, OH^-, O^{2-} and oxyanions from the acid are incorporated into the oxide with a concentration gradient towards the oxide-electrolyte interface. At steady state conditions the anhydrous alumina remains as columnar hexagonal support throughout the oxide and at the metal-oxide interface. Thompson's results[20] suggest that the thickness ratio of anhydrous alumina to acid anion contaminated material in porous alumina films is dependent on the electrolyte used: sulphuric acid (0.05) < oxalic acid (0.1) < phosphoric acid (0.5) < chromic acid (∞). This may be significant for ionic transport and the growth mechanism, but more recent results have failed to confirm these findings[18, 19].

2.2.1.1.3 Porous Oxide Growth

Coupled propagation of the metal-oxide and oxide-electrolyte interfaces determines how porous alumina is generated. The growth of porous alumina films at constant voltage has been determined to follow the processes outlined in Figure 2.3[11, 13, 15, 21].

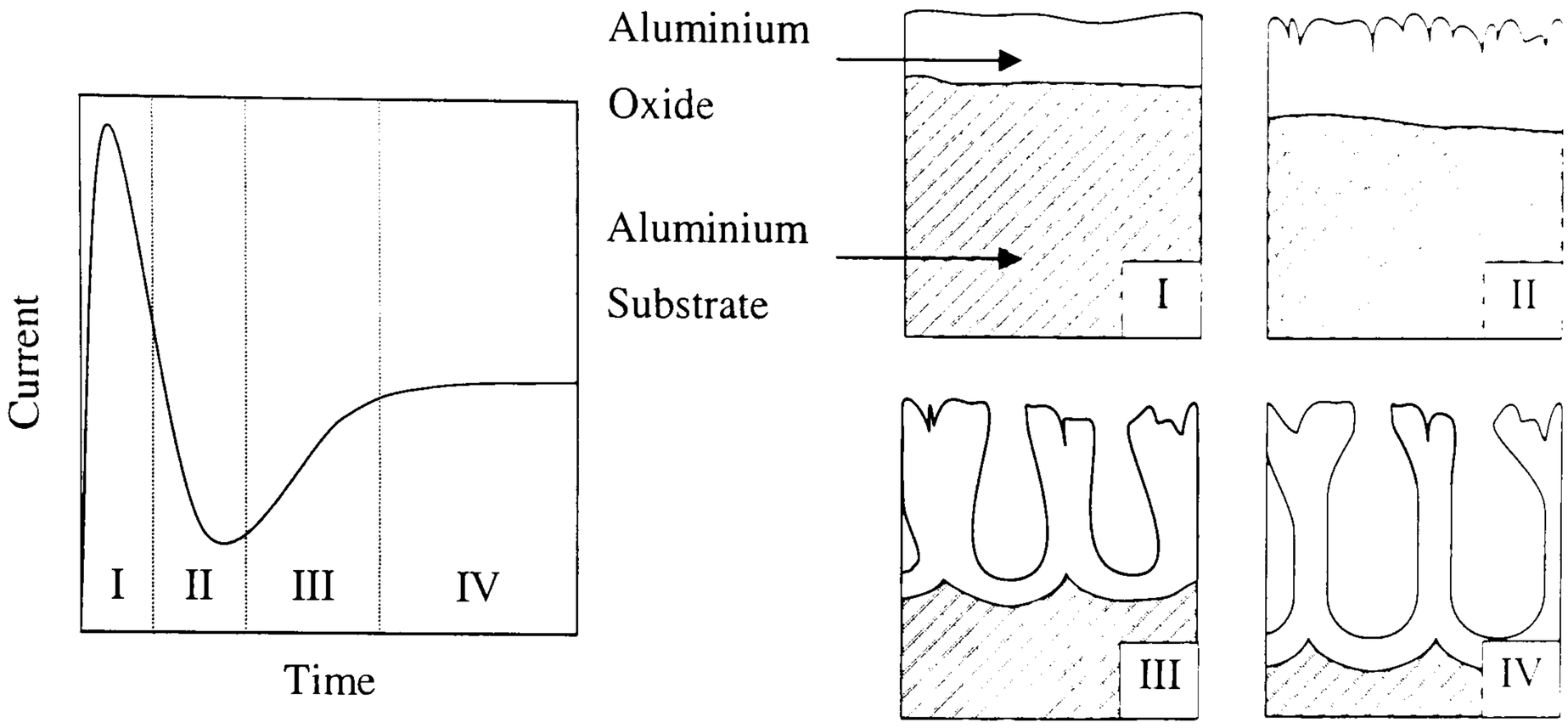

Figure 2.3. Schematic representation of pore development at constant potential, relating the pore formation to current. I – barrier layer formation, II – pore nucleation, III – pore selection, and IV – equilibrium growth[11, 13, 15, 21]

Stage I

Initially, ionic mobility through the natural oxide layer is high causing rapid oxidation at the oxide-electrolyte interface, with associated high currents. As the metal oxide interface moves deeper into the metal the barrier layer thickens and the rate of ion transfer, and oxidation, decreases.

Stage II

Pitting and cracks appear at the oxide/electrolyte interface prior to any true pore formation. Further anodising results in the propagation of individual paths to form nanopores. Initially pore density is very high.

Stage III

Pores increase in size, either by merging with adjacent pores, or by becoming established as the most effective dissolution sites.

Stage IV

Finally, the metal-oxide and oxide-electrolyte interfaces attain a constant and equal speed, associated with a steady current. The barrier layer thickness and pore base geometry regulate field enhanced dissolution at the pore base such that a specific density of uniformly sized pores is established.

Pores tend to nucleate first at grain boundaries, defects sites or depressions on the surface[21, 22]. On smooth substrates pores nucleate preferentially above grain boundaries.[23]

As a result the grain structure or surface roughness is commonly transferred to the pore structure, Figure 2.4[21, 22].

Figure 2.4. TEM micrograph showing pore nucleation along substrate grain boundaries[22]

Rapid pore nucleation along the substrate grain boundaries, Figure 2.4, is probably due to easier entry of ions into the film at defective sites leading to accelerated oxide growth[22]. Depressions in rough surfaces act as precursors to pores due to field enhancement at their bases. For a hexagonally close-packed pore array to develop from these initial conditions some interpore force must be present to cause lateral adjustment of pores during their development.

During steady state growth all main film parameters, barrier layer thickness, pore diameter, inter pore spacing, and the radius of the pore and cell bases, have been shown to be proportional to the applied potential, regardless of the electrolyte[22]. Proportionality constants are 2.8, 1.29 and 1.05 nm/V for the inter pore separation (Figure 2.5), pore diameter and barrier layer thickness, respectively[24]. The oxide film thickness is determined by the total charge passed.

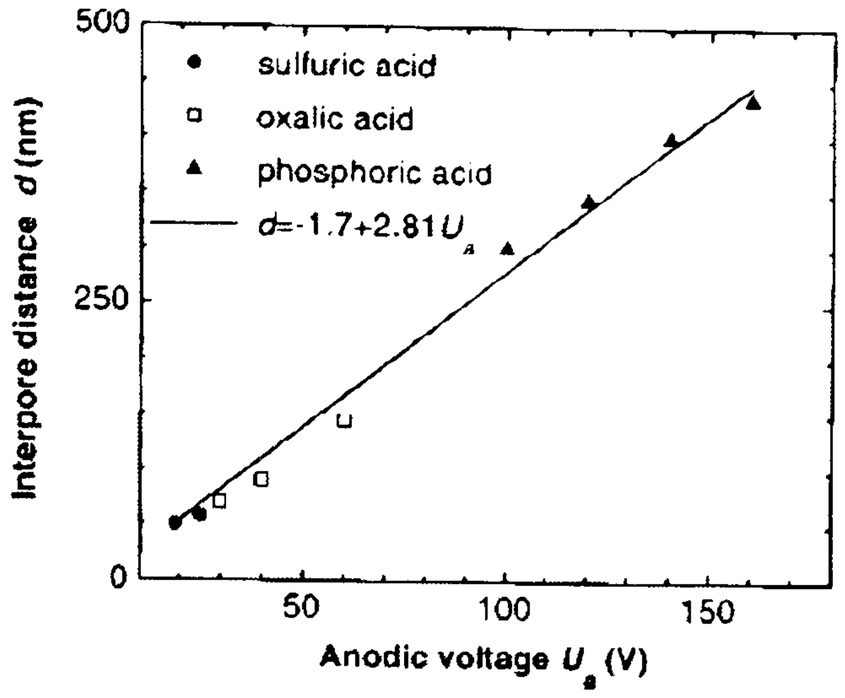

Figure 2.5. Proportionality between pore separation and anodic voltage for the three common electrolytes[25]

2.2.1.1.4 Theory of Porous Alumina Formation

The reason that porous alumina forms with such regularity during steady state growth has been addressed with several different explanations. Observed proportionalities between the geometrical parameters of the porous oxide and the applied voltage[22] have formed the basis of a structural-geometrical model[20, 24, 26]. In this model the electric field plays a key role in ionic transport and dissolution processes, and consequently controls the topography of the metal-oxide and oxide-electrolyte interfaces[21]. Similarly, a linear dependence of the pore size with applied potential can be predicted from a model based upon both the chemical reaction kinetics and pore base geometry[27, 28]. Assumptions that fix the geometry of pore base to be either hemispherical, or ninety degrees of a sphere[14], cause these models to predict a constant porosity although this is known not to be the case[29]. Importantly, the structural-geometrical model predicts that pores can be formed at any size, dependent only on the applied field. However, steady state pores can only be obtained at specific sizes dependent on the electrolyte used. At other potentiostatic conditions pores never achieve steady state growth, varying in diameter and splitting or terminating along their length[4].

The most complete explanation for pore formation is offered by Thamida *et al*[13]. The propagation of the metal-oxide and oxide-electrolyte interfaces are coupled by ionic transport and the applied field, but their topography is not constrained. However, propagation of the metal oxide interface is slaved to the oxide-electrolyte interface since the metal-oxide reaction kinetics is limited by the reaction rate at the oxide-electrode interface. Dissolution at the oxide-electrolyte interface is deemed dependent on the local

electrolyte pH. The importance of the pH of the electrolyte is supported by observations that the current, (i.e. oxide growth rate) increases with increasing acid concentration[21]. The diffusive time for ionic transport is assumed to be negligible when compared to the reaction times at the two oxide interfaces. Consequently, ionic transport is not rate dependent on the electric field, but an electric field of 2-3 V/nm is required to enable ionic transport across the barrier layer[13].

During the initial stages of oxide formation, the metal-oxide and oxide-electrolyte interfaces are flat, parallel and lie perpendicular to the direction of propagation. The oxide thickness increases until both interfaces move at the same speed. It is determined that the planar oxide thickness is proportional to the applied voltage, where the constant of proportionality is dependent on the pH of the electrolyte. Above a critical pH of 1.77 it is expected that pores would not form because the planar oxide thickens indefinitely.[13]

The development of pores is initiated by oscillations in the metal-oxide and oxide-electrolyte interfaces. Pores are formed where these oxcillations combine to amplify the local electric field. Where oscillations betweent the two interfaces are out of phase, no amplicfication or pore formation occurs, and the oscillation decays back to a planar oxide layer. In addition, only a certain range of wavelength perturbations are stable because lateral interactions between the 2 interfaces can destabilise pore formation. Due to these stabilising and destabilising influences on the topography of the oxide layer, pores of only a particular separation are favoured. The predicted pore separations are dependent on the applied voltage and electrolyte pH, and can be determined to be ~2 nm/V for $0 < pH < 1$.[13] Once pores are initiated they undergo a transient acceleration and finally approach a constant speed and shape. The exact pore shape and electric field distributions can be extracted as a function of pH. Consequently, the ratio of the pore to cell size (or porosity) is shown to be independent of potential but dependent on electrolyte pH and has good agreement with experimental results[13]. Lower pH electrolytes have a lower potential threshold for field enhanced dissolution at the pore tip. It should be remembered that the local pH and temperature conditions at the pore base may be significantly different to the bulk electrolyte properties.[16]

2.2.1.1.5 Hexagonal Self-Ordering

Whereas the structural-geometrical model suggests that porous oxide formation is not size selective, Thamida's model provides a mechanism for generation of only specific size

pores at steady state conditions. However, neither model predicts the hexagonal assembly of pores at certain steady state conditions, specific to the electrolyte used. Anodising at other conditions results in less or no self ordering, implying that pertubationless growth is essential for the construction of a regular array[30]. Optimum long range ordering occurs at 25V in 0.5 M sulphuric acid solution[31], 40V in 0.3 M oxalic acid solution[10, 32], and 195V in 0.3 M phosphoric acid solution[33], with inter-pore separation of 63, 100 and 500 nm respectively. Recently, self-ordered porous alumina has also been fabricated in citric acid characterized by a 600 nm inter-pore separation.[11]

Outside these experimentally determined self-ordering conditions little or no hexagonal structure is observed, although a variety of different pore distributions can produced by texturing the substrate aluminium prior to anodising[34]. However, where pore nucleation occurs randomly on the oxide surface, self-ordering can only be achieved with some inter-pore force[35], acting both during the inception stage of the pores and steady state growth[13]. Growth of coherent hexagonally ordered domains of pores proceeds with time, where expansion occurs by competitive ordering at the domain edges. Merged pores and point lattice defects can be observed where the structure has reorganised in an attempt to reconcile the differences in alignment of two adjacent domains[15]. This illustrates that there must be a lateral force. Changing conditions at the pore base may act to destabilise assembly for long growth periods, these include pH, temperature or ion concentration[15, 19].

Some authors have extended the structural-geometrical theory to predict hexagonal close packing of pores as a natural consequence, increasing in regularity with depth[14]. It is proposed that automatic levelling of the pore bases, resulting in hexagonal order, is the logical conclusion of the trend towards the equilibrium electric field distribution. However, this does not explain ordering at only specific conditions.

More recently the inter-pore force has been linked with stress generated at the metal-oxide interface, the interfacial-stress model[25]. Upon oxidation the atomic density of aluminium in alumina is a factor of two lower than in metallic aluminium[35]. For nonporous layers, with volume expansion ~2, interfacial stress is maximal and decreases with porosity. Under the influence of an electric field, Al^{3+} ions have mobility through the barrier layer and can be injected directly into the electrolyte without contributing to the oxide formation. Both this effect, and the dissolution of oxide at the pore-bases, reduce the expansion factor and associated stresses. The expansion factor associated with

hexagonally ordered oxide films grown at optimal ordering conditions is consistent for membranes formed in phosphoric, oxalic and sulphuric acid electrolytes[25, 35]. There is some discrepancy in the literature whether the optimal volume expansion for ordering is 1.4 [25] or 1.2 [35]. Investigation of the expansion factor and its relationship with applied voltage and electrolyte concentration can be seen in Figure 2.6.[24]

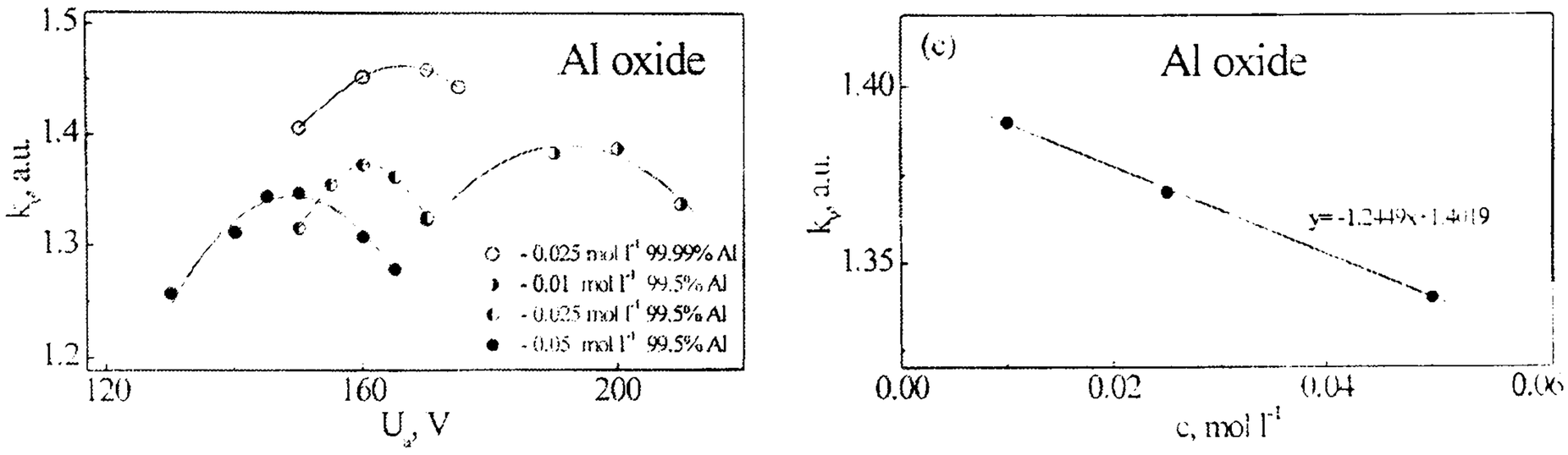

Figure 2.6. Dependence of the expansion factor, K_V, on applied voltage, U_a, and electrolyte concentration, c.[24]

The expansion factor, K_V, follows an inverted parabola with voltage, U_a, whilst the maxima of these parabola scales linearly with decreasing phosphoric acid concentration, increasing pH. Altering the anodising voltage from the known self-ordering conditions results in little or no hexagonal ordering. This provides an important mechanism that maximizes the volume expansion factor with voltage for a particular electrolyte, and suggests a route for pore-ordering at only a narrow ranges of voltages.

The interfacial-stress observations are supported by the 10% porosity rule[19]. Hexagonal ordering observed in the three commonly used electrolytes all have a porosity of ~0.1, and pore radius to cell radius ratio ~0.3. This porosity was produced when formation and dissolution of oxide was balanced and was morphologically most stable in terms of mechanical stress. Whereas Nielsch[19] believes the porosity at optimum ordering conditions to be a minimum, Ono's analysis[11] of the 'burnt' oxide regions suggests that the porosity continues to reduce, and hexagonal ordering is improved with increasing current density. Due to gas evolution and burning these high field regimes are often unobtainable. Despite these experimental observations the mechanism for hexagonal ordering of pores is not comprehensively exposed.

The role of pH on the formation of hexagonal structure was introduced by Thamida *et al*[13]. Modelled evolution of the pore structure from smooth substrates does not show significant hexagonal ordering. At steady-state conditions there is little lateral potential

gradient across the pore walls, and consequently there is little lateral dissolution as a result.[13] One suggested mechanism for the hexagonal ordering of disordered pores is horizontal mobility of ions in the barrier layer. The position of individual pores is adjusted by a change in shape of the pore base due to higher local ionic mobility in that region. This mechanism has been modelled in the Wheatstone bridge model, based upon simple circuit theory.[21] The size of the cell and barrier oxide for adjacent pores is considered to be electrically analogous to a Wheatstone bridge. Self ordering is achieved through spatial adjustment of the pore distribution in response to the feedback of the Wheatstone bridge.[21]

2.2.1.1.6 Synthesis of Porous Alumina Membranes – Procedure

Aluminium samples (10 mm × 10 mm) were cut from rolled high purity sheet (0.5 or 0.25 mm thickness, 99.99% purity, Advent), and annealed in a furnace at 450 °C overnight. Prior to anodising the samples, each was cleaned by sonicating in methanol, then DCM, and finally methanol before washing in MilliQ 18.2 MΩ water. These were placed into a custom built PTFE electrochemical cell to be anodised, figure 2.7.

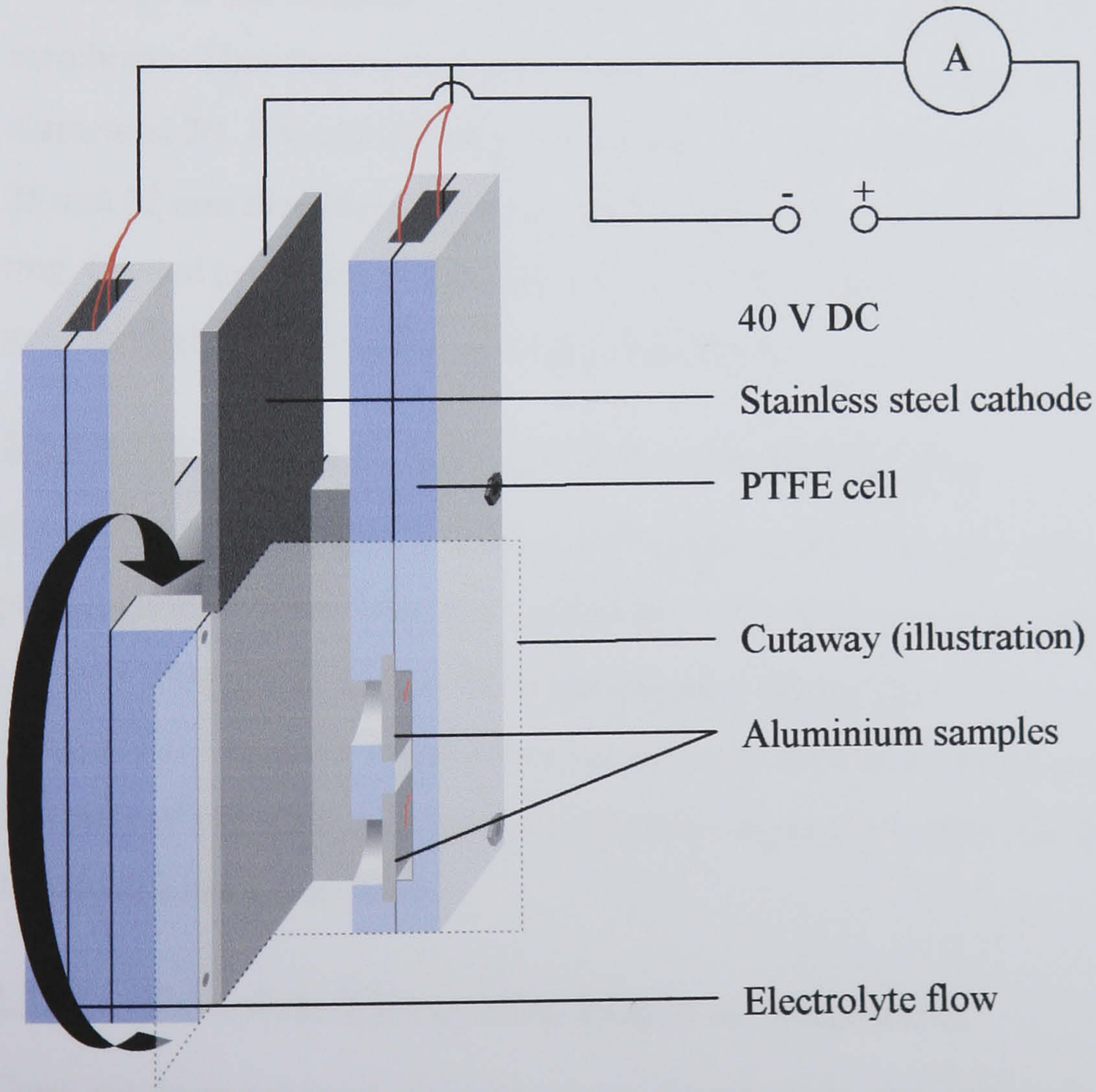

Figure 2.7. Schematic diagram of the electrochemical cell used to anodise aluminium substrates

The cell was designed such that it can be immersed in a beaker of electrolyte and only the stainless steel cathode and aluminium substrates are exposed to the electrolyte, whilst all contacts are kept dry. From the three commonly used electrolytes, only oxalic acid (Aldrich) at 0.3 M concentration was used during the course of this work. Four aluminium samples were anodised simultaneously, all independently connected in parallel to the power supply (TTI EX752M DC supply, I_{max} 2A) with the potential maintained at 40 V. Only one side of the aluminium samples is exposed to the electrolyte solution, each separated from the cathode by 10mm. The electrolyte within the beaker was vigorously stirred with a magnetic stirrer beneath the centre of the cell. Electrolyte flowed down through the centre of the cell to maintain the temperature and concentration of electrolyte at the aluminium substrate. During the course of each growth procedure the current was recorded to monitor the growth rate, and regime, Figure 2.3.

2.2.1.2 Whatman 'Anodisc' Filtration Membranes

Whatman 'Anodisc' filtration membranes consist of porous alumina, separated from the aluminium substrate and with the barrier layer removed. Consequently, pores are open at both sides of the membrane, although pores are not necessarily a uniform size through the membrane. They have a randomly ordered pore array, available with a range pore diameters; 20, 100 and 200 nm. The membranes are 66 μm thick, and are available in 13, 25 and 52 mm diameters; the larger membranes have a supporting polypropylene annular ring. Quoted porosities range from 25-50 %. The 20 nm filtration membranes have been used throughout the work presented in this thesis.

2.2.1.3 Whatman 'Cyclopore' Filtration Membranes

Polycarbonate Whatman 'Cyclopore' filtration membranes are produced by track-etching pure polymeric films. They are hydrophilic and available with a range of pore sizes between 100 nm and 12 μm. They are typically 20 μm thick and available in the same diameters as 'Anodisc' membranes. Membranes are free from contaminants, and stable at in variety of pH solution conditions and some organic solvents. The 200 nm filtration membranes have been used.

2.2.2 Template Electrodeposition of Nanowires

There are many reported methods used to fill the pores of template materials, including electrodeposition (the most common), electroless deposition, sol-gel deposition, and evaporation.[5] The techniques used during the course of this work are discussed below.

2.2.2.1 Electrodeposition

During electro-deposition the base of the template acts as an electrode in an electrochemical cell. For the fabrication of nanowires the template itself is insulating, but pore bases represent the least impedance path between the 2 electrodes.[22] Ions of the desired material are reduced from an electrolyte and aggregate at the pore's base under the influence of a constant, alternating or pulsed electric field. Electro-deposition into the pores of porous alumina films have been shown to result in the formation of polycrystalline[2] and single-crystal[36] structures.

The growth mechanism of nanowires within a porous template is complex, and must remain speculative. Zhang suggests that homogenous growth requires a slow rate of deposition[36]. Two factors can affect the growth rate, the applied potential and diffusion of ions to the deposition front. A certain over-potential is required for nucleation and growth processes, but the rate of nucleation at the deposition front, and size of these sites, increases with the potential.[37] The diffusion rate is most significantly controlled by the pore diameter and depth, although bulk ion concentration is important.[36] Hydrogen evolution at the deposition front becomes significant when deposition is diffusion limited, and disrupts the formation of homogenous nanowires. By reducing the number of nucleation sites at the deposition front and disruption due to hydrogen formation, fine crystalline nanowires without grain boundaries can be produced. Such nanowires grow with a preferential lattice orientation with respect to the axis of the pore, and are effectively single-crystal.[37]

A variety of electrolytes have been used during the course of this work. These are summarised below, and shall henceforth be referred to by their title.
Sulphuric: An aqueous electrolyte containing 0.02 M $HAuCl_3.3H_2O$, pH adjusted to 2 by the addition of 5 wt% sulphuric acid.
Hydrochloric: An aqueous electrolyte containing 0.02 M $HAuCl_3.3H_2O$ and 1 M NaCl, pH adjusted to 1.5 by the addition of 5 wt% hydrochloric acid.
Neutral: An aqueous electrolyte containing 0.02 M $HAuCl_3.3H_2O$, pH adjusted to 5 by the addition of 1 M NaOH.

2.2.2.2 Electroless Deposition

Electroless metal deposition is a process whereby metal is deposited on a surface from a solution via chemical reduction. An active metal seed must be present as a catalyst to

initiate deposition, and subsequent growth is autocatalytic. A commercial solution, Technic Oromerse Part B, has been used for all deposition procedures. The gold plating was performed as described by Menon *et al*[38] in a solution that was 7.9×10^{-3} M $Na_3Au(SO_3)_2$ (the diluted form of the commercial plating solution), 0.127 M Na_2SO_3, (Aldrich) and 0.625 M formaldehyde (Aldrich). Prior to deposition the solution and equipment used was cooled to 2-4 °C, and this temperature was maintained thoughout growth.

2.2.2.3 Deposition Procedure

Deposition into all the template membranes discussed above was undertaken in a custom built PTFE electrochemical cell, Figure 2.8.

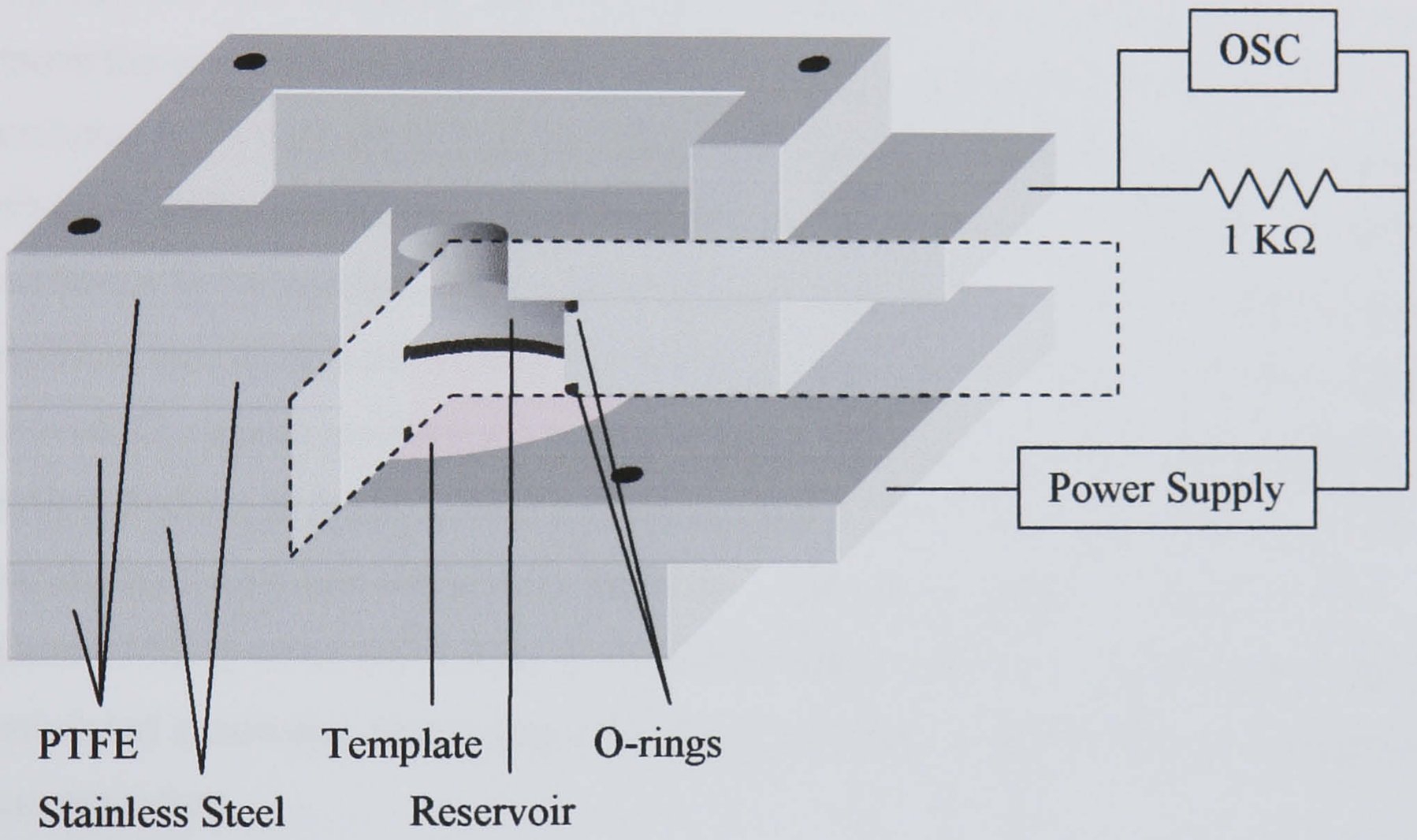

Figure 2.8. Diagram showing the cell used to template deposit gold into porous membranes

The template membrane is sandwiched between one stainless steel electrode, and a cylindrical electrolyte reservoir in the central PTFE block. A stainless steel counter-electrode fits above the reservoir, with a central hole to allow the escape of any gas produced during deposition, and excess electrolyte. The central reservoir is sealed with o-rings to prevent the leakage of electrolyte. The entire cell is bolted together, sandwiched by PTFE blanking plates on either side, with threaded bar and bolts. The porous alumina membranes are used whilst still attached to their aluminium substrate, which acts as the electrode base for the pores via contact with the bottom stainless steel plate. Whatman 'Cyclopore' and 'Anodisc' filtration membranes had a 500 nm silver electrode evaporated

onto one side for the same purpose. The evaporation was effected using an Edwards Auto 306 evaporator operating at a base pressure of 2×10^{-6} mbar.

Electroless deposition has only been conducted in Whatman 'Anodisc' and 'Cyclorpore' membranes, and was performed in the same cell with the electronics disconnected. The cell was filled with the electroless solution, sealed to prevent evaporation, and placed in a fridge at 4°C. The electroless solution filled the pores of the hydrophilic membrane, and gold reduction was catalysed by the evaporated silver film at the base of the pores.

2.2.2.4 Removing Nanowires from the Template Host

The procedure to liberate nanowires from their template host varied with each type of template used. For Whatman Anodisc and Cyclopore membranes it was first necessary to remove the evaporated silver electrode. This was achieved by sonicating the entire membrane in 70 wt% nitric acid for 1 hour. Aluminium oxide can be etched with sodium hydroxide, and nanowires were released from porous alumina and Whatman 'Anodisc' membranes by immersion into a 1 M solution for approximately 1 hour. After the oxide membrane was completely etched the aluminium substrate or supporting annular ring was removed. Cyclopore membranes were dissolved in chloroform, leaving nanowires in solution. Sodium hydroxide, or contaminated chloroform, was removed by repeatedly centrifuging the sample and pouring away the supernatant. After every cycle 18.2 $M\Omega cm^{-1}$ MilliQ water was added, and the sample sonicated to redistribute and clean the precipitated nanowires. Nanowires were transferred from water to HPLC methanol by the same procedure.

2.3: Nanowire Assembly

A variety of assembly techniques have been used to manipulate nanowires. Presented below is a summary of the background information for each technique.

2.3.1 Surfactant Based Assembly

By chemically modifying the surface properties of nanowires with surfactants, their interactions with polar fluids, other nanowires, and surfaces can be changed, thus providing a means for self-assembly. Surfaces were modified with organothiol surfactants.

2.3.1.1 Organic Thin Films

Organic thin films are close-packed organisations of molecules. These assemblies were first investigated at fluid-air interfaces by Langmuir[39] and Blodget[40]. Molecules were organised by compressive forces at the fluid-air interface, and could be transferred to solid substrates by physisorption[40]. In recognition of their work, monolayers and multilayers generated by this technique have become known as Langmuir-Blodget (LB) films.

Self-organisation of molecular films was first reported in by Zisman *et al*[41]. Rather than directing the organisation of molecules with compressive forces at interfaces, they were chemisorbed directly onto substrates. A single layer of molecules is assembled, followed by their spontaneous rearrangement to form an ordered structure. They are commonly referred to as Self-Assembled Monolayers, or SAMs.

2.3.1.2 Self-Assembled Monolayers

Self-assembled monolayers are formed spontaneously when molecules from a gas or liquid phase are exposed to a surface with which they bind strongly. The bonds can be covalent (organosilanes on SiO_2[42-47]), polar covalent (organosulphurs on gold[48]), or ionic (carboxylic acids on silver[49]). The energies associated with these interactions are exothermic and typically in the order of tens of kcal/mol, i.e. energetically favourable.[50] For this reason, the surfactant molecules try to occupy every available reaction site. In general, molecules used in SAM formation are surfactants with an active head group that interacts with the substrate, and a tail group that determines the new surface properties. Only one region of the molecule should have a strong affinity for the substrate, such that upon absorption all molecules are oriented in the same way[51].

Order within the monolayer is achieved by a rearrangement of the molecules towards a minimum energy configuration. The final arrangement arises from a combination of van der Waals and electrostatic forces, in addition to steric repulsion. It should be noted that it is rare that molecules involved in SAM formation are oriented exactly perpendicular to the surface. The degree to which they are tilted however depends on many factors, including steric influences, and the nature of the bond between the molecule and surface.

The functionality of the tail group can have a significant affect on the chemical and physical properties of the surface.[52] The tail-groups can be tailored for subsequent

reactions with biomaterials[53, 54], colloids[55], or polymers[56]. Substituted groups commonly found in the literature are methyl[52, 57, 58], hydroxyl[52, 59-61], carboxyl[62, 63], amine[52, 55], and fluorinated alkyl[64-67] units.

2.3.1.3 Self Assembled Thiol Monolayers on Gold

Although organothiol molecules have also been used to functionalise silver[52, 68-70], copper[52, 69, 70], platinum[71], mercury[72, 73], and iron[74, 75], they are most commonly assembled onto gold substrates[48]. The nature of the covalent bonding between thiol groups and gold substrates is sufficiently strong to displace most physisorbed impurities from a surface during monolayer formation[76], although clean substrates improve the reproducibility of SAM formation. The "adsorption times" of monolayers typically vary from minutes to several hours, depending on surfactant molecular structure, solvent, and solution concentration.[57] Initially, molecules are absorbed onto the gold surface at a rate defined by the solution concentration, and described by diffusion controlled Langmuir absorption. The thiol group undergoes cleavage of the sulphur-hydrogen bond, followed by the binding of the sulphur group to gold, and the formation of a thiolate. Following the initial rapid absorption the molecules undergo conformation changes to minimise the free energy of the SAM. The molecular tilt of molecules within the SAM from perpendicular is governed by the interaction between the sulphur and gold in addition to interactions between the tail groups. This section on alkyl thiols on gold was designed to act as brief introduction to this field, for a much more detailed review of alkanethiols the reader is directed towards the works of Ulman and Tredgold.[49, 50, 57, 77]

2.3.1.3.1 SAM formation procedure

Self assembled monolayers of thiol molecules were formed on planar gold surfaces, by immersion in solution overnight. Metal surfaces were fabricated by thermal evaporation onto silicon surfaces (Edwards Auto 306). A thin chromium film (10 nm) was first evaporated onto a freshly cleaned silicon surface, as an adhesion layer, followed by the deposition of 80 nm of 99.99% gold (Advent). All depositions were made at a base pressure of 2×10^{-6} mbar and the evaporation rates were maintained between 0.05 and 0.15 nm/s. The substrate surfaces were suitable for SAM formation if used immediately; otherwise they were cleaned in piranha solution at 80 °C for 20 s prior to SAM formation.

During the course of the work presented here, four commercially available thiols have been used; mercapto-1-undecanol ($HS-(CH_2)_{11}-OH$) [OH], mercaptoundecanoic acid (HS-

$(CH_2)_{10}$-COOH) [COOH], 4-aminothiophenol ($NH_2C_6H_4SH$) [ATP], and dodecanethiol ($HS-(CH_2)_{11}-CH_3$) [CH_3], all obtained from Aldrich. Two further thiols, a fluorinated [CF_3] thiol ($CF_3(CF_2)_9(CH_2)_6SH$) and an amine [NH_2] terminated thiol ($NH_2(CH_2)_2(OCH_2CH_2)_8NHC{=}OCH_2CH_2SH$), were supplied by the Seiko-Epson corporation. A thiolated biotin molecule [biotin] has been previously produced[78] and used from stock. These materials shall be referred to henceforth by their abbreviation, or terminal group, shown in square brackets. Surfaces were functionalised by immersion into 1 mM concentrations of thiol in HPLC grade methanol, and left overnight. After removal, surfaces were sonicated, and washed in further HPLC methanol, washed in 18.2 $M\Omega cm^{-1}$ MilliQ water and dried under N_2.

2.3.1.4 Patterned Self Assembled Monolayers

The ease of SAM formation, and the variety of molecules available, makes them an important route for changing surface functionality. Furthermore, patterned SAM surfaces can be generated by a variety of techniques with many potential applications. Several techniques are used to pattern SAMs on surfaces; electron or ion beam irradiation[79-86], SPM-surface interactions[87-90], micro-contact printing and UV irradiation[91-95]. Only micro-contact printing is discussed here, further information on the other techniques mentioned may be found in the cited references.

2.3.1.4.1 Micro-Contact Printing

The micro-contact printing technique was developed by Whitesides and Kumar.[96] Typically, the substrate is patterned with single species of SAM by transfer from a textured elastomeric stamp, with resolution > 30 nm[97, 98]. Textured stamps are commonly fabricated from polydimethylsiloxane (PDMS), moulded from an etched silicon "master". The master is fabricated using conventional lithographic photo-resist or electron beam-resist procedures.[99] The PDMS stamp is 'inked', dried, and lightly pressed onto the substrate, Figure 2.9.

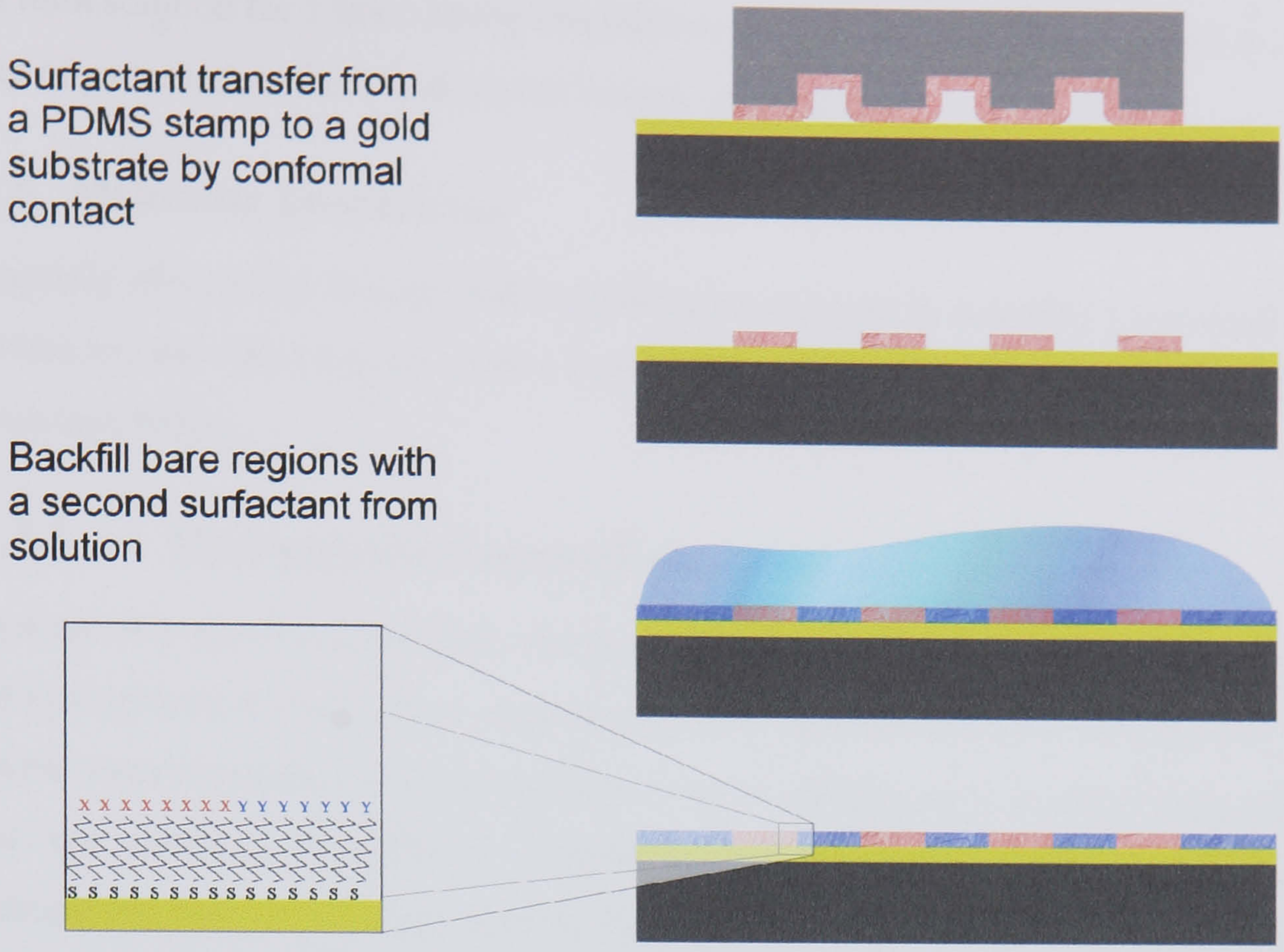

Figure 2.9. Schematic diagram of microcontact printing a patterned SAM

Molecules absorbed onto the PDMS stamp are transferred to the substrate upon contact. Finally, the bare regions of substrate are back-filled by incubating in a solution containing a different SAM material.[97, 100] Although quick, cheap, and effective this technique is not without its problems. The resolution of the pattern is limited by the master, and ultimately the PDMS material.[101] Furthermore, the reproducibility of the process is dependent on the stamps resistance to degradation, the replication of the contact pressure that is applied to the stamp, and the surface roughness.

2.3.1.4.2 Patterned SAMS – Experimental Procedure.

Silicon substrates were cleaned in piranha solution and washed in MilliQ water (resistivity = 18.2 $M\Omega cm^{-1}$). A 100 nm gold film was evaporated onto the Si surfaces, bound with a 10 nm Cr adhesion layer. During microcontact printing a polydimethylsiloxane (PDMS – Sylgard 184) textured stamp was coated with one thiol material by immersion in a 7 mM methanol based thiol solution for 60 seconds, and dried under nitrogen. The textured PDMS surface was brought into conformal contact with the gold substrate for 10 seconds. Where the textured stamp touches the gold surface surfactant is transferred from the stamp to the gold surface. The remaining bare regions of the substrate were 'backfilled' by immersing the substrate in the second 3 mM methanol

based thiol solution for 1 hour. Using this technique it has been possible to produce a variety of patterned surfaces with repeat lengths above 2 μm.

2.3.1.5 Molecular Interactions

The capacity of a variety of noncovalent binding interactions to assemble functionalised nanowires has been investigated. These interactions, and their experimental application, are discussed below.

2.3.1.5.1 Hydrophobic Interactions

The hydrophobic effect is associated with the ordering of water, or another polar solvent, around hydrophobic material. Non-polar hydrophobic material is unable to hydrogen bond with water molecules; and consequently water molecules form an ordered hydrogen bonded cage around the hydrophobic material. This provides an entropic driving force for the hydrophobic material to aggregate and thereby reduce the hydrophobic surface area available to the solvent. However, this ordering effect is only effective over the range of ordering in the water molecules, typically a few angstroms. Since the first observations of the hydrophobic interaction[102, 103] experimental evidence has suggested that other, long range hydrophobic interactions exist[104-106]. Suggested mechanisms for this long-range interaction include electrostatic charge or dipole-dipole interactions[107], water structure[102], phase metastability[108], and sub-microscopic bubbles[109] although none offer a complete explanation.

Hydrophobic interactions have been investigated as a possible route to drive the assembly of nanowires. The behaviour of nanowires functionalised with a hydrophobic surfactant in aqueous solutions has been investigated. Their interaction with the solvent may cause nanowires to aggregate in order to minimise the total surface area exposed to the solvent. In addition, hydrophobic nanowires have been interacted with patterned hydrophilic / hydrophobic surfaces, in methanol.

2.3.1.5.2 Surface Wettability

The wettability of a surface corresponds to minimisation of cohesive forces within the water droplet and adhesive forces between the surface and droplet[110]. Hydrophilic surfaces strongly interact with water, via dipole-dipole and hydrogen bonding. These adhesive forces dominate the behaviour of a water droplet, which will spread across the surface. Hydrophobic surfaces do not undergo hydrogen bonding, and have weak dipole-

dipole and van der Waals interactions with water. The cohesive forces within a water droplet on the surface are dominant, and the droplet tends to bead to minimise contact area with the surface.

The interaction of the water with the surface is largely dependent on the chemical functionality of the surface. SAMs can be used to modify the wettabilty of surfaces to be either hydrophilic (OH or COOH terminated) or hydrophobic (CH_3 or CF_3 terminated). In this section we consider perhaps the simplest mechanism for the positioning of nanowires. A droplet of nanowire solution is placed upon a surface with patterned surface with stripes of contrasting hydrophobicity / hydrophilicity, Figure 2.10.

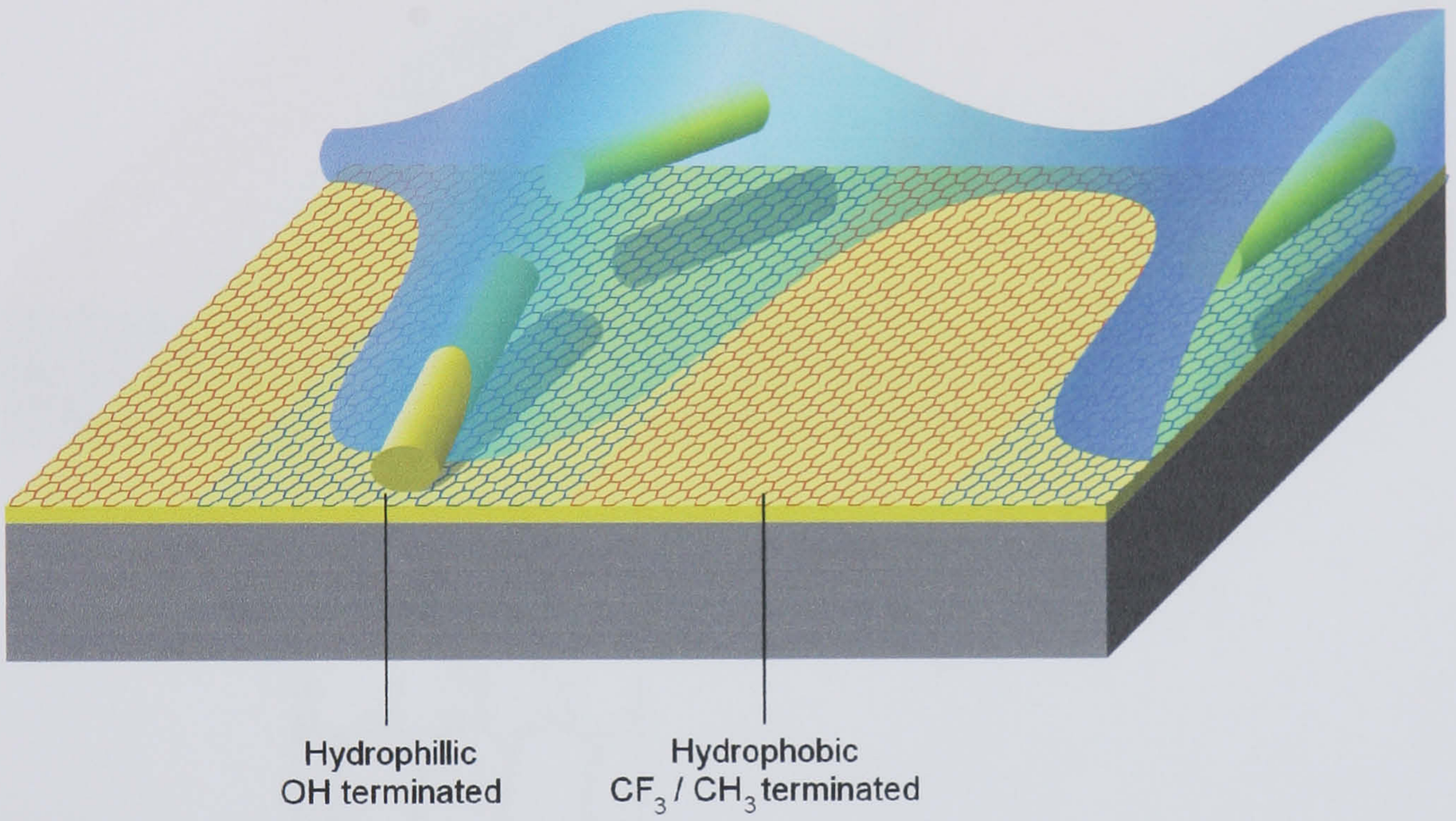

Figure 2.10. Schematic diagram of nanowire assembly on surfaces with patterned wettability. Solvent preferentially wets the hydrophilic regions of the surface, drawing nanowires into these regions

The behaviour of the droplet is determined by the surface-fluid interaction, and this in turn may determine how nanowires within the droplet behave. The situation is complicated since the nanowires may have either a hydrophilic or hydrophobic surface, and their final position may also depend upon this.

2.3.1.5.3 Hydrogen Bonding

Hydrogen bonding is a force of attraction between a hydrogen atom in one molecule and a small atom of high electro-negativity, such as O, F or N, in another molecule. The hydrogen atom has a partial positive charge that induces a local dipole. The hydrogen

bond is a dipole-dipole attraction between the positively charged hydrogen and an electronegative atom in another molecule.

Using patterned SAMs comprised of COOH and OH regions allows one to look at surfaces with similar wettability, but that interact with COOH functionalised nanowires quite differently. The carboxylic acid terminal groups of mercaptoundecanoic acid can bind by hydrogen bonding[111, 112], and this process has been investigated as a mechanism for attaching the wires onto the COOH regions of the surface, Figure 2.11.

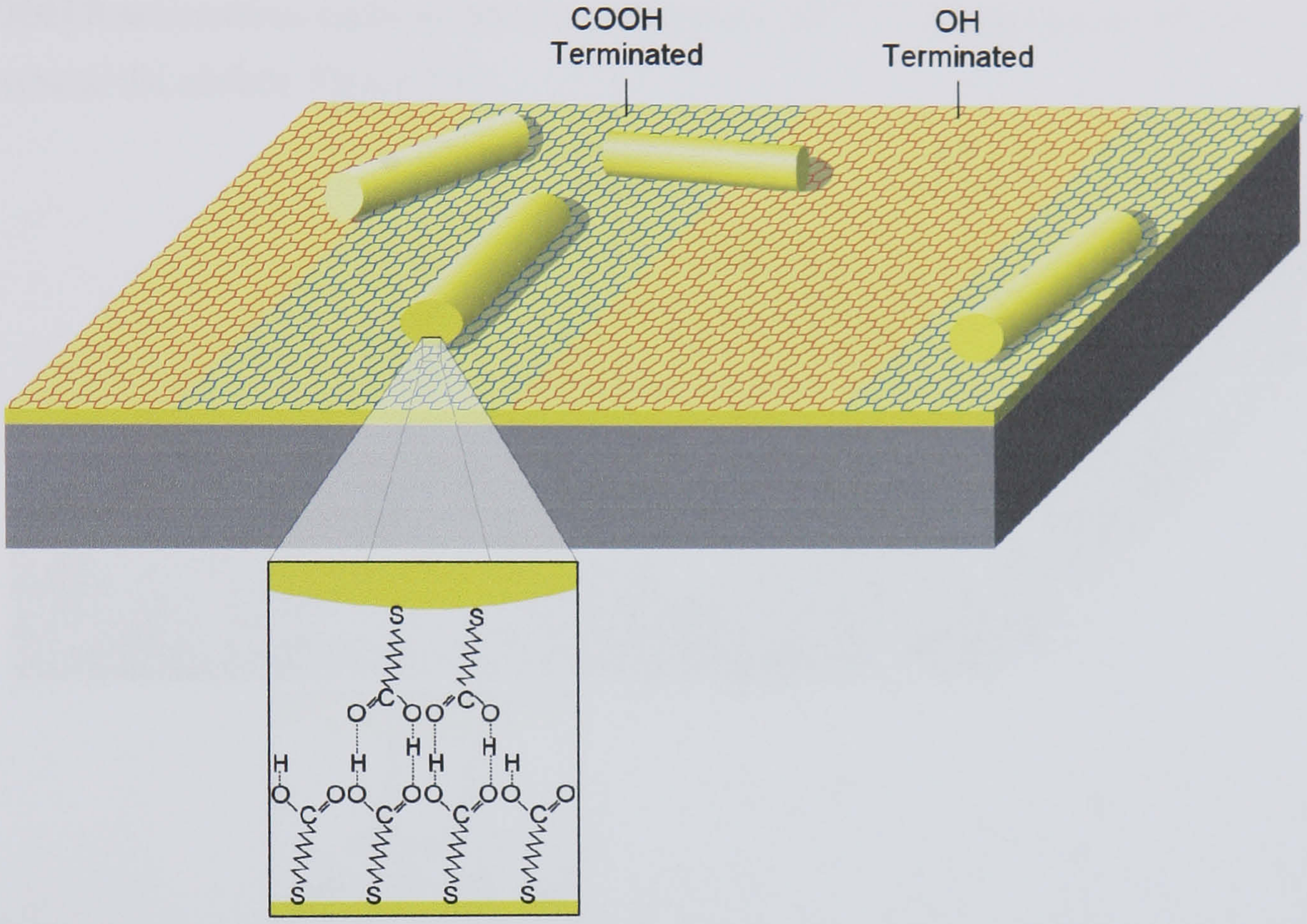

Figure 2.11. Schematic diagram showing chemical attachment of nanowires to reactive surface regions by hydrogen bonding

2.3.1.5.4 Carboxylate Complexes with Transition Metal Ions

As discussed in the previous section, the electronegative oxygen atoms in a carboxylic acid group tend to pull the electron away from any bound hydrogen. The remaining proton can more easily leave the molecule, and the remaining negative charge is then distributed symmetrically between the two oxygen atoms. Carboxylates, the anions of carboxylic acids, can bind to a metal ion through one or both oxygen atoms, and are also capable of binding to two metal ions by co-ordinating one oxygen with each metal ion. The formation of carboxylate complexes with divalent metal ions can be used to bind molecules containing carboxylic acid groups. Similarly, metal ions can be selectively

trapped by carboxylic acid groups of SAM surfaces, and used to form carboxylate salt multilayers[113].

The use of carboxylate salt formation as an assembly technique between COOH functionalised surfaces is a logical step. Surfaces identical to those prepared for the previous section are exposed to 1 M $CdCl_2$ aqueous solutions. In such solutions the carboxylic acid terminal groups are expected to deprotonate, and form a carboxylate salt with metals ions from solution. An identical procedure was used to expose these surfaces to COOH functionalised surfaces, and the carboxylate salt[113-115] is expected to bind the nanowire to the surface, Figure 2.12.

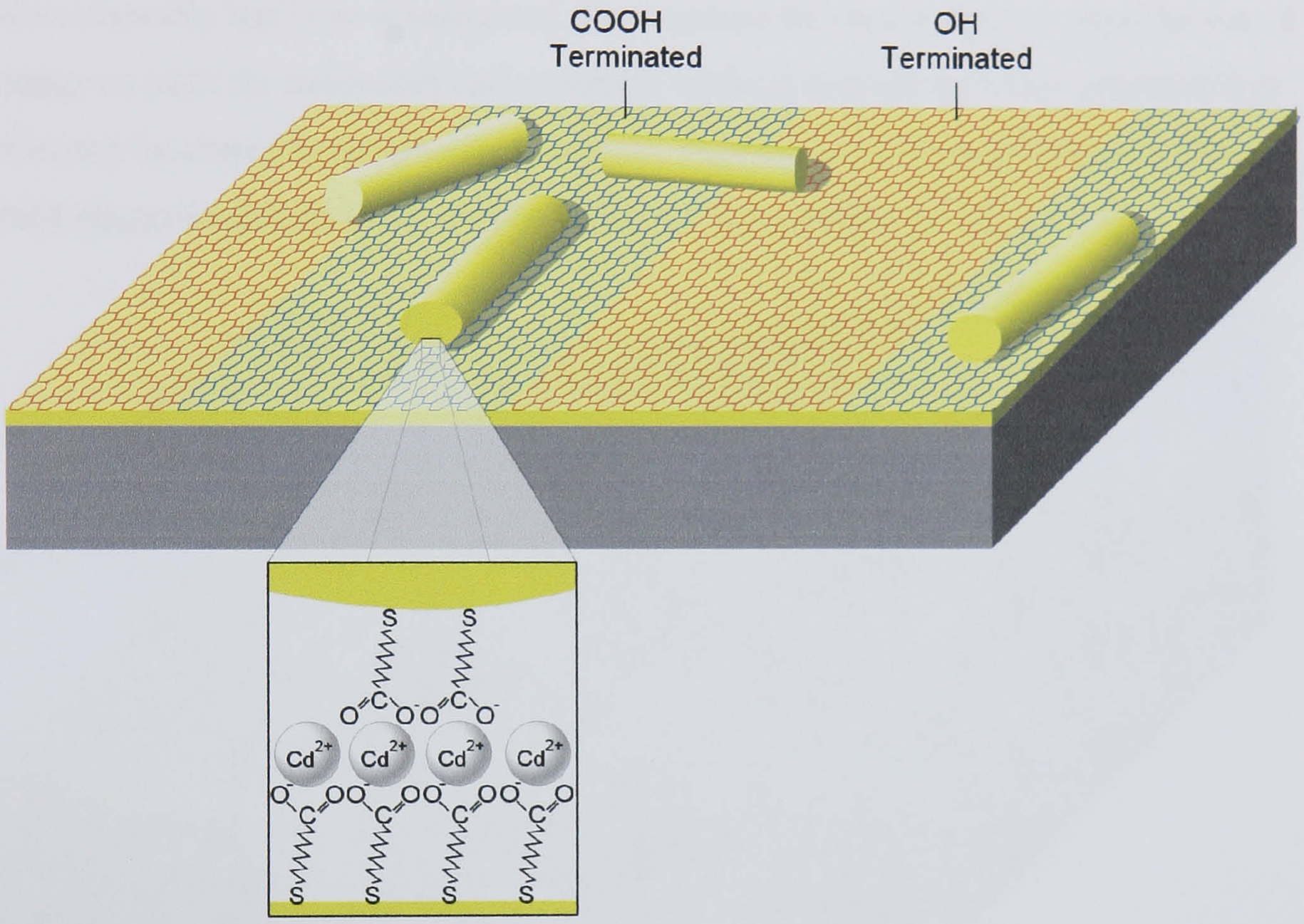

Figure 2.12. Schematic diagram showing chemical attachment of nanowires to reactive surface regions by carboxylate salt formation

2.3.1.5.5 Electrostatic Interactions

The interaction of charged groups within a molecule, or between molecules, results in a force determined by Coulomb's Law. These forces may cause the deformation of single molecules, the formation or molecular assemblies, or repulsive separation of molecules. The forces between like charges are repulsive and between opposite charges they are attractive, and consequently the molecular orientation is usually important. The origin of charged groups is dependent on the pH of the solution. Increasing salt concentration

reduces the strength of charged interactions by providing an excess of ions in solution that shield the charged groups. Although many chemical groups can become charged, the following discussion shall concentrate on the ionization of carboxylic acid and amine groups. Whitesides[116] determined that the creation of a charged group from a neutral one at the interface between functionalised surfaces and water is more difficult than that in a homogeneous aqueous solution. Subsequent investigations have shown that COOH SAM surfaces deprotonate to COO^- with a pKa value of ~5.5[117, 118], and NH_2 SAMs protonate to NH_3^+ with a pKa value of ~7.5[117-120].

The capability of electrostatic interactions between nanowires and surfaces to drive nanowire assembly has been investigated. Electrostatic forces are derived from the use of surfactants on both the nanowires and patterned surfaces that can be either protonated or deprotonated by changing the pH of the solvent. Nanowires have been interacted with patterned charged surfaces in an attempt to control their assembly, Figure 2.13.

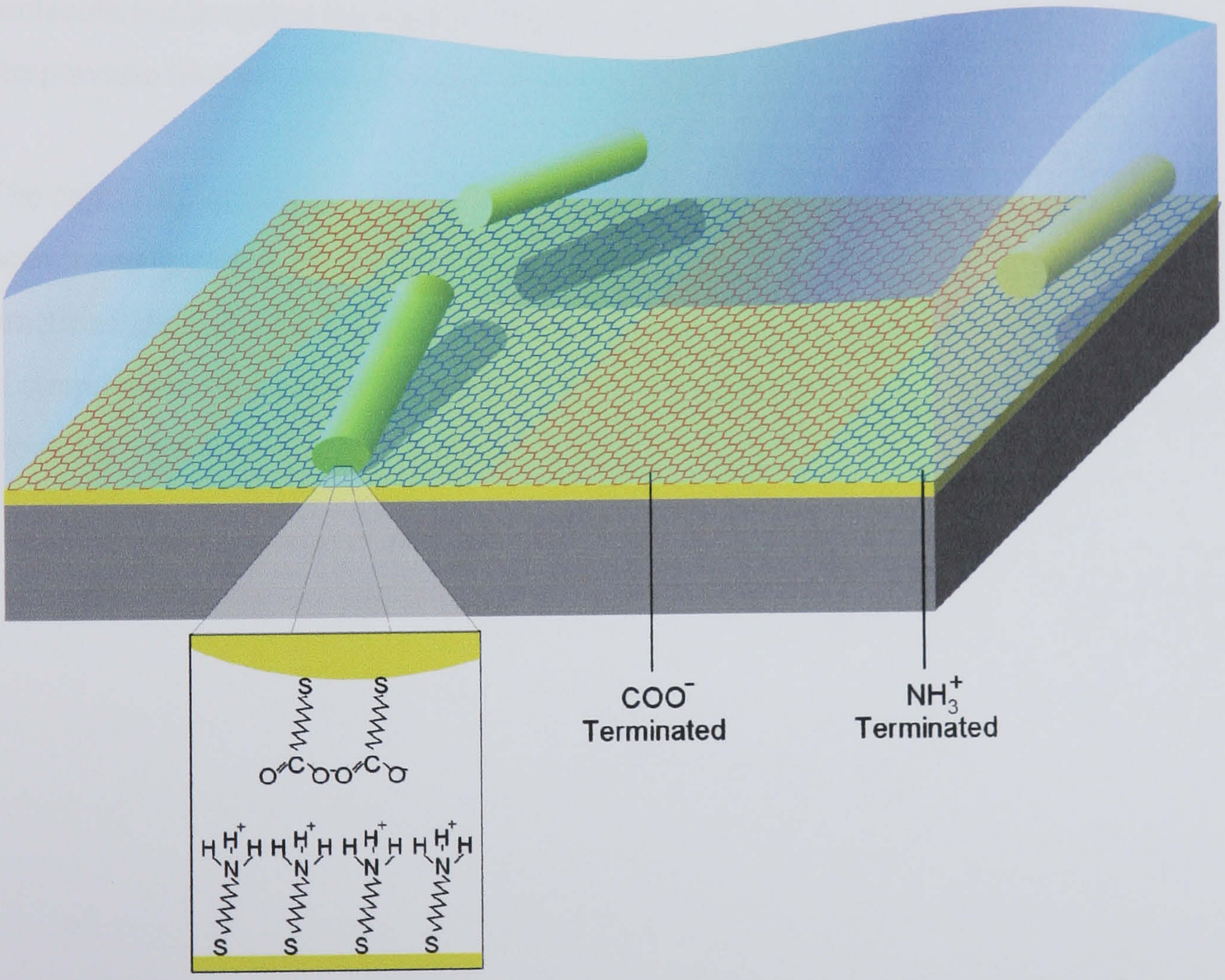

Figure 2.13. Schematic diagram of nanowire assembly due to electrostatic interactions between negatively charged nanowires and negative regions of a negatively / positively charged striped surface

In addition to the assembly of nanowires on surfaces, nanowires functionalised with surfactants that may be either protonated or deprotonated have been allowed to interact in solution.

2.3.1.5.6 Biotin Binding

Biotin is a small molecule that binds with one of four binding sites on avidin, neutravidin, or streptavidin molecules. The avidin-biotin interaction is the strongest known noncovalent interaction between protein and ligand, with very high affinity $K_a \sim 10^{13}$ M^{-1}.[121] The interaction mechanism between streptavidin and biotin[122, 123] has hydrophobic, van der Waals, and hydrogen bonding components, in addition to a binding surface loop which folds over the ligand. The bond formation between biotin and avidin, once formed, is unaffected by wide extremes of pH, temperature, organic solvents and other denaturing agents. The four binding sites of each streptavidin molecule are arranged in two opposing pairs. When binding streptavidin to planar biotin surfaces, two sites per streptavidin molecule are bound to the surface and the remaining two sites are unoccupied. The bound streptavidin thus presents a matrix of well ordered binding sites.[78]

The capability of biotin-streptavidin linkages to bind nanowires to patterned surfaces has been investigated. Both the nanowires and certain regions of the surface were functionalised with the thiolated biotin molecules, and allowed to interact in the presence of streptavidin. It is expected that nanowires remain bound to the biotin surface regions, providing selective attachment, figure 2.14.

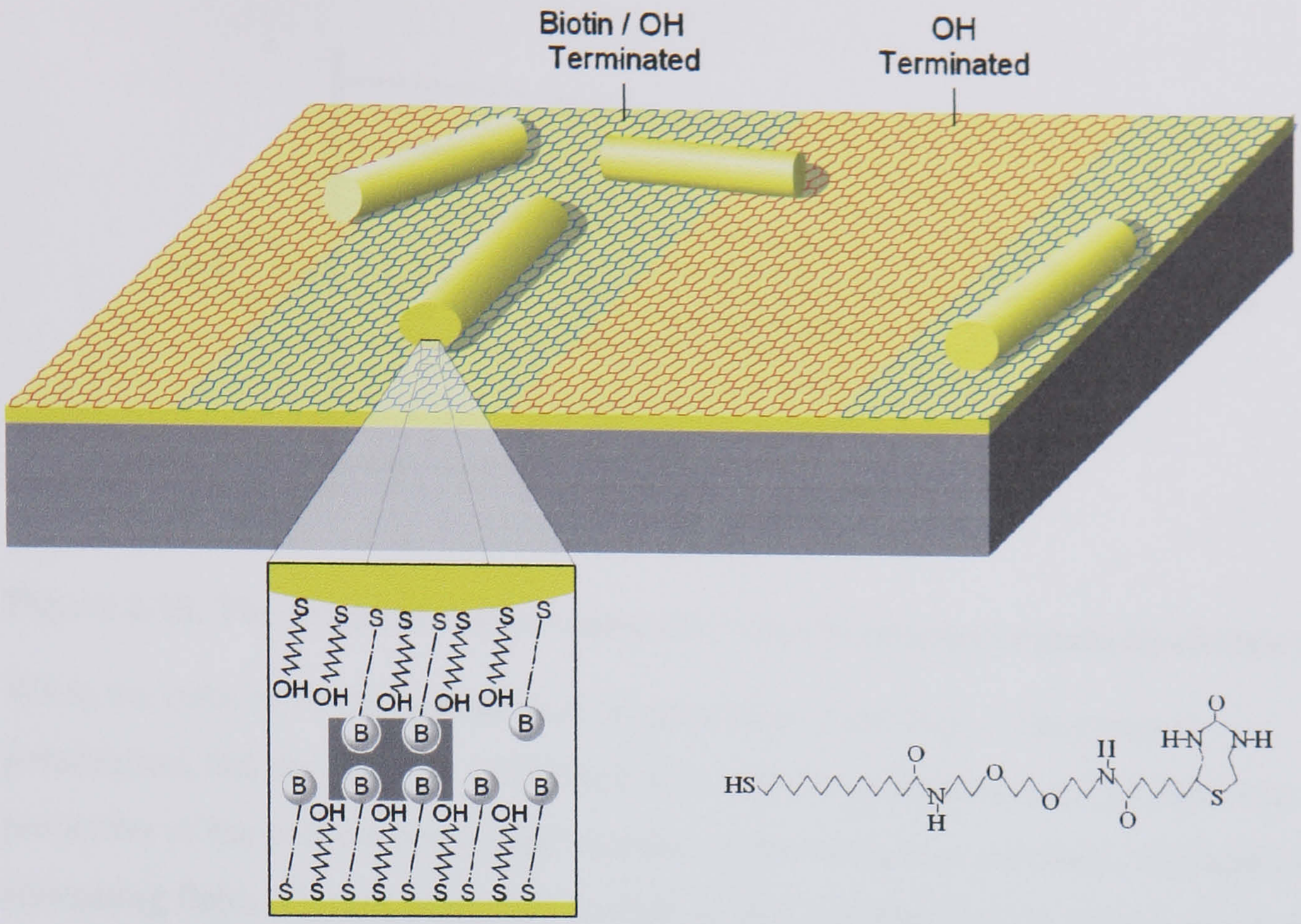

Figure 2.14. Schematic diagram showing attachment of biotin functionalised nanowires to biotin functionalised surface regions with a streptavidin linker

In addition to the assembly of nanowires on surfaces, nanowires functionalised with biotin have been allowed to interact in solution, in the presence of streptavidin. Specific nanowire aggregations are expected.

2.3.2 External Forces

A review of techniques using directed assembly or external forces to assemble nanowires has already been discussed in the introduction. Discussed below are non-surfactant based techniques to assemble nanowires used during the course of this work.

2.3.2.1 Dielectrophoresis

Dielectrophoresis is the use of non-uniform electric fields to selectively move neutral particles in a liquid dielectric medium[124, 125]. When a polarisable object is subject to an electric field a dipole moment is induced. Equal and opposite charges accumulate at either end of the particle but, because the field strength is inhomogeneous, the charges at one end experience a larger force than those at the other resulting in a net dielectrophoretic force, F_{DEP}, Figure 2.15.

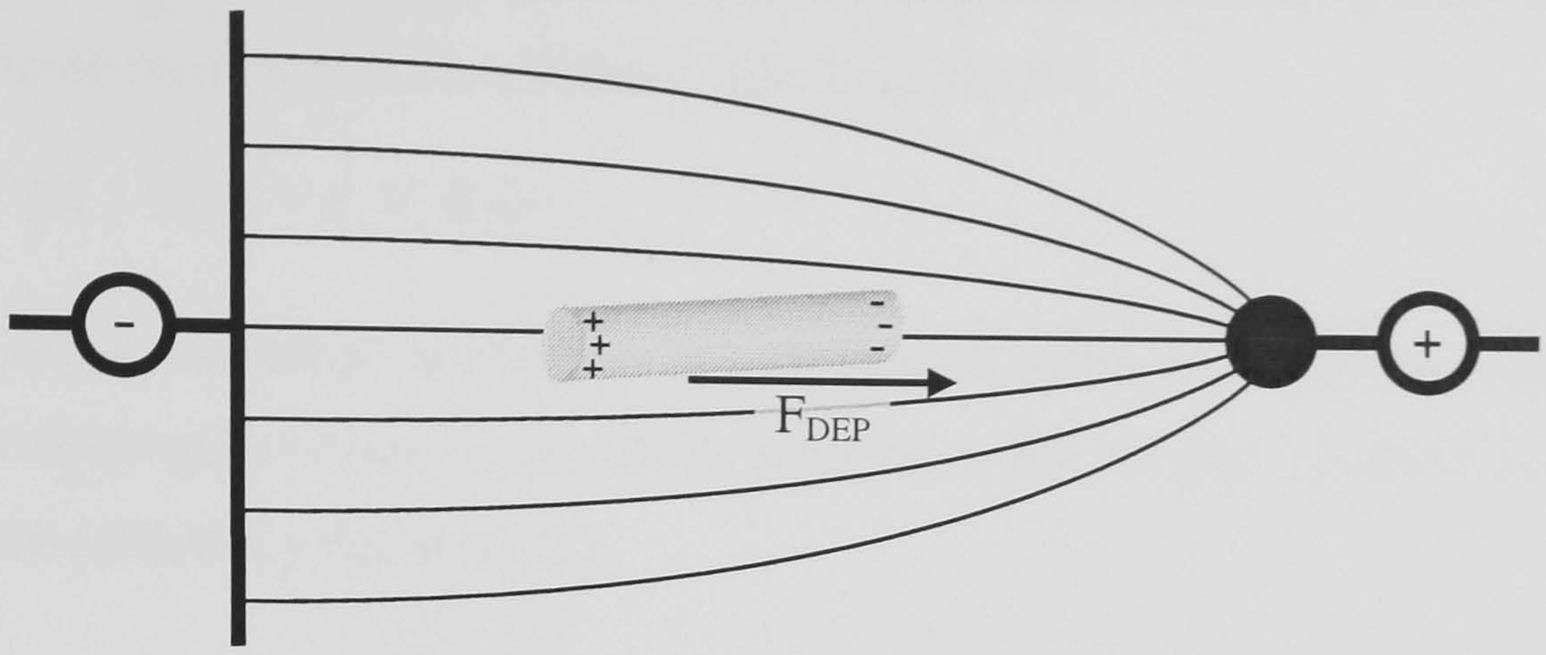

Figure 2.15. The origin of dielectrophoretic force in an inhomogeneous electric field

When the polarity of the applied field is reversed so is the sign of the induced polarisation, but the direction of the dielectric force remains constant. The dielectric properties of the particle control the response of the induced polarisation with transient or alternating fields. Consequently the strength of the dielectric force is dependent on the applied field frequency. Figure 2.15 depicts a case where the particle is more polarisable than the medium, and the force acts in the direction of increasing field strength, positive dielectrophoresis. The opposite case is also possible, where particles are less polarisable than the surrounding medium. For negative dielectrophoresis net particle movement is towards the regions of lowest field intensity.

The dielectrophoretic force can be approximated with a Taylor series expansion of the interaction between the electric field and the induced dipole, which ignoring 2nd order and higher terms is given by Equation 2.3.[125]

Equation 2.3 $$F_{DEP} = (m(t) \cdot \nabla) E(t)$$

Where E is the electric field, and m the induced dipole moment of the nanowire. The exclusion of higher-order terms means the dipole moment approximation is only valid when the particles are small in comparison to variations in the electric field. To accurately determine the dielectrophoretic force a Maxwell stress tensor should be used[124], however, this common approximation is sufficient for qualitative discussion of dielectrophoretic assembly.

In a spatially inhomogeneous field the force acting on each side of the particle will be different, causing the particle to move in the medium[126]. For anisotropic objects like

nanowires, a torque is produced which effectively aligns the nanowire with the field. The induced dipole moment can be calculated with Equation 2.4.

Equation 2.4 $m(t) = \varepsilon_m V_p K E(t)$

Where ε_m is the absolute permittivity of the medium, V_p is the volume of the particle and K is the complex polarisation factor, which depends on the complex permittivity of the particle and medium by Equation 2.5

Equation 2.5 $K = \dfrac{\varepsilon_p^* - \varepsilon_m^*}{\varepsilon_m^* + (\varepsilon_p^* - \varepsilon_m^*)n}$

Here, ε^* is the complex permittivity and the indices p and m refer to the particle and the medium respectively. The Lorentz depolarization factor, $n = n_x+n_y+n_z$, describes the shape anisotropy of the particle, where each component describes how a certain particle orientation interacts with the electric field. Unlike isotropic spherical particles where $n_{r1}=n_{r2}=n_{r3}=1/3$, cylindrical particles are highly anisotropic and their polarisability is dependent on their orientation with respect to the electric field. For a long cylindrical wire the polarisability along the length of the wire is much greater than either radial orientation, consequently component depolarisation factors are $n_L \approx 0$ and $n_{r1} = n_{r2} \approx 0.5$. If the x axis is arbitrarily chosen as the line bisecting the two electrodes, and it is accepted that the dielectrophoretic torque aligns the wire with the field, $n_x \approx 0$ and the cases for other orientations, n_y and n_z, need not be considered. The complex polarisation factor simplifies to Equation 2.6.

Equation 2.6 $K = \dfrac{\varepsilon_p^* - \varepsilon_m^*}{\varepsilon_m^*}$

The imaginary component of the complex permittivity, ε^*, contains the conductivity, σ, and angular frequency of the applied field, ω, Equation 2.7.

Equation 2.7 $\varepsilon^* = \varepsilon - i\sigma/\omega$

Since the electric field and nanowire polarisation are in phase the time averaged dielectrophoretic force acting on a homogeneous dielectric particle, can be expressed by Equation 2.8 and Equation 2.9.[127]

Equation 2.8 $$F_{DEP} = \tfrac{1}{2}\mathrm{Re}\{m \cdot \nabla E^*\}$$

Equation 2.9 $$F_{DEP} = \tfrac{1}{2}\pi r^2 l \varepsilon_m \mathrm{Re}\{K\}\nabla |E_{rms}|^2$$

Where E_{rms} is the root-mean-square value of the electric field, and the particle volume is calculated from its radius, r, and length, l. If the real part of the complex depolarisation factor, $\mathrm{Re}\{K\}$, is positive then the nanowires will undergo a net movement in the direction of increasing field strength (and vice versa). After a nanowire aligns on the electrode, the local electric field is reduced preventing additional wires from assembling in close proximity to the first.

It is evident that the magnitude of the dielectrophoretic force is dependent on the applied potential, equation 2.9, its frequency, equation 2.7, and the mismatch between the dielectric permittivities of the particle and medium, equation 2.6. These relationships are shown explicitly in Equation 2.10 and Equation 2.11.

Equation 2.10 $$F_{DEP} = \pi r^2 l \varepsilon_m \mathrm{Re}\{K\}\left|\frac{dV_{rms}}{dx}\nabla_x\left(\frac{dV_{rms}}{dx}\right)\right|$$

Equation 2.11 $$\mathrm{Re}\{K\} = \frac{\omega^2(\varepsilon_m\varepsilon_p - \varepsilon_m^2) + (\sigma_m\sigma_p - \sigma_m^2)}{e_m^2\omega^2 + \sigma_m^2}$$

For assembly, the dielectrophoretic force should be greater than other component forces acting on the particle. Dimaki *et al*[126] have calculated the velocity of a nanowire under the influence of dielectrophoretic and viscous drag forces. Similarly, fluid flow, static frictional forces, the rate of particle precipitation and nanowire-surface interactions may influence assembly. Here, the dielectrophoretic forces are calculated but competitive forces during assembly are not considered quantitatively.

Dielectrophoretic forces have been used to manipulate the assembly of gold nanowires from methanol solutions. The nanowire solution was exposed to an electric field by contact with a planar electrode on an insulating substrate. Their construction is summarised below.

2.3.2.1.1 Lithographic Fabrication of Electrodes

Gold electrodes were fabricated on glass by a combination of electron beam lithography and photolithography. First, two rounded triangular electrodes with a separation of 2 μm

were defined in positive resist using electron beam lithography. After developing and washing the sample the exposed resist was removed to reveal the glass substrate. A thin chromium film (10 nm) was then evaporated onto the surface, as an adhesion layer, prior to the deposition of 80 nm of 99.99 % gold (Advent). Unexposed resist, and its metal coating, were removed by sonicating the sample in methanol. The second fabrication stage was the creation of contact pads for each electrode. Photolithography was used to define 2 mm^2 pads separated by 75 μm and centred on each electrode. Once again the structures were metalised with 10 nm of Cr and 80 nm of Au, and the excess material removed by sonication in methanol.

2.3.2.1.2 Dielectrophoretic Nanowire Assembly Procedure

Nanowire assembly was controlled by applying an alternating potential between the electrodes, in series with a 1 kΩ current limiting resistor, R_L, Figure 2.16.

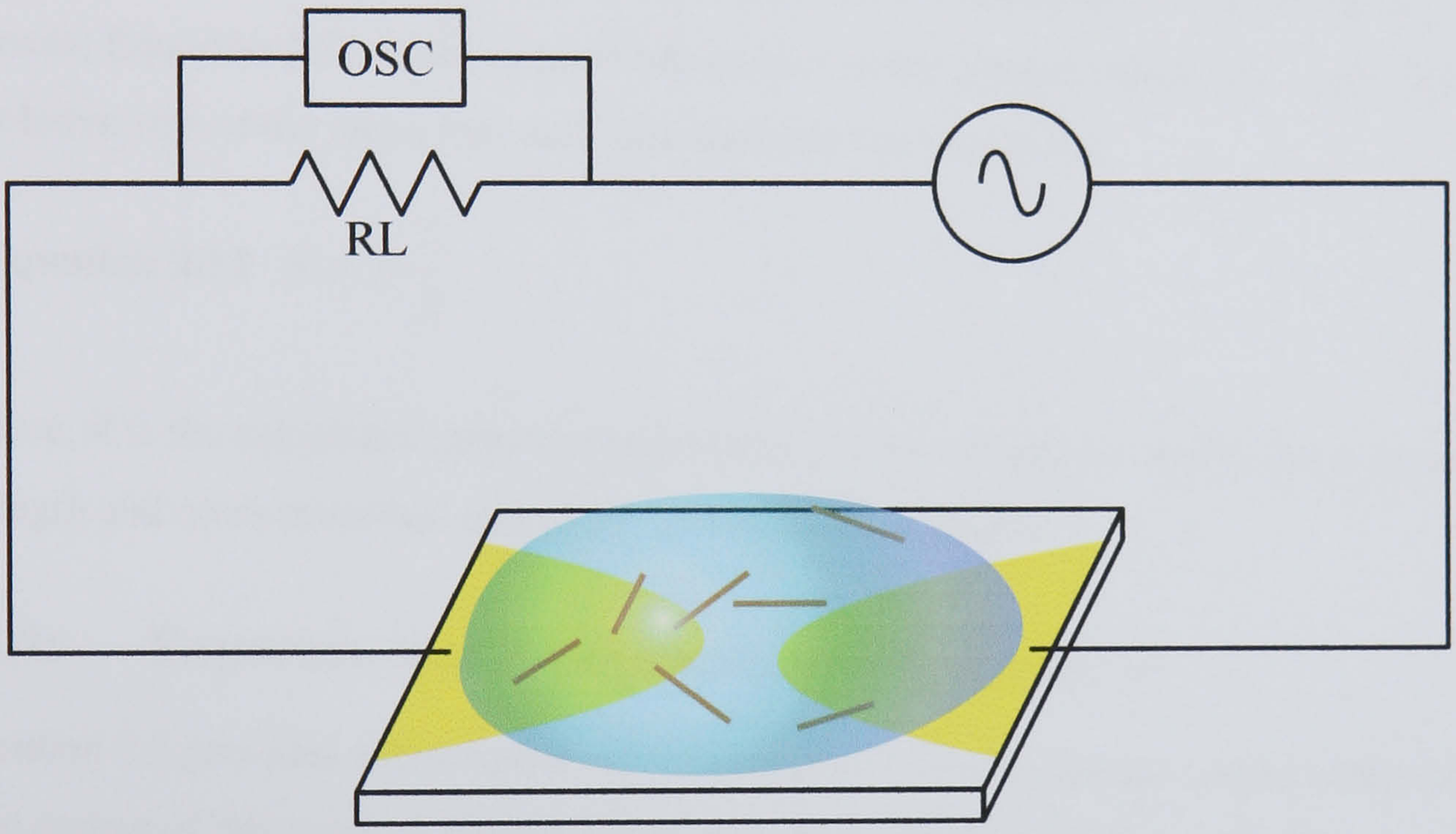

Figure 2.16. Schematic diagram detailed the procedure for dielectrophoretic assembly of nanowires

The electrodes were then exposed to a methanol based nanowire solution for a period of 15 s. Movement of nanowires towards the regions of highest field intensity, and alignment with the field, should encourage nanowire assembly at electrode edges, particularly in the region of the electrode gap. After 15 s, excess nanowire solution was removed and the electrode washed with methanol, whilst the potential was maintained until the excess methanol had evaporated. The current was monitored to provide an

insight into the assembly procedure, by measuring the potential drop across the current limiting resistor, R_L, with a digital oscilloscope,

2.3.2.1.3 Transport Properties of Nanowires

Nanowires assembled between electrodes could be subjected to electrical characterisation to determine their transport properties. Conduction in bulk materials is determined by the mobility of electrons in the conduction band. This is, in part, determined by the electron mean free path, which for bulk gold is approximately 40-50 nm[128]. Kreibig and von Fragstein[129] have proposed that electron scattering at the surface of materials must contribute to the mean free path, and scattering must be enhanced in small particles where the mean free path is limited by the physical dimensions of the nanoparticle. The adjustment of the mean free path is dependent on the nanoparticle geometry. Sondheimer[130] presents a review of the necessary adjustments for a variety of basic geometries, including nanowires. Classical geometric resistance calculations may still be made, Equation 2.12, with a simple adjustment to the sample resistivity, dependent on the relative size of the mean free path and diameter for nanowires.

Equation 2.12 $R = \rho \frac{L}{A}$

Here, R is the calculated nanowire resistance, ρ is the resistivity, and L and A are the length and cross sectional area of the nanowire respectively.

2.4: Experimental Equipment and Procedures

Section 2.5 provides a description of the characterisation techniques undertaken during the course of this work. A discussion of their theoretical basis, operation and experimental application is also included.

2.4.1 Scanning Electron Microscopy

The scanning electron microscope images surfaces with a beam of electrons rastered across the sample. Electrons are generated by either thermionic or field emission, or a combination of the two, a Schottky emitter. The beam is collimated by an electromagnetic condenser lens, focussed by an objective lens, and scanned across the surface by deflection in an electromagnetic field. Secondary electrons released from the surface are measured with detectors reliant on scintillation. The output light flashes are then detected and amplified by a photomultiplier tube. The detected secondary electron signal is

correlated with the scan position to generate an image, similar to that seen through an optical microscope.

2.4.1.1 Instrumentation

Two electron microscopes have been used during the course of this work. A high resolution LEO 1530 FEGSEM and a field emission gun attached to Thermo VG Scientific ESCALAB 250 X-ray photoelectron spectrometer, discussed in section 2.5.2. Both use a Schottky electron source, outlined below.

2.4.1.1.1 Schottky Electron Source

The electron source is a Shotkey emitter, which offers high brightness, coherence and a narrow energy range. A Schottky emitter incorporates both thermionic, and field emission, of electrons from a tungston tip. Field emission results from electrons 'tunneling' past the work function of the tip, aided by the presence of a high electrical field gradient.

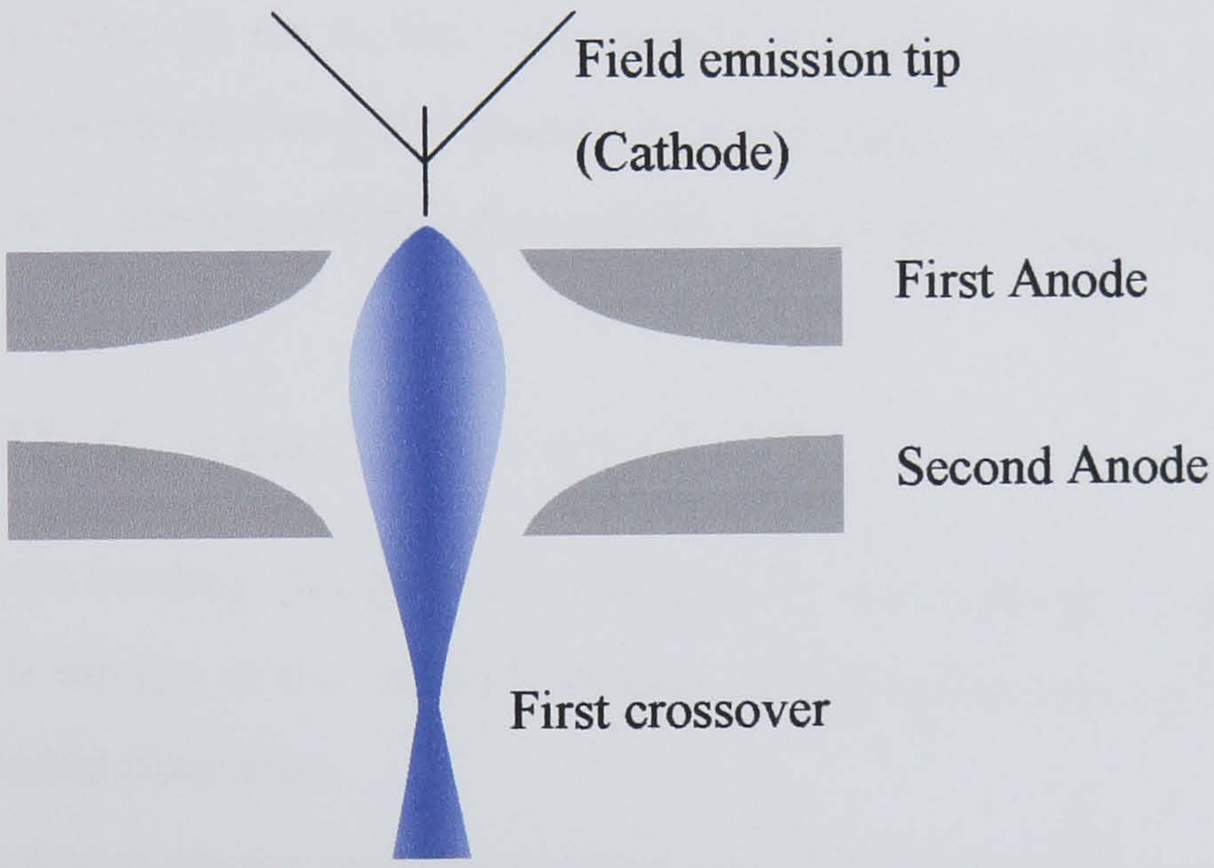

Figure 2.17. Field emission electron gun

The voltage difference between the first anode and the cathode determines the emission current. The second anode is at ground potential, and the voltage difference between this and the cathode determines the acceleration given to the electrons. The shape of the anodes is carefully selected to minimize aberrations. While electrons are emitted from the surface of the tip, their apparent source is a single point beneath the surface. Because of the electrical fields present, electrons tend to be emitted tangential to the surface which, for a hemispherical tip, results in an apparent source at the focus of the hemisphere. The tip is typically a single crystal tungsten wire sharpened by electrolytic etching, with

diameter of 100 to 1000 Å. The emission process itself depends on the work function of the metal, which can be affected by adsorbed gases. Thus, the tungsten tip can be very sensitive to surface contamination and high vacuum is required to maintain cleanliness.

2.4.1.2 SEM Measurement Procedure

Nanowires are imaged after dropcasting them from solution onto clean silicon substrates. Insulating samples have a conductive 2 nm platinum surface coating applied to the sample surface with an Agar 208HR sputter coater. The LEO FEGSEM was operated at pressures below 10^{-7} mbar with accelerating voltages of 1.5 kV and a typical working distances of 3 mm. The ESCA250 SEM component was operated at 7 kV at pressures below $5x10^{-9}$ mbar. Scanning electron microscopy is capable of differentiating between different species of organothiol monolayers on gold[131], this is very useful for imaging patterned SAMs, where image contrast highlights different thiol regions.

2.4.2 X-ray Photoelectron Spectroscopy

The X-ray Photoelectron Spectroscopy (XPS) technique uses X-rays to eject electrons from atoms present on the surface of a sample. The electrons are sampled and an energy spectrum measured allowing the chemical composition of the surface to be determined. The technique is based upon the photoelectric effect formulated by Einstein in 1905, equation 2.13.

Equation 2.13. $E_B = h\upsilon - KE$

Where E_B is the binding energy of the electron, $h\upsilon$ is the energy of the photon source and KE the kinetic energy of the emitted electron. When a photon is incident on matter, there are three possible outcomes:

1) The photon passes through without interaction, no energy is transferred and no electrons are ejected.

2) The photon is scattered by an electron in an atomic orbital, with partial energy transfer, but the electron remains bound. This inelastic scattering is known as Compton scattering.

3) The photon interacts with an atomic orbital electron with complete energy transfer. The energy absorbed by the electron results in its promotion to a higher energy orbital, or complete ejection if sufficient energy is supplied.

The distribution of core electronic orbitals is unique and well defined for every element. Negatively charged electrons are attracted to the positively charged nucleus, and arranged

in a series of discrete energy levels. The strongest interaction is observed for those electrons closest to the nucleus, and it is these that will be most affected by the nuclear charge. Consequently, it is these closely bound electrons that provide the best measure for atomic identification. After an incident X-ray photon has caused the photoemission of a core electron the atom is left in an ionized state, Figure 2.18.

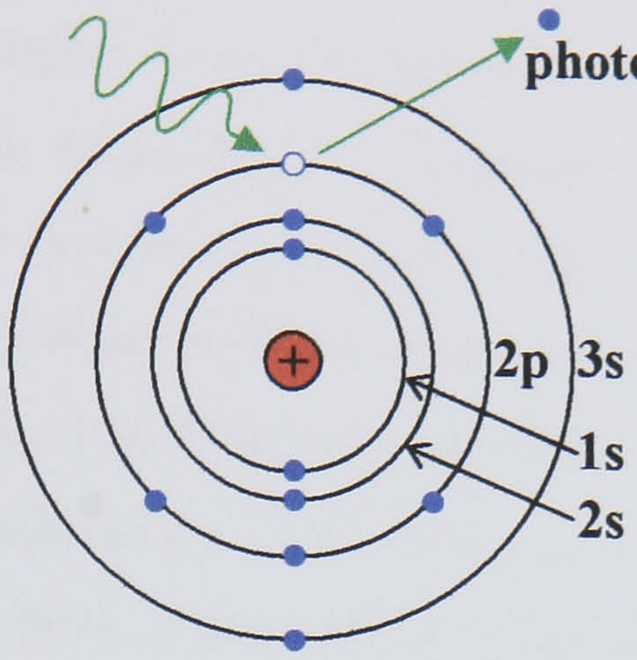

Figure 2.18. The XPS photoemission process

In this case, an electron from a higher energy level can drop down to fill the "vacant hole" in the core level. Consequentially, the atom will have an excess of energy which can be lost by emitting a photon (X-ray) or by emitting a second electron from a higher energy level. The latter process is referred to as an Auger emission and forms the basis of Auger electron spectroscopy.

To enable the photoemission of core electrons, soft X-rays (energy 200 – 2000 eV) are used. If sufficient energy is imparted to the electrons to cause their ejection, their energy spectrum provides information about what elements are present on the surface, what their chemical states are, and their relative quantities.

2.4.2.1 Instrumentation

All XPS measurements presented in this thesis were performed in a Thermo VG Scientific ESCALAB 250. In addition to monochromatic and non-monochromatic XPS, the system also allows surface characterisation with ultraviolet photoelectron spectroscopy and low resolution scanning electron microscopy. The system is maintained at UHV conditions, to prevent photoelectron interaction with gas molecules and surface contamination. Discussed here are the system components provided for monochromatic XPS, and their operation.

2.4.2.1.1 The X-Ray Source

X-rays are generated by bombarding an aluminium source with electrons. The electron beam originates from a cathode, heated by electron-bombardment from a filament. This electron beam is passed though an aperture and lens system prior to striking an aluminium anode. Upon striking the anode, electrons decelerate rapidly emitting photons with a broad range of energies, where the minimum wavelength is associated with the maximum electron energy. Superimposed on this spectrum are fluorescence peaks, where the bombarding electrons have displaced a core electron. This core electron is replaced by an electron from a higher orbital, with the associated excess energy is ejected as a photon with a discrete wavelength. The commonly referred to K_α X-ray peak is associated with the ejection of an electron in the n = 1 (K) shell, and its replacement with an electron from the n = 2 (L) shell. For an aluminium atom this photon has energy of 1468.8 eV.

Although both monochromatic and non-monochromatic sources were available, monochromatic sources were used for all experiments to avoid problems associated with the use of non-monochromatic X-rays. These problems include the observation of satellite peaks in the XPS spectra (due mainly to the weaker K_β fluorescence line interacting with the sample), lower resolution due to broader X-ray spectra, and Bremsstrahlung radiation which may cause sample degradation.

For monochromatic XPS, only a specific wavelength from the X-ray spectra is interacted with the sample. The K_α peak is chosen because it is the most intense region. The X-rays are incident on a quartz crystal, positioned such that only the K_α X-rays satisfy the Bragg condition. The coherent X-ray K_α beam, with energy of 1486.7 ± 0.3 eV, is then interacted with the sample.

2.4.2.1.2 The Analysis chamber

The X-ray beam enters the analysis chamber at approximately 45° to the horizontal, interacts with the sample and the emitted photoelectrons are sampled vertically. The sample is attached to a stage with x, y movement to expose a specific area, height control to ensure the X-rays are coincident with the area from which photoelectrons are sampled, and angular adjustment to allow a variety of photoelectron take-off angles.

Röntgen's first observations of X-rays demonstrated their ability to penetrate materials that are opaque to light. In comparison, photoelectrons are greatly attenuated by matter

and it is this factor that limits the sampling depth of XPS, and the reason it is a surface specific technique. The sampled depth is typically of the order of 10-50 Å. For homogenous substrates the orientation of the sample relative to the direction in which the photoelectrons are sampled does not influence the observed energy spectra. If the same substrate has an overlayer, the contribution of this overlayer is dependent on the sample orientation. The substrate has the greatest contribution to the XPS spectra when photoelectrons are sampled perpendicular to the substrate. Other angles increase the contribution of the overlayer to the measured spectra.

Where photoelectrons are emitted from a surface, their maximum energy is constrained by both the binding energy of the atom from which they originate, and the work function of the surface itself. Samples characterised by XPS share a common earth with the spectrometer used to analyse the energy spectra of emitted photoelectrons. As such, the Fermi levels of the sample and spectrometer equilibrate and photoelectron energy is measured relative to this Fermi level, i.e. the effect of the surface work function is negated. Where insulating samples are characterised it was necessary to expose the surface with low energy electrons, to compensate for those photoelectrons that were emitted.

2.4.2.1.3 The Spectrometer

The electrons are sampled though an input lens system designed to capture the maximum possible number of emitted photoelectrons, and transfer them to the analyser with minimum loss. The analyser is a narrow pass filter which allows only electrons within a specified energy range to meet the detector. Photoelectrons entering the analyser may be slowed to increase the energy resolution, but this reduces the intensity of the sampled electrons. Photoelectrons travel in a hemispherical path though the analyser defined by an applied potential and meet one of six channeltron detectors, each positioned to measure a different energy range. Each electron incident on a channeltron triggers an avalanche of electrons, subject to an external applied voltage. The measured signal is amplified and recorded to form the energy spectrum.

2.4.2.2 Spectral Analysis

Presented here is a brief description of the analysis techniques commonly applied to XPS spectra, used to yield information regarding the elemental surface constituents, their relative quantities and chemical states.

2.4.2.2.1 Peak Identification

Firstly, each peak observed must be identified as being associated with a specific element and electronic orbital. Each electron within an atom can be identified with a unique set of quantum numbers; n is the principal quantum number associated with the separation of the electron and nucleus, l is the orbital quantum number associated with orbital angular momentum of the electron, and s is the spin quantum number associated with an inherent magnetic field. Whereas n can take values of 1,2,3..., l is constrained to values of 0,1,2...n – 1, and s can only take values of ±½. The j-j coupling nomenclature has become the basis of labelling electrons for XPS. Here, the total angular momentum of the electron is characterised by a quantum number $j = l + s$. Each peak is labelled by combination of the quantum numbers $(n)(l)(j)$, where the letters s, p, d, f are used to designate the values l = 0, 1, 2, 3... The total angular momentum, j, is a multiple of one half and the denominator is commonly dropped since it is implicit, i.e. $2p_{3/2}$ becomes $2p_3$.

The j-j nomenclature is inadequate to describe Auger emission, where final state is doubly ionised. X-ray notation is adopted; n = 1, 2, 3, 4 ... are described by K, L, M, N ... respectively and the discrete levels associated with l and j are numbered sequentially with a suffix, for examples see table 1.

Quantum Numbers			X-ray	X-ray
N	*l*	*j*	Suffix	Level
1	0	1/2	1	K
2	0	1/2	1	L_1
2	1	1/2	2	L_2
2	1	3/2	3	L_3
3	0	1/2	1	M_1
3	1	1/2	2	M_2
3	1	3/2	3	M_3
3	2	3/2	4	M_4
	Etc		etc	etc

Table 2.1. X-ray notation

The transition is written as a combination of the two X-ray levels, for example $KL_1\ L_3$.

2.4.2.2.2 Spin-Orbit Splitting

For $l > 0$ an energy level doublet arises due to spin-orbit coupling. The two states correspond to the parallel and anti-parallel nature of the spin and orbital angular momentum vectors of the remaining electron. The relative intensity of the doublet peaks is given by the relative degeneracy of each state, given by $2j + 1$, thus the observed peak area ratios are given in table 2.

Subshell	*j* values	Area ratio
S	1/2	-
p	1/2 : 3/2	1 : 2
d	3/2 : 5/2	2 : 3
f	5/2 : 7/2	3 : 4

Table 2.2. Spin-orbit splitting parameters

2.4.2.2.3 Peak Intensity

The relative intensity of core level peaks is due to the photoelectron cross-section, α. Values of α have been previously calculated and derived from X-ray mass absorption coefficients. The relative concentrations of various atomic species observed in XPS spectra are calculated by determining the peak area, and adjusting the value by the sensitivity factor associated with that peak. Sensitivity factors are documented in a variety of sources, although those reported in Briggs and Sear have been used.[132]

2.4.2.2.4 Chemical Shift

The chemical combination of atoms can be determined by analysing high resolution XPS spectra. Assemblies of elements increase the energy required for photoemission from that required in their pure form, peaks are shifted to higher binding energies. The largest shifts are observed where atoms are in combination with highly electronegative atoms[132].

Beamson and Briggs[133] published high resolution XPS spectra of many polymers documenting the chemical shifts of the carbon 1s, nitrogen 1s, fluorine 1s and oxygen 1s peaks are documented. Unless otherwise stated, XPS spectra have been compared with these references.

2.4.2.3 XPS measurement procedure

XPS spectra were collected with a chamber pressure maintained below 10^{-8} mBarr. A 150 W, monochromatic Al K_α X-ray beam was used to illuminate a 500 μm^2 region of the surface. Photoelectrons were collected at a take-off angle of 90°, with the pass energy set to 20 eV (150 eV for survey spectra). Measured spectra were analysed as above, and compared with collated reference data.

2.4.3 Transmission Electron Microscopy

Transmission electron microscopy is analogous to an optical microscope, except electrons are used instead of light. Whereas light has a wavelength typically of ~500 nm, electrons used for TEM are accelerated at several hundred kV, giving much smaller wavelengths:

200 kV electrons have a wavelength of 0.025 Å. However, the resolution of the TEM is limited by aberrations inherent in electromagnetic lenses, to about 1-2 Å.
The resolution of the TEM allows direct observation of the size and morphology of nanostructured materials[134].

The electrons are focused with electromagnetic lenses and projected at the sample. Interaction between these electrons and the sample has three possible outcomes: They may pass undeflected through the sample, they may be scattered without energy loss, or they may be scattered with an associated energy loss. Contrast in the image may be derived from either scattering event. The image brightness is associated with the transmission of unscattered electrons, and consequently related to the sample thickness. Scattering events between electrons and crystalline samples show diffraction effects characteristic of the wave-like behaviour of electrons. The scattered electron intensity is dependent on the alignment between the electron beam and crystal orientations within the sample. Bragg diffraction from regions with different crystal orientations may result in diffraction contrast present in the image. The image may be observed either on a fluorescent screen, or recorded on film or digital camera.

2.4.3.1 Instrumentation and Experimental Procedure

The TEM used to obtain the images presented in this work was a Philips CM200 field emission gun transmission electron microscope, with a SIS CCD camera for direct recording of digital images. The electron source is a Schottky emitter, as discussed previously. The TEM system is kept under vacuum to prevent electrons scattering with gas molecules, sample contamination and to maintain the field emission gun. Samples were prepared by placing a dilute solution of nanowires on a carbon coated copper grid (400 mesh) and allowing the solvent to evaporate. The sample was then loaded into the TEM via a fast entry lock.

2.4.4 Atomic Force Microscopy

Atomic Force Microscopy (AFM) is a scanning probe technique capable of detailed surface analysis with atomic resolution. The technique relies upon interactions between an atomically sharp tip and the surface. The interaction strength is associated with deflection of the tip cantilever, or modification of its behaviour. This basic arrangement has been optimised for a variety of imaging methods in addition to standard topographic techniques. Surface images can be characterised for sample conductivity, surface

potential, magnetism, friction and chemical functionality. Non-imaging techniques have been developed to measure the interaction forces between the tip and surface, allow surface manipulation or effect surface modification.

Discussed here is the background for topographic images, of which there are two main types, contact mode, and tapping mode. In contact mode the tip is pressed into the surface with a constant force, and dragged across the sample surface. The tip is deflected by short-range repulsive interactions between the sample and tip. These deflections are typically measured with a beam deflection system. This design uses a laser shining onto and reflecting off the back of the cantilever and onto a segmented photodiode to measure the probe motion[135]. In contact mode, damage to both the tip and surface may occur due to a lack of force control. In ambient conditions, contaminants or absorbed fluid that accumulate on the surface increase the attractive force on the tip, drawing it into the surface and potentially cause damage[136]. Tapping mode was developed to reduce damage to both the tip and sample. During tapping mode the tip is held at a constant height above the surface, typically 10-100 nm. As the cantilever is rastered across the surface it is also oscillated at close to its resonant frequency.[136, 137] Changes in the tip-surface interaction strength, F, are measured by monitoring the changes in the resonant frequency. This detection method is sensitive to changes in the force, rather than to the interaction forces themselves, equation 2.14.

Equation 2.14 $$F = -\frac{\partial V}{\partial z}$$

Here, V is the applied potential and z the separation. The force can be related to the spring constant of the cantilever, equation 2.15.

Equation 2.15 $$F = -kz$$

Any change in the interaction strength between the tip and surface results in a change in effective spring constant of the cantilever, and consequentially its resonant frequency, ω, equation 2.16.

Equation 2.16 $$\omega = \left(\frac{k}{m}\right)^{1/2}$$

The sensitivity of the cantilever is determined by its mass, m. Changes in the resonant frequency result in a much larger change in the amplitude of oscillation.

2.4.4.1 Instrumentation

The AFM system consists of an atomically sharp tip attached to a cantilever positioned parallel to the sample surface. The sample is attached to a piezoelectric tube scanner which rasters the sample beneath the tip. The behaviour of the tip is monitored with a laser beam reflected from the back surface of the cantilever, and detected on a split photodiode detector, figure 2.19.

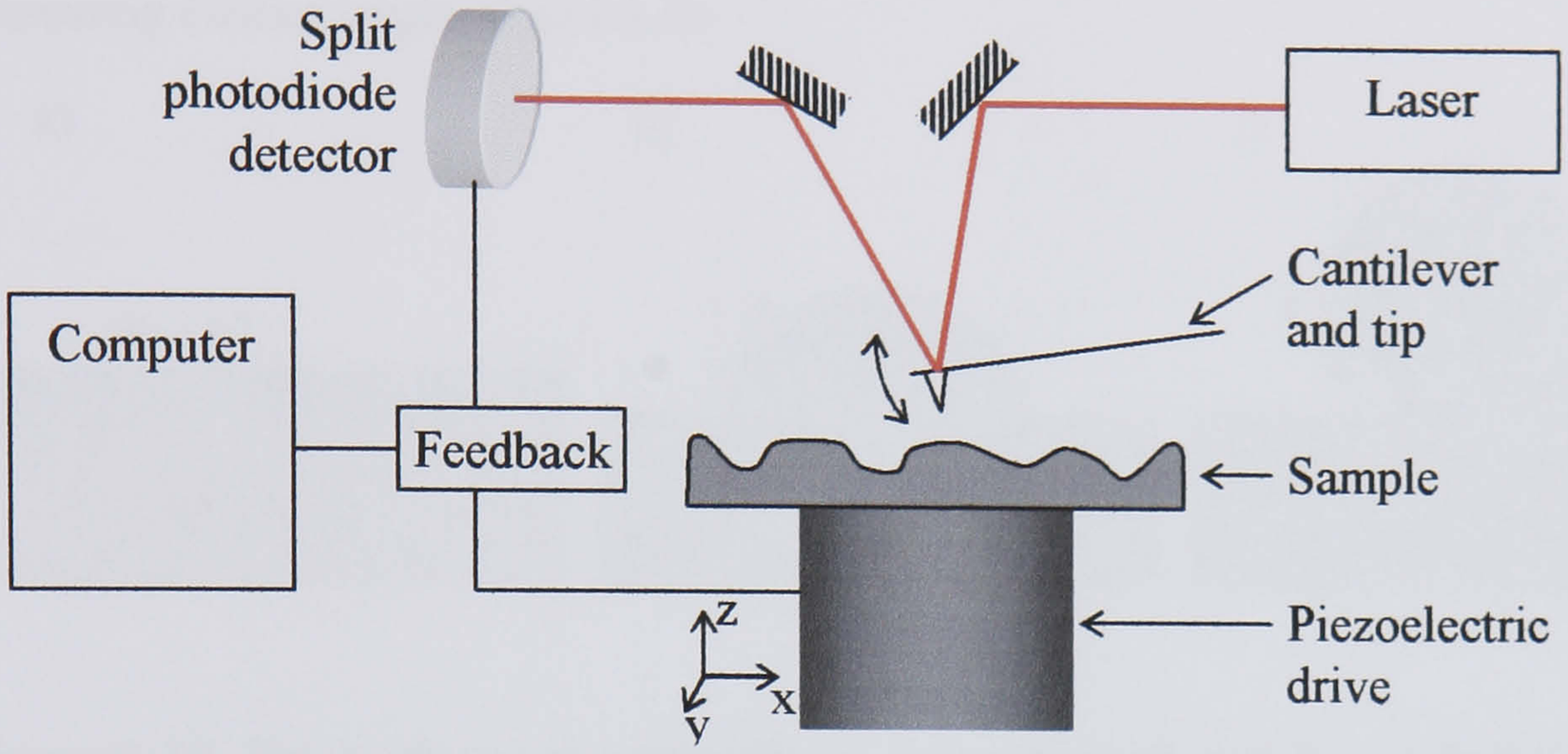

Figure 2.19. Schematic showing the basic arrangement of components in and AFM

A variety of cantilevers are available, those commonly used for tapping mode have typical spring constants of 20-100 N/m with resonance at 100 – 400 kHz. To reduce the influence of external vibrations the system is isolated on a vibration damping support. The ultimate resolution is dependent on the sharpness of the tip, resolutions of 0.1 Å in the x and y directions and 0.01 Å perpendicular to the surface are possible with an atomically sharp tip. However, most tips are either blunted or have some form of artefact. The final image observed is a convolution of the tip shape and size, surface topography, and alignment of the surface and tip.

2.4.4.2 Measurement Procedure

AFM images were obtained using a Digital Instruments Nanoscope IV in tapping mode with a Nanosensors NCL 50 silicon tips. These tips have a ~10 nm tip radius, resonate at 150 kHz and have a force constant of 48 N/m. Surface manipulation was performed on a Digital Instruments Nanoscope IV, which is similar in conception and design to the system described above, used with the same tips.

2.4.5 Contact Angle Goniometry

The behaviour of a droplet of solvent on a surface can reveal information about the surface roughness, surface energy and chemical homogeneity.[110, 138] The droplet either completely or partially wets the surface, determined by the competition of interactions between solvent molecules and between the solvent and the surface. For water, the wettability is categorised as hydrophilic, semi-hydrophobic or hydrophobic, with increasing contact angle, figure 2.20.

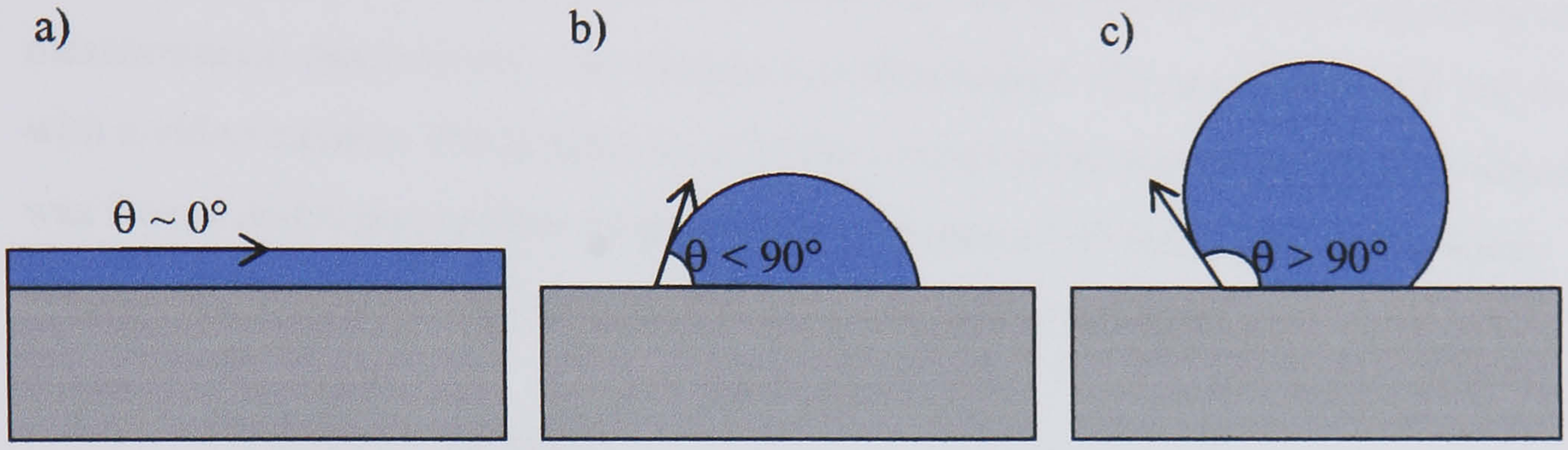

Figure 2.20. The surface can normally be characterized as being a) hydrophilic, b) semi-hydrophobic, or c) hydrophobic

The final shape of the water droplet corresponds to minimisation of cohesive forces within the water droplet and adhesive forces between the surface and droplet[110]. The interaction of the water with the surface is largely dependent on the chemical functionality of the surface. Hydrophilic surfaces, such as OH and COOH, undergo dipole-dipole and hydrogen bonding interactions with water. Semi-hydrophobic surfaces tend to have strong dipole moments but cannot hydrogen bond. Hydrophobic surfaces, such as CH_3, contain non-polar groups which do not undergo hydrogen bonding, and have only weak dipole-dipole and Van der Waals interactions. This chemical sensitivity makes the technique particularly suitable for the investigation of self-assembled monolayers, where the strength of interaction is dependent on the terminal groups in addition to any exposed section of the assembled molecules.

2.4.5.1 Contact Angle Hysteresis

Rather than measuring static contact angles, further information can be made about the surface with dynamic measurements. Dynamic contact angles are measured when the contact area between droplet and surface expands or contracts, "advancing" or "receding". The difference between these measurements for an ideal surface would be zero, but commonly a difference – the hysteresis, is observed. Hysteresis is attributed to

pinning of the contact point at points on the surface, usually due to either surface roughness or chemical heterogeneity. Chemical heterogeneity on SAM surfaces can be attributed to poor packing, disorder, domain boundaries or contamination.

2.4.5.2 Goniometry Measurement Procedure

Sample wettability was measured with a home-built contact angle goniometer in the ambient environment. Millipore water was dispensed onto the surface with a microsyringe and the droplet volume increased or decreased for advancing and receding measurements respectively. The sample was illuminated with a sodium lamp and imaged with a video camera. When movement of the contact point was observed the video image was frozen and captured. The contact angle is measured on both sides of the water droplet, and measurements averaged across each surface analysed.

2.4.6 Photolithography

Photolithography is a process for transferring images from a mask to a surface. The surface is coated with a photoresist, which may be pattered with ultra-violet light. Upon exposing this resist to ultra-violet light the structure of the polymer resist undergoes a structure change. Two types of resist are commonly available; positive resist is 'softerned' by exposure to UV radiation and are subsequently removed, negative resist is 'hardened' by exposure to UV radiation, and the unexposed regions are subsequently removed. The removal of resist is performed by washing with a developer solution. To complete the pattern transfer from mask to substrate, bare regions of the substrate undergo some modification, for example etching, ion-implantation or the addition of an overlayer. The remaining resist layer provides protection to the underlying regions of the substrate during this final processing step. After modification of the exposed regions of the surface, protective resist may be easily removed.

2.4.6.1 Procedure

Photoresists are sensitive to a wide range of wavelengths of light, typically 200 - 500 nm, which can result in unintentional exposure from the blue and violet components of normal white light. For this reason, photolithography fabrication was undertaken in a special, filtered light, clean room area. Prior to use, substrates were piranha cleaned, rinsed with milliQ 18.2 $M\Omega cm^{-1}$ water, dried under nitrogen and baked at 150 °C for 5 minutes. Positive photoresist S1813 (Shipley) was spin coated onto the substrate at 3000 rpm for 30 s, and baked at 60 °C for 1 min to evaporate excess solvent. To improve the resolution

of fabricated structures the substrate was immersed in dichlorobenzene for 30 s. This partially hardens the resist surface, and after exposure the resist structures are undercut. The resist was exposed though a patterned mask to UV light for 10 s. To develop the photoresist each substrate was immersed into Shipley MF-319 developer for 1 min, and subsequently rinsed with water. Samples were transferred immediately to the evaporator (Edwards Auto 306) for the formation of a metal overlayer. After evaporation, unexposed resist, and its metal coating, was removed by sonication in methanol. Due to the undercut nature of the resist the resolution of evaporated structures is improved, and excess resist is more easily removed.

2.4.7 Electron Beam Lithography

Analogous to the use of electrons to advance the resolution of optical microscopy with TEM/SEM, electron beam lithography is capable of defining surface features below the limits of optical lithography. The system is closely related to scanning electron microscopy, the path of an electron beam is directed across the surface and is used to expose a thin film of resist on the surface. Although the spot size of the electron beam can be very small (0.5nm), the resolution of the system is limited by the scattering distance of electrons upon hitting the resist. Resolutions down to approximately 20 nm are possible.

2.4.7.1 Instrumentation

A Raith50 electron column with a tungsten thermionic emission filament was used for electron beam lithography.

2.4.7.2 Experimental Procedure

Prior to use, substrates were piranha cleaned, rinsed with milliQ 18.2 $M\Omega cm^{-1}$ water and dried under nitrogen. Before depositing the resist overlayer, samples underwent a dehydration bake (5 minutes at 150 °C) and were primed with hexamethyldisilizane (HMDS) by spin coating at 3000 rpm for 30 s to improve adhesion of the resist. PMMA 950A4 positive resit was spun onto the surface at 3000 rpm for 60 s, and a final bake at 130 °C for 2 minutes was performed. It was not necessary to treat the resist with dichlorobenzene, since secondary electrons generated when the electron beam strikes the substrate cause a similar 'undercut' effect. After e-beam writing, exposed regions of the resist are broken up into polymer fragments. These exposed areas are removed by exposing the substrate in 1:1 MIBK:IPA (MIBK is Methyl IsoButyl Ketone and IPA is IsoPropyl Alcohol), and finally the sample was washed with excess IPA. Samples were

transferred immediately to the evaporator (Edwards Auto 306) for the formation of a metal overlayer. After evaporation, unexposed resist, and its metal coating was removed by sonication in either methanol or acetone.

2.4.8 Conductivity Measurements

The conductivity of nanowires was measured on gold electrodes using the apparatus shown in figure 2.21.

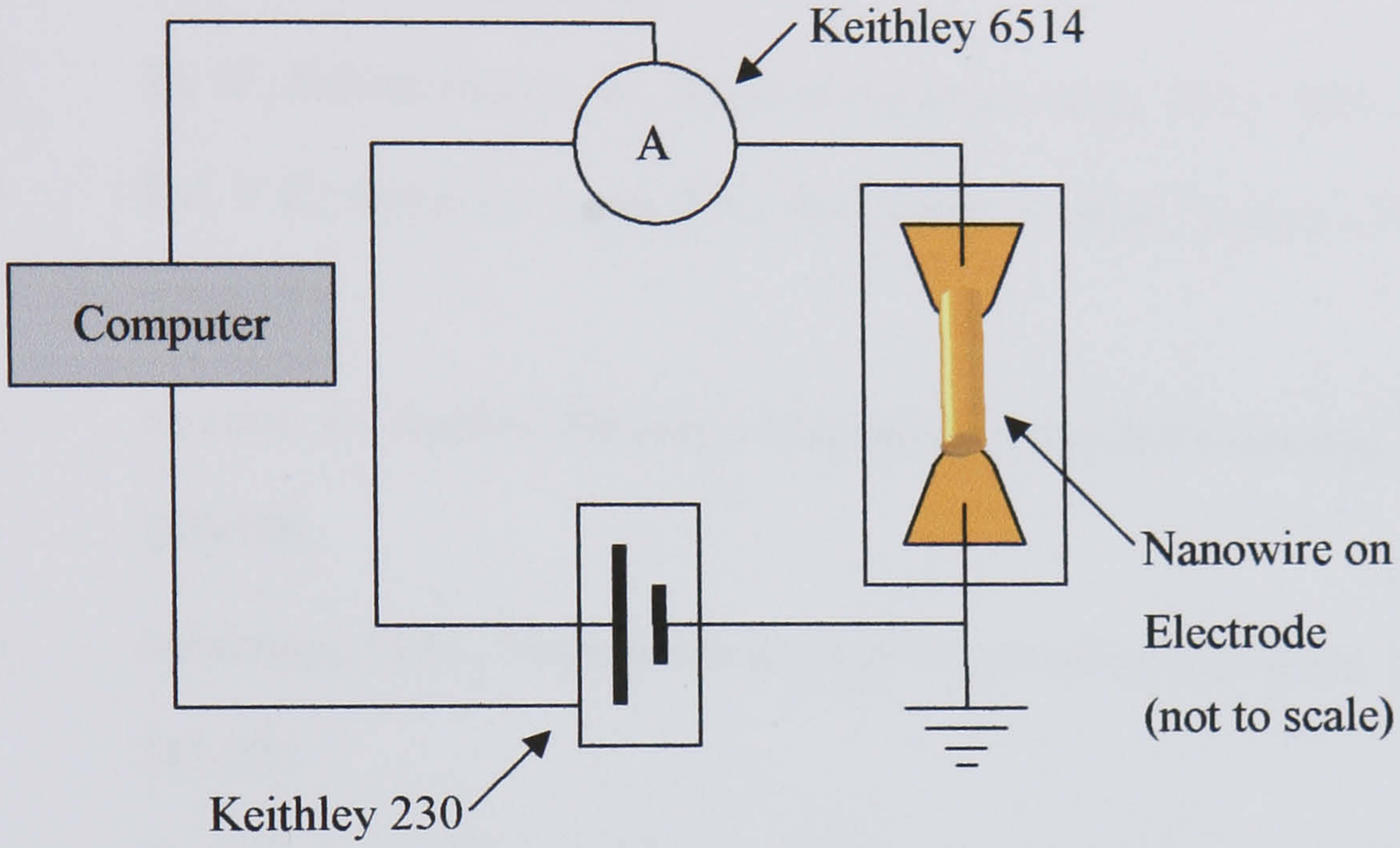

Figure 2.21. Schematic diagram depicting the nanowire transport measurement apparatus

Contacts were made to the electrodes with either wires bound with silver paint, or brass spring contacts. Voltage was then applied to the sample through a computer controlled Keithley 230 Programmable Voltage Source, with the resulting current measured by a Keithley 6514 Electrometer, also computer controlled.

2.5: References

1. *Handbook of Chemistry and Physics*. 82 ed, ed. Lide, D.R. 2001: Chapman & Hall/CRC.
2. Piraux, L.; Dubois, S.; DemoustierChampagne, S., Nuclear Instruments & Methods in Physics Research Section B- Beam Interactions with Materials and Atoms, 1997. **131**(1-4): p. 357-363.
3. Yi, G.; Schwarzacher, W., Applied Physics Letters, 1999. **74**(12): p. 1746 - 1748.
4. Sui, Y.C.; Gonzalez-Leon, J.A.; Bermudez, A., et al., Carbon, 2001. **39**(11): p. 1709-171.
5. Huczko, A., Applied Physics a-Materials Science & Processing, 2000. **70**(4): p. 365-376.
6. Lohrengel, M.M., Materials Science & Engineering R-Reports, 1993. **11**(6): p. 243-294.
7. Brandli, C.; Jaramillo, T.F.; Ivanovskaya, A., et al., Electrochimica Acta, 2001. **47**(4): p. 553-557.
8. Lehmann, V.; Stengl, R.; Luigart, A., Materials Science and Engineering B-Solid State Materials for Advanced Technology, 2000. **69**: p. 11-22.
9. Lehmann, V.; Gruning, U., Thin Solid Films, 1997. **297**(1-2): p. 13-17.
10. Masuda, H.; Satoh, M., Japanes Journal of Applied Physics Part 2 - Letters, 1996. **35**(1B): p. L126 - L129.
11. Ono, S.; Saito, M.; Ishiguro, M., et al., Journal of the Electrochemical Society, 2004. **151**(8): p. B473-B478.
12. Sauer, G.; Brehm, G.; Schneider, S., et al., Journal of Applied Physics, 2002. **91**(5): p. 3243-3247.
13. Thamida, S.K.; Chang, H.C., Chaos, 2002. **12**(1): p. 240-251.

14. Sullivan, J.P.; Wood, G.C., Proceedings of the Royal Society of London A. 1970. **317**: p. 511 - 543.

15. Li, F.Y.; Zhang, L.; Metzger, R.M., Chemistry of Materials, 1998. **10**(9): p. 2470-2480.

16. Nagayama, M.; Tamura, K., Electrochimica Acta, 1968. **13**(8): p. 1773-&.

17. Jessensky, O.; Muller, F.; Gosele, U., Journal of the Electrochemical Society, 1998. **145**(11): p. 3735-3740.

18. Ono, S.; Masuko, N., Corrosion Science, 1992. **33**(3): p. 503-&.

19. Nielsch, K.; Choi, J.; Schwirn, K., et al., Nano Letters, 2002. **2**(7): p. 677-680.

20. Thompson, G.E.; Wood, G.C., Nature, 1981. **290**(5803): p. 230-232.

21. Pan, H.; Lin, H.Y.; Feng, Y.P., et al., Ieee Transactions on Nanotechnology, 2004. **3**(4): p. 462-467.

22. Bandyopadhyay, S.; Miller, A.E.; Chang, H.C., et al., Nanotechnology, 1996. **7**(4): p. 360-371.

23. Behnke, J.F.; Sands, T., Journal of Applied Physics, 2000. **88**(11): p. 6875-6880.

24. Jagminas, A.; Bigeliene, D.; Mikulskas, I., et al., Journal of Crystal Growth, 2001. **233**(3): p. 591-598.

25. Li, A.P.; Muller, F.; Birner, A., et al., Journal of Applied Physics, 1998. **84**(11): p. 6023-6026.

26. Parkhutik, V.P.; Shershulsky, V.I., Journal of Physics D-Applied Physics, 1992. **25**(8): p. 1258-1263.

27. Shimizu, K.; Kobayashi, K.; Thompson, G.E., et al., Philosophical Magazine a-Physics of Condensed Matter Structure Defects and Mechanical Properties, 1992. **66**(4): p. 643-652.

28. Hoar, T.P.; Mott, N.F., Journal of Physics and Chemistry of Solids, 1959. **9**(2): p. 97-99.

29. Sui, Y.C.; Saniger, J.M., Materials Letters, 2001. **48**(3-4): p. 127 - 136.

30. Asoh, H.; Nishio, K.; Nakao, M., et al., Journal of the Elctrochemical Society, 2001. **148**(4): p. B152 - B156.

31. Masuda, H.; Hasehwa, F., Journal of the Electrochemical Society, 1997. **144**(5): p. L127 - L130.

32. Masuda, H.; Fukuda, K., Science, 1995. **268**(5216): p. 1466-1468.

33. Masuda, H.; Yada, K.; Osaka, A., Japanese Journal of Applied Physics Part 2-Letters, 1998. **37**(11A): p. L1340 - L1342.

34. Masuda, H.; Yamada, H.; Satoh, M., et al., Applied Physics Letters, 1997. **71**(19): p. 2770-2772.

35. Jessensky, O.; Muller, F.; Gosele, U., Applied Physics Letters, 1998. **72**(10): p. 1173-1175.

36. Zhang, X.Y.; Zhang, L.D.; Lei, Y., et al., Journal of Materials Chemistry., 2001. **11**(6): p. 1732 - 1734.

37. Gao, T.; Meng, G.W.; Zhang, J., et al., Applied Physics a-Materials Science & Processing, 2001. **73**(2): p. 251-254.

38. Menon, V.P.; Martin, C.R., Analytical Chemistry, 1995. **67**(13): p. 1920 - 1928.

39. Langmuir, I., Trans. Faraday Soc., 1920. **15**: p. 62.

40. Blodgett, K.B., J. Am. Chem. Soc., 1934. **56**: p. 495.

41. Bigelow, W.C.P., D.L.;Zisman, W.A., J. Colloid Interface Sci., 1946. **1**: p. 513.

42. Aue, W.A.; Hastings, C.R.; Augl, J.M., J. Chromatogr., 1970. **53**: p. 487.

43. Kirkland, J.J., Chromatogr. Sci., 1971. **9**: p. 206.

44. Weetall, H.H.; Hersh, L.S., Biochim. Biophys. Acta, 1970. **206**: p. 44.

45. Weiner, S.J.; Kollman, P.A.; Case, D.A., et al., J. Am. Chem. Soc., 1984. **106**: p. 765.

46. Sagiv, J., J. Am. Chem. Soc., 1980. **92**: p. 102.

47. Maoz, R.; Sagiv, J., J. Colloid Interface Sci., 1984. **100**: p. 465-496.

48. Nuzzo, R.G.; Allara, D.L., J. Am. Chem. Soc., 1983. **105**: p. 4481-4483.

49. Ulman, A., Chemical Reviews, 1996. **96**(4): p. 1533-1554.

50. Ulman, A., *An introduction to ultrathin organic films from Langmuir-Blodgett to self-assembly*. 1991, Boston London: Academic Press.

51. Sellers, H.; Ulman, A.; Shnidman, Y., et al., Journal of the American Chemical Society, 1993. **115**(21): p. 9389-9401.

52. Laibinis, P.E.; Whitesides, G.M., Journal of the American Chemical Society, 1992. **114**(6): p. 1990-1995.

53. Martele, Y.; Callewaert, K.; Naessens, K., et al., Materials Science & Engineering C-Biomimetic and Supramolecular Systems, 2003. **23**(3): p. 341-345.

54. Nivens, D.A.; Conrad, D.W., Langmuir, 2002. **18**(2): p. 499-504.

55. Cant, N.E.; Critchley, K.; Zhang, H.-L., et al., Thin Solid Films, 2003. **426**: p. 31-39.

56. Silberzan, P.; Leger, L., Comptes Rendus De L' Academie Des Sciences Serie Ii, 1991. **312**(10): p. 1089-1094.

57. Ulman, A., *Self-assembled monolayers of thiols*. 1998, San Diego: Academic Press.

58. Evans, S.D.; Urankar, E.; Ulman, A., et al., Journal of the American Chemical Society, 1991. **113**(11): p. 4121-4131.

59. Nuzzo, R.G.; Dubois, L.H.; Allara, D.L., J. Am. Chem. Soc., 1990. **112**: p. 558-569.

60. Bain, C.D.; Troughton, E.B.; Tao, Y.-T., et al., J. Am. Chem. Soc., 1989. **111**: p. 321-335.

61. Nemetz, A.; Fischer, T.; Ulman, A., et al., Journal of Chemical Physics, 1993. **98**(7): p. 5912-5919.

62. Ulman, A., Advanced Materials, 1990. **2**(12): p. 573-582.

63. Chidsey, C.E.D.; Loiacono, D.N., Langmuir, 1990. **6**: p. 682-691.

64. Cheadle, E.M., *PhD Thesis: Characterisation of Self-Assembled Monolayers.* PhD Thesis. 2002, Leeds: University of Leeds. 162.

65. Cheadle, E.M.; Batchelder, D.N.; Evans, S.D., et al., Langmuir, 2001. **17**(21): p. 6616-6621.

66. Hoffmann, P.W.; Stelzle, M.; Rabolt, J.F., Langmuir, 1997. **13**(7): p. 1877-1880.

67. Mostefai, M.; Auriac, Y.; Shanahan, M.E.R., et al., International Journal of Adhesion and Adhesives, 1998. **18**(4): p. 273-281.

68. Ulman, A., J. Mater. Educ, 1989(11): p. 205.

69. Walzcak, M.M.; Chung, C.; Stole, S.M., et al., J. Am. Chem. Soc., 1991. **113**: p. 2370-2378.

70. Ihs. A; B., L., Langmuir, 1994. **10**: p. 734.

71. Shimazu, K.; Sato, Y.; Yagi, I., et al., Bull. Chem. Soc., 1994(67): p. 863.

72. Demoz, A.; Harrison, D.J., Langmuir, 1993. **9**: p. 1046.

73. Muskal, N.; Turyan, I.; Shurky, A., et al., J. Am. Chem. Soc., 1995. **117**: p. 1147.

74. Stratmann, M., Adv. Mater., 1990. **2**(4): p. 191-195.

75. Volmer, M.; Stratmann, M.; Viefhaus, H., Surface and Interface Analysis, 1990. **16**(1-12): p. 278.

76. Colvin, V.L.; Goldstein, A.N.; Alivisatos, A.P., Journal of the American Chemical Society, 1992. **114**(13): p. 5221-5230.

77. Tredgold, R.H., *Order in organic films.* 1994, Cambridge: Cambridge University Press.

78. Booth, C.; Bushby, R.J.; Cheng, Y.L., et al., Tetrahedron, 2001. **57**(49): p. 9859-9866.

79. Gillen, G.; Wight, S.; Bennett, J., et al., Applied Physics Letters, 1994. **65**: p. 534.

80. Ada, E.T.; Hanley, L.; Etchin, S., et al., Journal of Vacuum Science & Technology B, 1995. **13**(6): p. 2189-2196.

81. Balaur, E.; Djenizian, T.; Boukherroub, R., et al., Electrochemistry Communications, 2004. **6**(2): p. 153-157.

82. Kaltenpoth, G.; Volkel, B.; Nottbohm, C.T., et al., Journal of Vacuum Science & Technology B, 2002. **20**(6): p. 2734-2738.

83. Weimann, T.; Geyer, W.; Hinze, P., et al., Microelectronic Engineering, 2001. **57-8**: p. 903-907.

84. Golzhauser, A.; Geyer, W.; Stadler, V., et al., Journal of Vacuum Science & Technology B, 2000. **18**(6): p. 3414-3418.

85. Jager, B.; Schurmann, H.; Muller, H.U., et al., Zeitschrift Fur Physikalische Chemie-International Journal of Research in Physical Chemistry & Chemical Physics, 1997. **202**: p. 263-272.

86. Kuller, A.; El-Desawy, M.A.; Stadler, V., et al., Journal of Vacuum Science & Technology B, 2004. **22**(3): p. 1112-1117.

87. Li, X.M.; Auletta, T.; van Veggel, F., et al., Organic & Biomolecular Chemistry, 2004. **2**(3): p. 296-300.

88. Wouters, D.; Schubert, U.S., Angewandte Chemie-International Edition, 2004. **43**(19): p. 2480-2495.

89. Barsotti, R.J.; O'Connell, M.S.; Stellacci, F., Langmuir, 2004. **20**(12): p. 4795-4798.

90. Kooi, S.E.; Baker, L.A.; Sheehan, P.E., et al., Advanced Materials, 2004. **16**(12): p. 1013.

91. Calvert, J.M.; Chen, M.S.; Dulcey, C.S., et al., Journal of Vacuum Science & Technology B, 1991. **9**(6): p. 3447-3450.

92. Dressick, W.J.; Calvert, J.M.; Dulcey, C.S., et al., Abstracts of Papers of the American Chemical Society, 1992. **204**: p. 185.

93. Calvert, J.M.; Brandow, S.L.; Chen, M.S., et al., Abstracts of Papers of the American Chemical Society, 1993. **205**: p. 11.

94. Huang, J.; Hemminger, J.C., J. Am. Chem. Soc., 1993. **115**: p. 3342-3343.

95. Ferris, M.M.; Rowlen, K.L., Applied Spectroscopy, 2000. **54**(5): p. 664-668.

96. Kumar, A.; Biebuyck, H.; Whitesides, G.M., Langmuir, 1994. **10**: p. 1498.

97. Michel, B.; Bernard, A.; Bietsch, A., et al., Ibm Journal of Research and Development, 2001. **45**(6): p. 870-870.

98. Schmid, H.; Michel, B., Macromolecules, 2000. **33**(8): p. 3042-3049.

99. Wilbur, J.L.; Kumar, A.; Kim, E., et al., Advanced Materials, 1994. **6**(7-8): p. 600-604.

100. Delamarche, E.; Schmid, H.; Bietsch, A., et al., Journal of Physical Chemistry B, 1998. **102**(18): p. 3324-3334.

101. Michel, B.; Bernard, A.; Bietsch, A., et al., Ibm Journal of Research and Development, 2001. **45**(5): p. 697-719.

102. Israelachvili, J.N.; Pashley, R.M., Journal of Colloid and Interface Science, 1984. **98**(2): p. 500-514.

103. Israelachvili, J.; Pashley, R., Nature, 1982. **300**(5890): p. 341-342.

104. Hato, M., Journal of Physical Chemistry, 1996. **100**(47): p. 18530-18538.

105. Meyer, E.E.; Lin, Q.; Israelachvili, J.N., Langmuir, 2005. **21**(1): p. 256-259.

106. Ederth, T.; Liedberg, B., Langmuir, 2000. **16**(5): p. 2177-2184.

107. Tsao, Y.H.; Evans, D.F.; Wennerstrom, H., Science, 1993. **262**(5133): p. 547-550.

108. Christenson, H.K.; Claesson, P.M., Science, 1988. **239**(4838): p. 390-392.

109. Tyrrell, J.W.G.; Attard, P., Langmuir, 2002. **18**(1): p. 160-167.

110. Johnson, K.E.; Dettre, R.H., *Wettability and Contact Angles*, in *Surface and Colloidal Science*, Matijevic, E., Editor, John Wiley & Sons: New York.

111. Decher, G., Science, 1997. **277**(5330): p. 1232-1237.

112. Sukhishvili, S.A.; Granick, S., Macromolecules, 2002. **35**(1): p. 301-310.

113. Freeman, T.L.; Evans, S.D.; Ulman, A., Langmuir, 1995. **11**(11): p. 4411-4417.

114. Sastry, M.; Patil, V.; Mayya, K.S., Journal of Physical Chemistry B, 1997. **101**(7): p. 1167-1170.

115. Evans, S.D.; Ulman, A.; Goppertberarducci, K.E., et al., Journal of the American Chemical Society, 1991. **113**(15): p. 5866-5868.

116. Whitesides, G.M.; Biebuyck, H.A.; Folkers, J.P., et al., Journal of Adhesion Science and Technology, 1991. **5**(1): p. 57-69.

117. Vezenov, D.V.; Noy, A.; Rozsnyai, L.F., et al., Journal of the American Chemical Society, 1997. **119**(8): p. 2006-2015.

118. vanderVegte, E.W.; Hadziioannou, G., Langmuir, 1997. **13**(16): p. 4357-4368.

119. Zhang, H.; He, H.X.; Wang, J., et al., Applied Physics a-Materials Science & Processing, 1998. **66**: p. S269-S271.

120. Giesbers, M.; Kleijn, J.M.; Stuart, M.A.C., Journal of Colloid and Interface Science, 2002. **252**(1): p. 138-148.

121. Chaiet, L.; Wolf, F.J., Archives of Biochemistry and Biophysics, 1964. **106**(1-3): p. 1-&.

122. Hendrickson, W.A.; Pahler, A.; Smith, J.L., et al., Proceedings of the National Academy of Sciences of the United States of America, 1989. **86**(7): p. 2190-2194.

123. Weber, P.C.; Ohlendorf, D.H.; Wendoloski, J.J., et al., Science, 1989. **243**(4887): p. 85-88.

124. Liu, H.; Bau, H.H., Physics of Fluids, 2004. **16**(5): p. 1217-1228.

125. Evoy, S.; DiLello, N.; Deshpande, V., et al., Microelectronic Engineering, 2004. **75**(1): p. 31-42.

126. Dimaki, M.; Boggild, P., Nanotechnology, 2004. **15**(8): p. 1095-1102.

127. Chan, R.H.M.; Fung, C.K.M.; Li, W.J., Nanotechnology, 2004. **15**(10): p. S672-S677.

128. Klar, T.; Perner, M.; Grosse, S., et al., Physical Review Letters, 1998. **80**(19): p. 4249-4252.

129. Kreibig, U.; Vonfrags.C, Zeitschrift Fur Physik, 1969. **224**(4): p. 307-&.

130. Sondheimer, E.H., Advances in Physics, 2001. **50**(6): p. 499-537.

131. Lopez, G.P.; Biebuyck, H.A.; Whitesides, G.M., Langmuir, 1993. **9**(6): p. 1513-1516.

132. Briggs, D.; Seah, M.P., *Practical Surace Analysis*. Vol. Vol 1-Auger and X-ray Photoelectron Spectroscopy. 1990: Wiley.

133. Beamson, G.; Briggs, D., *High Resolution XPS of Organic Polymers*. 1992: Wiley.

134. Watt, I.M., *The Principles and Practice of Electron Microscopy*. 1985, Cambridge: Cambridge University Press.

135. Weisenhorn, A.L.; Hansma, P.K.; Albrecht, T.R., et al., Applied Physics Letters, 1989. **54**(26): p. 2651-2653.

136. Vickerman, J.C., *Surface Analysis - The Principle Techniques*. 1997, Chichester: John Wiley & Sons Ltd.

137. Weisendanger, R., *Scanning Probe Microscopy and Spectroscopy: Methods and Applications*. 1998, Cambridge: Cambridge University Press.

138. Isrealachvili, J.N., *Intermolecular and Surface Forces: With Applications to Colloidal and Biological Systems*. 1985, London: Academic Press, Inc.

Chapter 3: Fabrication and Characterisation of Template Materials and Nanowires

This chapter presents results illustrating the various nanowire fabrication techniques that have been employed. The objectives of this chapter are:

1) Characterise the structure and growth of anodised porous aluminium oxide.
2) Characterise the structure of Whatman 'Cyclopore' and 'Anodisc' commercial filtration membranes.
3) Demonstrate the use of these materials as templates for the fabrication of gold nanowires.
4) Characterise nanowires manufactured by each template deposition procedure investigated.
5) Characterise the functionalisation of gold nanowires with thiol based SAMs.

3.1: Template Materials

Template deposition requires a suitable host template that is stable to the deposition requirements, and that allows removal of deposited structures if required. During the course of this work three template materials were used, porous alumina membranes, and Whatman 'Anodisc' and 'Cyclopore' filtration membranes.

3.1.1 Porous Aluminium Oxide

Porous aluminium oxide is a thick oxide layer formed electrochemically on aluminium substrates when they are anodised, under specific conditions. Porous alumina is characterized by cylindrical pores of uniform diameter, perpendicular to the plane of the film. Whilst pores are open at the oxide surface, an oxide barrier layer closes each pore at its base and attaches the membrane to the aluminium substrate.

The initiation of pores on the oxide surface is consistent with substrate grain boundaries, defects sites or depressions in the surface.[1] Prior to anodising, aluminium substrates were annealed and washed, although no polishing was undertaken. As such, pores were observed to nucleate at depressions in the metal surface, figure 3.1.

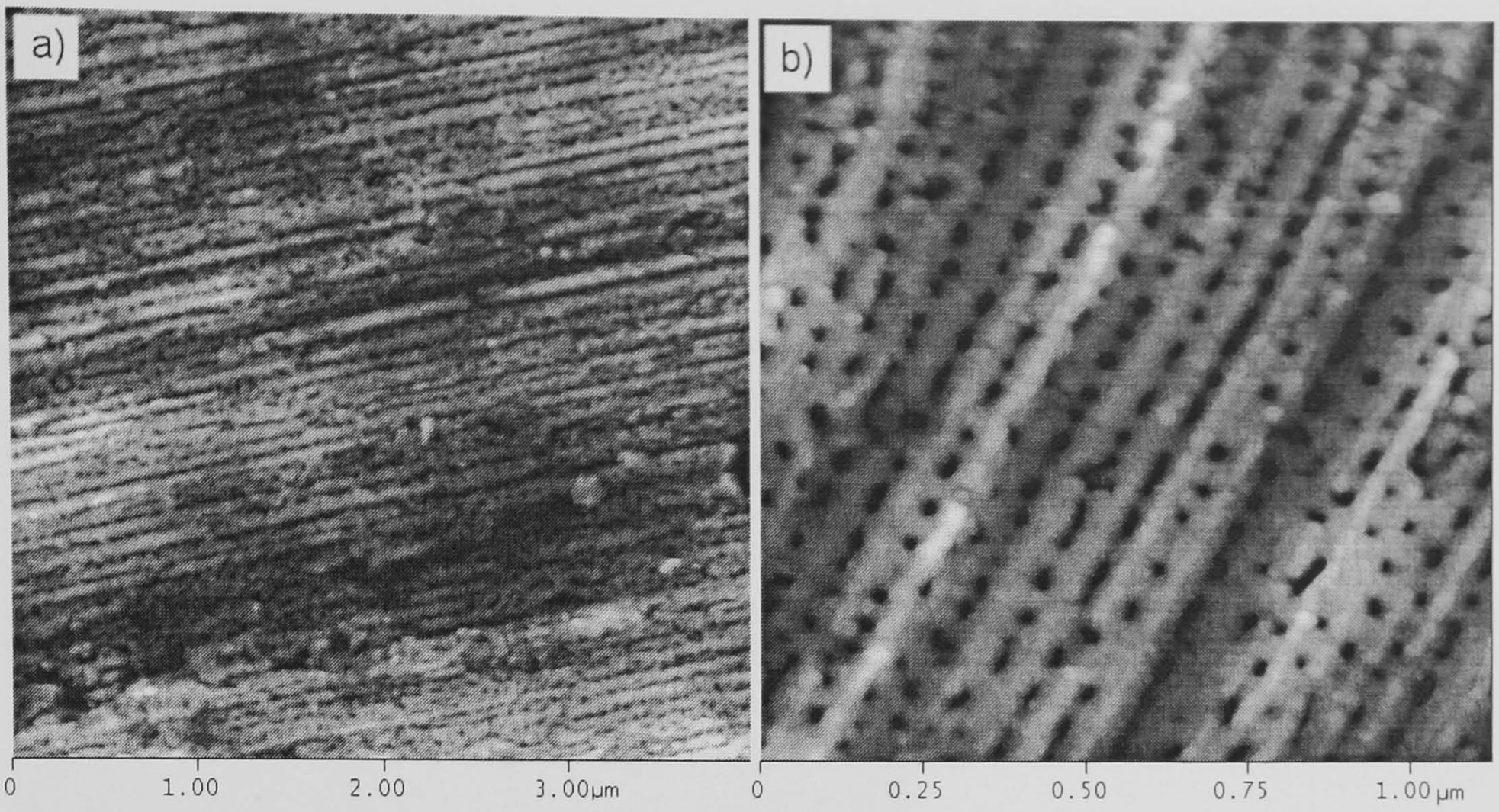

Figure 3.1. AFM image of two separate porous alumina surfaces, after a) anodising at 40V in 0.3 M oxalic acid for 5 hours 40 minutes, and b) 1 hour at the same conditions

Substrate aluminium foils received from manufacturers are rolled to the specified thickness. Consequently, pores nucleate initially in tracks caused during the rolling process. Pores are irregularly sized and shaped although no measurement of their dimensions is attempted due to complications with tip convolution. Interpore separation in figure 3.1b is approximately 90 nm although there is some variation parallel and perpendicular to the track direction.

At the electrochemical conditions used, 40 V in 0.3 M oxalic acid, pores should develop into a hexagonal arrangement, with a uniform pore diameter and separation of 40 nm and 100 nm respectively.[2, 3] Due to texturing of the aluminium substrate by pore penetration, the position and arrangement of the pores at the base of the membrane may be determined by investigating the textured surface of the substrate. This requires the use of selective etching techniques. By immersing the sample in 1.8 wt% chromic acid combined with 6 wt% phosphoric acid in aqueous solution at 60°C overnight, the oxide coating could be removed whilst leaving the substrate intact (figure 3.2).

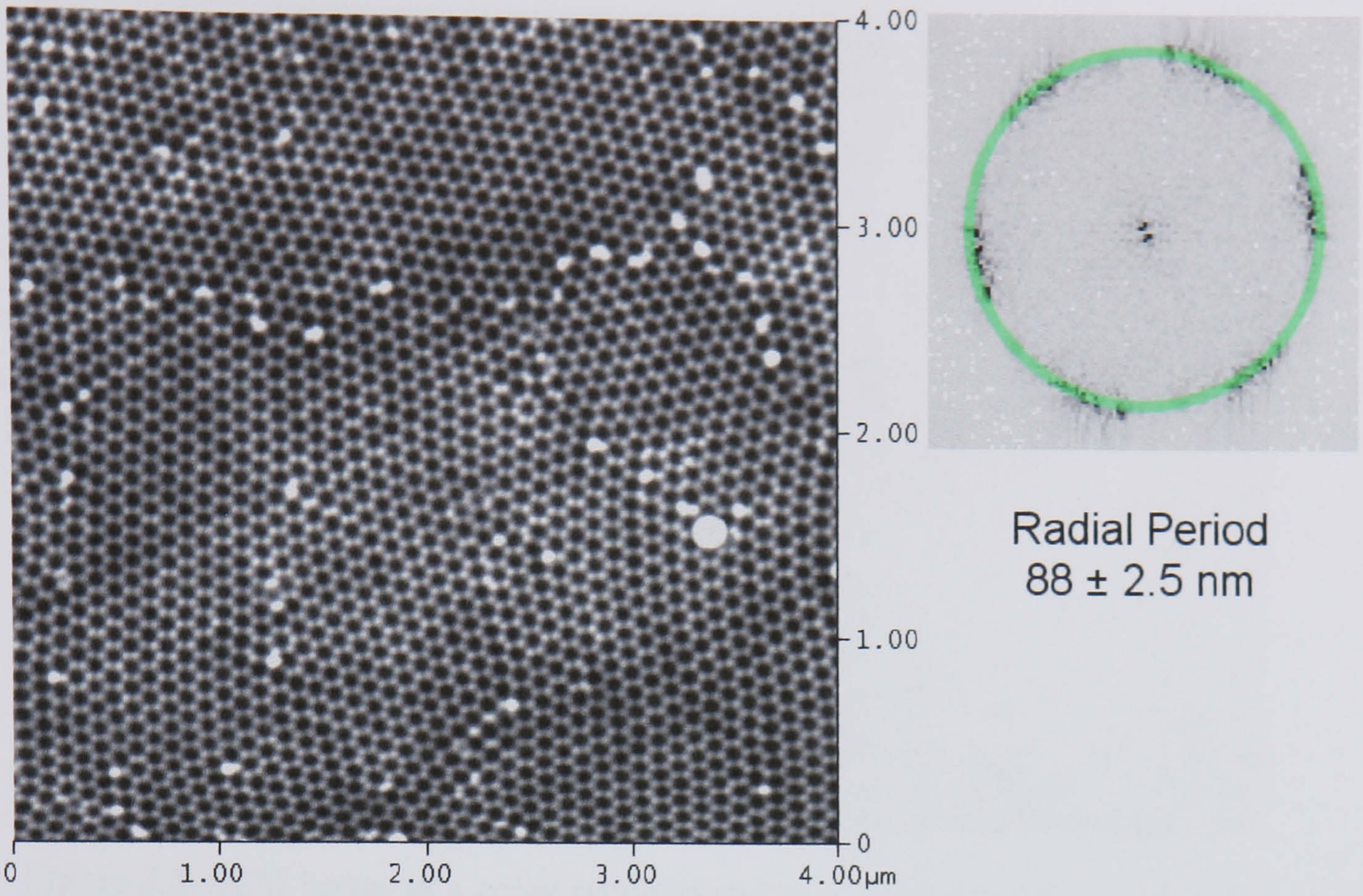

Figure 3.2. AFM image of the aluminium substrate, after anodising at 40 V in 0.3 M oxalic acid for 5 hours 40 minutes and etching in phosphoric/chromic acid overnight, and the associated Fourier transform of the image.

The aluminium substrate demonstrates how pore regularity and arrangement is improved during growth, when compared to the top surface of the oxide, figure 3.1a. Associated with the development of steady state pore development is a planar metal-oxide interface, the surface imaged in figure 3.2 is flatter than the top surface of the porous oxide, figure 3.1a. The size of hexagonally ordered domains is approximately 2 μm^2. The interpore separation is best identified with Fourier analysis, which has been used to determine a value of 88 ± 6 nm.

Similarly, by etching the sample in an aqueous solution containing 0.1 M cupric chloride ($CuCl_2$) and 20 wt% hydrochloric acid (at room temperature) the substrate aluminium can be selectively etched from the oxide membrane. This technique was used to observe the oxide barrier layer that forms between the substrate and porous oxide regions, figure 3.3.

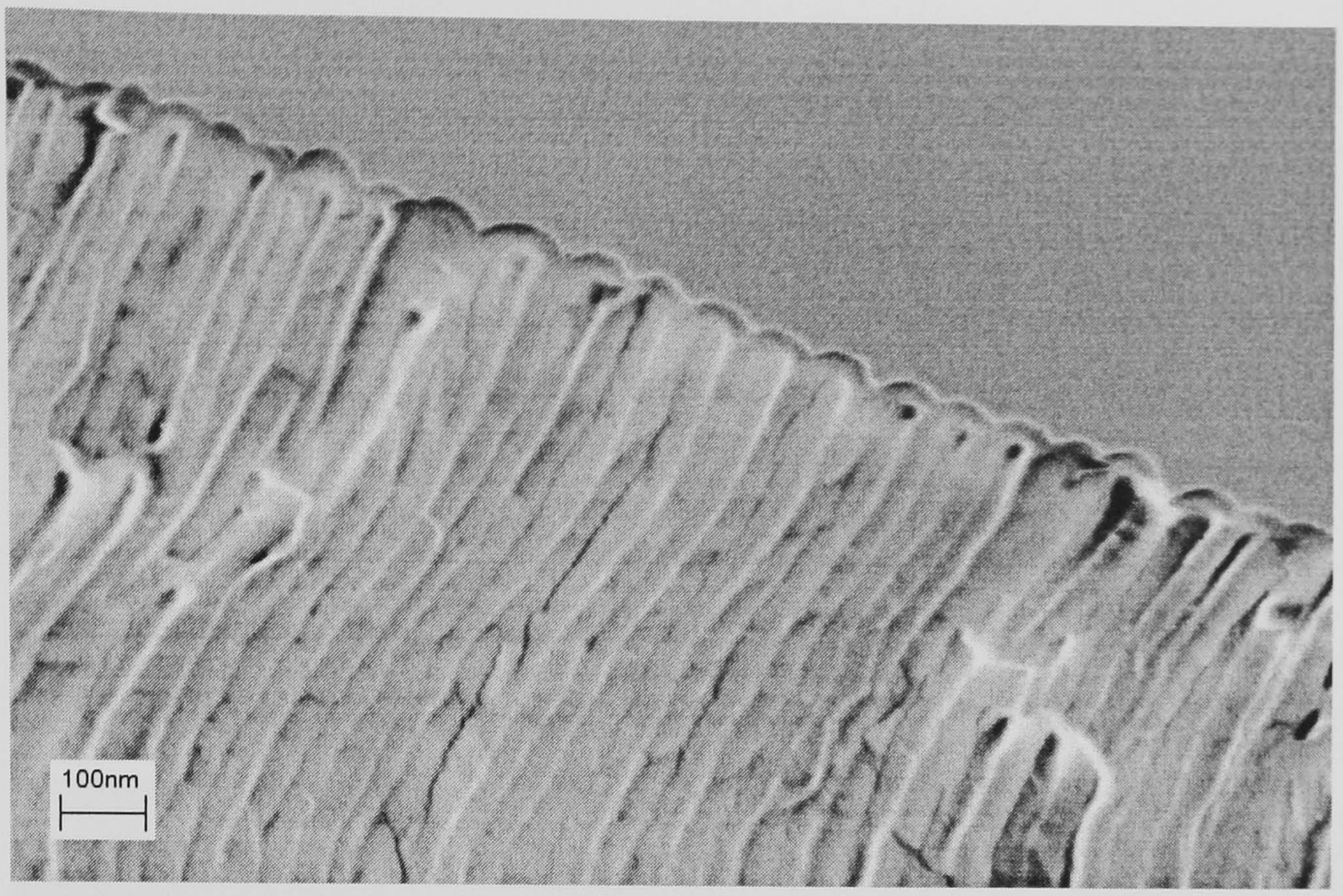

Figure 3.3. SEM image of a cross-section through a porous oxide membrane anodised at 40 V in 0.3 M oxalic acid for 3 hours and removed from the substrate. A sputtered 2 nm platinum coating was applied to prevent charging.

The base of the porous oxide membrane shows the final pore arrangement, its development, and the oxide barrier layer. The barrier oxide thickness of is approximately 27 ± 3 nm, smaller than expected from calculations based upon the 1.05 nmV^{-1} proportionality[4]. Evidence for self-levelling of the pore bases during steady state pore development can be seen from the planar barrier layer.

Once separated from the aluminium substrate the porous oxide can be etched with 5 wt% phosphoric acid solution or 1 M sodium hydroxide. These techniques are commonly used to etch back the barrier layer and enlarge the pore's diameter. Figure 3.4 shows a sequence of topographic AFM images detailing the progress of a phosphoric acid etching procedure through the barrier layer.

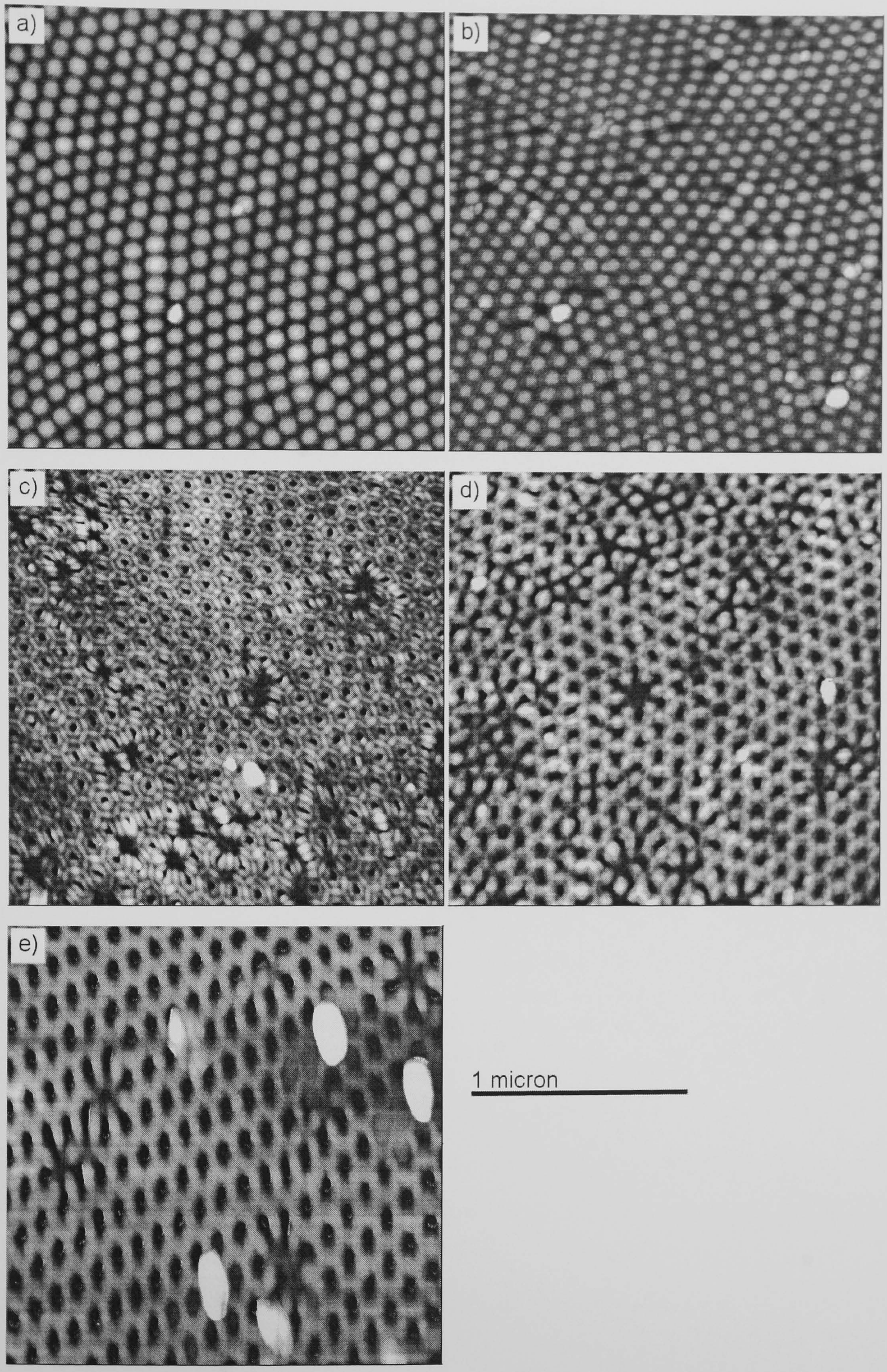

Figure 3.4. AFM sequence showing an etch procedure through the barrier layer of a porous alumina membrane. a) after etching away the aluminium substrate, b) – e) after successive exposures to 5 wt% phosphoric acid for 30 minutes

The oxide texture associated with the pore bases (and which imprints the aluminium substrate) can be observed in figure 3.4a. After etching in 5 wt% phosphoric acid for 30 minutes, figure 3.4b, the surface is smoothed such that the surface roughness reduces from 5.1 nm to 3.9 nm. After etching the membrane for 1 hour, figure 3.4c, the barrier layer is removed and the pores are opened at the base of the membrane. Additionally, each pore is outlined by a hexagon, which is proposed to be less susceptible to the etching procedure. This is speculated to be the amorphous alumina support structure observed by Thompson *et al.*[5] The hexagonal support material can also be observed in figure 3.4b, albeit less clearly. After 1 hour 30 minutes total exposure to the phosphoric acid solution, figure 3.4d, removal of the acid anion contaminated alumina regions increases the pore diameter. Further etching of the contaminated alumina causes the pores to appear hexagonal after 2 hours exposure, figure 3.4e, due to the remaining amorphous alumina support. Continued etching causes the amorphous alumina support to fail and the surface becomes too irregular to observe with the AFM.

Textured aluminium substrates are the basis of Masuda's 2-step porous alumina growth procedure, when combined with selective etch procedures described above.[3] Using the 2-step anodising technique, the textured metal surface created after the removal of the first oxidation stage was used to initiate pores with a regular arrangement throughout the second anodising stage. By this process membranes were manufactured with pores hexagonally ordered at both surfaces, figure 3.5.

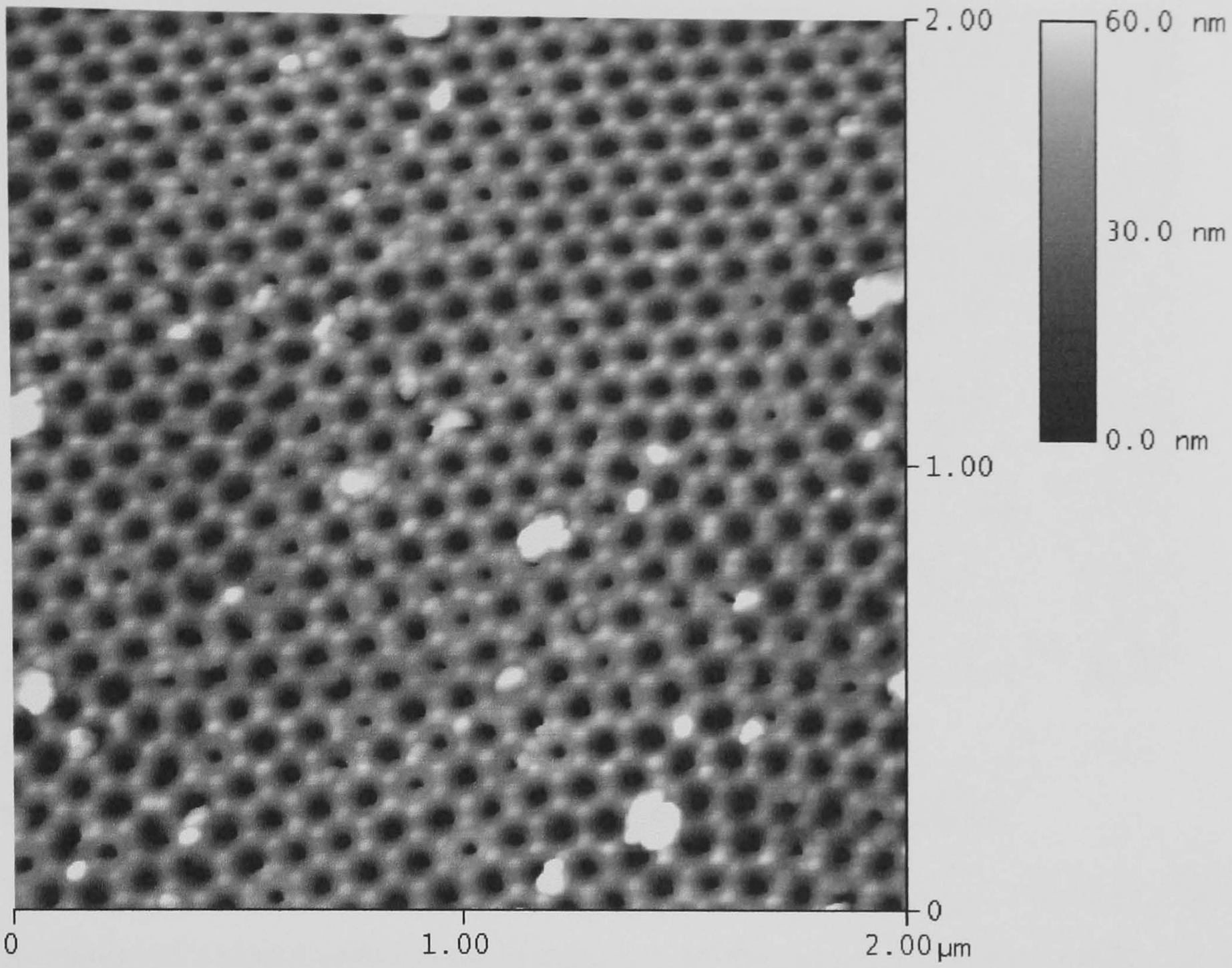

Figure 3.5. AFM image of the top surface of a porous alumina membrane fabricated by the 2-step process. Anodising times for the first and second anodising stages were 5 hours 30 minutes and 2 hours respectively.

The top surface of the porous oxide surface retains the hexagonal arrangement of the previous anodising stage. The steady state pore arrangement initiated at oxide surface continues though the oxide resulting in pores that are straight and parallel, figure 3.6, except at domain boundaries where the competitive ordering process continues.

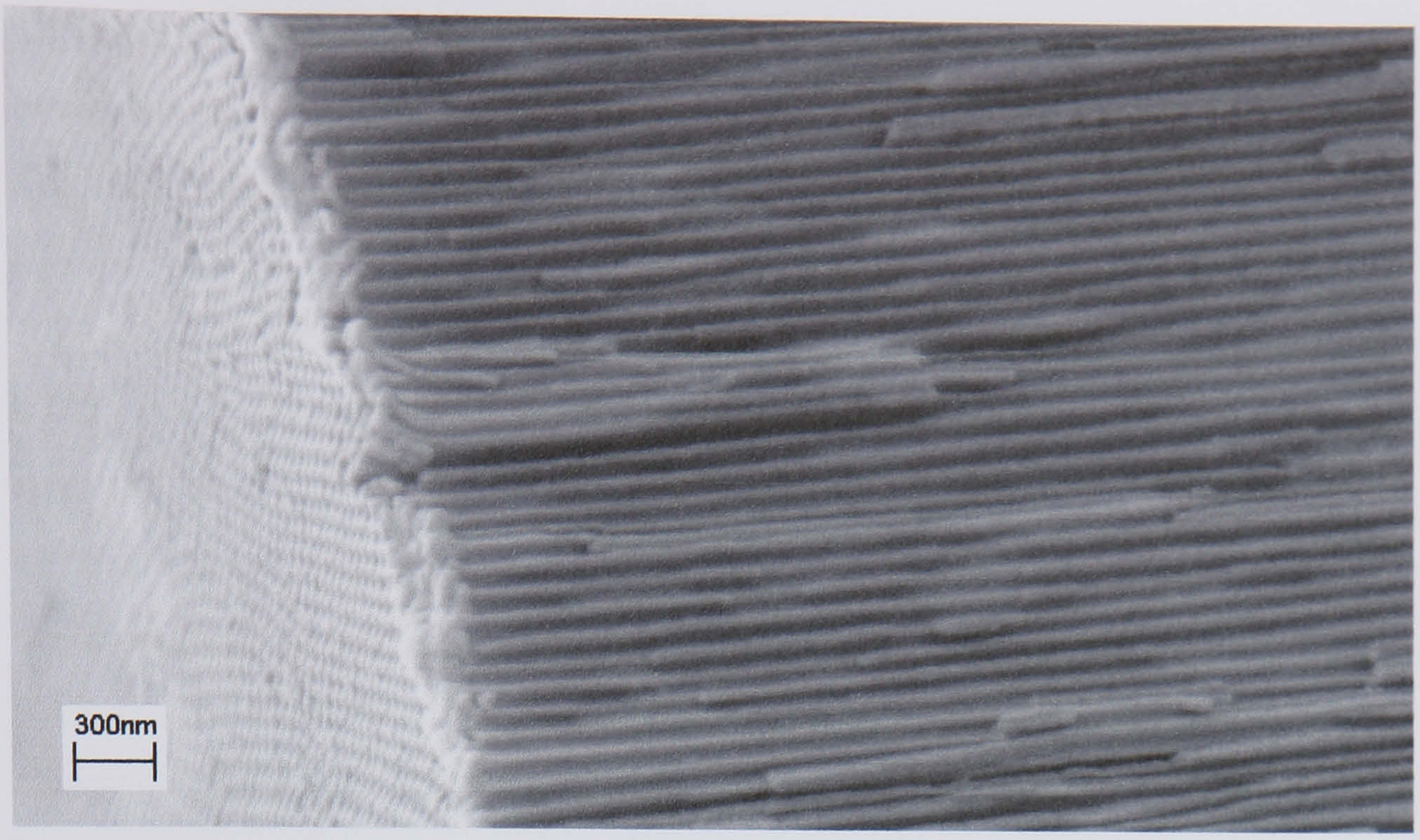

Figure 3.6. SEM image of a porous alumina membrane after 2-step growth. A sputtered 2 nm platinum coating was applied to prevent charging.

The development of steady state porous oxide growth has previously been linked to the formation of a planar oxide-metal interface. The flattening of the oxide surface can be observed after short anodising periods, figure 3.7.

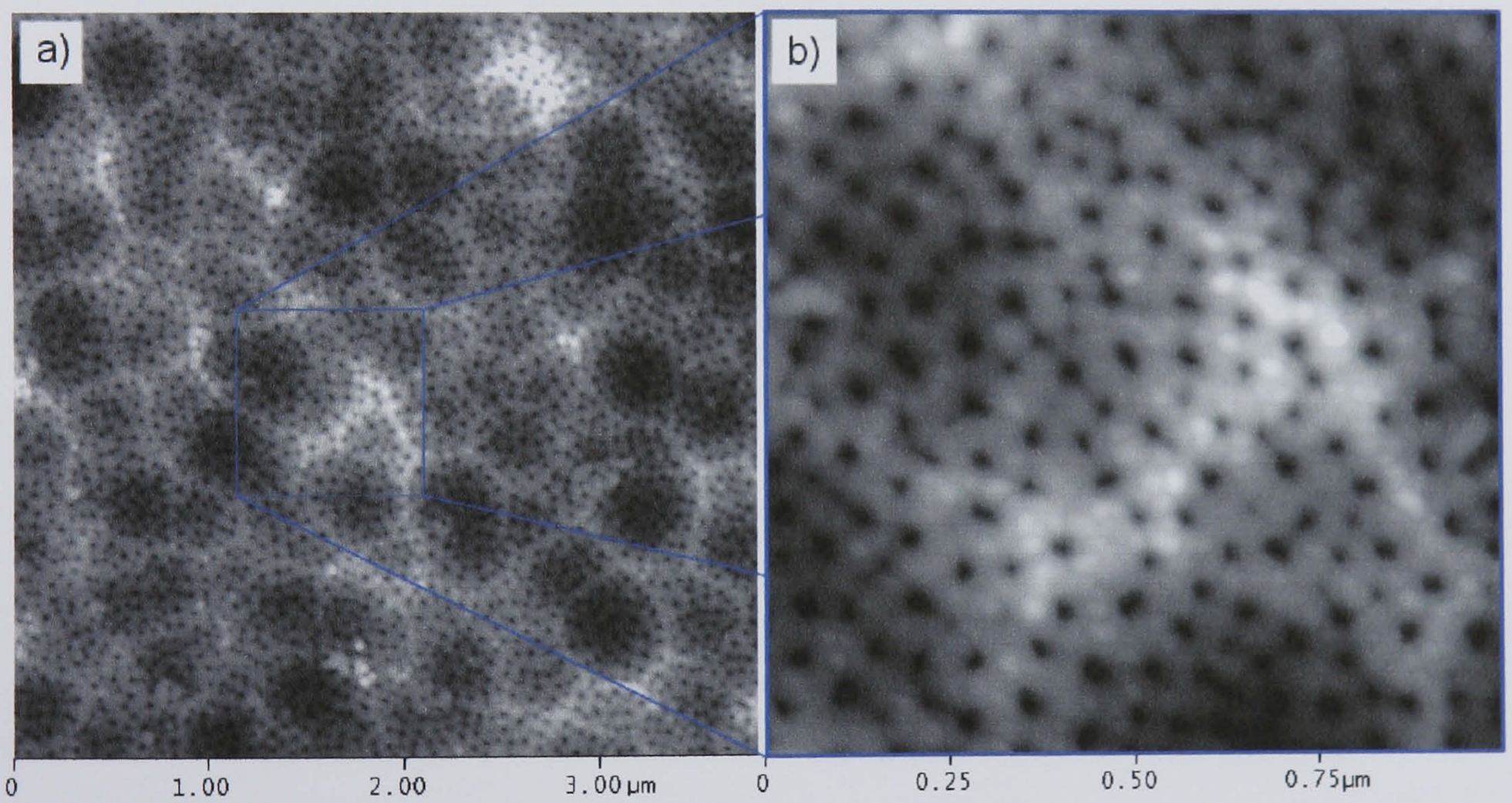

Figure 3.7. AFM image of a 2-step porous oxide showing the development of a planar metal-oxidation interface showing a) bulk smoothing and b) development of pore regularity

Figure 3.7 displays the surface following a 2-step porous oxide growth procedure, where the times for the first and second growth stages were 10 minutes and 2 hours respectively. The development of a planar metal-oxide interface can be observed compared against

those surfaces shown in figure 3.1a. Similarly, figure 3.7b shows that pores have established a more uniform density across the surface than figure 3.1b, a precursor to the development of hexagonal structure.

All the porous alumina fabricated during the course of this work has been fabricated in 0.3 M oxalic acid electrolyte, at 40 V. No attempts have been made to grow different sized porous oxides, or use alternative electrolytes. However, by changing the electrochemical conditions during growth, the scale of the porous oxide may also be changed. This premise is the basis of the voltage reduction technique[6] used to thin the barrier layer at the base of membranes, and also capable of separating it from the aluminium substrate. The voltage reduction technique has been used to thin the barrier layer from approximately ~40 nm at 40 V to ~10 nm at 10 V. The voltage was scaled in 10 % reductions, and the current allowed to stabilise between every adjustment. Figure 3.8 shows a porous alumina membrane grown using the voltage reduction technique, separated from the aluminium substrate and imaged with the FEGSEM.

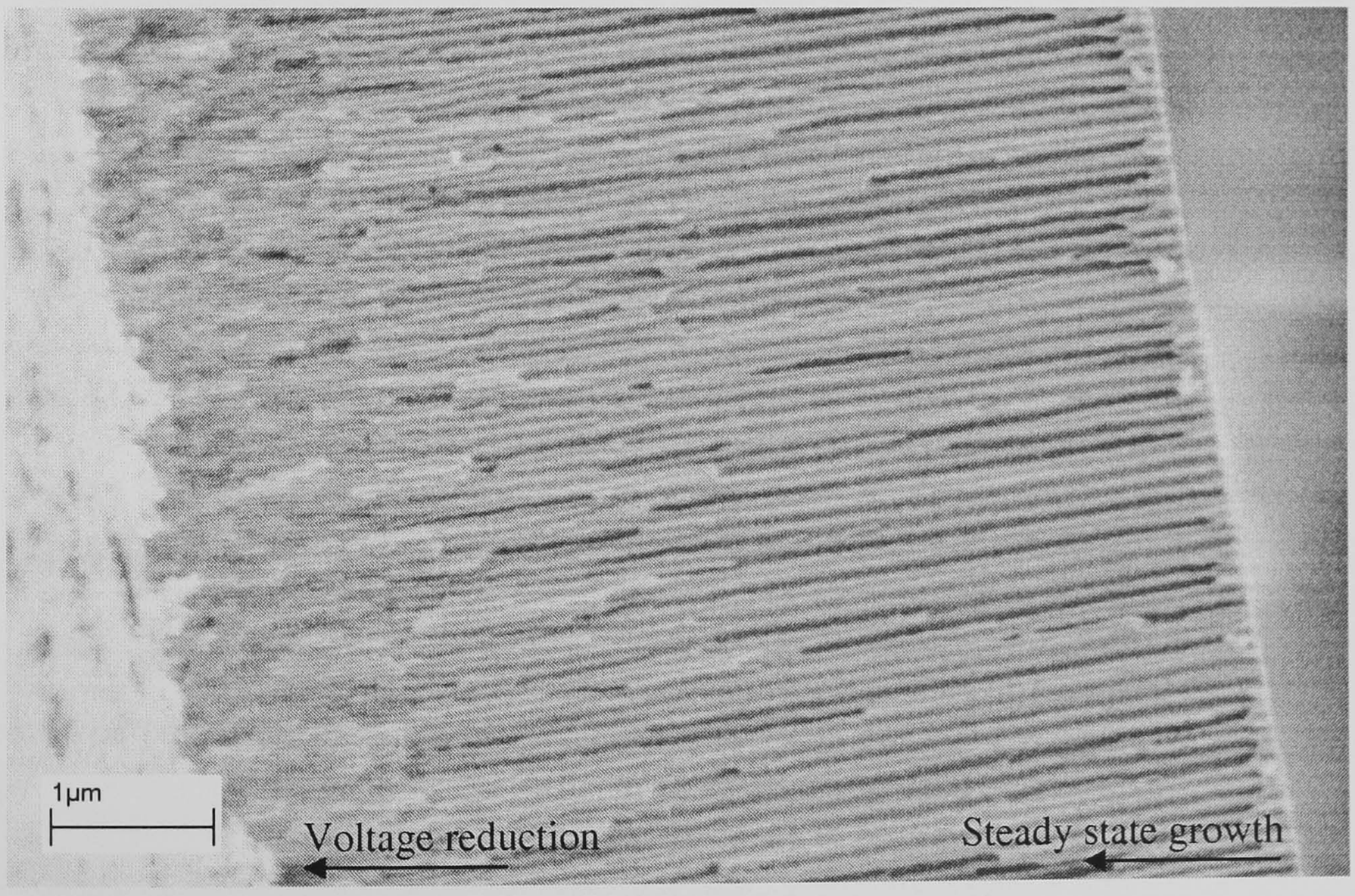

Figure 3.8. SEM image of a 2-step porous alumina membrane grown using the voltage reduction technique. A sputtered 2 nm platinum coating was applied to prevent charging.

Approximately half way though the oxide growth the pores can be observed to split. Throughout the rest of the oxide growth pores continue to split until they are predicted to be approximately 10 nm in diameter at the base of the membrane.

3.1.2 Whatman 'Anodisc' Membranes

Whatman 'Anodisc' filtration membranes are porous aluminium oxide membranes separated from the aluminium substrate with the barrier layer removed. Membranes are 66 μm thick, have a randomly ordered pore array, and are available with a range of pore diameters. Those used during the course of this work are specified with a 20 nm pore diameter, although this is only present at the filtration surface of the membrane. Pore diameter at the opposite surface and through the majority of the membrane is 175 ± 25 nm, figure 3.9.

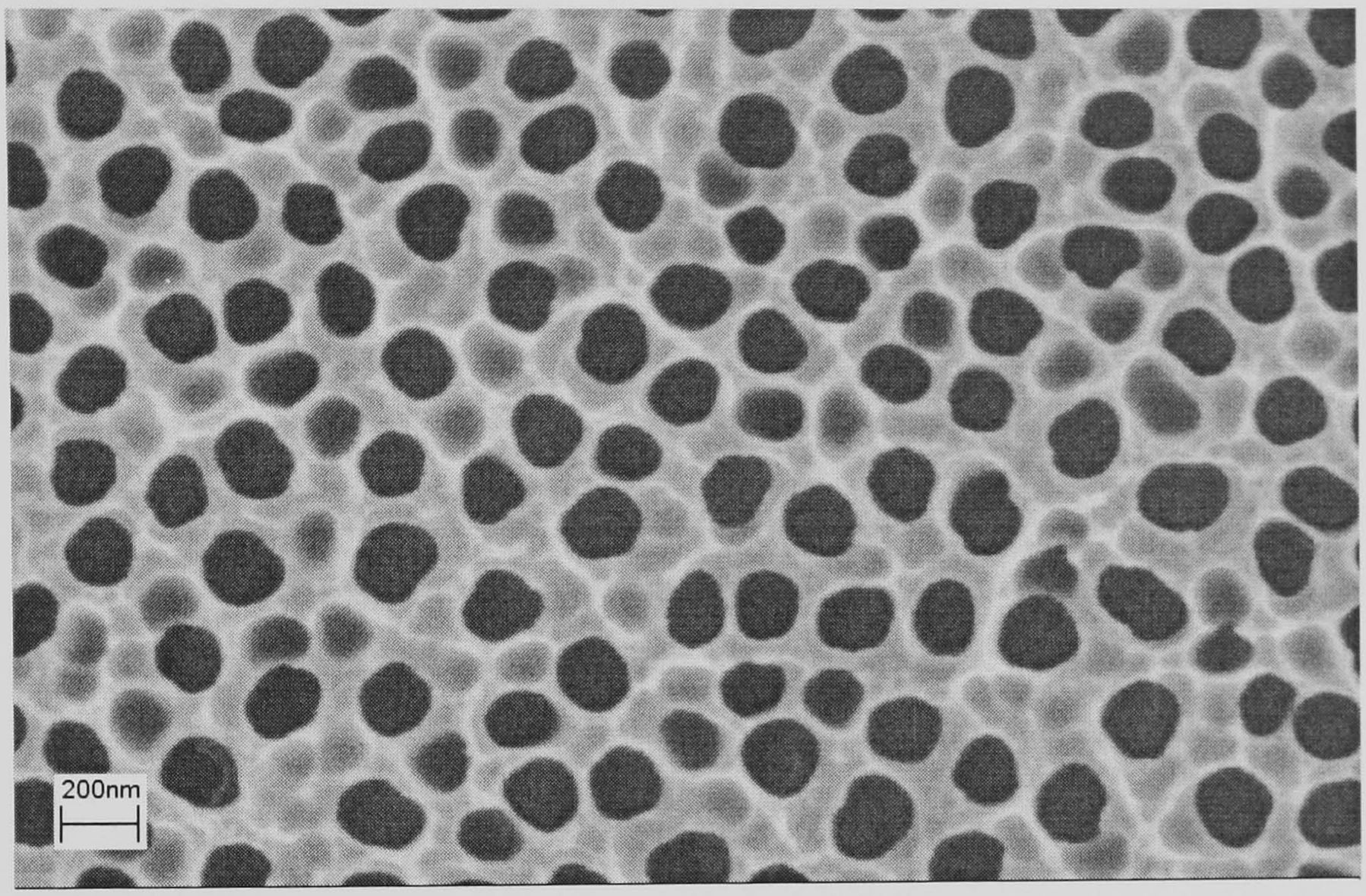

Figure 3.9. SEM image of the non-filtration surface of a Whatman 'Anodisc' membrane. A sputtered 2 nm platinum coating was applied to prevent charging.

Within approximately 1 μm of the filtration surface each pore splits to form a network of smaller pores which act as the filtration surface, figure 3.10.

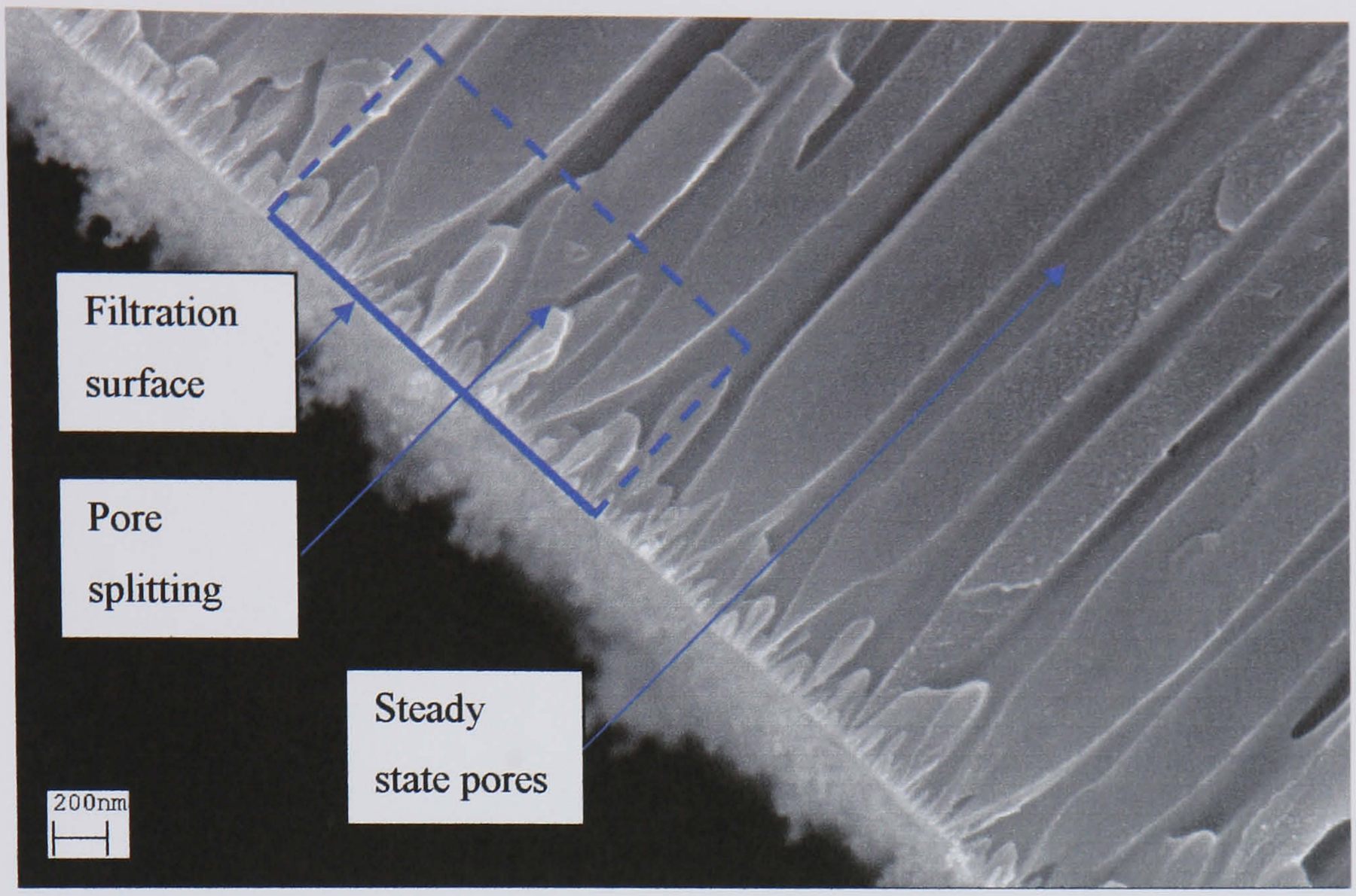

Figure 3.10. SEM image of a cross-section through an Anodisc membrane at the filtration surface, showing pore splitting. A sputtered 2 nm platinum coating was applied to prevent charging.

By imaging the membrane cross-section, the total membrane thickness was measured to be 55 μm. Whatman 'Anodisc' membranes could be etched by the same procedures described for the treatment of porous aluminium oxide.

3.1.3 Whatman Cyclopore Membranes

Whatman 'Cyclopore' filtration membranes are polycarbonate nuclear track etched membranes. Although available in a variety of sizes, the membranes used had a specified 200 nm pore diameter and 7-20 μm thickness. The pore density is lower than that of porous alumina membranes, figure 3.11.

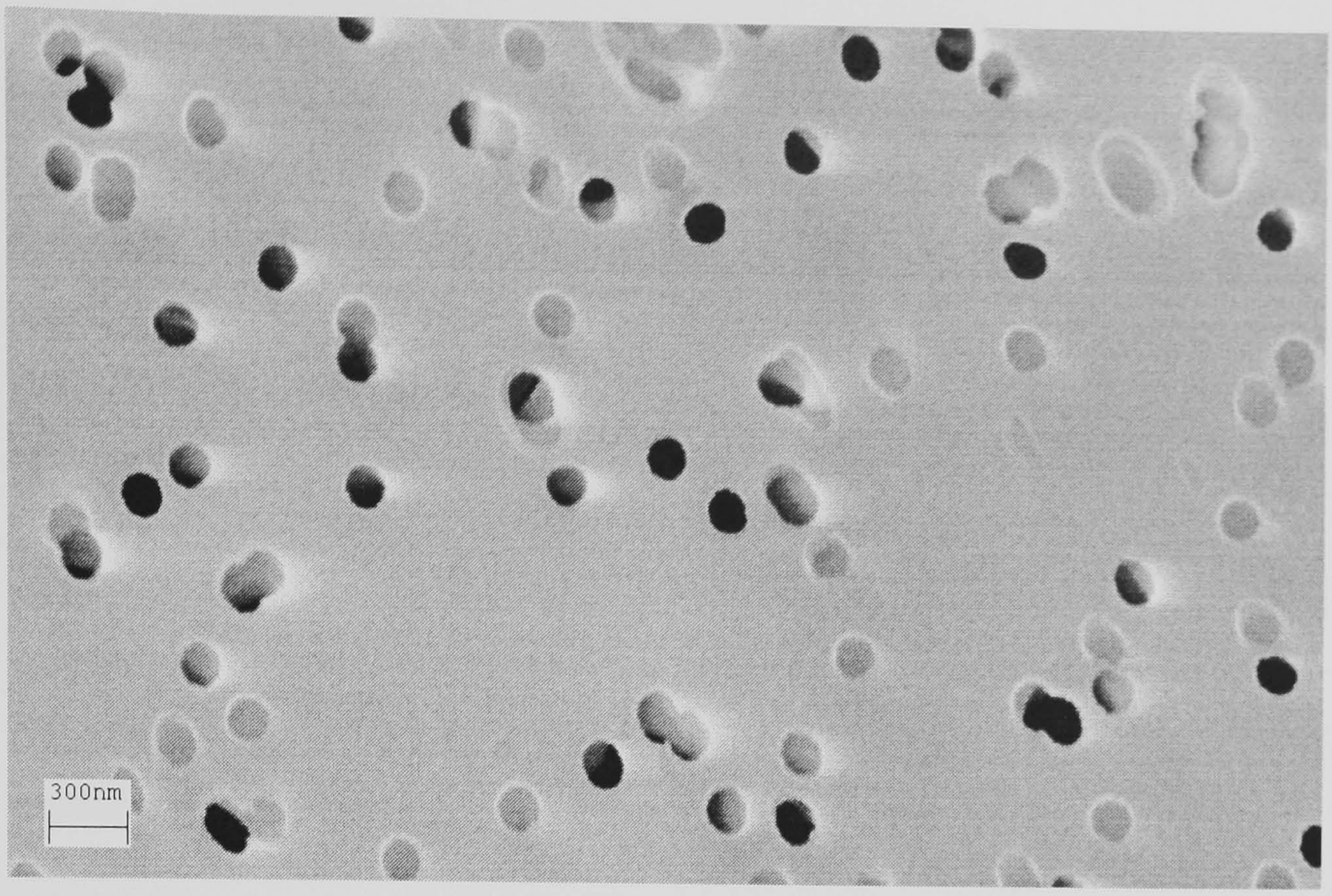

Figure 3.11. SEM image of the filtration surface of a 'Cyclopore' membrane, with a sputtered 2 nm platinum coating to prevent charging

The pore density in 'Cyclopore' membranes is approximately half that in 'Anodisc' membranes, and an order of magnitude lower than porous aluminium oxide formed at 40 V in 0.3 M oxalic acid. Additionally, the pores are not all directly perpendicular to the plane of the membrane.

3.2: Nanowire Fabrication

Various template deposition techniques have been utilised to form nanowires in the templates mentioned above, these are summarised below.

3.2.1 Electrodeposition in Porous Aluminium Oxide

Electrochemically fabricated porous aluminium oxide was used as a template with the aluminium substrate and oxide barrier layer intact. The aluminium substrate was used as the base electrode.

Electrodeposition with a constant applied potential was unsuccessful. The presence of the highly resistive barrier layer made deposition susceptible to defect sites in the oxide. Cracks, or pores with the least resistive barrier layer, dominated the growth process preventing uniform deposition. Additionally, after long deposition periods the oxide was separated from the aluminium substrate. This is attributed to the accumulation of

hydrogen at the metal-oxide interface[7], and continued anodising of the oxide in the acidic electrolyte.

More uniform deposition was achieved with an alternating applied potential. For electrodeposition into oxide membranes where the voltage reduction technique had not been used to thin the barrier layer, a 25 V_{pp} (peak-peak) 50 Hz applied potential was necessary. Where the voltage reduction technique was used during the final stages of oxide formation to thin the barrier layer, an 8.5 V_{pp} (50 Hz) applied potential was sufficient. The deposition of gold within the pores was apparent by a change in the template's colour. The alumina template turned from transparent to a vibrant purple colouration, isolated oriented gold wires within the template structure were the origin of surface plasmon effects.

By etching filled porous alumina oxides by the procedures outlined earlier, the deposited nanowires could be exposed. A porous aluminium template was fabricated by the 2-step procedure, with 3 hrs 50 mins and 1 hr 30 mins growth stages respectively. At the end of the second growth stage the barrier layer was thinned by the voltage reduction technique in 10 % steps with a final voltage of 9.5 V. Gold was deposited at 8.5 V_{pp} for 1 hour from the sulphuric electrolyte. The aluminium substrate was removed from the template oxide by etching in hydrochloric acid and cupric chloride, and the pore bases imaged with AFM, figure 3.12.

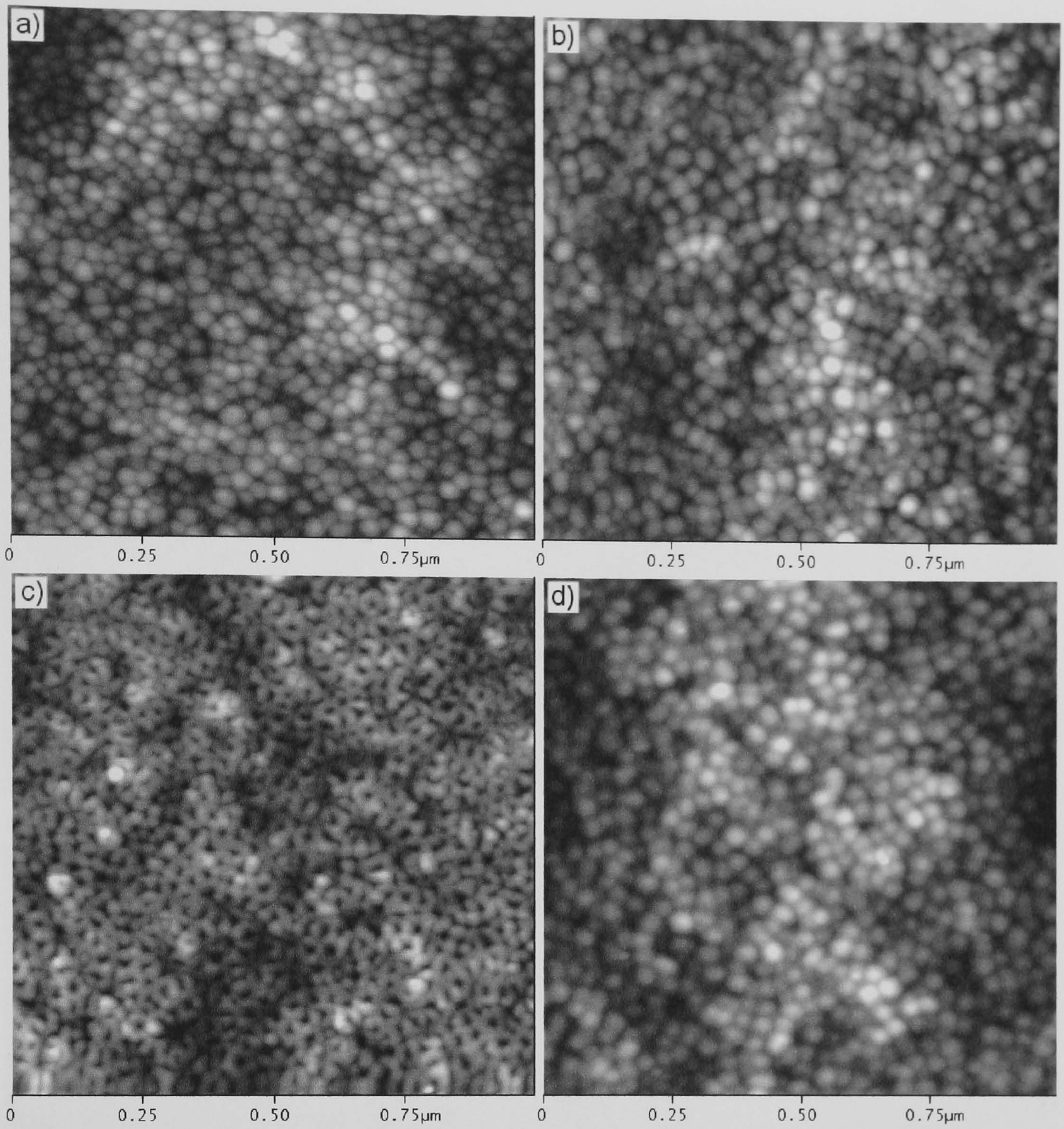

Figure 3.12. AFM sequence charting the progress of an etch procedure through the barrier layer of a porous alumina membrane. a) after etching away the aluminium substrate, b) – d) images after sequential exposures to 5 wt% phosphoric acid for 7, 10 and 5 minutes, respectively.

Once again, the series of images present in figure 3.12 demonstrates the progress of an etch sequence with 5 wt% phosphoric acid at room temperature, similar to figure 3.4. Initially, the pore bases were observed as expected, figure 3.12a. After etching for 7 minutes in 5wt% phosphoric acid the barrier was smoother, figure 3.12b, and average surface roughness decreases. After an additional 10 minutes etching the barrier layer was removed and pores were opened, figure 3.12c. Continued etching for 5 minutes exposes the tips of the nanowires. Further etching causes the surface to become too irregular for

AFM, as the nanowires stand proud from the membrane. This effect can be observed with the high resolution SEM after 22 s exposure to 1.25 M NaOH, figure 3.13.

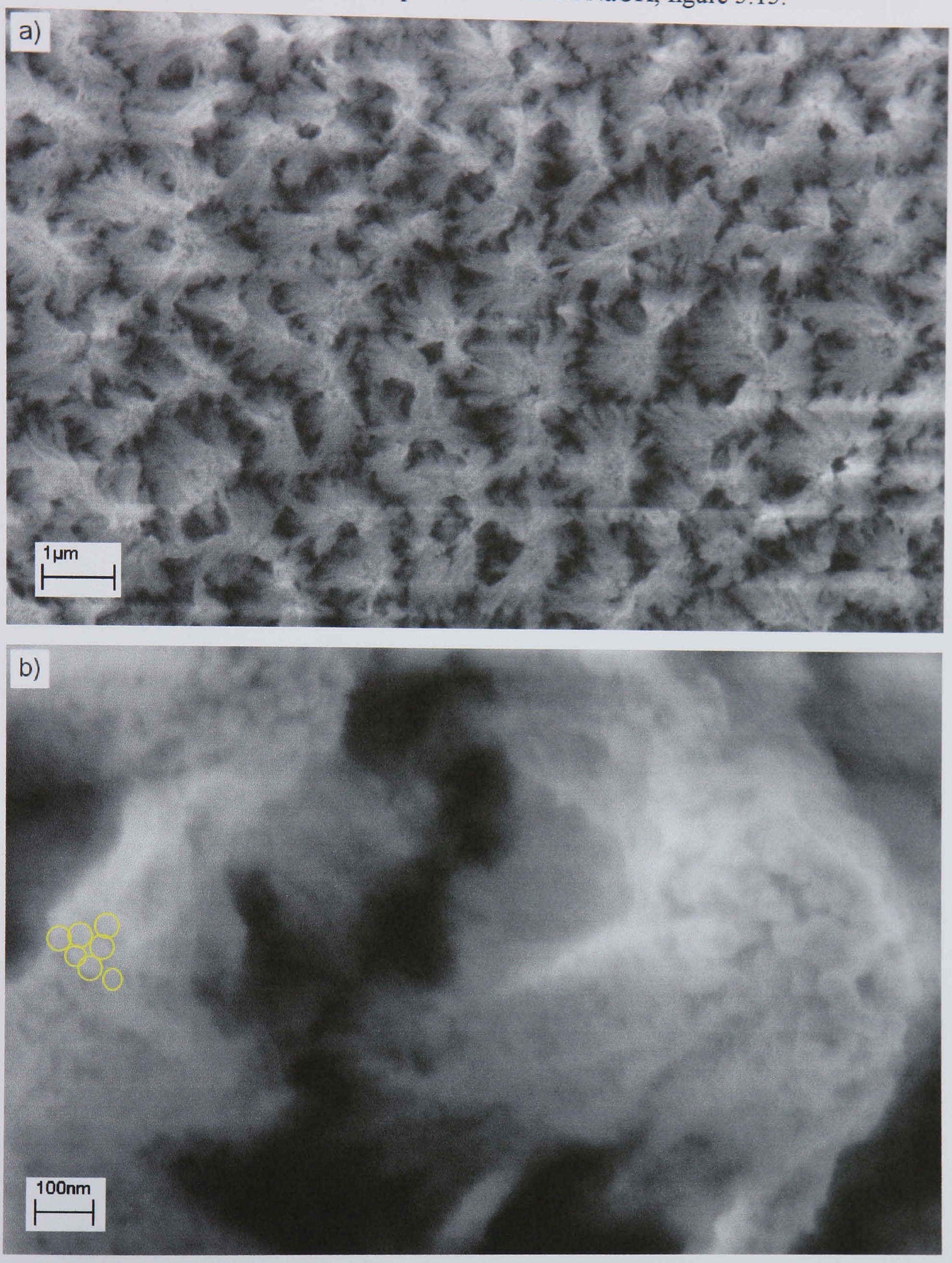

Figure 3.13. SEM images of nanowires extending from the porous alumina template shown in figure 3.12 after continued etching for 22 s in 1.25 M NaOH.

Individual nanowires can be resolved, and are outlined, in figure 3.13b and both images show how, after extending from the membrane, they clump together. The nanowires may require mutural support, or may aggregate due to hydrophobic interactions in solution.

Usually, the nanowires were removed from the membrane by dissolving the aluminium oxide completely by immersion in 1 M aqueous sodium hydroxide, as discussed in the previous chapter. After this procedure, nanowires could be dropcast from solution onto silicon substrates for observation, figures 3.14 and 3.15.

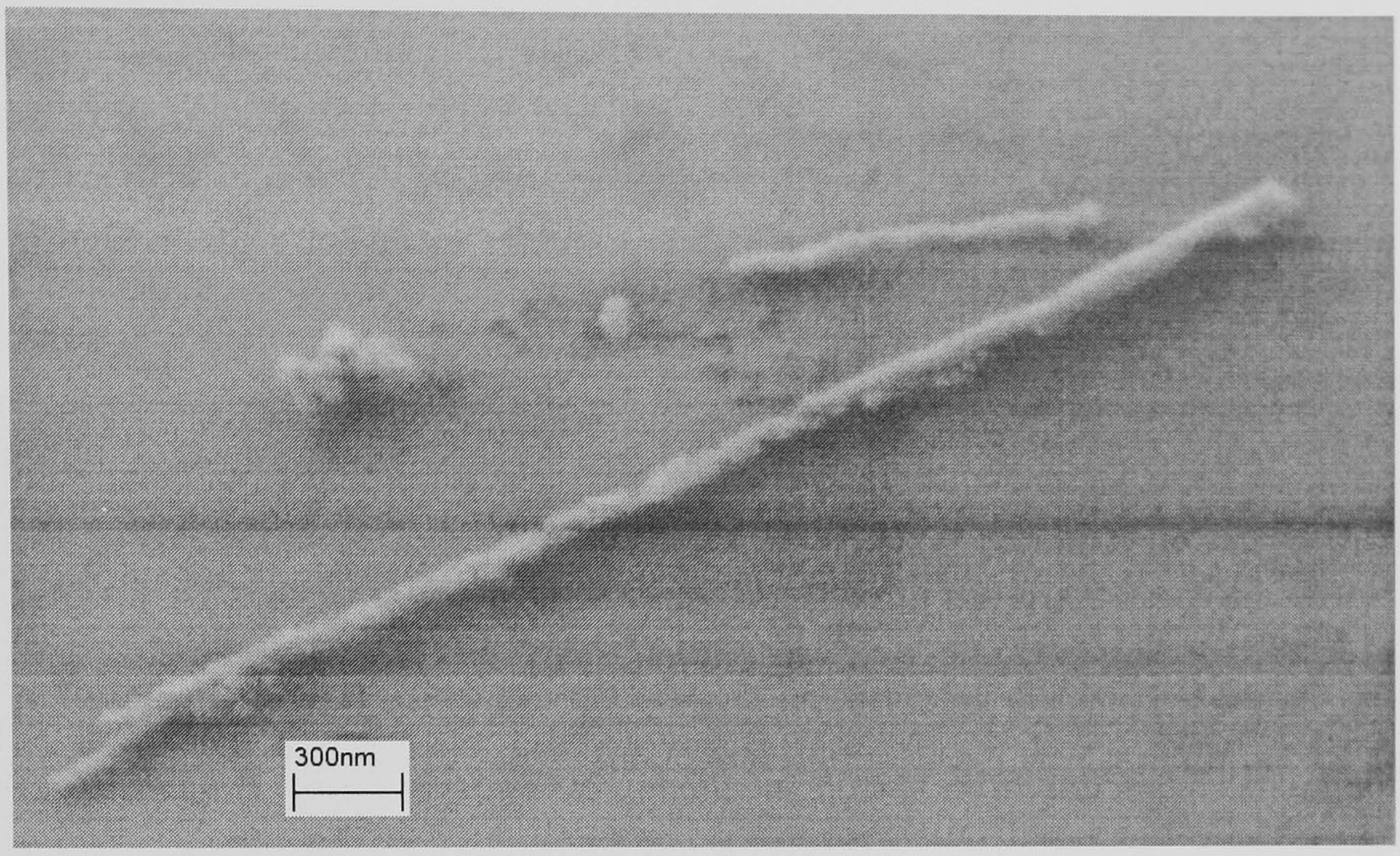

Figure 3.14. SEM image of gold nanowires fabricated in porous alumina membranes, after release and deposition onto silicon surfaces

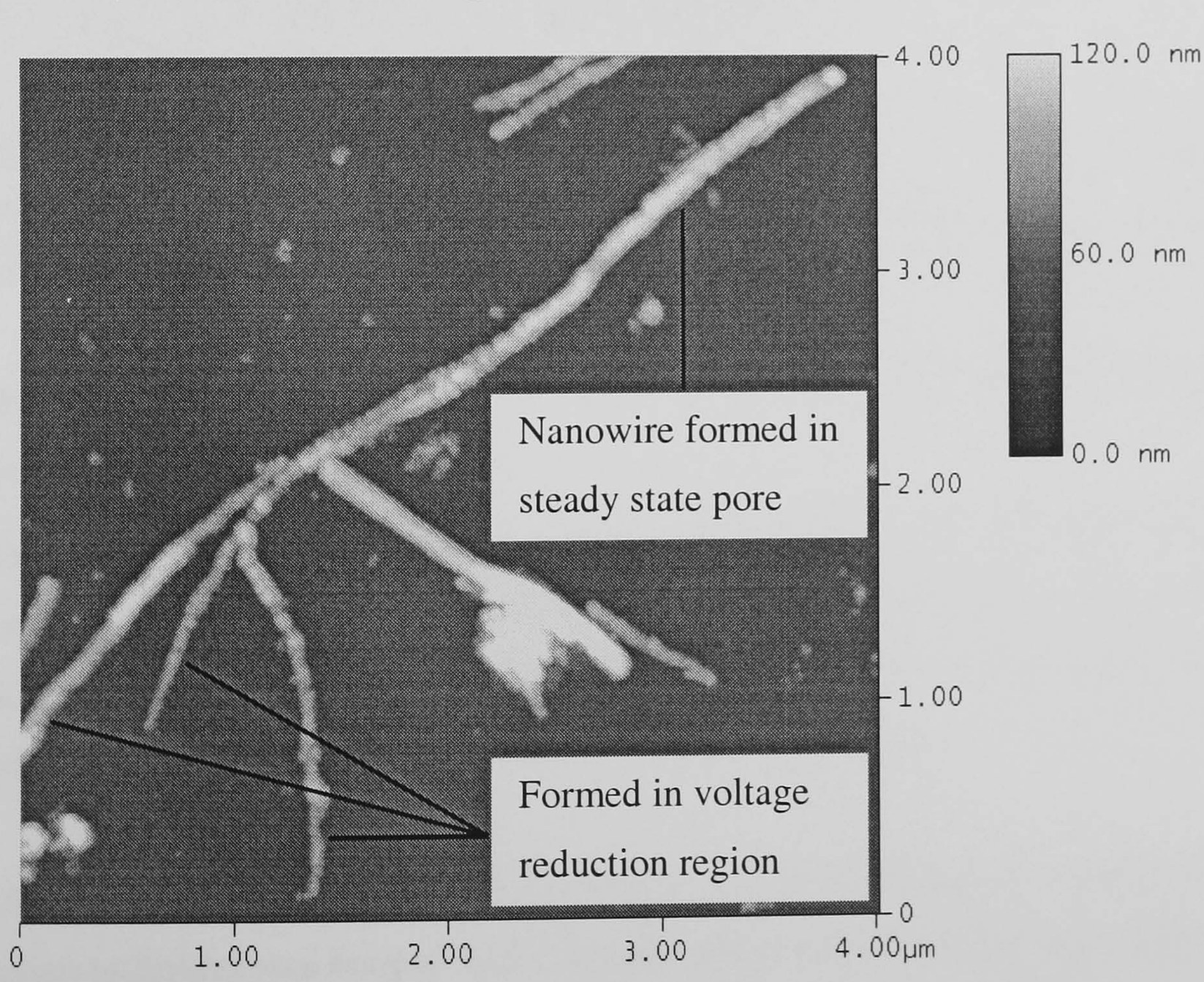

Figure 3.15. AFM image of a gold nanowire, fabricated in a porous alumina membrane

The nanowire imaged in figure 3.15, shows how gold deposition in the voltage reduction region leads to secondary wires at the base of the main wire. Although the pore structure grown by the voltage reduction technique should reduce the pore size to approximately 10 nm diameter, the smallest wires shown here have a diameter (determined from the measured height) of 20 nm. It is assumed that smaller wires are broken during the cleaning procedure. The bulk of the nanowires have a diameter of 55-60 nm, from height measurements. To better determine the diameter of the nanowires a separate wire was imaged at higher resolution, figure 3.16, and the average height difference between the red and green areas was calculated

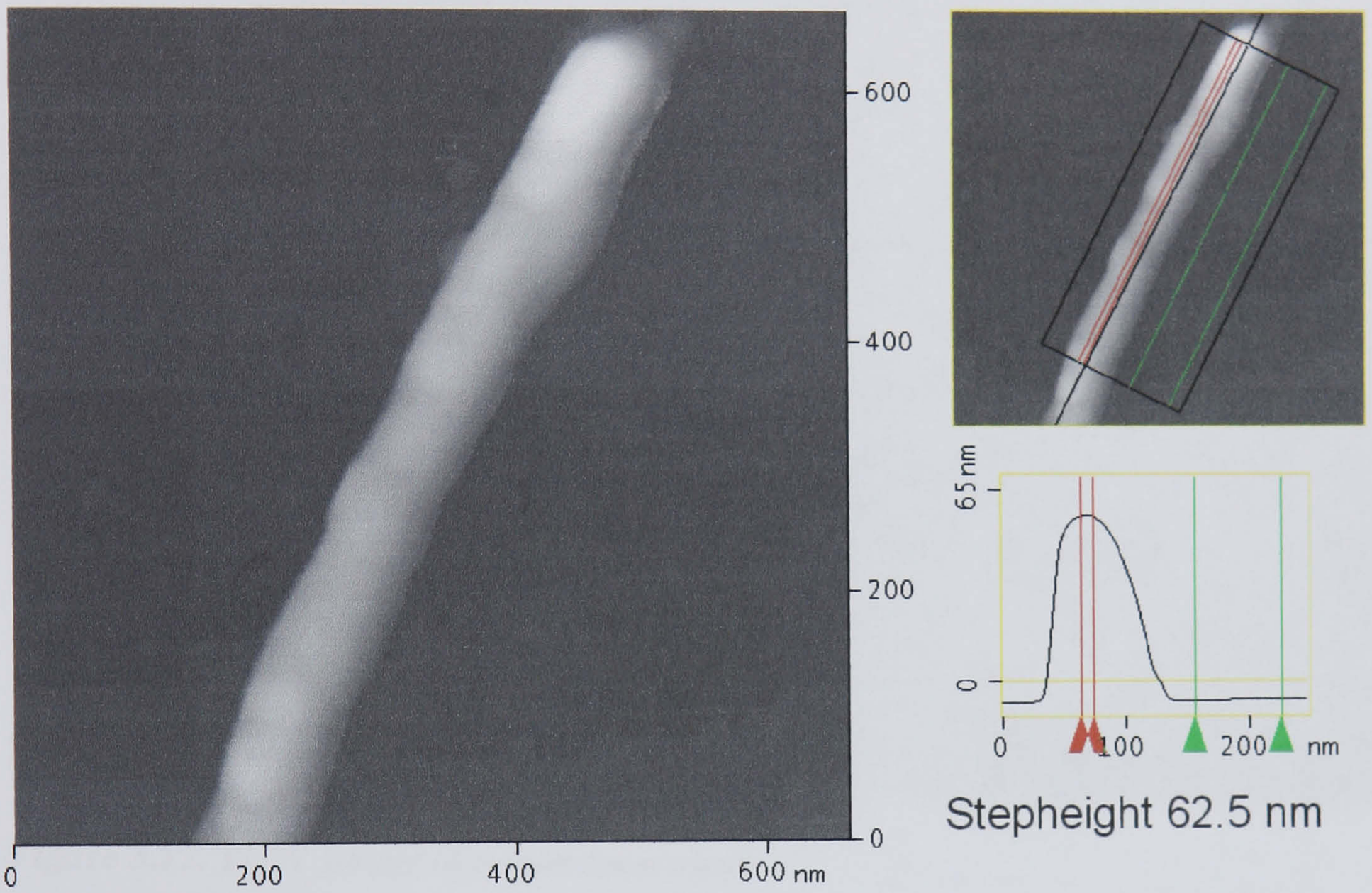

Figure 3.16. AFM image of a gold nanowire on silicon surface, used to determine the nanowire diameter

By comparing the topographic profile of this single nanowire a diameter measurement of 62.5 nm can be obtained. This is larger than expected for the membranes as grown, and in relation to the measured pore separation. It is thought that the electrolyte may act to etch the pores and increase their diameter during the growth process.

A sample of nanowires fabricated in porous aluminium membrane with the voltage reduction technique was imaged with a transmission electron microscope, figure 3.17.

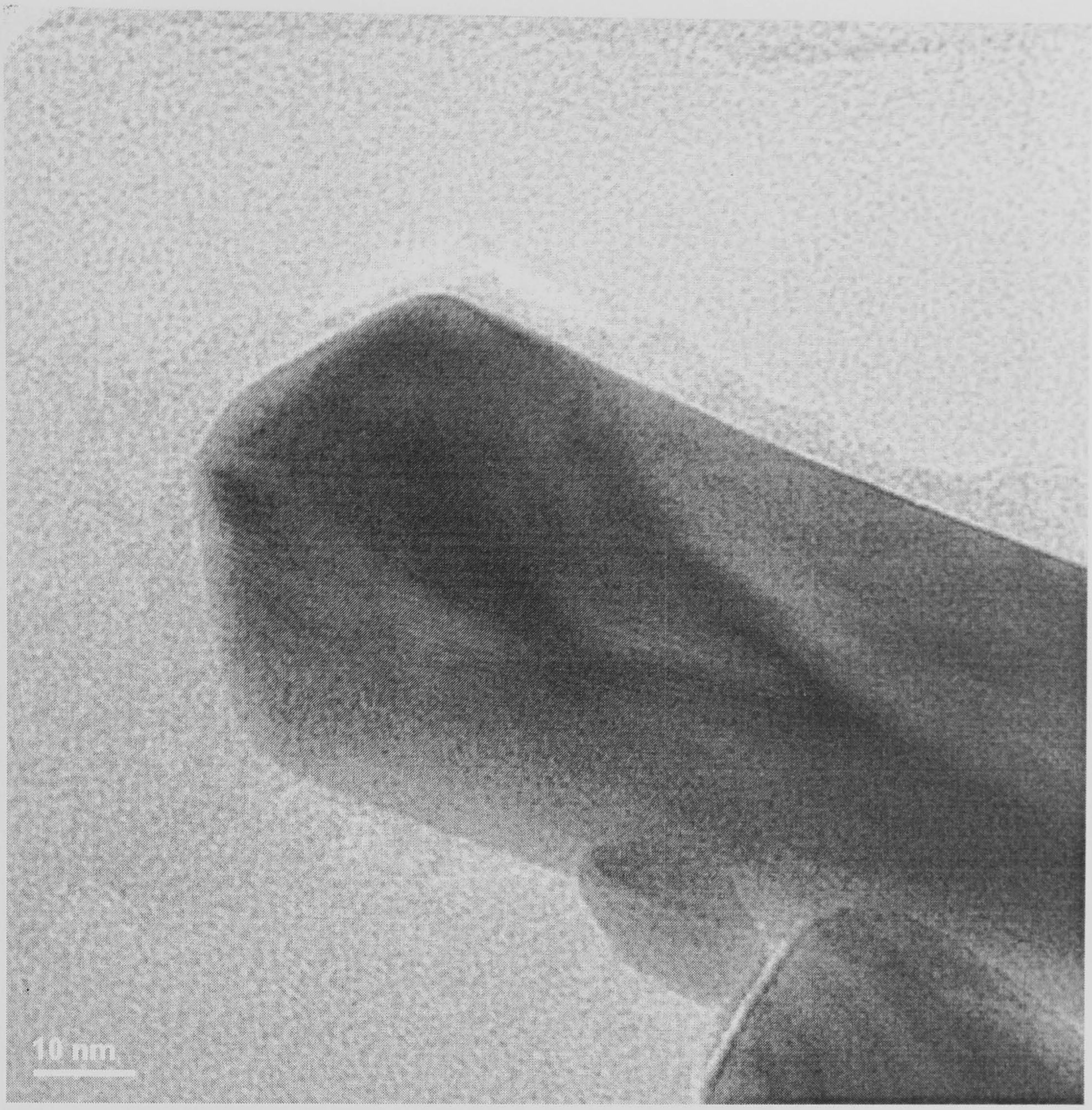

Figure 3.17. TEM image of a gold nanowires

Measurements of the nanowire diameter from those imaged shows they have a range of 45-50 nm. The facetted end structure shown in figure 3.17 is typical, and may be due to the wetting properties of the template and electrolyte, or more likely the crystalline structure of the nanowire. The crystal structure of these gold nanowires can be observed at their edges. Here, the nanowire is thin enough to allow high transmission and interference from multiple crystalline domains is less likely. Atomic resolution has been demonstrated for a region of figure 3.17, figure 3.18.

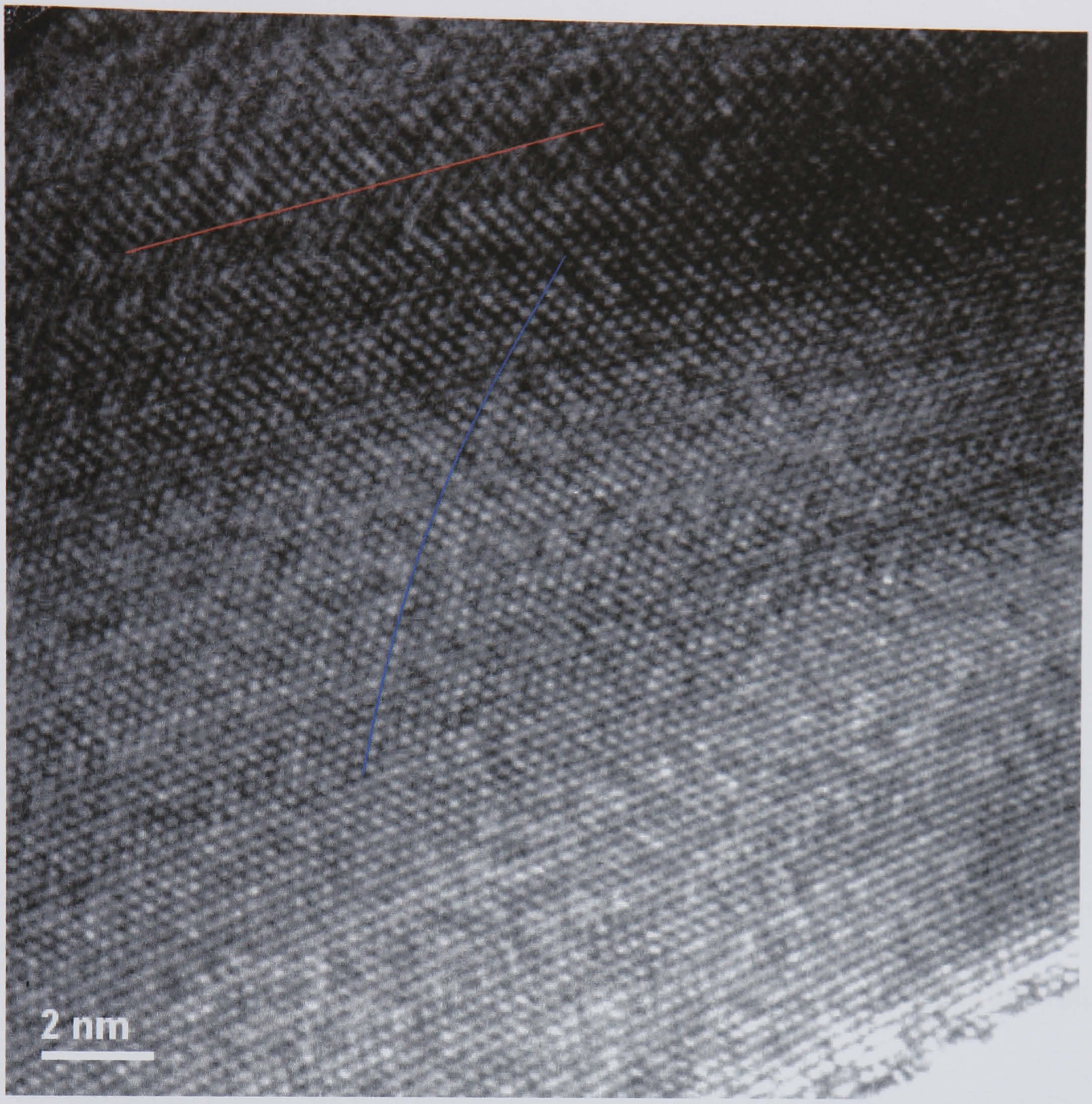

Figure 3.18. TEM atomic resolution image at the nanowire edge

Bragg condition transmission across the centre of the image allows observation of the crystal structure in one (presumably coherent) region of the nanowire. The structure displays a hexagonal atomic arrangement with some bending / distortion (highlighted in blue) and fault lines (highlighted in red) also observed.

To determine the lattice structure associated with these nanowires, a nanowire section showing few defects was imaged and the Fourier transform analysed, figure 3.19.

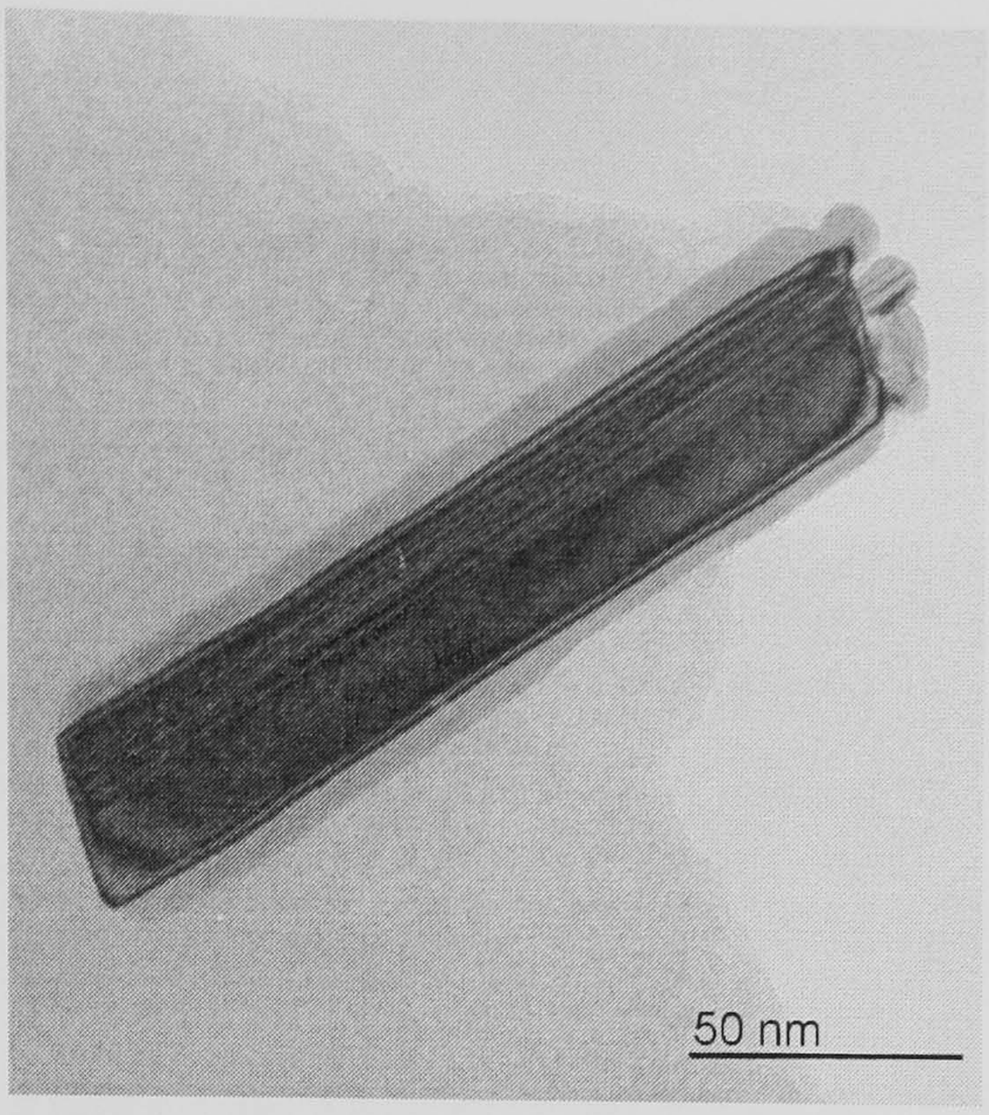

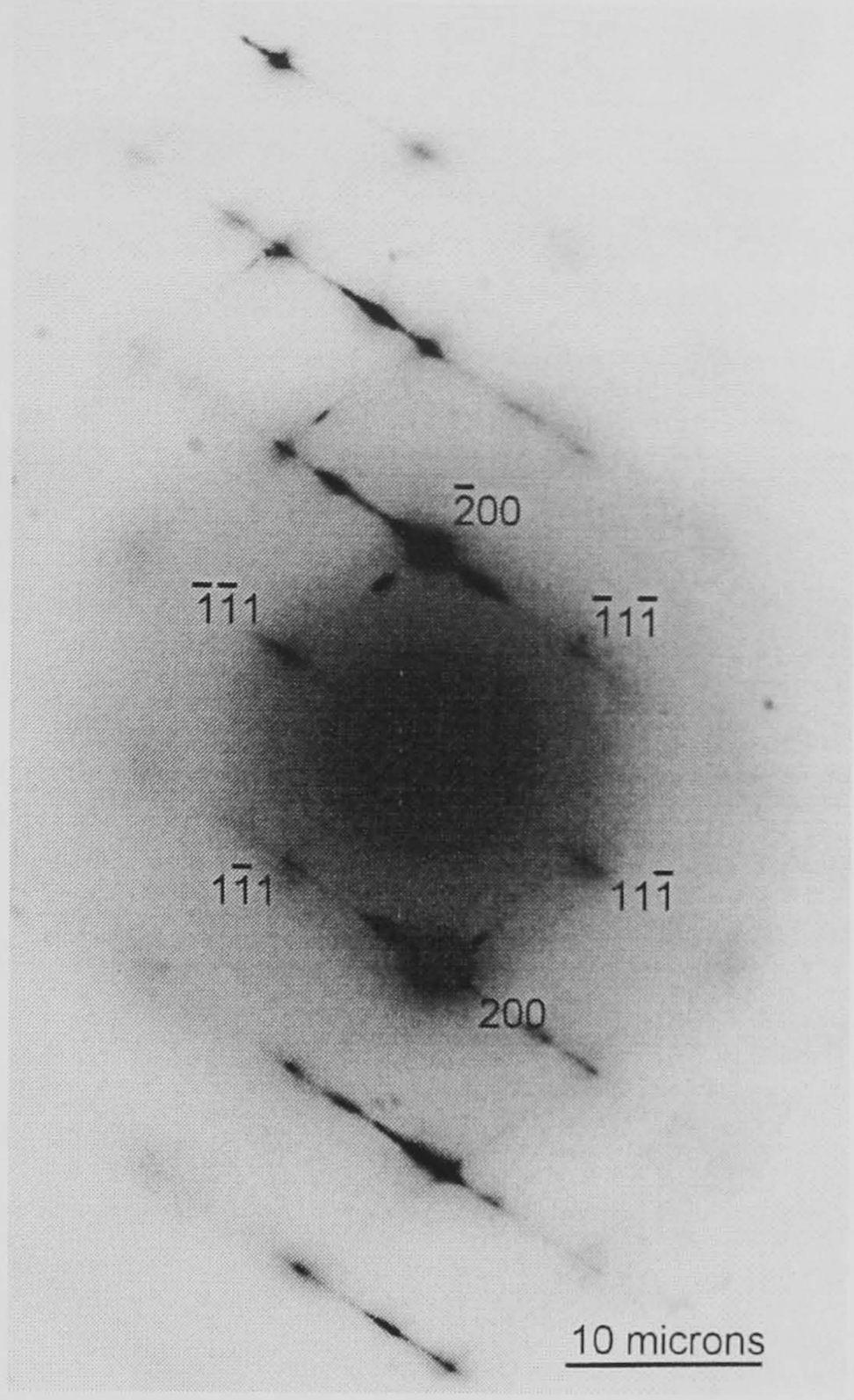

Figure 3.19. TEM image of nanowire section and its diffraction pattern to determine the crystal structure.

The diffraction pattern can be indexed as a fcc lattice structure with the [110] zone axis parallel to the beam direction, in agreement with previous work[7]. Lattice spacing associated with $h^2+k^2+l^2 = 3$ and 4 are 0.25 nm and 0.28 nm, respectively.

By imaging diffraction contrast along the length of a single wire, at different angles, faults in the crystal structure are highlighted. The action of tilting the sample with respect to the electron beam enables Bragg diffraction to highlight areas with different crystal orientation with changes in contrast, figure 3.20.

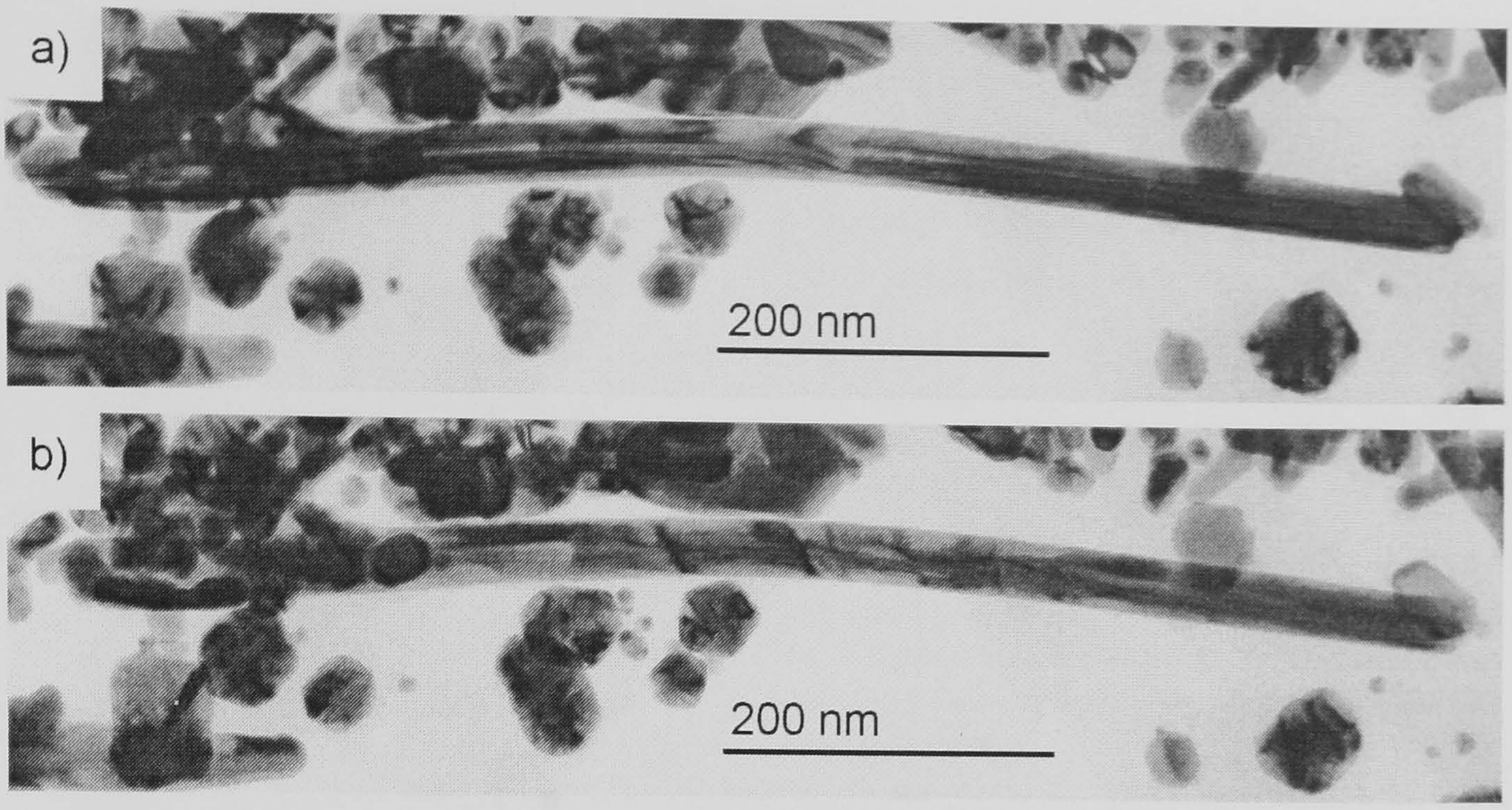

Figure 3.20. TEM showing Bragg diffraction from a nanowire at a) perpendicular and b) 13 degrees tilt

In figure 3.20a longitudinal faults are apparent, however, by tilting the sample at 13°, figure 3.20b, transverse faults are observed. A potential source for the longitudinal faults is pore splitting at the base of the oxide, during growth crystal orientations will compete at the junction of dendritic pores. Transverse faults may be due to the cyclic growth potential.

3.2.2 Electrodeposition in Whatman Anodisc Membranes

The hydrated surface of porous aluminium oxide membranes requires the use of acidic electrolytes with high chloride concentrations. At higher pH, and lower chloride concentrations, the gold salt present in the electrolyte becomes partially or fully hydrated, by replacing the chloride ions.[8-10] The source for these OH^- ions can either be from solution, or the hydrated surface of the porous alumina. Where a chloride is replaced with a hydroxide from the pore walls it is possible for gold salt to spontaneously form a metallic deposit on the template, without the need for a reducing agent.[11] Consequently, electrodeposition in Anodisc membranes has been undertaken with both the sulphuric and hydrochloric electrolytes. Normally growth was performed with the hydrochloric electrolyte, typically at 1 V_{pp} (15 Hz) for 30 minutes in accordance with the description in chapter 2. After nanowires were removed from the template, cleaned and dropcast on silicon they could be imaged with SEM, figure 3.21.

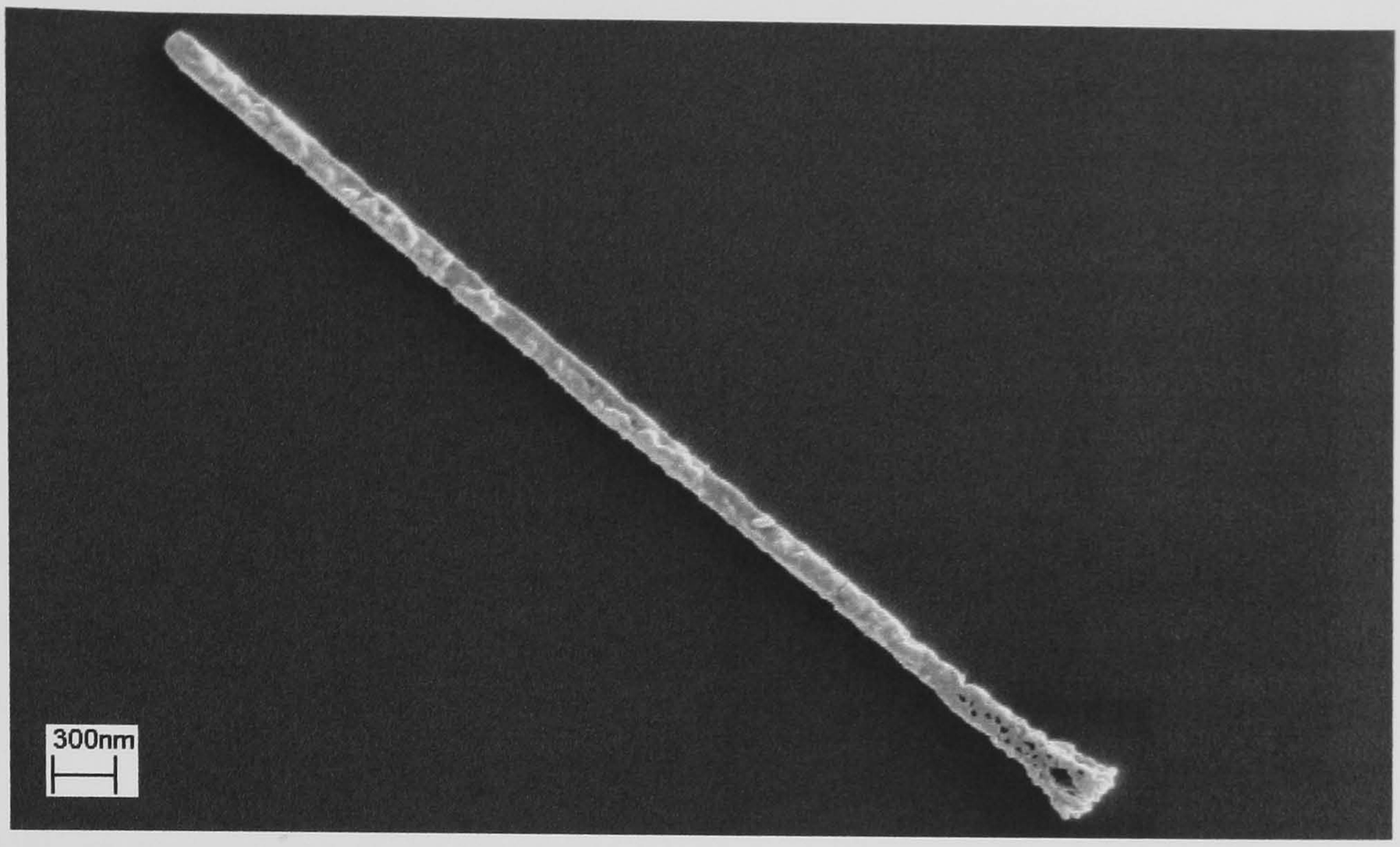

Figure 3.21. Scanning electron micrograph of a well formed gold nanowire, electrodeposited into an Anodisc membrane, after release and dropcasting on silicon.

Whereas figure 3.21 shows a well formed homogenous nanowire, such uniformity was not always achieved. Figure 3.22 shows an SEM image of a less well formed nanowire, electrodeposited in an Anodisc membrane by an identical procedure to that detailed for figure 3.21, except that growth was performed for 1 hour.

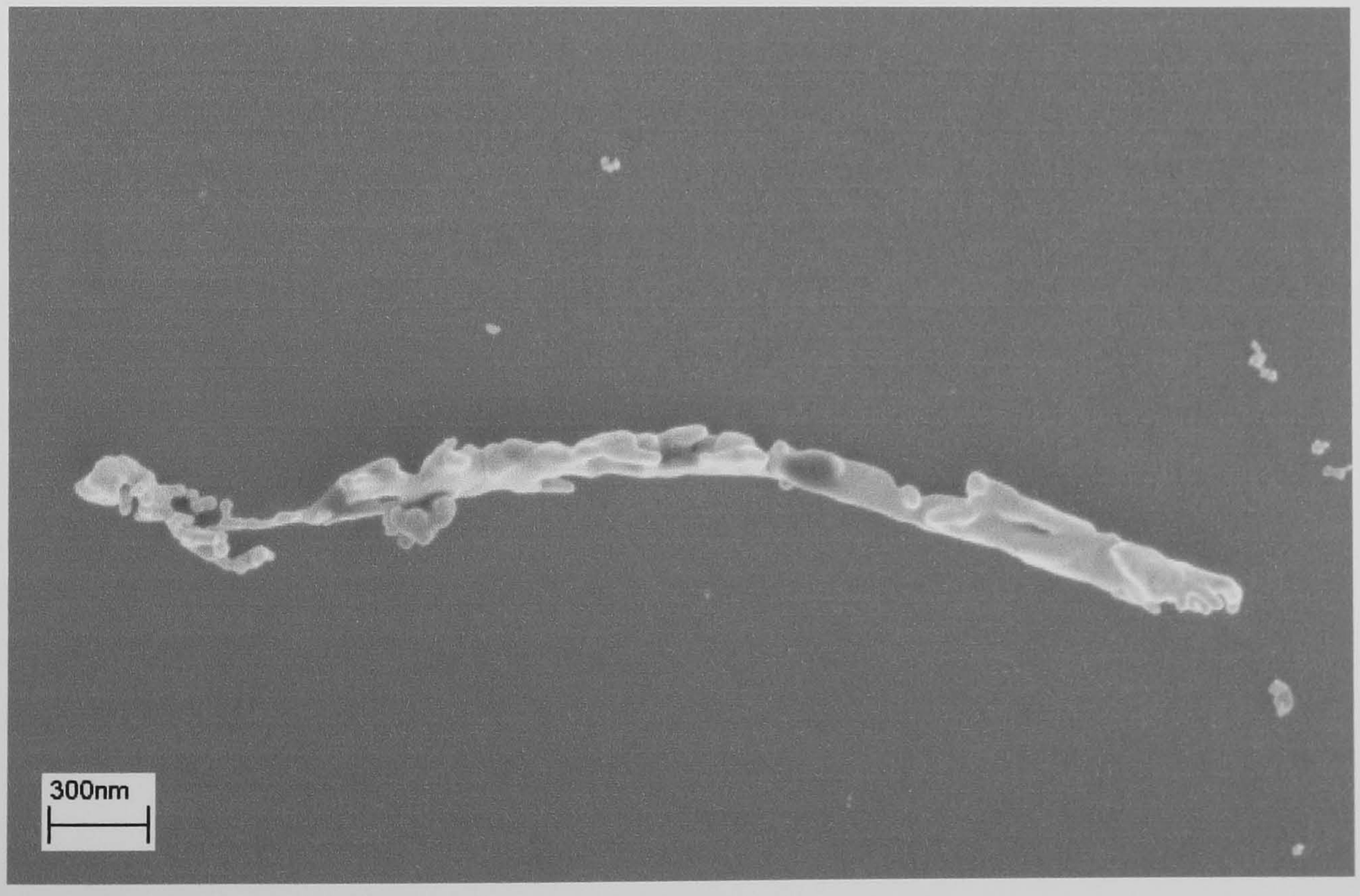

Figure 3.22. Scanning electron micrograph of a poorly formed gold nanowire, electrodeposited into an Anodisc membrane, after release and dropcasting on silicon.

Nanowires could be observed to either poorly formed, figure 3.22, or well formed 3.21, with no observed intermediate state. In addition, the quality of electrodeposited nanowires was associated with the batch of membranes in which they were grown. If nanowires formed with poor quality from one membrane in a batch, other membranes showed identical growth characteristics. The problem is thought to be associated with the wettability of these membranes. Although alumina is naturally hydrophilic, hydrocarbon may increase the contact angle on planar substrates to >80°.[12, 13] The source of this contamination may be atmospheric.[13] It is believed that electrolyte was unable to completely fill pores in contaminated batches of alumina membranes, causing the deposition of poor quality nanowires.

To test the composition of the nanowire solutions, samples were investigated by X-ray photoelectron spectroscopy. Nanowires, and other solution constituents, were allowed to precipitate onto piranha cleaned silicon substrates. After precipitation, the silicon substrate was removed and dried under nitrogen. Almost complete surface coverage was achieved by this process, which in return allows fast and accurate spectroscopy, figure 3.23.

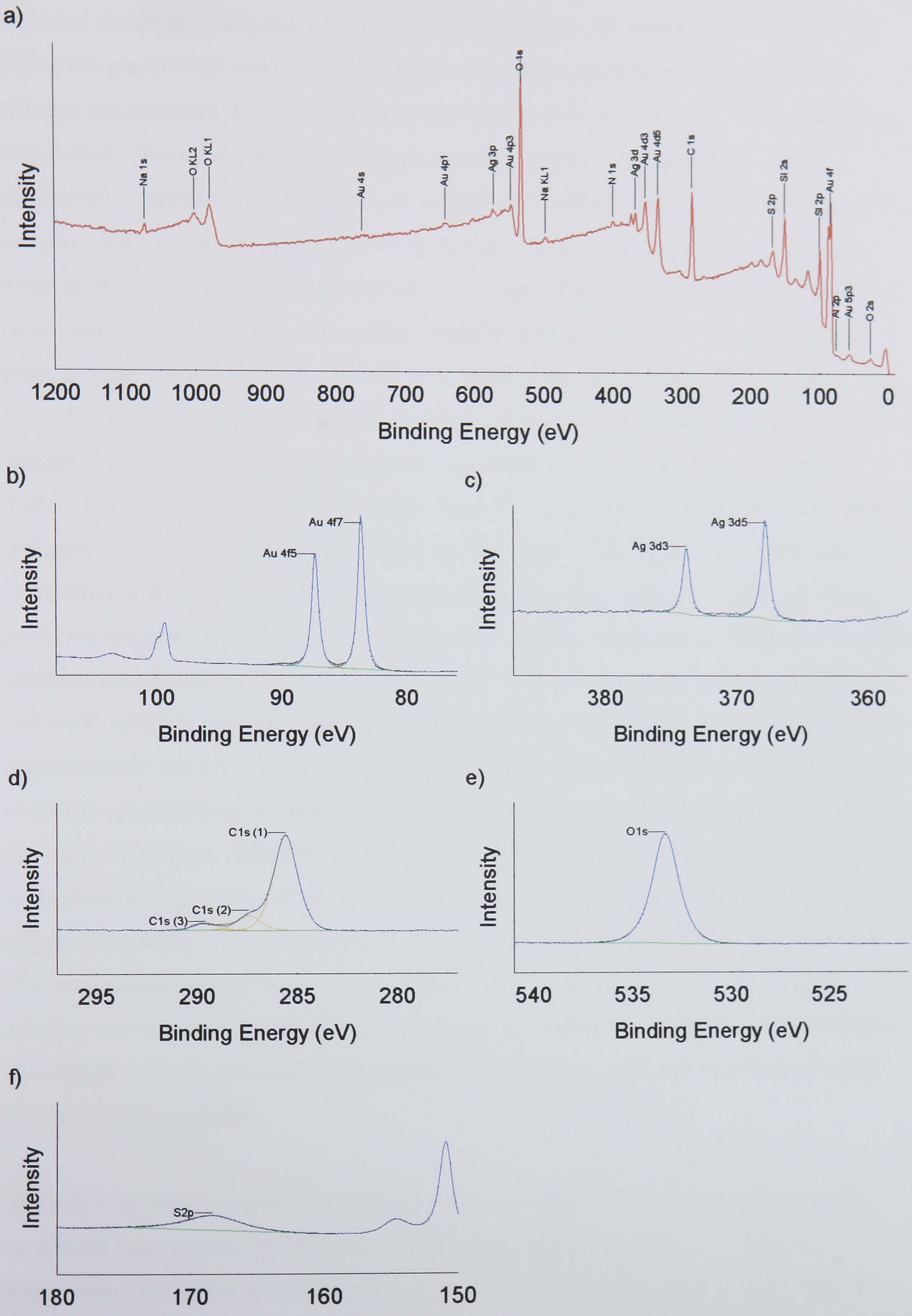

Figure 3.23. XPS spectra for gold nanowires on a silicon surface including a) survey spectra, and high resolution scans of the b) gold 4f, c) silver 3d, d) carbon 1s, e) oxygen 1s and f) sulphur 2p regions.

The XPS indicates the presence of several elements in the solution. In addition to the expected observation of gold, silicon, carbon and oxygen, the survey scan, figure 3.23a, shows the presence of sodium, silver, sulphur, nitrogen and aluminium. Sodium and nitrogen are probably derived from the sodium hydroxide and nitric acid etch procedures respectively. Remnants of the aluminium oxide template are the probable cause of aluminium contamination. The presence of silver is common in the analysis of nanowire samples, and has been very difficult to remove completely. By taking high-resolution scans of the gold 4f and silver 3d regions, 3.23b and 3.23c, the surface concentration of each metal can be calculated. The gold 4f doublet is positioned at 83.7 eV for the $4f_7$ peak, and the doublet is split by 3.7 eV. The fitted peaks are constrained with a peak area ratio of 0.75:1. The silver 3d doublet is positioned at 367.9 eV for the $3d_5$ peak, and the doublet is split by 6.0 eV. The fitted peaks are constrained with a peak area ratio of 0.66:1. After adjusting the measured peak areas by the sensitivity factors for these silver and gold peaks, the concentration of gold on the surface is found to be 6.3 times the concentration of silver. Significant amounts of carbon and oxygen are observed. Three peaks are required to fit the carbon 1s spectrum, each representative of different chemical combinations of carbon. The sulphur 2p, figure 3.23f, can be fit with a peak centred at 168.4 eV, which is not characteristic of elemental sulphur, expected to form a doublet at approximately 163 eV. The width of this peak suggests that it actually represents several chemical combinations of sulphur, probably oxidised and possibly in combination with the observed sodium. The XPS spectra presented in figure 3.23 does not highlight any unexpected contaminants. However, XPS characterisation of nanowires dropscast on silicon often showed zinc contamination, with a binding energy doublet above 1100 eV. This contamination was traced back to the use of unclean glassware or exposing the solution to metal implimnets, for example tweasers. To eliminate all zinc contamination, as in figure 3.23, all glassware was piranha cleaned prior to use, and exposure to metal implements was avoided.

The rate of nanowire growth has been determined from a series of experiments where nanowires were grown for different periods under otherwise identical conditions. Nanowires were grown for durations of 1, 2, 3, 5 and 8 minutes. After release from the membranes and transfer to HPLC methanol they were imaged with SEM to determine the length distribution within a sample, these results are shown in figures 3.24a to 3.24e.

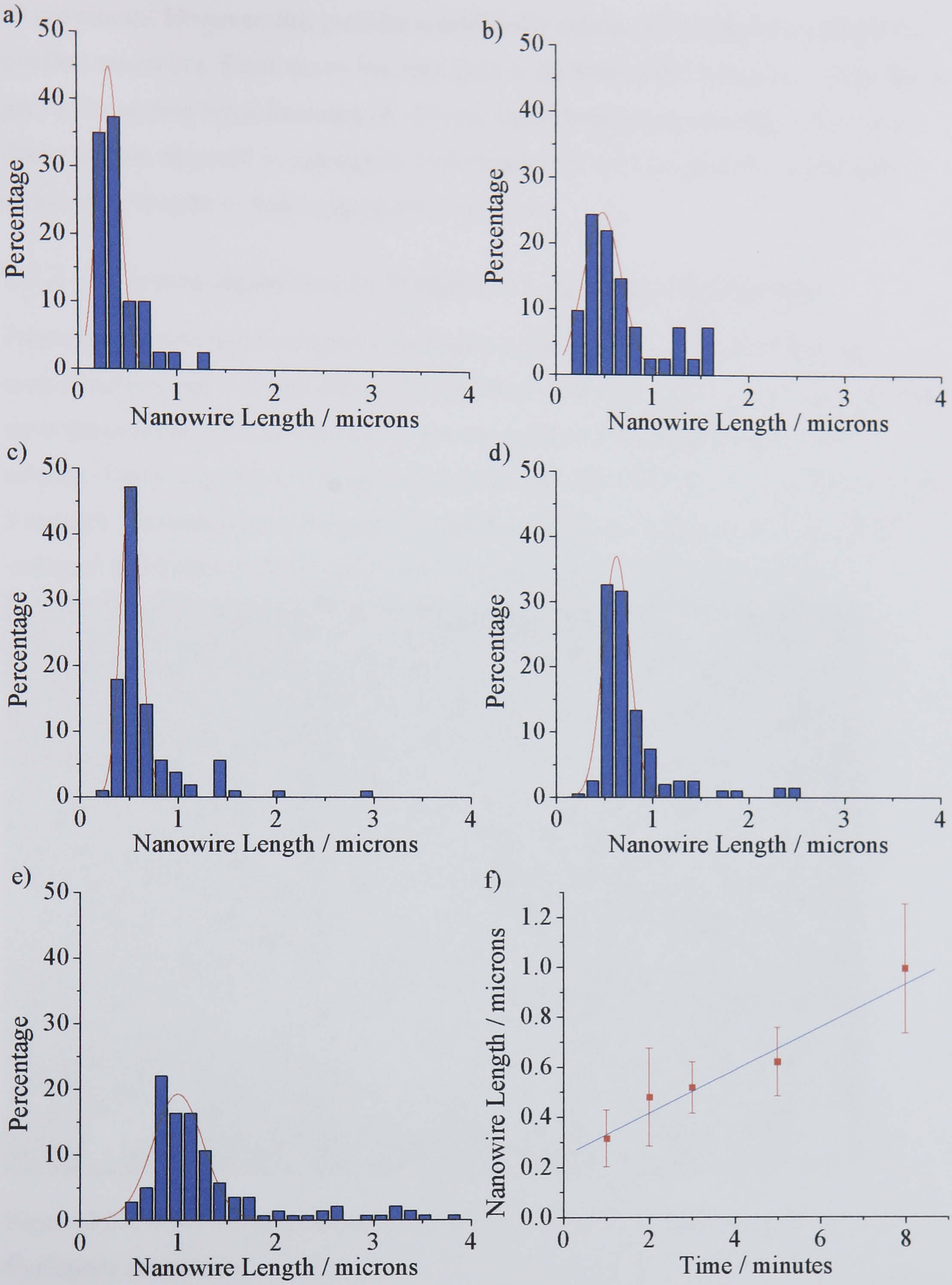

Figure 3.24. Nanowire lengths after a) 1, b) 2, c) 3, d) 5, and e) 8 minutes growth, fitted with a Gaussian distribution to determine f) the nanowire growth rate.

Each distribution is fitted with a Gaussian curve to determine the mean length, and this is plotted in figure 3.24f, where the error values are the standard deviation of each sample. The growth rate graph, figure 3.24f, would be expected to pass through the origin, but instead the line of best fit intersects the y axis at 245 nm, and the gradient is

90 nm/minute. However, this gradient is artificially reduced by a failure to measure the smallest nanowires. Short nanowires may form at the base of the membrane, where due to pore splitting they have diameters of ~20 nm. Upon dropcasting onto the surface, these nanowires are observed in aggregates. Unfortunately it was not possibly to accurately measure the lengths of these aggregated nanowires.

3.2.3 Electrodeposition in Whatman Cyclopore Membranes

Prior to deposition into Cyclopore membranes a 500 nm thick silver electrode was evaporated onto the filtration side of the membrane. The pH neutral electrolyte was used, since the template was not expected to spontaneously catalyse elemental gold from solution. Electrodeposition was typically conducted with a 1 V_{pp} (15 Hz) applied field for 5 minutes. The nanowires produced were removed from solution, suspended in HPLC methanol and dropcast on silicon prior to imaging with the SEM, figure 3.25.

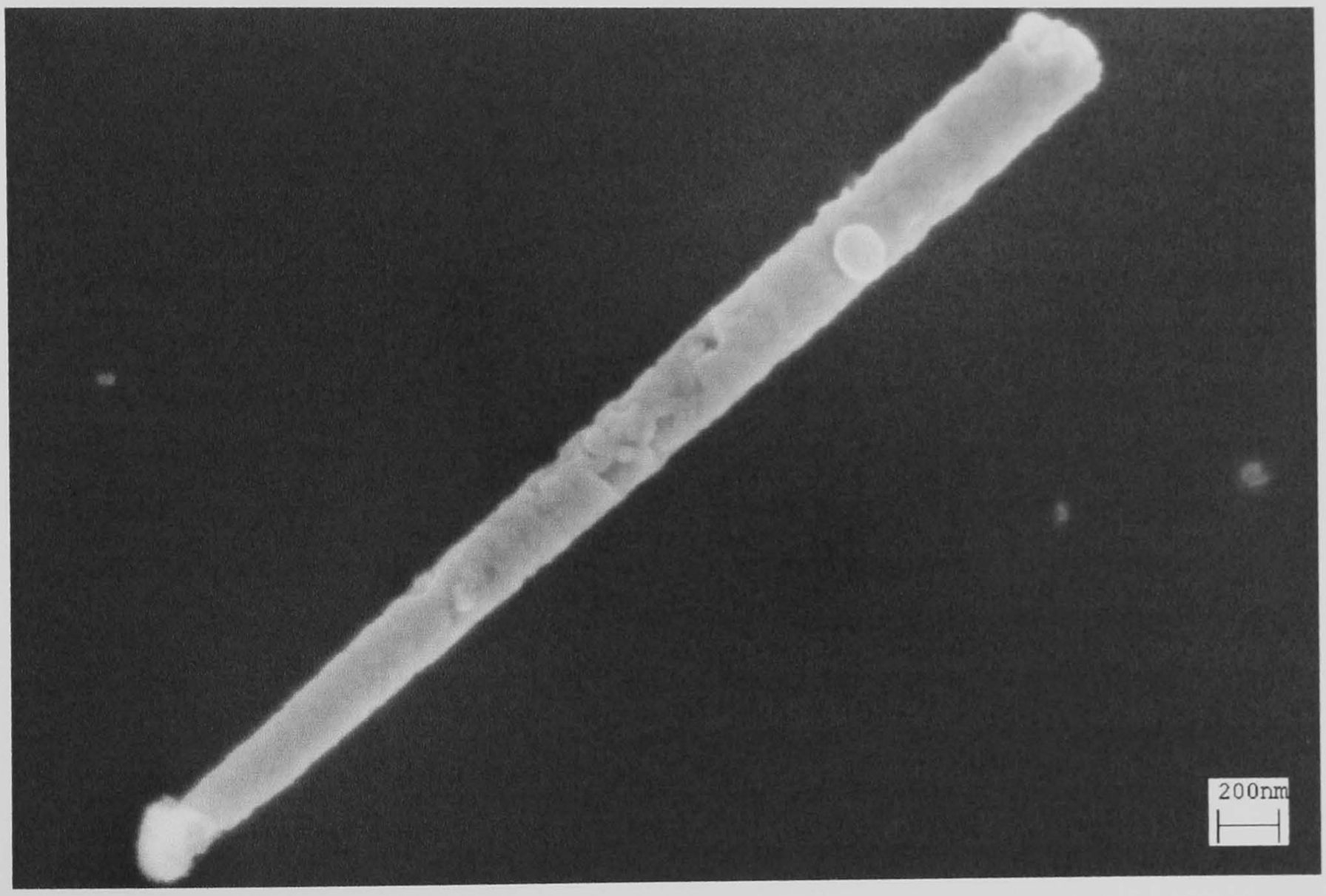

Figure 3.25. SEM image of a typical gold nanowire after 5 minutes growth in a Cyclopore membrane

The tapered structure shown in figure 3.25 is characteristic of all nanowires deposited in Cyclopore membranes. The shape is thought to be replicated from the Cylopore templates, which is believed to originate from the changing energy of heavy ions used to track-etch of these membranes.

Changing the time of electrodeposition can be used to adjust the length of observed nanowires. After 1 minute of growth, partial length nanowires are observed although the total nanowire yield is low in comparison with longer times, figure 3.26.

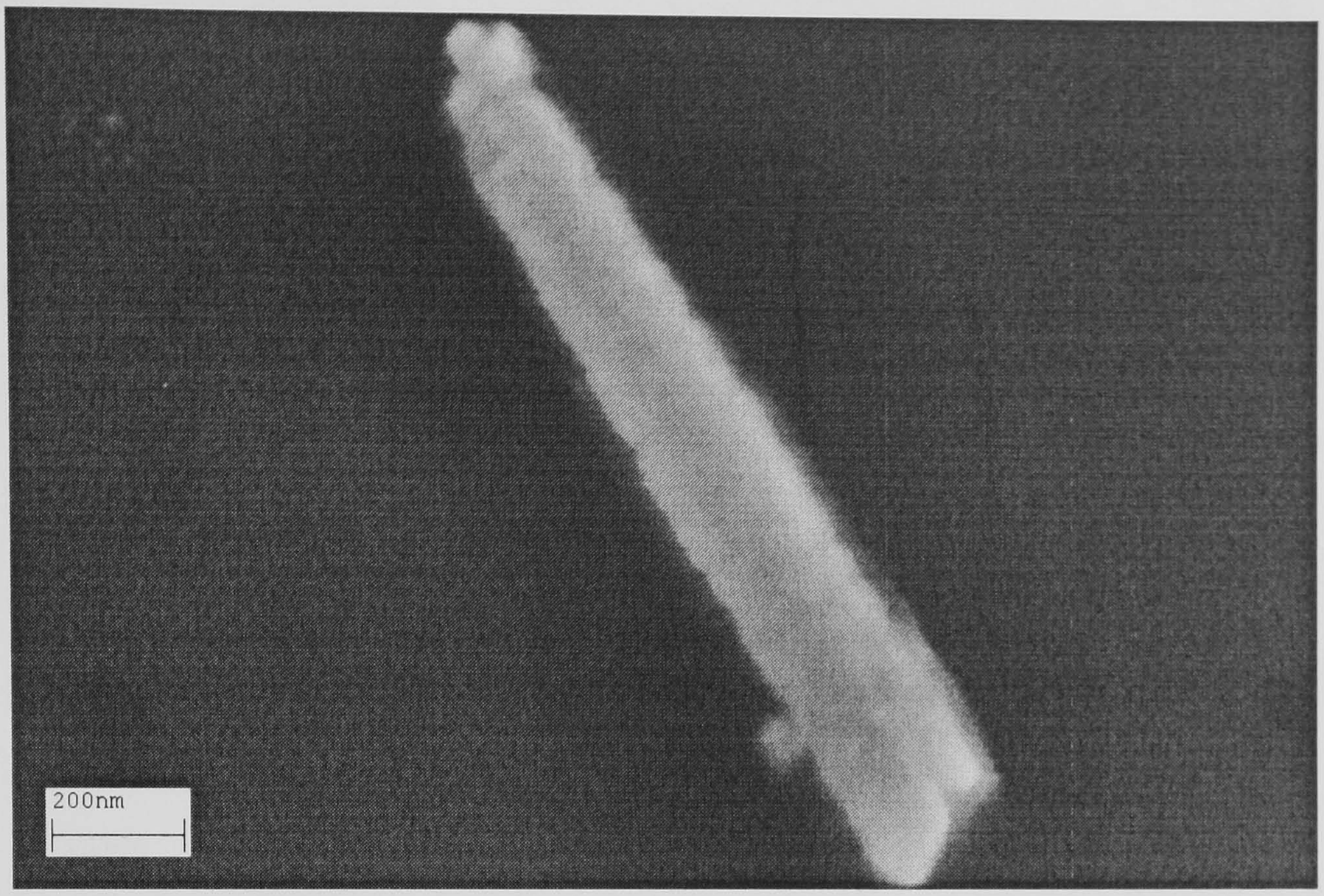

Figure 3.26. Gold nanowire electrodeposited into Cyclopore membranes after 1 minute's growth

At all deposition times longer than 3 minutes, observed nanowires were almost always 2.5 – 3 μm long, presumably limited by the thickness of the track-etched pores, figure 3.27.

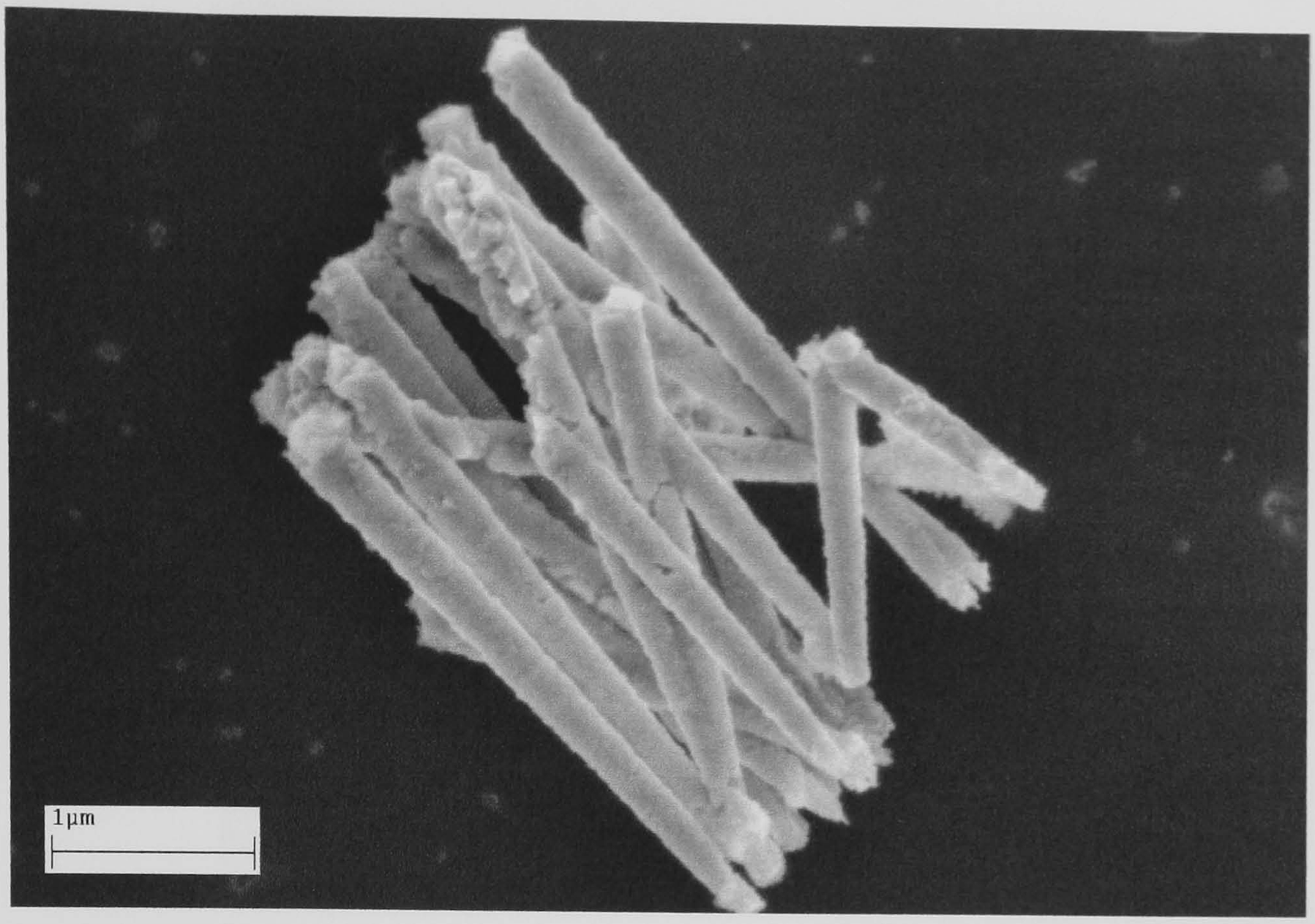

Figure 3.27. Gold nanowires electrodeposited into 'Cyclopore' membranes for 3 minutes

It is believed that deposition occurs preferentially in favourable pores first until they are filled, and only then does deposition occur in less favourable pores. The determining factor in which pores are favoured may be the active electrode area at the base of the pore, supported by the variation in the pore and nanowire tapering observed in figures 3.25 and 3.27. Nanowires are not observed to grow beyond the confines of the template, although at long deposition times some disordered continued growth may be observed, figure 3.28.

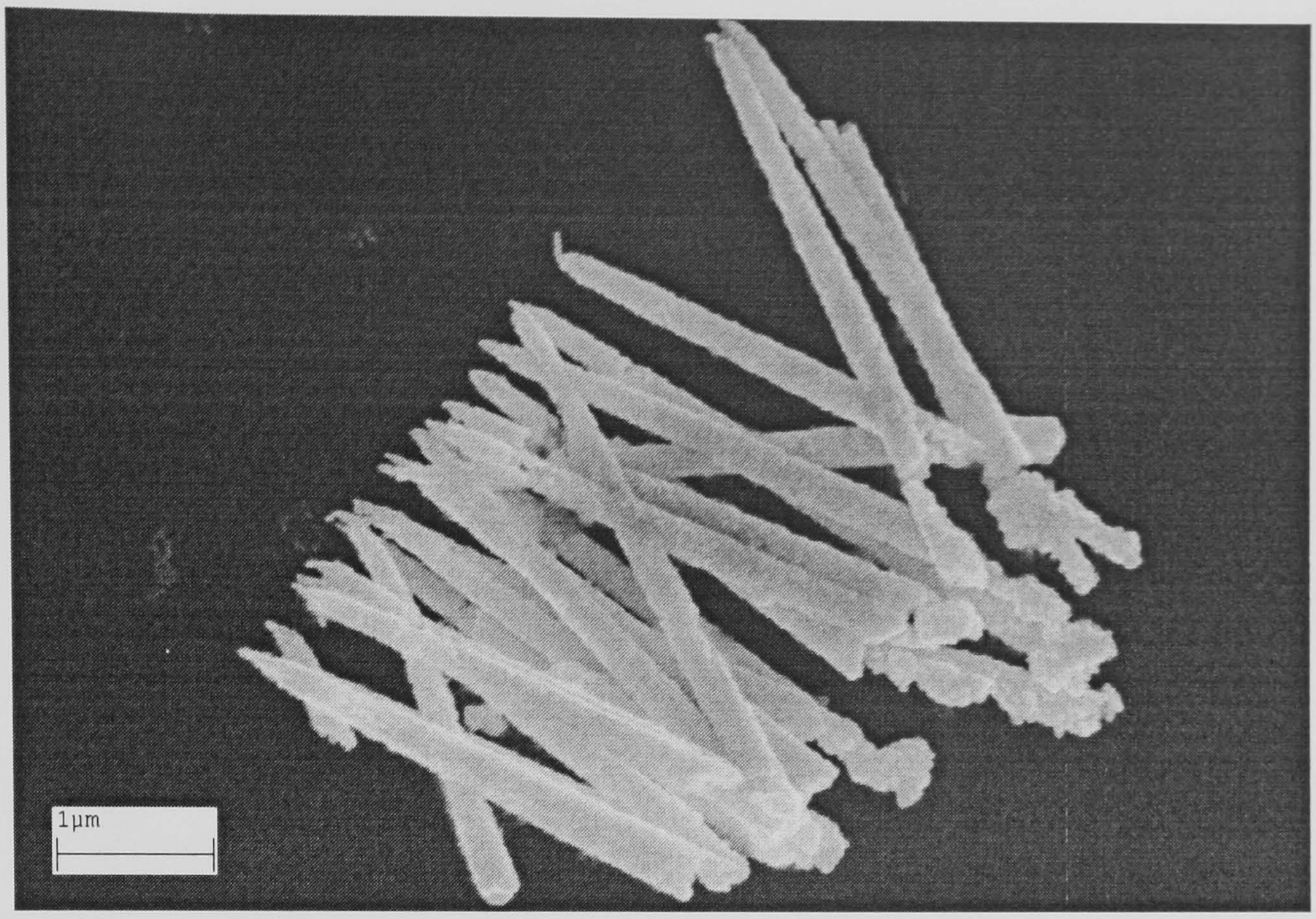

Figure 3.28. Gold nanowires grown in Cyclopore membranes after 30 minutes growth

3.2.4 Electroless Deposition in Whatman 'Anodisc' Membranes

Complete reduction of metallic gold from the electroless solution took approximately 1 hour at the conditions described in chapter 2. To slow the growth process the reduction, or complete removal, of Na_2SO_3 extended this time from 1 hour to up to 2 days. An example of nanowires grown by electroless deposition in an Anodisc membrane (without Na_2SO_3) is shown in figure 3.29.

Figure 3.29. SEM image of a nanowire formed by electroless growth, without Na_2SO_3, dropcast on silicon

The structure of the nanowire shown in figure 3.29 is characteristic of all nanowires grown by this technique. They consist of a well-formed section, thought to be formed at the base of the membrane closer to the silver electrode, and a more porous section. Typically, the porous section thins and becomes more irregular along the length of the nanowire. Finally, the nanowire diameter decreases below the expected pore diameter (when compared to figure 3.21) and the end of the nanowire is very poorly formed, prior to terminating. This structure is thought to be dependent on the growth kinetics of electroless deposition, however, attempts to slow the growth, by reducing both the salt concentration and temperature, do not show significant improvement. The range of lengths within a single sample has a high variation, when compared with those grown by electrodeposition, figure 3.30.

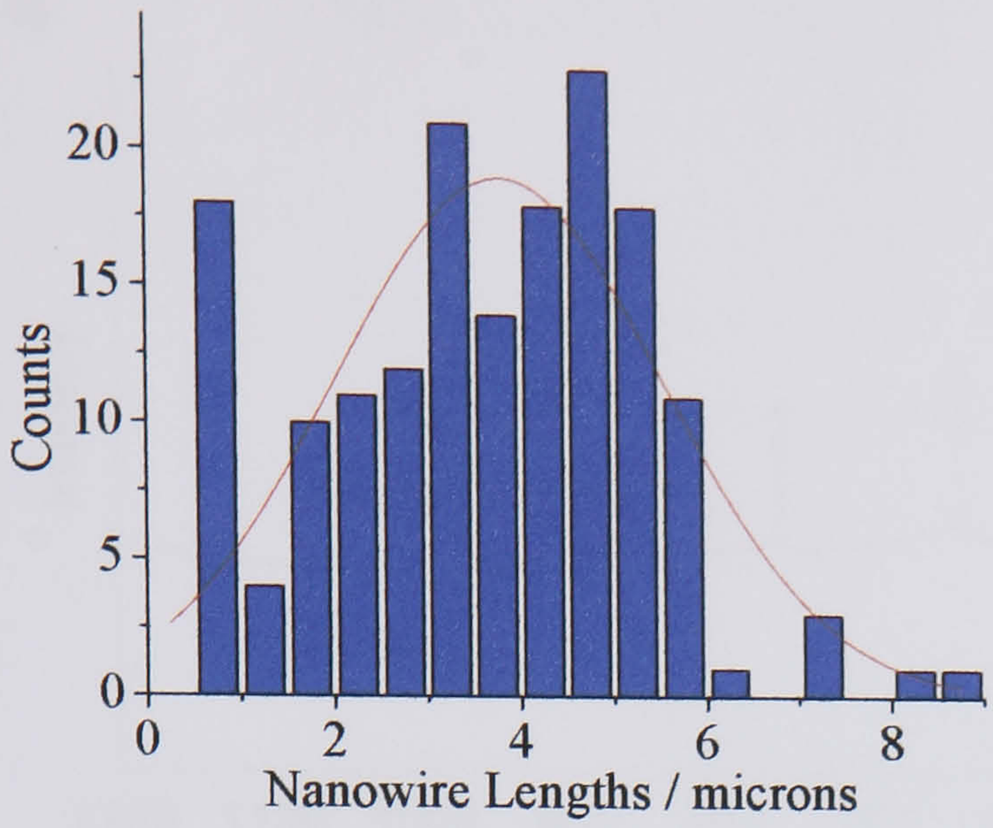

Mean Length = 3.8 μm

Standard Deviation = 1.8 μm

Figure 3.30. Nanowire length after electroless growth in Anodisc membranes

3.3: Functionalised Nanowires

Nanowires suspended in methanol, or those embedded in membranes, may be functionalised with a variety of thiol surfactants. Typically, thiol was added to nanowire solutions at 1 mM concentration and left overnight to allow the formation of a monolayer. Subsequently, the thiol solution was removed, by filtering the nanowires through an 'Anodisc' or 'Cyclopore' filtation membrane, and replaced with HPLC methanol. A minimum of 3 filtration cycles were required, with the nanowires sonicated between each stage, to remove excess thiol material. Alternatively, a membrane containing nanowires could be exposed to thiol solution such that one or both ends (or other exposed regions of the nanowire) could be functionalised. After removal from the thiol solution, nanowires were liberated from the membrane by the usual procedure. The surface properties of nanowires were modified with the materials outlined below. To characterise the attachment of thiol to the surface of the nanowires, a dense solution of nanowires was dropcast on silicon, and subjected to X-ray photoelectron spectroscopy.

3.3.1 Hydroxyl Functionalised Nanowires

Electrodeposited gold nanowires (formed in Anodisc membranes with the hydrochloric electrolyte) were functionalised with mercapto-1-undecanol [OH] by the solution method described above. For comparison purposes a SAM of [OH] was formed on gold from a 1 mM solution in methanol, figure 3.31.

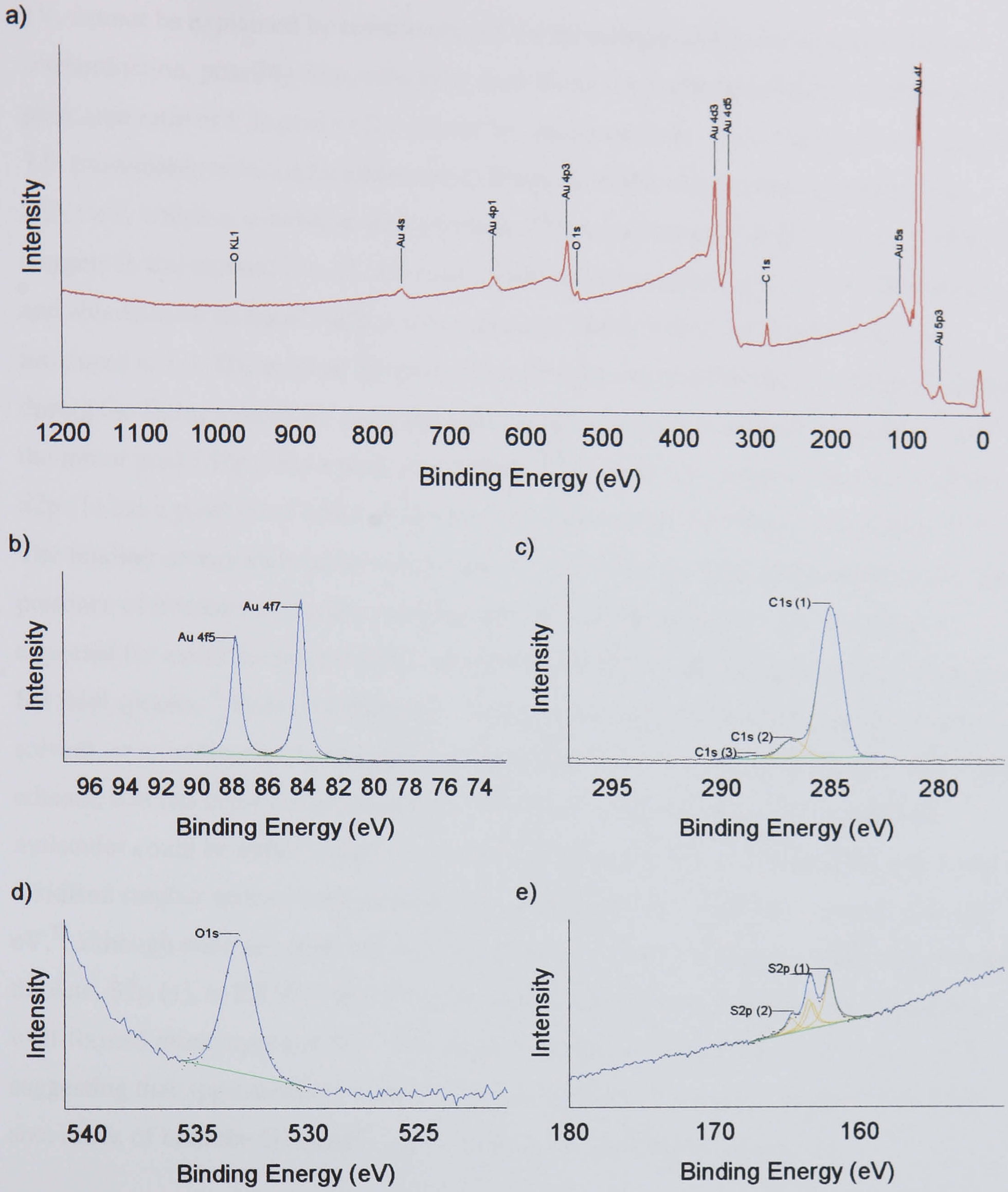

Figure 3.31. XPS spectra for a SAM of [OH] on gold including a) survey spectra, and high resolution scans of the b) gold 4f, c) carbon 1s, d) oxygen 1s and e) sulphur 2p

The XPS spectra reveal all the expected constituents for a monolayer of [OH] ($SH(CH_2)_{11}OH$). The gold spectrum is fitted in accordance with the discussion in chapter 2, with a 0.75 peak area ratio, and the doublet is split by 3.7 eV. The carbon 1s spectrum is fitted with 3 peaks. The main peak (1) is associated with saturated hydrocarbons, i.e. the alkyl chain of the thiol molecule, and is positioned as expected at 285.0 eV. Peak 2, centred at 286.8 eV, is associated with the COH terminal group. Peak 3, centred at 288.3

eV, cannot be explained by constituents of the monolayer and is due to some carbon contamination, possibly free carboxylic acid. From the surfactants structure, the expected peak area ratio of C1s peaks (1) / (2) can be calculated to be 10:1. The measured ratio is 7.9, presumably reduced by attenuation effects. A single oxygen peak is observed at 533.1 eV, which is consistent with previous XPS measurements of this surface.[14] Both oxygen 1s and carbon, C1s (2) are associated with the terminal group of the monolayer, and should have an equal surface concentration. The O1s to C1s (2) peak area ratio measured is 1.0. The sulphur 2p spectrum is fit with two doublet pairs, constraints applied during the fitting procedure cause the peaks of each doublet to be split by 1.2 eV.[15] and the minor peak ($S2p_1$) has a peak area half the $S2p_3$ peak. The larger of the two doublets S2p (1) has a position of 162.1 eV for the $S2p_3$ as expected for thiol bound to gold.[15-18] The binding energy shift between doublets (1) and (2) of the S2p spectrum is 1.2 eV. The presence of intensity at binding energies that are slightly higher (~1 eV) than those expected for metal thiolates suggests that some sulphur containing species are present as SH thiol species.[16] Unbound thiol molecules are generally due to either a poor choice of solvent, or a inadequate rinsing step.[15] Here it is probably the use of methanol, rather than ethanol, that has contributed most to the presence of unbound thiol. These unbound molecules could be either lying on top of the SAM or partially penetrating into the SAM. Oxidised sulphur species such as sulphonate appear at binding energies greater than 166 eV,[15] although none are observed in these spectra. The surface concentration of the bound thiolate, S2p (1), is 2.8 % of that for gold, lower than the value expected for a complete well-formed monolayer (~4 %).[16] The relative total peak area of S2p (2) to S2p (1) is 2, suggesting that approximately a third of the molecules observed are unbound. The peak area ratios of both the O1s and C1s (2) peaks to the S2p(1+2) peak are 1.4.

The XPS spectra observed for [OH] functionalised nanowires are shown in figure 3.32.

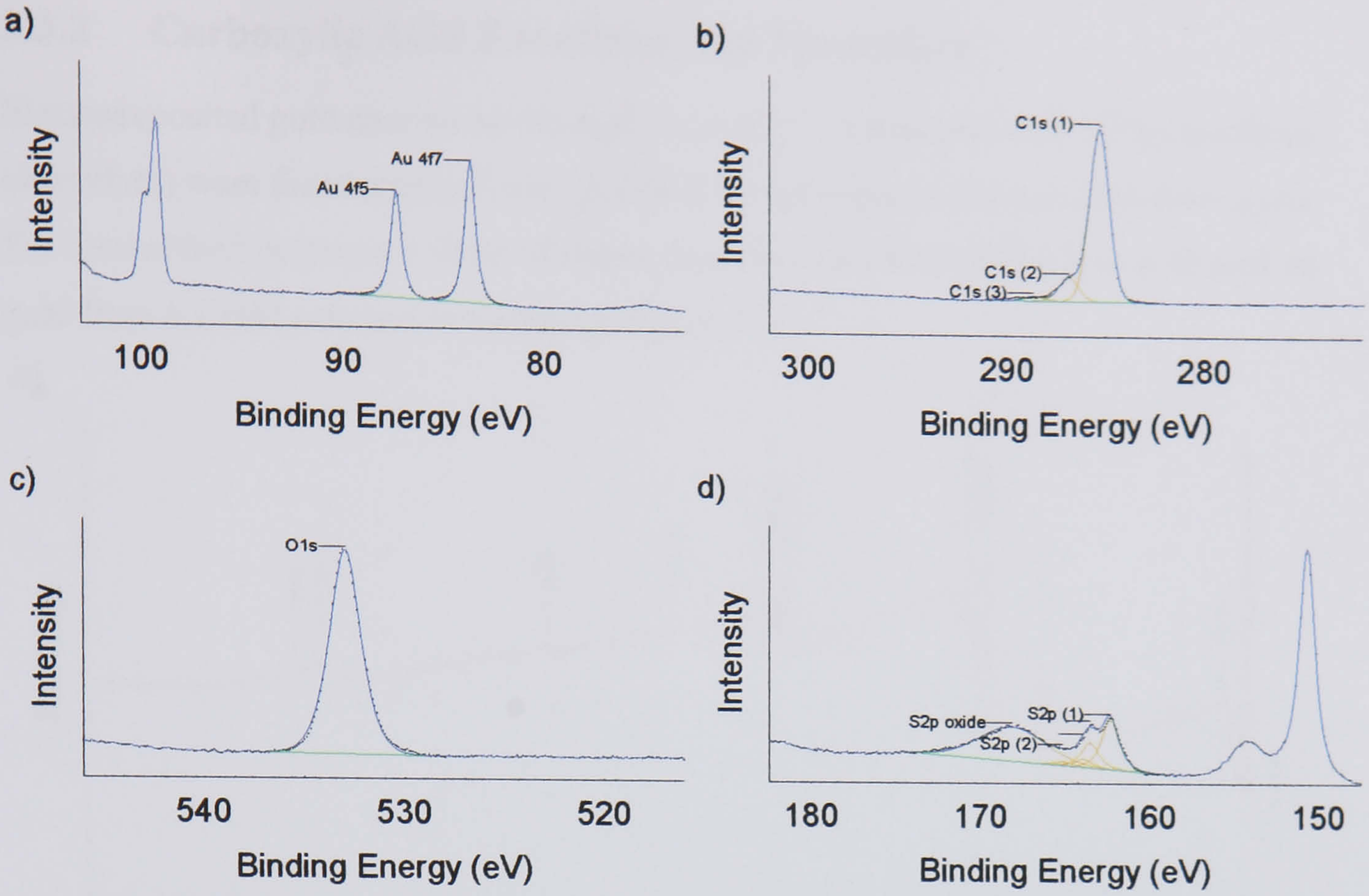

Figure 3.32. XPS spectra for [OH] functionalised nanowires on silicon, including high resolution scans of the a) gold 4f, b) carbon 1s, c) oxygen 1s and d) sulphur 2p regions

The gold signal is immediately apparent, and the additional peaks observed at higher binding energies in figure 3.32a are associated with the silicon 2p doublet. The separations of the carbon 1s peaks are consistent with the planar SAM, although individually they are all positioned at binding energies ~0.3 eV higher. The oxygen 1s peak is positioned at 533.0 eV. Figure 3.32d demonstrates the presence of bound thiol, in addition to the broad oxide peak also observed for bare nanowires, figure 3.23f. Now, three species of thiol are observed. The bound thiol S2p (1) is positioned at 162.4 eV for the $2p_3$ peak, the unbound thiol S2p (2) is positioned at 163.9 eV, and the oxidised thiol peak, at ~168 eV, is consistent with that measured in figure 3.23f in both position and peak area. The relative concentration of unbound SH thiol is lower than observed for the planar SAM, and constitutes 15 % of the total bound thiol observed. The measured surface concentration of sulphur (1) to gold is 10.7 %. This observation is too high for a planar monolayer. The shape of nanowires may contribute to this high measurement; since the system is no longer planar but associated with a particulate a higher ratio may be expected. Alternatively, thiol may also be bound to silver contamination in the solution, originating from the evaporated silver electrode.

3.3.2 Carboxylic Acid Functionalised Nanowires

Electrodeposited gold nanowires (formed in Anodisc membranes with the hydrochloric electrolyte) were functionalised with [COOH] by the solution method described above. For comparison purposes a SAM of mercaptoundecanoic acid [COOH] was formed on gold from a 1 mM solution in methanol, figure 3.33.

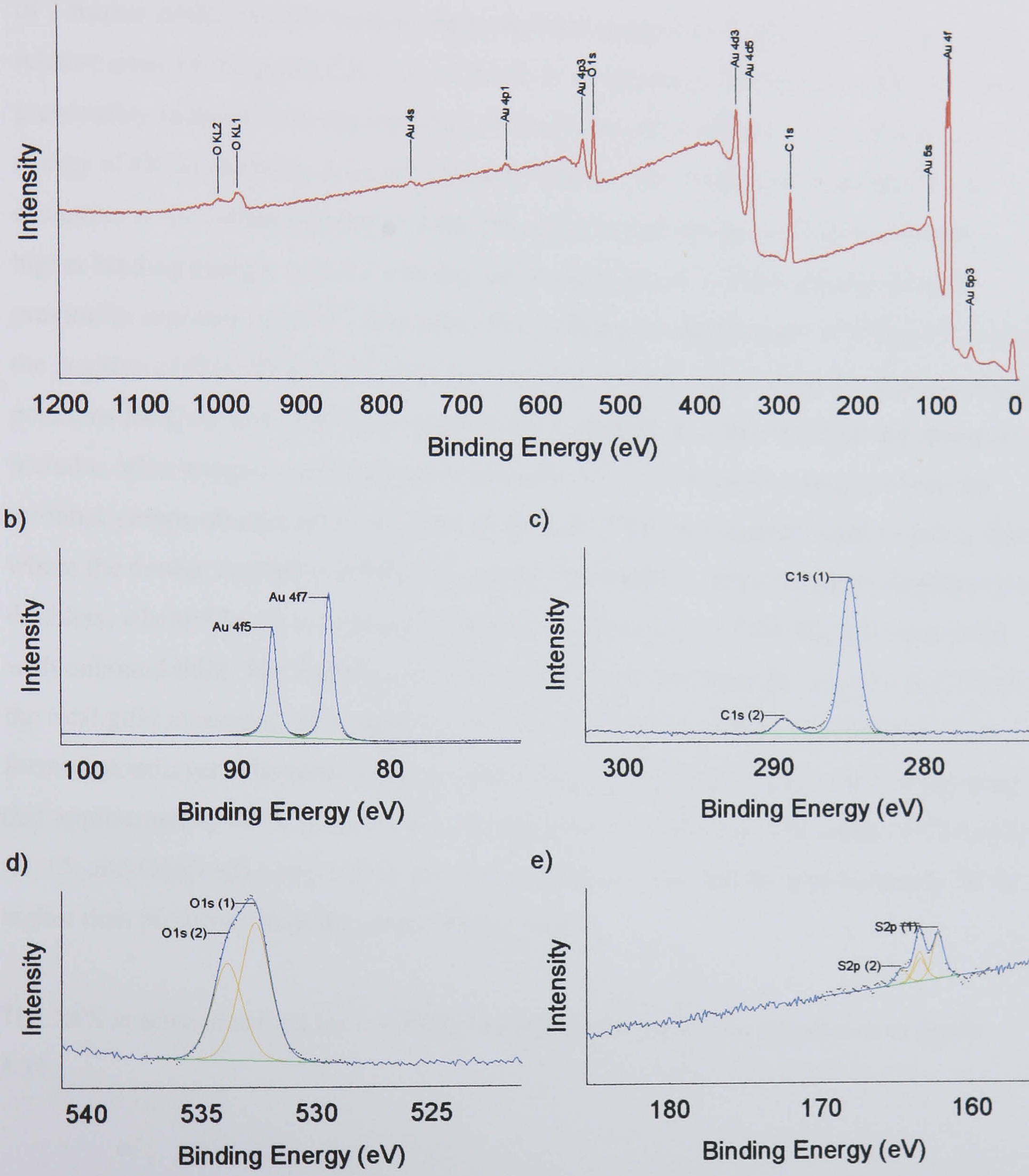

Figure 3.33. XPS spectra for a SAM of a [COOH] on gold including a) survey spectra, and high resolution scans of the b) gold 4f, c) carbon 1s, d) oxygen 1s and e) sulphur 2p regions

The XPS spectra reveal all the expected constituents for a monolayer of [COOH] ($SH(CH_2)_{10}COOH$). The carbon 1s spectrum shows 2 peaks, including the saturated hydrocarbon peak 285.0 eV, peak 1. Peak 2, at a binding energy of 289.3 eV, is associated with the carbon of the carboxylic acid terminal group.[19] The C1s spectrum shows a flat plateau between the two fitted peaks, presumably associated with a range of carbon contaminants. However, this region has not been fit since it required the addition of 2 further peaks without basis in the monolayer composition, due to its breadth. The relative areas of the peaks C1s (1) to C1s (2) is measured to be approximately 9, which is presumably reduced from the expected 10:1 ratio by attenuation effects. The binding energy of O(1s) electrons does not generally change due to functional groups[18]. The exception is for carboxyl groups where the singly bound oxygen will have a slightly higher binding energy, and the splitting observed in figure 3.33d is consistent with previously reported spectra[18]. The peak O1s (1) has a binding energy of 532.6 eV, whilst the position of O1s (2) is 533.8 eV, approximately 0.4 eV higher than the expected peak positions for C=O and COH they respectively represent. It is possible that the spectrum includes other oxygen contributions, potentially from hydrogen bonding between the terminal groups of adjacent molecules, or the loss of the hydrogen to form a carboxylate where the double bonded is effectively shared. The sulphur spectrum again displays two doublets, where S2p (1) is associated with the S-Au moiety and the S2p (2) associated with unbound thiol. The surface concentration of the bound thiolate, S2p (1), is 2.1% of the total gold measured, once again lower than the value expected for a complete well-formed monolayer. The relative area of the S2p (2) to the S2p (1) peaks is 2, suggesting that approximately 40 % of the molecules observed are unbound. The ratios of C1s(1+2) C1s(2) and O1s(1+2) compared to the total sulphur content are all approximately 30 % higher than predicted from the molecules structure.

The XPS spectra observed for [COOH] functionalised nanowires are shown in figure 3.34.

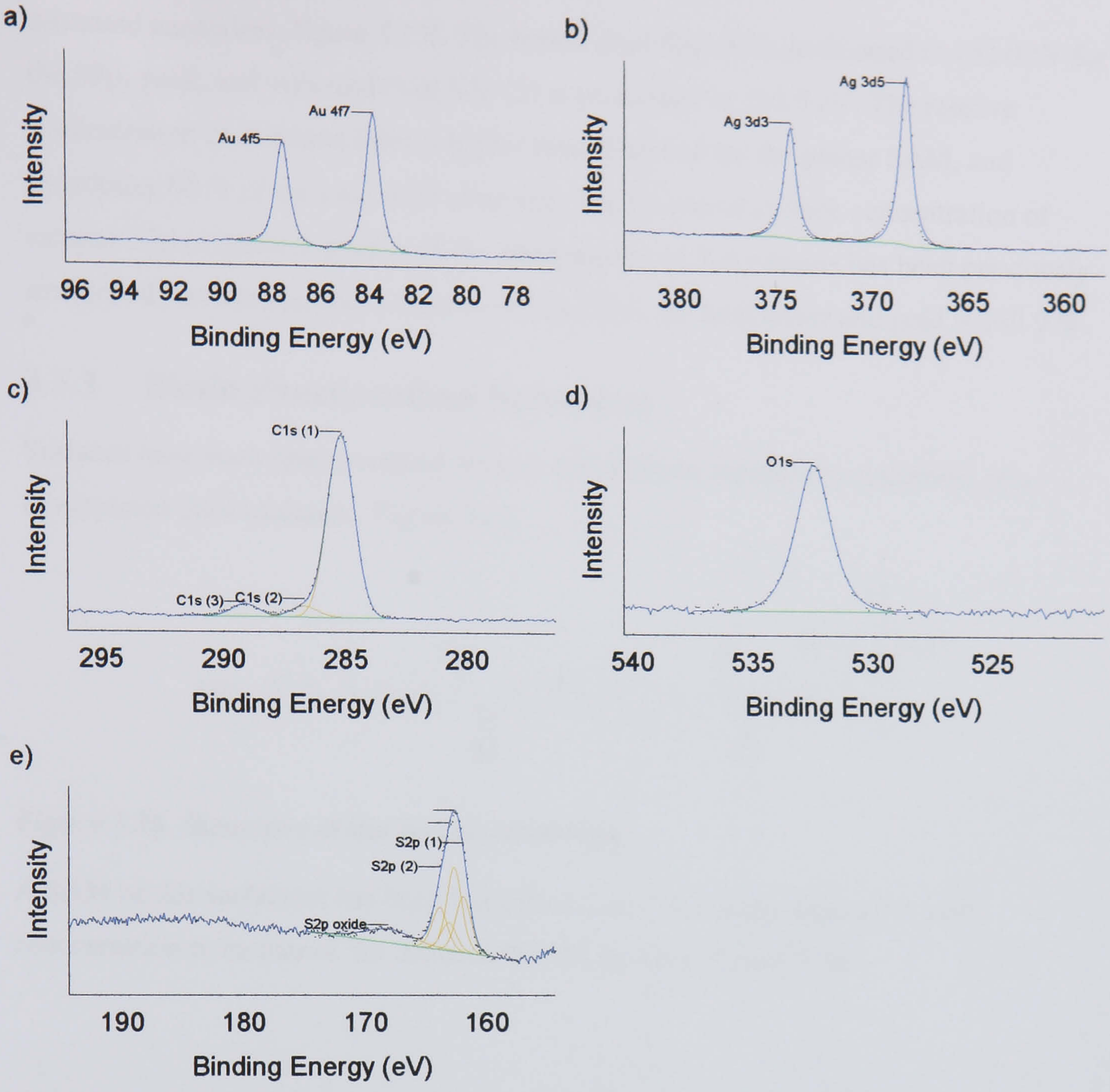

Figure 3.34. XPS spectra for [COOH] functionalised nanowires on silicon, including high resolution scans of the a) gold 4f, b) silver 3d, c) carbon 1s, d) oxygen 1s and e) sulphur 2p regions

The silver spectrum is particularly strong for this sample, and has been recorded in figure 3.34b. Indeed, there is three times more silver than gold observed on this surface. This is not entirely unexpected, during the precipitation of nanowires and other particulates onto the surface silver has been observed to settle on the top, in the form of silver flakes. Consequently, where silver is present in the sample, it will dominate the XPS characterisation. The carbon 1s peaks (1) and (2) are positioned at 285.1 eV and 289.2 eV, consistent with the observation of alkyl chain and carboxylic acid in figure 3.33. The oxygen spectrum, figure 3.34d, is fit with a single peak centred at 532.5 eV, no evidence of the doublet observed for the planar SAM is observed. The sulphur spectrum is not as well resolved as previously, but can still be fitted with a doublet pair associated with the bound and unbound thiol, and an oxidised contribution consistent with measurements on

uncoated nanowires, figure 3.23f. The bound thiol S2p (1) is positioned at 162.0 eV for the $S2p_3$ peak, and unbound thiol S2p (2) is positioned at 162.8 eV. The relative concentration of unbound thiol is higher than observed for the planar SAM, and constitutes 60 % of the total thiol observed. The measured surface concentration of sulphur S2p (1) peak to gold is 28 %. The possibly of S-Ag bonds has been previously mentioned, but surface concentration of S2p (1) to the total silver and gold is still 9 %.

3.3.3 Biotin Functionalised Nanowires

Surfaces have been functionalised with an active biotin moiety by attachment of a biotinylated thiol molecule, Figure 3.35.

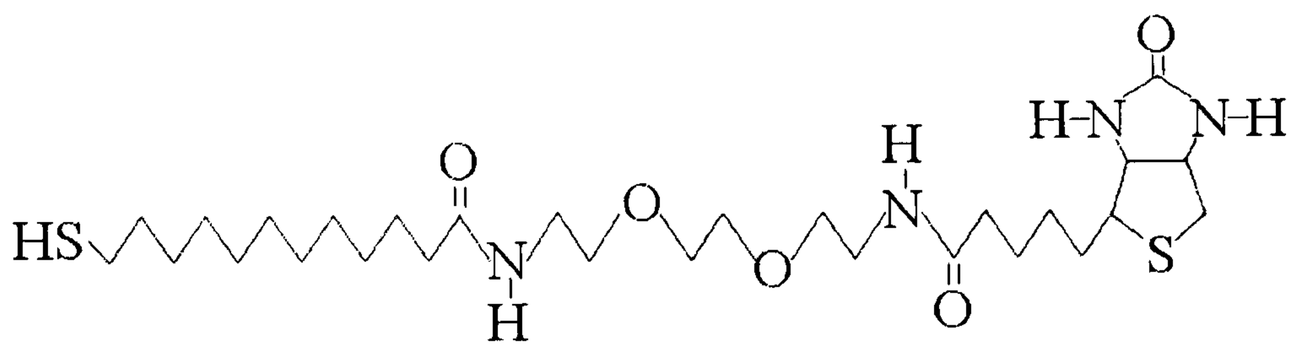

Figure 3.35. Structure of the biotinylated thiol.

A SAM of this surfactant has been formed on a gold substrate, from a 0.1 mM concentration in methanol, for characterisation by XPS, Figure 3.36.

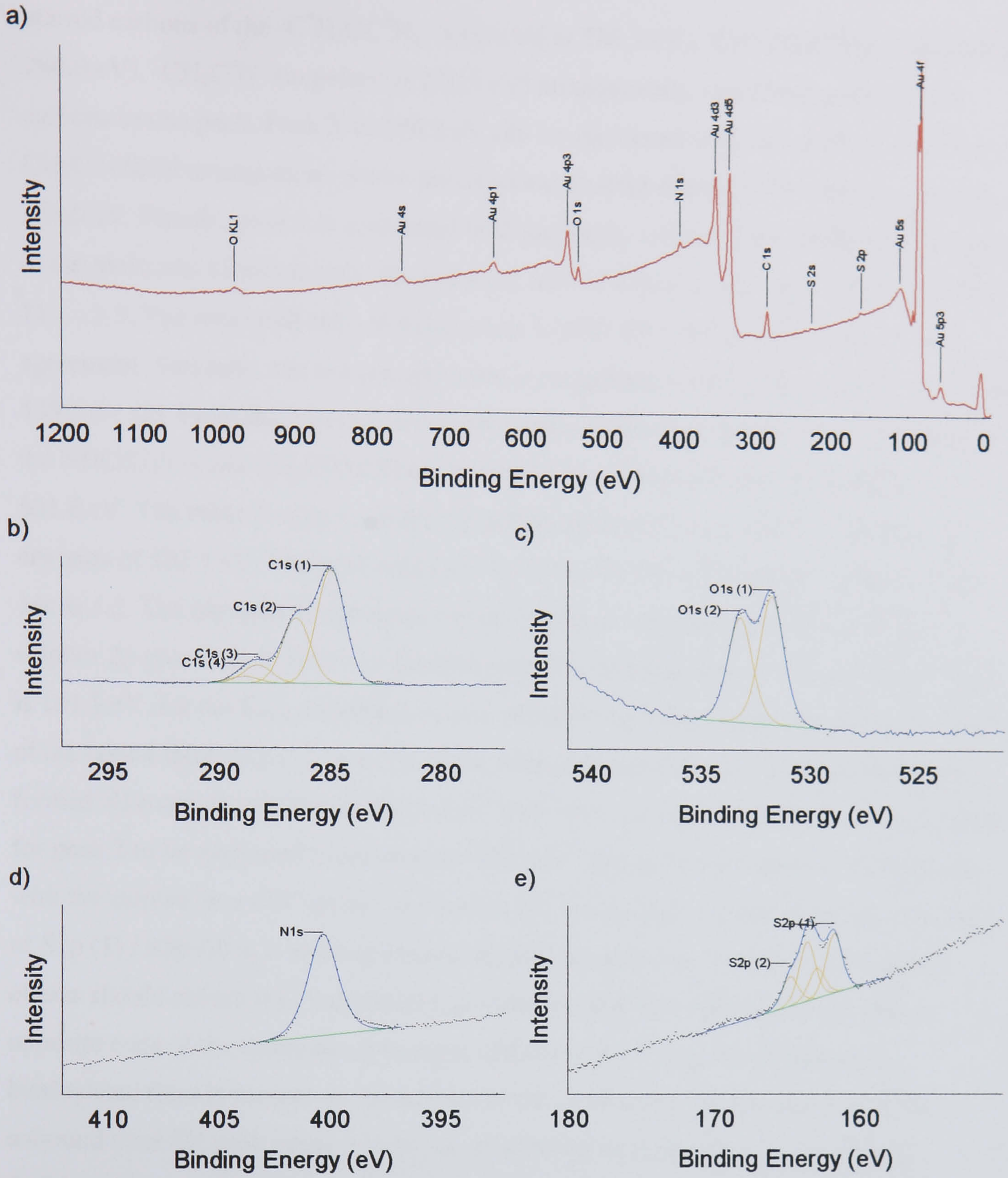

Figure 3.36. XPS spectra for a SAM of biotin on gold including a) survey spectra, and high resolution scans of the b) carbon 1s, c) oxygen 1s, d) nitrogen 1s and e) sulphur 2p regions

The XPS spectra reveal all the expected constituents of the biotin monolayer, with no unexpected elements present. The structure of the thiol molecule is exposed by analysis of the carbon 1s and oxygen 1s spectra, figures 3.35b and 3.35c respectively. The familiar saturated hydrocarbon peak (1) at 285.0 eV, is associated with 16 of the 29 carbon of the biotinylated molecule, in addition to a contribution from the starred carbon atoms present in the two -C*H_2C(O)NH- groups. There are three additional peaks all composed entirely of more complex carbon combinations. Peak 2, at 286.6 eV, can be associated with the

starred carbons of the -$C^*H_2OC^*H_2$- (expected at 286.3 eV), -$C(O)NHC^*H_2$- (expected at 286.0 eV), -CH_2C^*N- (expected at 286.5 eV) arrangements, contributing a total of 8 carbons to this peak. Peak 3, at 288.3 eV can be associated with two carbons from the $CH_2C^*(O)NH$ arrangement, where the expected binding energy of the starred carbon is 288.0 eV. Finally, peak 4 is associated with the single carbon of the -NHC(O)NH- group in the molecule. Consequently, the expected ratio of C1a (1) : (2) : (3) : (4) is 100 : 44.4 : 11.1 : 5.5. The measured ratio of these peaks is 100 : 55 : 15 : 6, which is in broad agreement. Similarly, the oxygen spectrum is comprised of two peaks at 531.8 eV (1) and 533.3 eV (2). From the five oxygen atoms present in the biotinylated thiol, 3 oxygens in the NHC(O)NH and $CH_2C(O)NH$ arrangements are expected to have binding energies of 531.8 eV. The other 2 oxygens in the CH_2OCH_2 groups are expected to have binding energies of 533.5 eV. The peak area ratio for O1s (1) / O1s (2) determined from figure 14c is 1.2. The nitrogen 1s spectrum can be fit with a single peak at 400.4 eV. The sulphur 2p spectra is fit with two doublet pairs, The binding energy for the S2p (1) peak is 161.8 eV, for the $S2p_3$ contribution, and 163.6 eV for peak 2. The surface concentration of the bound thiol, S2p (1), is 4.2 % of the total gold measured, consistent with a well formed alkanethiol monolayer. The 1.8 eV shift between S2p (1) and S2p (2) is too great for peak 2 to be attributed to an unbound SH thiol. The position of peak 2 is consistent with the sulphur in a CSC group, as found in the biotin region of the molecule. The ratio of S2p (1) / S2p (2) is 1, entirely consistent with expectations. However, attenuation effects should reduce this, particularly considering that the sulphurs occupy sites at opposite ends of the molecule. It is suggested that a small quantity of unbound biotinylated thiol is present on the surface of the monolayer, and the position of the unbound thiol SH peak cause it to be incorporated predominantly into the S2p (2) doublet. When compared to the S2p (1) peak, other elements have a lower than expected surface concentration. The total nitrogen observed is 2.3 times greater than the sulphur, the predicted value is 4, whereas for O1s (1+2) it is 3.7, compared to a predicted value of 5.

Surfaces functionalised with a SAM containing biotin terminated molecules with a 100 % concentration have been shown to not bind streptavidin effectively.[20,14] The low binding of the protein is thought to be a result of the close packing of biotin groups that hinder molecular recognition with the biotin.[21] A mixed monolayer containing the biotinylated molecules and shorter alkanethiols has been shown to reduce steric hindrance to protein binding.[20] Consequently, where biotin-streptavidin attachment is required, the

biotinylated thiol has been used in combination with mercapto-1-undecanol as a mixed monolayer. Typically, the concentration of each species in a mixed monolayer can be controlled with the solution concentration, although their ratios are not equivalent. Long chain molecules are preferentially absorbed onto the surface over shorter chains, even where there are no specific interactions between the adsorbates and solvent.[22,16] However, this is often driven by stabilisation afforded by intramonolayer hydrogen bonds between the hydroxyl tail groups of alkanethiols.[23]

To reduce steric hindrance, biotin functionalised surfaces were formed by immersion in a mixed solution of 80 % [OH] 20 % biotin in methanol, with a total concentration of 10^{-4} M. On removal from solution, SAMs were rinsed with methanol, then milliQ water and dried in a stream of N_2. This procedure has been previously determined to generate surfaces with optimal ability to bind streptavidin, using ethanol solutions.[14] These mixed monolayers on gold have also been characterised with XPS, Figure 3.37.

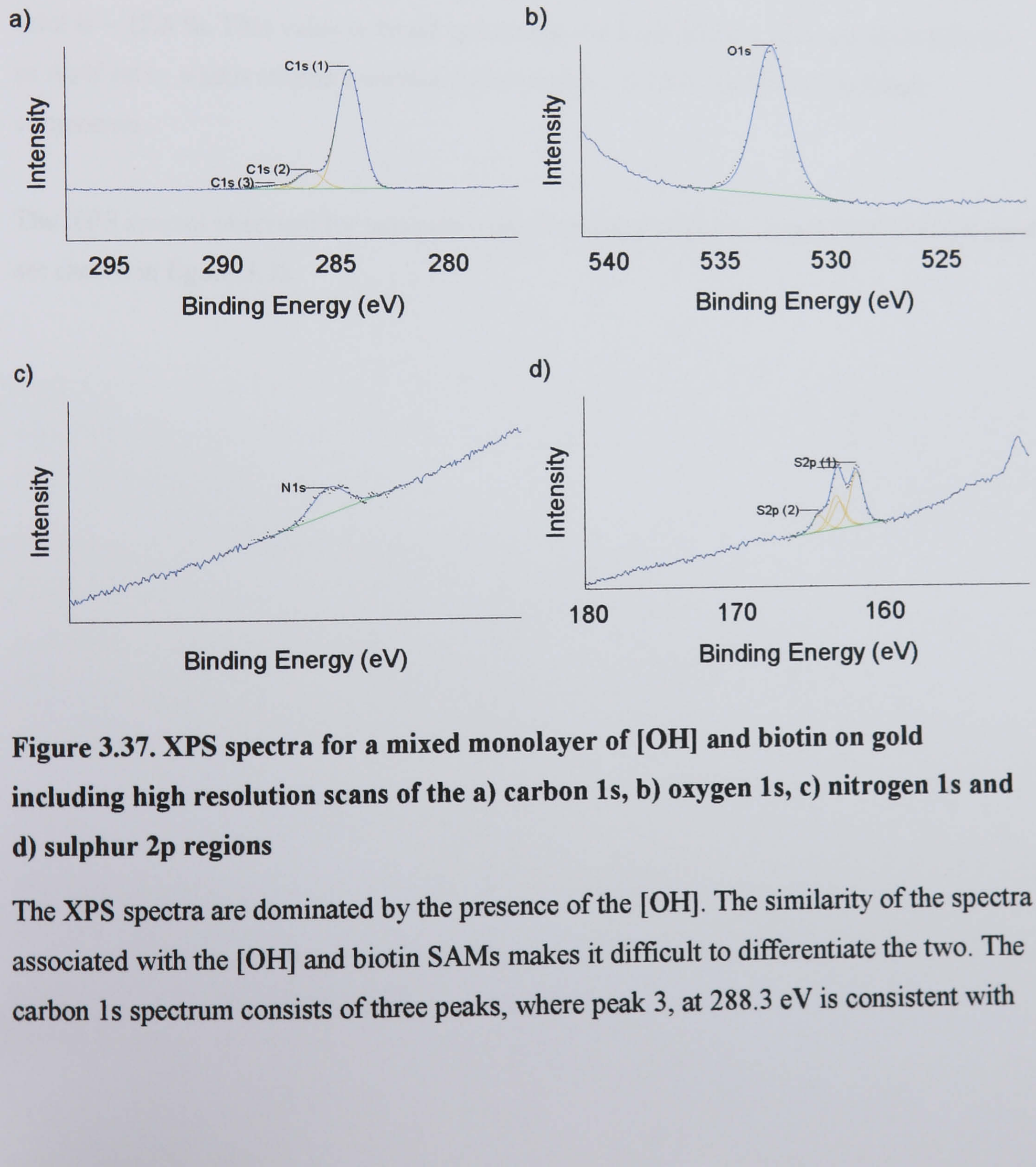

Figure 3.37. XPS spectra for a mixed monolayer of [OH] and biotin on gold including high resolution scans of the a) carbon 1s, b) oxygen 1s, c) nitrogen 1s and d) sulphur 2p regions

The XPS spectra are dominated by the presence of the [OH]. The similarity of the spectra associated with the [OH] and biotin SAMs makes it difficult to differentiate the two. The carbon 1s spectrum consists of three peaks, where peak 3, at 288.3 eV is consistent with

peak 3 in figure 3.36b. Determining the surface concentration of biotinylated thiol from C1s (3) is problematic since its area is strongly dependent on the background fit. The oxygen spectrum can be fit with a single peak at 532.7 eV, and the three components due to the COH terminal group of the mercapto-1-undecanol and the two oxygen groups of the Biotin cannot be accurately resolved. The sulphur 2p spectrum shows two doublets separated by 1.2 eV. The CSC species present in the biotinylated thiol cannot be resolved from the spectra. The best determination of biotinylated thiol concentration can be made from the nitrogen 1s spectrum, where the N1s peak is solely derived from the biotinylated component. The surface concentration of the S2p (1) peak is 3.7 % of the total gold measured. The ratio of S2p (1) / S2p (2) is 1.6, suggesting that unbound thiol remains on the surface. Comparison between the N1s peak and the total sulphur content is deemed the best way to determine the surface concentration of biotinylated thiol. The area ratio of N1s to S2p (1+2) peaks is 0.29. When this is compared to the 100 % biotin surface, where the same ratio was 2.3, it can be calculated that the surface concentration of biotinylated thiol is ~ 12.5 %. This value is broad agreement if the calculation is based upon the N1s to Au4f ratio, which returns a surface concentration of 15 % for the biotinylated component.

The XPS spectra observed for nanowires functionalised with the mixed biotin / [OH] thiol are shown in figure 3.38.

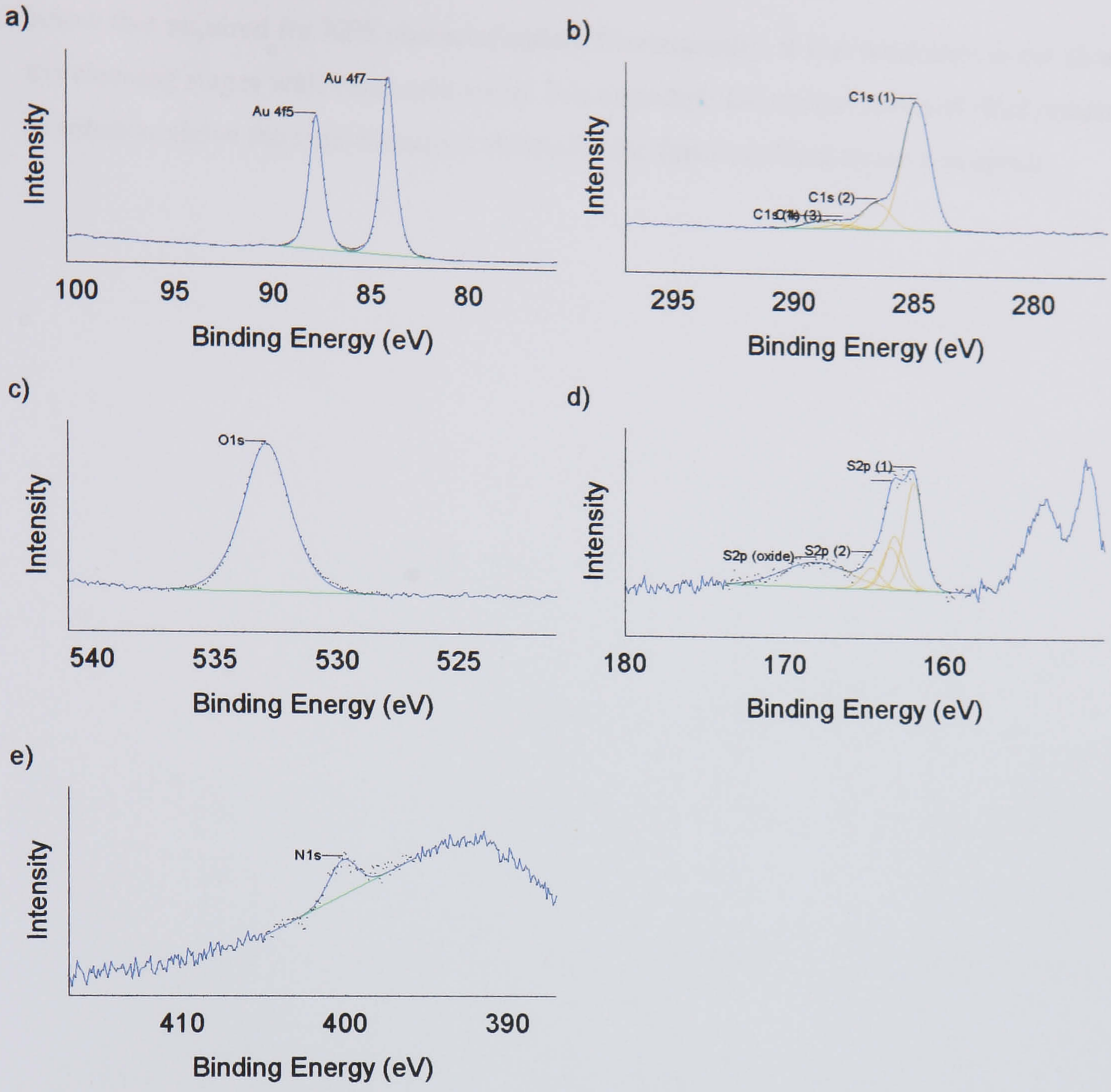

Figure 3.38. XPS spectra for [COOH] functionalised nanowires on silicon, including high resolution scans of the a) gold 4f, b) carbon 1s, c) oxygen 1s, d) sulphur 2p, and nitrogen 1s regions

The observed spectra for gold, carbon, oxygen and nitrogen are analogous to those measured for a planar SAM, figure 3.37. The only significant difference is the surface concentration of bound and unbound thiol. The measured concentration of bound thiol, S2p (1), to gold is ~10 %, consistent with measurements of other functionalised nanowires.

3.3.4 Hydrophobic Nanowires

Due to the hydrophobic nature of nanowires after functionalising with either the [CF3] or [CH3] hydrophobic surfactants it has not been possible to obtain XPS spectra of these samples. Whilst handling hydrophobic functionalised nanowires in aqueous solutions aggregation lead to a loss of nanowires, reducing the density of nanowires in solution

below that required for XPS characterisation. Consequently, it was necessary to cut short the cleaning stages with these nanowires. It is expected that excess unbound thiol remains in solution above the concentrations shown for the functionalised nanowires above.

3.4: References

1. Bandyopadhyay, S.; Miller, A.E.; Chang, H.C., et al., Nanotechnology, 1996. **7**(4): p. 360-371.

2. Masuda, H.; Satoh, M., Japanes Journal of Applied Physics Part 2 - Letters, 1996. **35**(1B): p. L126 - L129.

3. Masuda, H.; Fukuda, K., Science, 1995. **268**(5216): p. 1466-1468.

4. Jagminas, A.; Bigeliene, D.; Mikulskas, I., et al., Journal of Crystal Growth, 2001. **233**(3): p. 591-598.

5. Thompson, G.E.; Wood, G.C., Nature, 1981. **290**(5803): p. 230-232.

6. Furneaux, R.C.; Rigby, W.R.; Davidson, A.P., Letters to Nature, 1989. **337**: p. 147 - 149.

7. Zhang, X.Y.; Zhang, L.D.; Lei, Y., et al., Journal of Materials Chemistry., 2001. **11**(6): p. 1732 - 1734.

8. Murphy, P.J.; LaGrange, M.S., Geochimica Et Cosmochimica Acta, 1998. **62**(21-22): p. 3515-3526.

9. Peck, J.A.; Tait, C.D.; Swanson, B.I., et al., Geochimica Et Cosmochimica Acta, 1991. **55**(3): p. 671-676.

10. Diaz, M.A.; Kelsall, G.H.; Welham, N.J., Journal of Electroanalytical Chemistry, 1993. **361**(1-2): p. 25-38.

11. Yokoyama, T.; Matsukado, Y.; Uchida, A., et al., Journal of Colloid and Interface Science, 2001. **233**(1): p. 112-116.

12. Paula-Santos, F.; Campos, E.; Costa, M., et al., Materials Research, 2003. **6**(3): p. 353.

13. M.R. Alexander, T.L., G.E. Thompson, E. McAlpine and A.J. Roberts, *Changes in the Al Surface upon Exposure to Ambient Conditions*. 2000. Kratos.

14. Booth, C.; Bushby, R.J.; Cheng, Y.L., et al., Tetrahedron, 2001. **57**(49): p. 9859-9866.

15. Castner, D.G.; Hinds, K.; Grainger, D.W., Langmuir, 1996. **12**(21): p. 5083-5086.

16. Martins, M.C.L.; Ratner, B.D.; Barbosa, M.A., Journal of Biomedical Materials Research Part A, 2003. **67A**(1): p. 158-171.

17. Laibinis, P.E.; Whitesides, G.M., Journal of the American Chemical Society, 1992. **114**(6): p. 1990-1995.

18. Freeman, T.L.; Evans, S.D.; Ulman, A., Langmuir, 1995. **11**(11): p. 4411-4417.

19. Evans, S.D.; Ulman, A.; Goppertberarducci, K.E., et al., Journal of the American Chemical Society, 1991. **113**(15): p. 5866-5868.

20. Perez-Luna, V.H.; O'Brien, M.J.; Opperman, K.A., et al., Journal of the American Chemical Society, 1999. **121**(27): p. 6469-6478.

21. Spinke, J.; Liley, M.; Schmitt, F.J., et al., Journal of Chemical Physics, 1993. **99**(9): p. 7012-7019.

22. Bain, C.D.; Whitesides, G.M., Journal of the American Chemical Society, 1989. **111**(18): p. 7164-7175.

23. Bain, C.D.; Evall, J.; Whitesides, G.M., Journal of the American Chemical Society, 1989. **111**(18): p. 7155-7164.

Chapter 4: Characterisation of Surfactant Mediated Nanowire Assembly.

This chapter explores the potential of surfactant based interactions to direct the assembly of nanowires. The surface properties of nanowires and / or substrates have been modified with a variety of SAMs. The driving force for assembly arises from competition between nanowire-nanowire, nanowire-surface, nanowire-fluid and fluid-surface interactions. This chapter presents specific examples of assembly, and supporting results, for the following cases:

1) Nanowire aggregation stimulated by hydrophobic interactions between functionalised nanowires.
2) Nanowire assembly from solution onto patterned hydrophilic / hydrophobic surfaces.
3) The attachment of carboxylic acid functionalised nanowires to patterned surfaces by hydrogen bonding.
4) The attachment of carboxylic acid functionalised nanowires to patterned surfaces via carboxylate salt formation.
5) The attachment of biotin functionalised nanowires to streptavidin activated regions of patterned surfaces.
6) Aggregation of biotin functionalised nanowires in solution after the introduction of a streptavidin.
7) Nanowire assembly, via electrostatic interactions, onto patterned charged surfaces. Both nanowires and surfaces were functionalised with acid and / or amine surfactants that become charged at specific solvent conditions.
8) Aggregation of nanowires functionalised with acid and / or amine terminated surfactants in solution, via electrostatic interactions.

4.1: Nanowire Aggregation due to Hydrophobic Interactions

Hydrophobic interactions in aqueous media and polar solvents cause strong adhesive forces, which have long range interactions (~10-100 nm) and are pH insensitive.[1, 2] This interaction has been discussed previously in chapter 2.

Here, nanowires have been coated with a hydrophobic surfactant in an attempt to cause their aggregation. Nanowires were fabricated in laboratory grown porous aluminium oxide membranes, which had undergone both the 2-step growth procedure and voltage

reduction technique. Gold was electrodeposited into the template from the sulphuric electrolyte (section 2.2.2.1) with an 8.5 V_{pp} (50 Hz) applied field. The aluminium substrate was removed from the filled porous template using the selective cupric chloride / hydrochloric acid etch procedure. Nanowires were functionalised with dodecanethiol [CH_3] as follows: After initially etching the membrane in 1 M NaOH for 5 seconds, the sample was washed with millipore 18.2 $M\Omega cm^{-1}$ water, then methanol, before immersion into a solution of 1 mM [CH3] in methanol overnight. After removal from the thiol solution, the template was once again cleaned with methanol, then millipore water, before exposing again to 1 M NaOH for 5 seconds. This cycle was repeated until the template started to degrade, and a final etch in 1 M NaOH was used to completely dissolve the membrane. By this procedure, nanowires were progressively exposed and functionalised. Excess thiol was more efficiently removed by washing the entire membrane containing captive nanowires. Nanowires were cleaned from the sodium hydroxide solution by the usual procedure. For comparative purposes, SAMs of [CH3] were formed on planar gold substrates from identical methanol based solutions, figure 4.1.

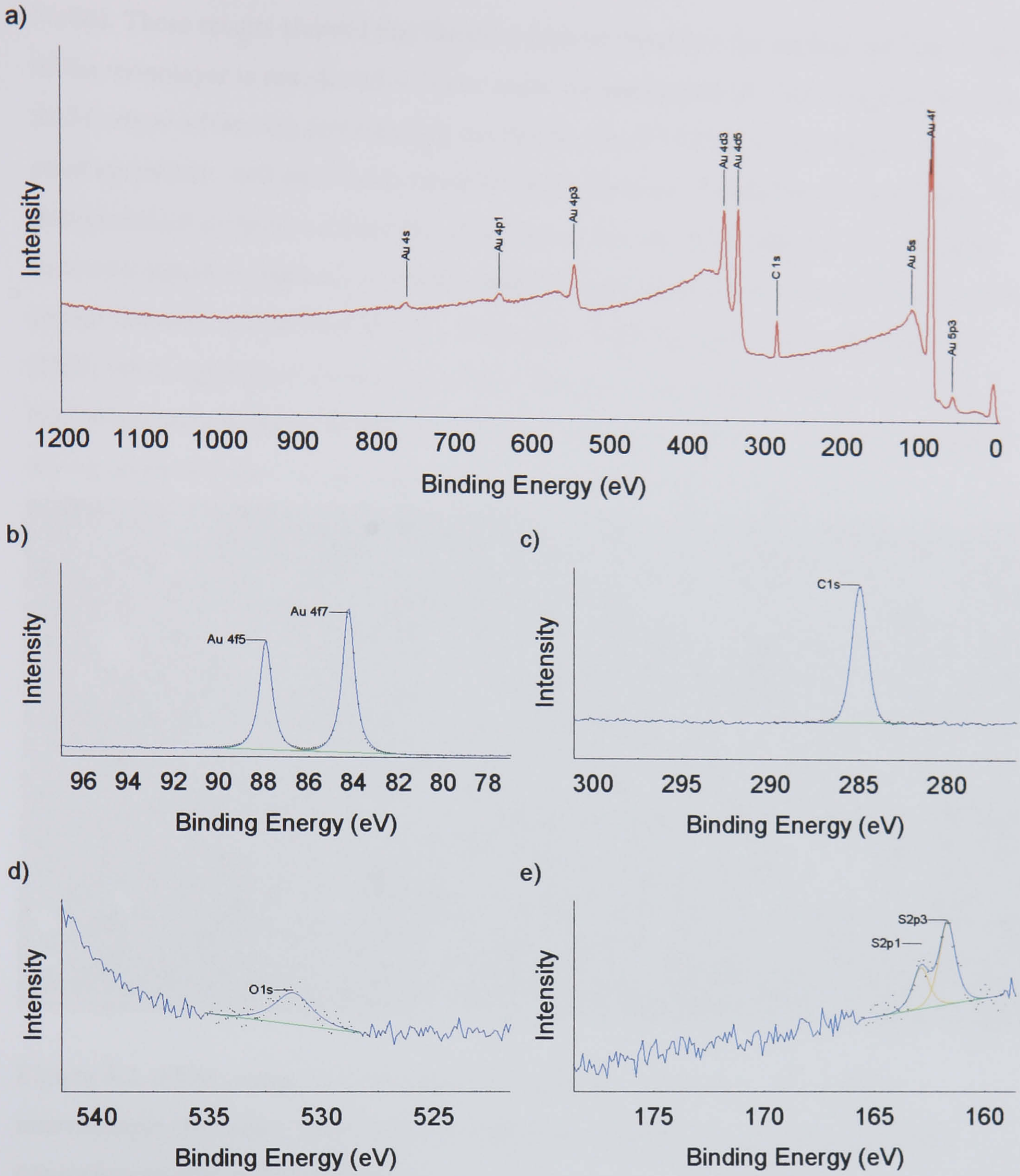

Figure 4.1. XPS spectra for a [CH3] SAM on gold including a) survey spectra, and high resolution scans of the b) gold 4f, c) carbon 1s, d) oxygen 1s and e) sulphur 1s regions

The XPS spectra for [CH3] ($CH_3(CH_2)_{11}SH$) is comparable with previously reported results.[3] A small oxygen peak at 531.3 eV is observed. Only a single peak is required to fit the carbon 1s spectrum, associated with the saturated hydrocarbon and positioned at 285.0 eV. The sulphur 2p spectra is fit with a single doublet pair, $S2p_1$ and $S2p_3$. The surface concentration of the bound thiolate is 4.5 % of the total gold measured, in line with expectations for a well formed monolayer.[4] To ensure this surface was not degraded by sodium hydroxide, XPS characterisation was repeated after 5 hours exposure to 1 M

NaOH. These results showed that the thiol remains bound to the surface, and the structure of the monolayer is not altered. Contact angle measurements of water droplets on these SAMs show advancing and receding contact angles of 110° and 101° respectively, in good agreement with previously reported values for these SAMs formed in ethanol.[5] The dodecanethiol surfactant causes the nanowires to become hydrophobic, and nanowire-nanowire adhesive interactions should result in aggregation. Nanowire solutions usually appear disperse, with a faint brown colouration. However, after functionalising with [CH3] small aggregates are seen in solution and the remaining solvent is colourless. Nanowires were dropcast from these solutions onto clean silicon substrates, and after drying under nitrogen, were imaged with atomic force microscopy, Figure 4.2.

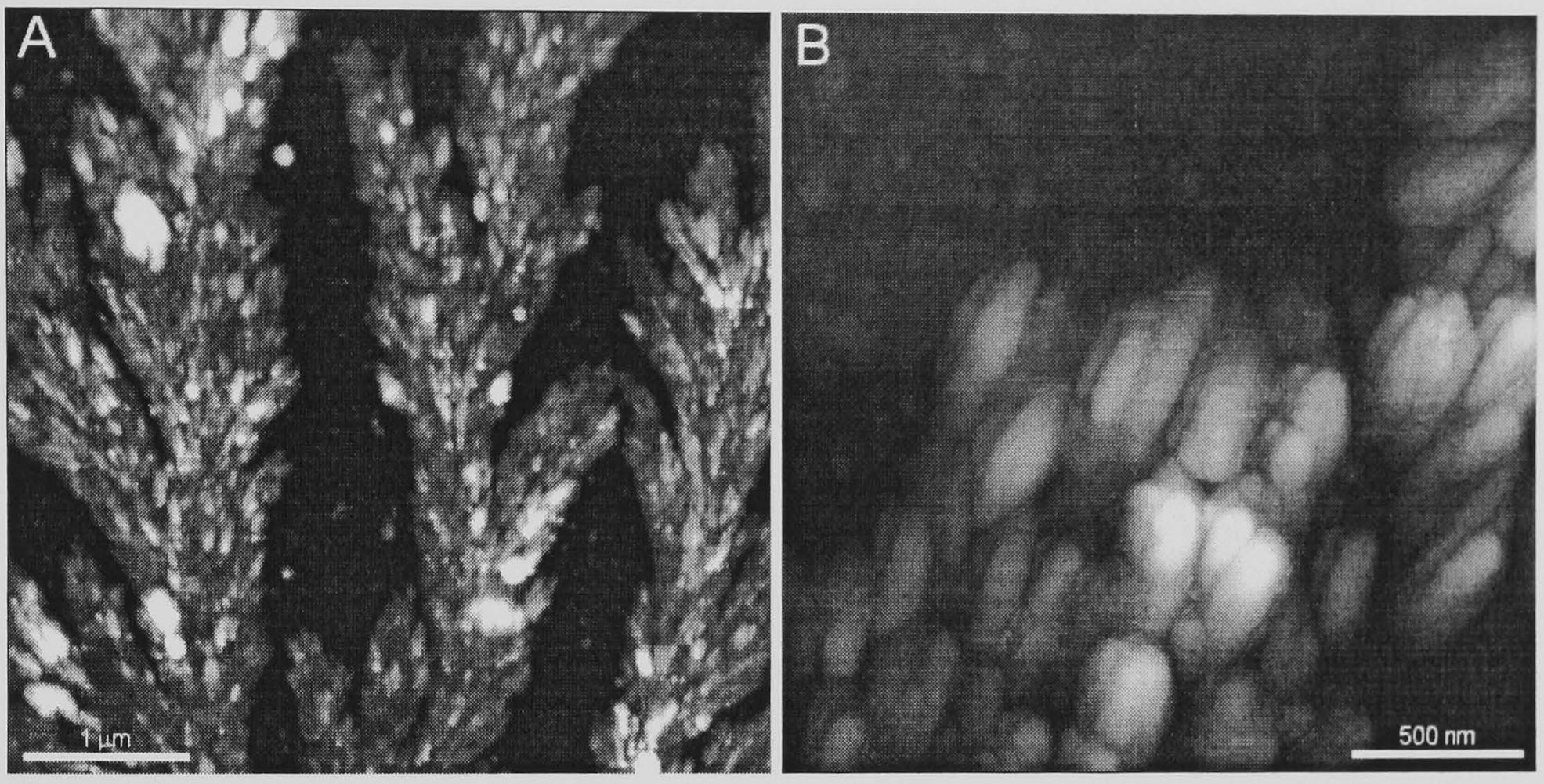

Figure 4.2. AFM images of hydrophobic nanowire aggregation showing a) macroscopic 'fern-like' structures, and b) high resolution image of component nanowires in one of the 'fronds'

Nanowire aggregation causes 'fern-like' assemblies of nanowires on these surfaces. Component nanowires are typically oriented parallel to the direction of the 'frond', similar to nematic liquid crystal arrangements. In previous work, both semetic and nematic arrangements of nanowires have been observed.[6-8] This aggregation is attributed to two associated factors; capillary forces between nanowires upon solvent evaporation, and hydrophobic surfactant interactions in solution. This type of organized aggregation was only observed when nanowires were functionalised with a hydrophobic monolayer.

4.2: Nanowire Assembly onto Surfaces with Patterned Wettability

The interaction of water with surfaces has been previously discussed in chapter 1. Surfaces with patterned wettability were used to manipulate the behaviour of solvent containing nanowires. The flow of solvent across these surfaces has been investigated as a route to assemble nanowires onto surfaces. Gold substrates were patterned with stripes of contrasting hydrophobicity / hydrophilicity by microcontact printing. Two hydrophobic surfactants have been used, [CH3] and [CF3], in conjunction with [OH] for the hydrophilic regions. For comparison purposes, SAMs of these surfactants have been produced on planar gold substrates. The [OH] thiol has already been characterised in the previous chapter, and results for [CH3] are shown in figure 4.1. XPS characterisation of the [CF3] thiol is shown in figure 4.3.

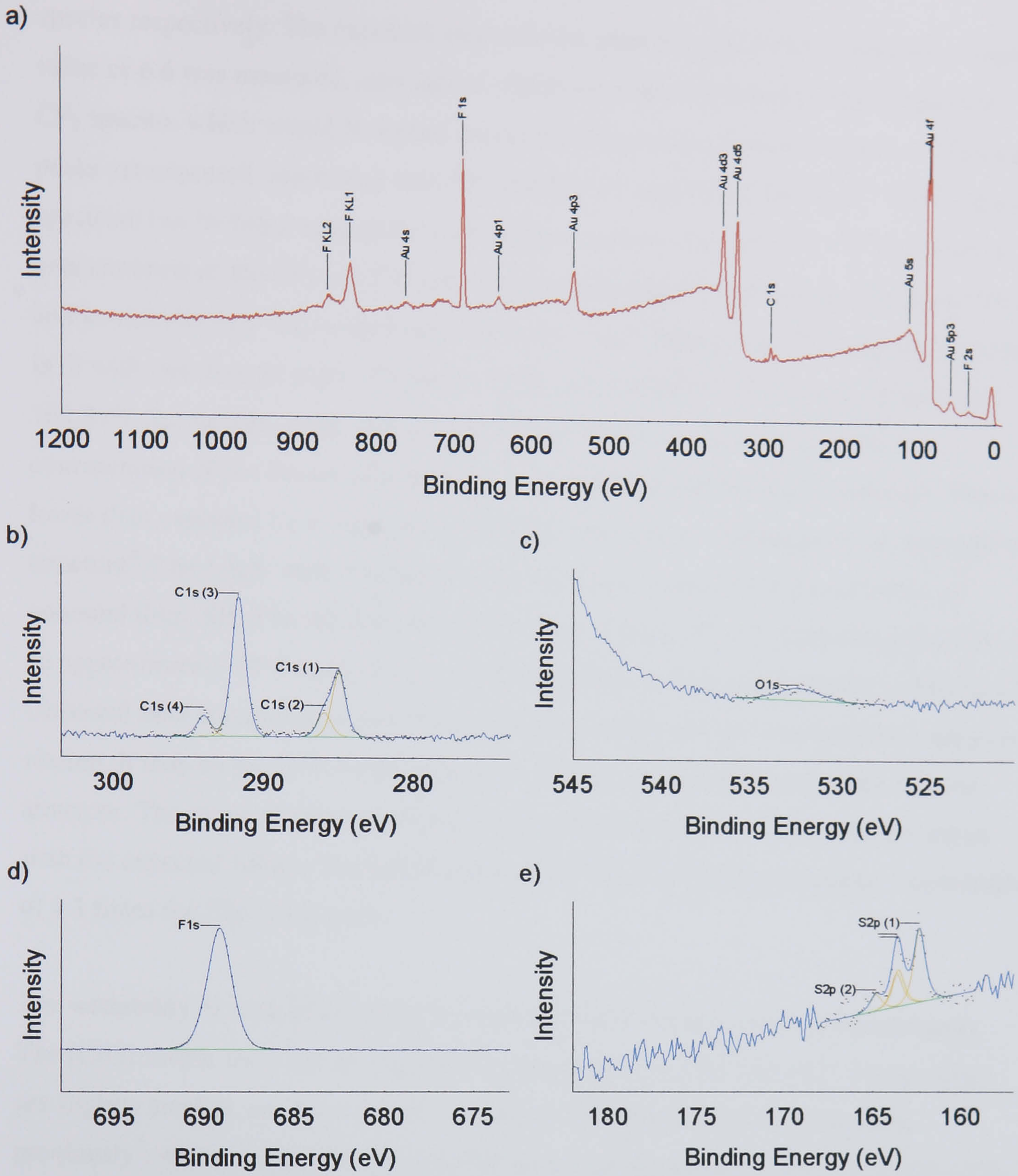

Figure 4.3. XPS spectra for a SAM of the flourinated [CF3] thiol on gold including a) survey spectra, and high resolution scans of the c) carbon 1s, c) oxygen 1s, d) flourine 1s and e) sulphur 2p regions.

The XPS spectra reveal all the expected constituents of a [CF3] ($CF_3(CF_2)_9(CH_2)_6SH$) monolayer. A small oxygen peak at 532.2 eV is also observed. The carbon 1s spectra can be fit with 4 peaks representing the different carbon moieties within the monolayer. The saturated hydrocarbon peak is observed as expected at 285.0 eV, peak 1. A shoulder, fit by peak 2 centred at 286.0 eV, is associated with hydrocarbons in close proximity to the fluorinated regions, i.e. CH_2CF_2. Peak 3 has a binding energy of 291.7 eV and peak 4 is positioned at 294.0eV, these are associated with the CF_2 and CF_3 fluorinated carbon

species respectively. The expected area ratio for peak 3 / peak 4 is 9. Although a lower value of 6.6 was measured, attenuation effects are expected to reduce the signal of the CF_2 species, which would be buried deeper within an ordered monolayer. Two fluorine peaks are expected, associated with CF_2 at 689.7 eV and CF_3 at 688.2 eV. The fluorine spectrum can be fitted adequately with a single peak centred at 689.2 eV. The relative concentration of the CF_2 and CF_3 species means that the CF_3 species cannot be resolved, and its contribution will be included within the single fitted peak. The sulphur 2p spectra is fit with two doublet pairs. The larger of the two doublets, S2p (1), has a position of 162.3 eV for the $S2p_3$ peak, as expected for a gold-thiolate bond. The surface concentration of the bound thiolate, S2p (1), is 2.9 % of the total gold measured. This is lower than expected for a complete well-formed monolayer and suggests an incomplete structure[4]. The 1.3eV shift between sulphur doublets (1) and (2) is characteristic of unbound thiol, SH. The relative size of S2p (2) to S2p (1) is 2.22, suggesting that there is an approximately 30 % contribution of unbound thiol to the spectra present in Figure 4.3. Unbound thiol is commonly associated with the use of a non-ideal solvent, or inadequate rinsing. It may be positioned on top of the monolayer, or partially embedded into the structure. The ratios of other species to the total sulphur content show good agreement with the expected values. The terminal group, fit with C1s (4), has a surface concentration of 1.1 times the S2p (1+2) peak.

The wettability of each of these SAMs were measured with contact angle goniometry. The [CF3] SAMs show advancing and receding angles of 118° and 102°. These values are slightly smaller, and have a greater hystersis than similar surfaces measured previously[3], where values of 119° and 106° have been reported for $HS(CH_2)_{11}(CF_2)_5CF_3$. The larger hysteresis is commonly due to a more disordered surface, this and the generally lower measurements are probably due to the presence of unbound thiol. Contact angle measurements of the [CH3] surfaces have been reported in section 4.1. The [OH] surfaces show advancing and receding contact angles of 40° and 20°. This is considerably higher than previously report values, where advancing and receding contact angles below 30° and 15° respectively have been reported.[5, 9] However, these high energy surfaces are renown for their propensity to be contaminated and to undergo reorganisation. Excess thiol on the monolayer surface will also increase the surface hydrophobicity.

Patterned hydrophilic / hydrophobic striped surfaces were fabricated in a variety of scales, with 1, 2, 5 and 10 μm wide stripes. Textured PDMS stamps, approximately 10

mm square, were used to print hydrophobic stripes onto the centre region of the gold substrate. Subsequent immersion of the substrate into methanol containing 3 mM [OH] functionalised the unexposed regions with the hydrophilic surfactant. The behaviour of a water droplet receding across a 10 μm striped surface of [OH] and [CF3] illustrates the effect of patterned wettability, Figure 4.4.

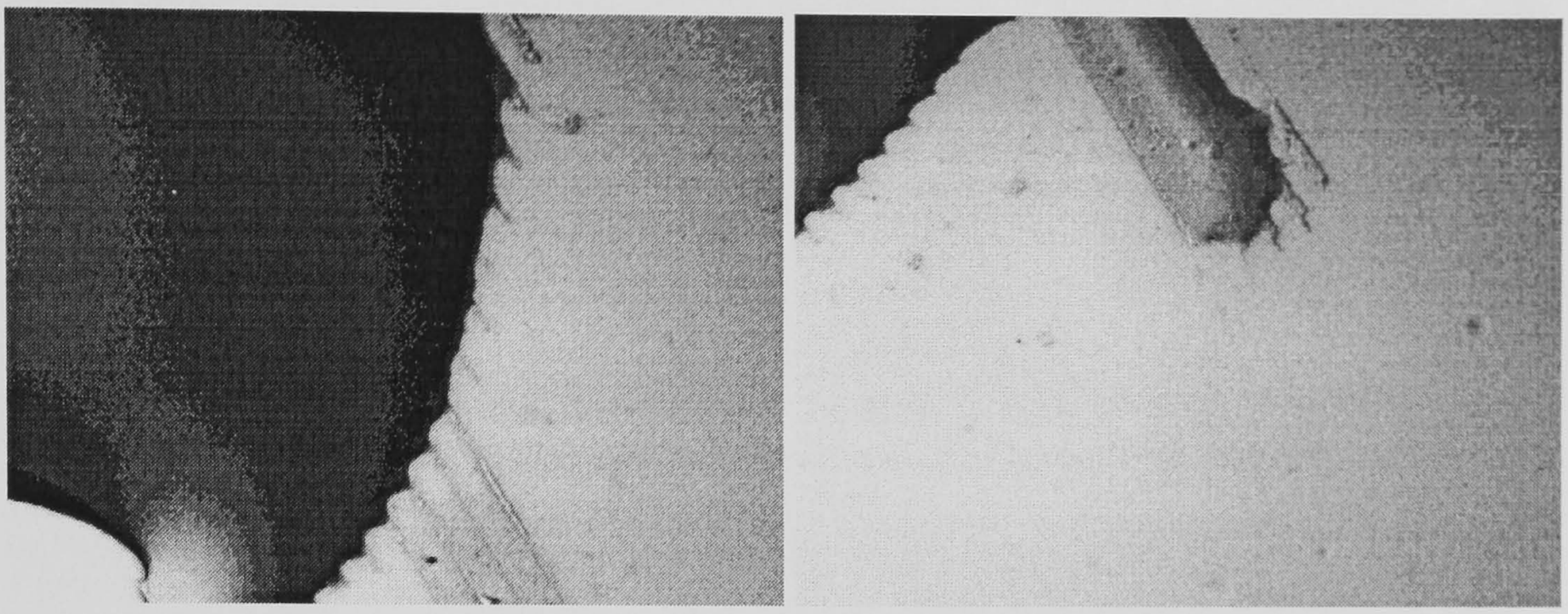

Figure 4.4. Optical images of a water droplet receding across a surface patterned with alternating 10 μm wide stripes of [OH] and the [CF3]

As the water recedes, fingers of the main droplet remain on hydrophilic stripes of the surface, whilst hydrophobic regions preferentially de-wet. After the main droplet has withdrawn, micro-droplets of water remain on the hydrophilic regions before evaporating.

A range of assembly experiments have been conducted to assess the relative importance of solvent de-wetting and hydrophobic interactions. Hydropillic [OH] functionalised gold nanowires in methanol were placed upon striped [OH] / [CF3] surfaces. Similarly, hydrophobic [CF3] functionalised gold nanowires in methanol were interacted with striped [OH] / [CH3] surfaces. Nanowires used for this work, and all further results presented in this chapter were formed in the Anodisc membranes. Electrodeposition was performed at an applied potential of 1 V_{pp} (15 Hz) for 30 minutes, from the hydrochloric electrolyte.

Droplets of functionalised nanowires in methanol were placed on to these patterned surfaces, and the solvent was allowed to evaporate. As the volume of solvent decreases, the droplet was observed to retreat from the patterned hydrophobic region, onto the surrounding planar hydrophilic area.

The nanowires functionalised with [OH] assembled selectively onto the hydrophilic regions of 1 μm striped [OH] / [CF3] surfaces, aligned with the striped pattern, Figure 4.5.

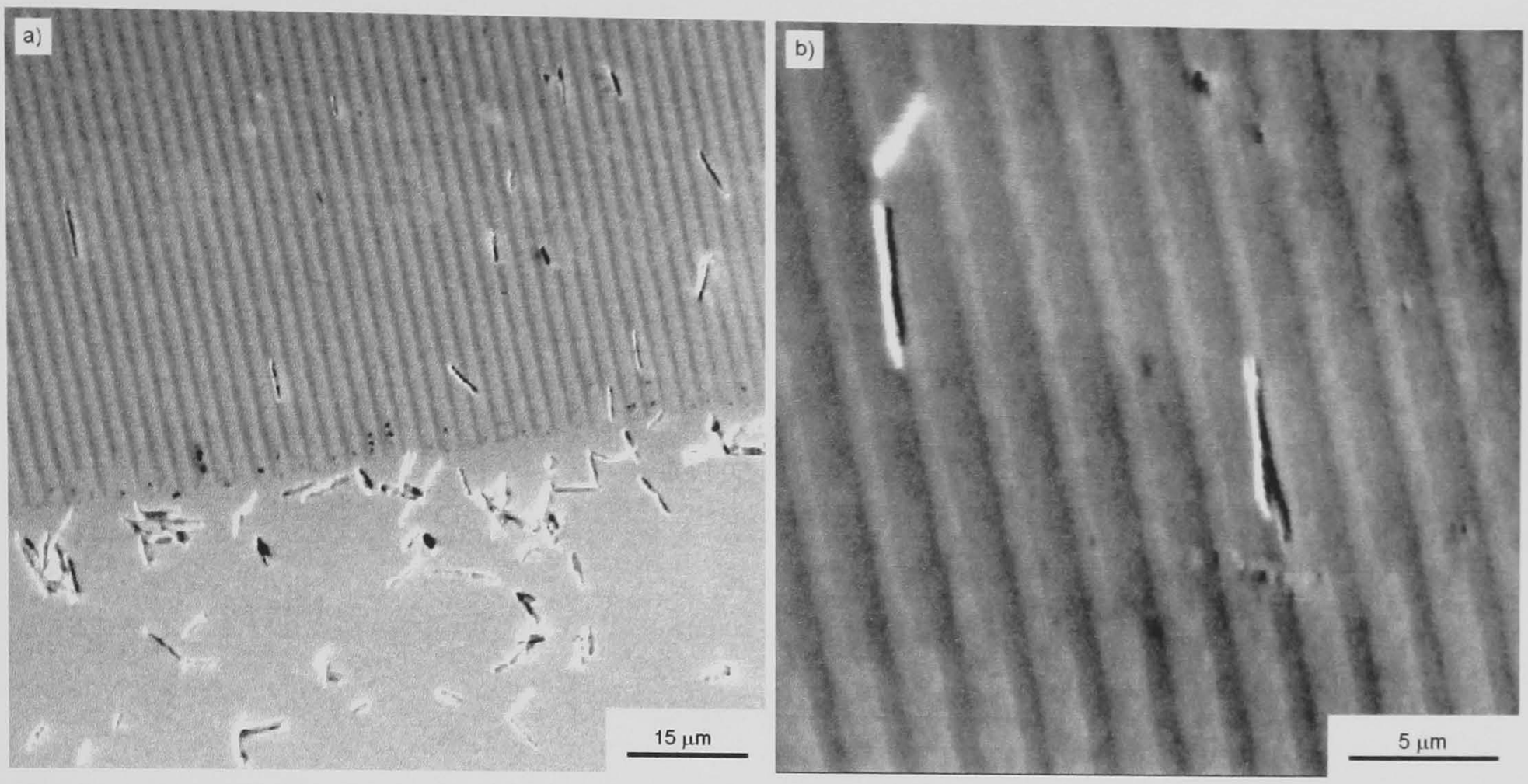

Figure 4.5. SEM images showing [OH] functionalized nanowires assembled onto 1 μm wide [OH] regions of a [OH] (light) / [CF3] (dark) patterned surface.

The different species of thiol in the patterned SAM could be differentiated by contrast in the scanning electron microscope. They were identified at the edge of the stamped region, the darker stripes are the [CF3] regions, and the lighter regions are [OH]. The assembly of nanowires onto striped hydrophilic / hydrophobic surfaces is driven by the surface-fluid interaction. The nanowire coverage on the patterned region of the surfaces is of lower density than those on the [OH] region surrounding the patterned region. The droplet containing the nanowires flowed from the more hydrophobic patterned region onto the surrounding hydrophilic [OH] regions. Nanowires suspended in the solution are thus drawn from the stamped region and precipitate in higher concentration at its edge as the solvent dries. Those nanowires already precipitated onto the surface are believed to be drawn onto the hydrophilic stripes, by the flow of solvent across the patterned region.

The assembly of nanowires onto 5 μm striped [CF3] / [OH] surfaces shows similar behaviour, Figure 4.6.

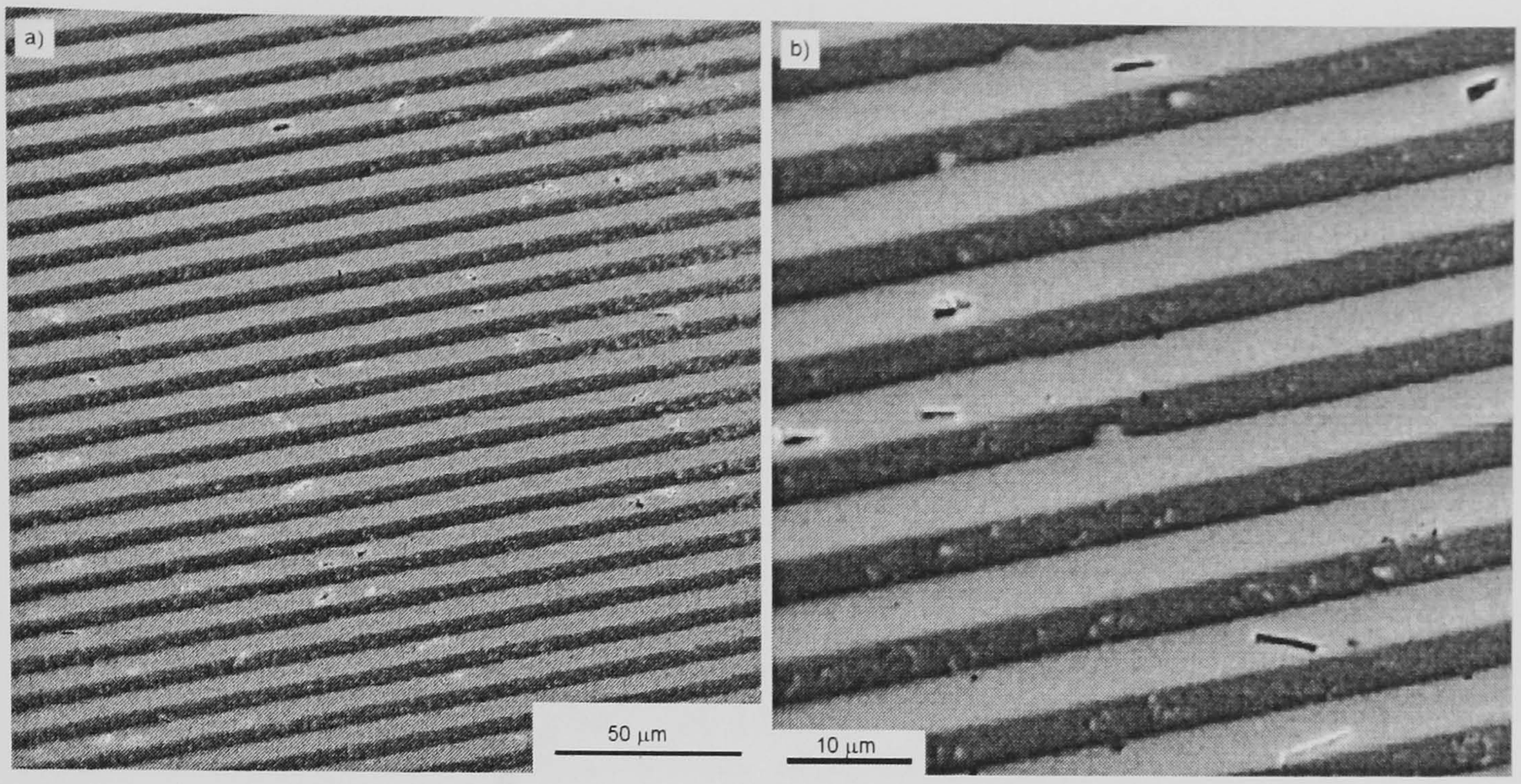

Figure 4.6. SEM images showing [OH] functionalized nanowires assembled onto 5 μm wide [OH] regions of a [OH] (light) / [CF3] (dark) patterned surface.

Nanowires predominantly align on a single stripe of the 1 μm patterned surfaces, although those wires that are not aligned are positioned such that each end lies upon a hydrophilic region, figure 4.5b. Nanowires assembled onto 5 μm striped surfaces, figure 4.6, are positioned onto a single hydrophilic stripe, although the larger stripes allow a greater range of orientations. The forces orienting the wire are believed to be associated with the scale and geometry of the droplet at the point of assembly. This would explain the greater angular distribution observed for nanowires assembled onto 5 μm striped surface.

The surface-fluid interaction, believed to be primarily determined by the wettability of the patterned surface, drives the assembly of hydrophilic nanowires onto hydrophilic surface regions. The contribution of the fluid-nanowire interaction, and its effect, is explored in the next experiment presented: Hydrophobic nanowires, functionalized with [CF3], were assembled onto [CH3] / [OH] patterned surfaces, Figure 4.7.

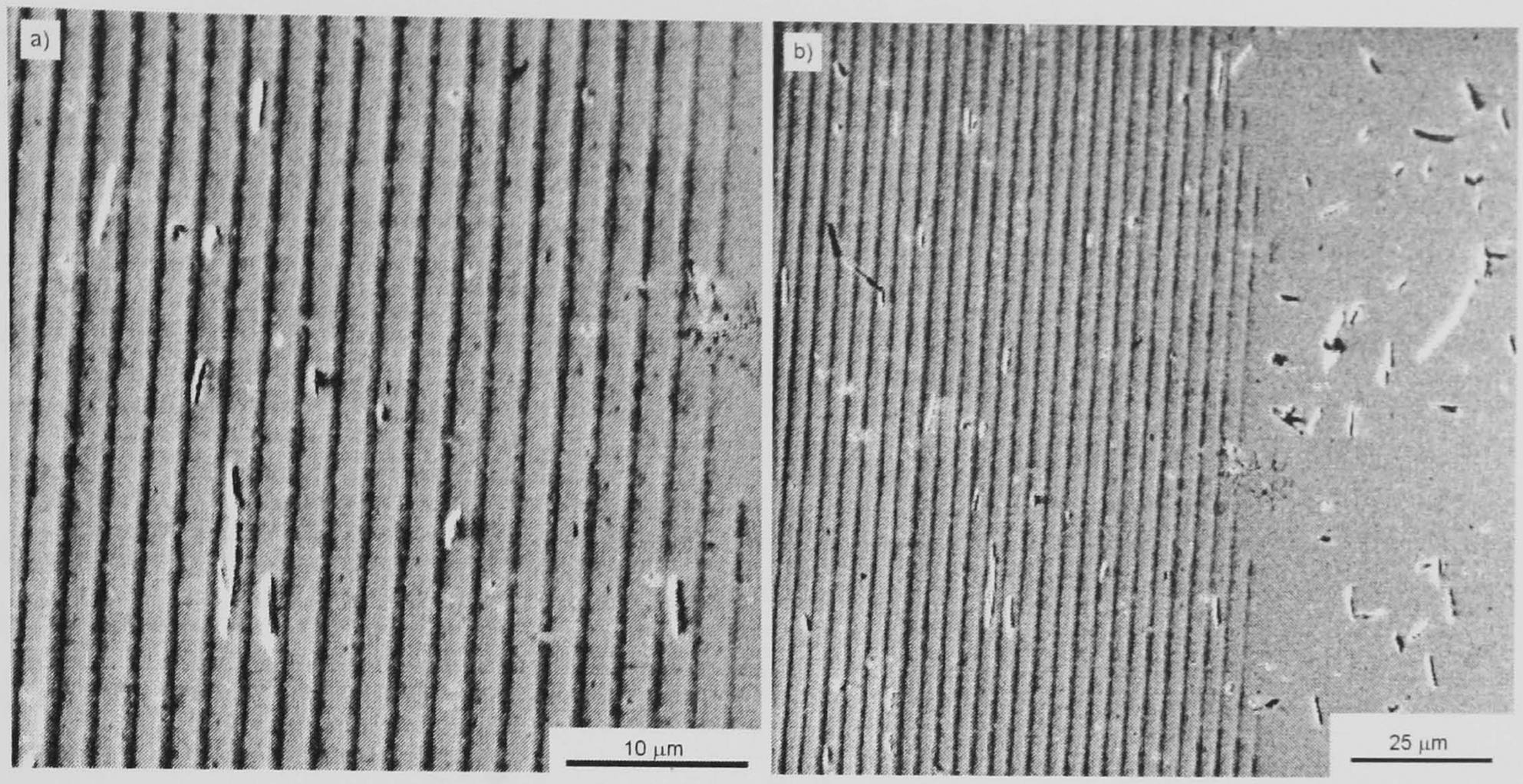

Figure 4.7. SEM images showing [CF3] functionalized nanowires assembled onto 1 μm wide [OH] terminated regions of a [OH] (light) / [CH3] (dark) patterned surface.

Nanowires functionalised with [CF3] were observed to assemble onto the lighter [OH] regions of the mercaptoundecanol / dodecanethiol patterned surface. Whereas previously the driving force for assembly was solely due to the surface wettability, assembly in figure 4.7 is complicated by the hydrophobic nanowires. Nanowires functionalised with the [CF3] moiety introduce hydrophobic interactions between the surface and the nanowire.[10-13] These additional interactions might be expected to assemble nanowires onto the hydrophobic regions, in the same way that nanowire aggregation is observed in the previous section. The interaction between nanowire and fluid is also changed, and the hydrophobic nature of the nanowires may be expected to favour placement of nanowires at the edge of the fluid regions. Despite these new factors, assembly forces drive these nanowires onto the hydrophilic regions of the surface. Consequently, surface wettability is believed to dominate the assembly process for these examples.

4.3: Nanowire Attachment by Hydrogen Bonding

Hydrogen bonding has been investigated as a binding mechanism to attach [COOH] functionalised nanowires to similarly functionalised regions of patterned surfaces. [COOH] functionalised nanowires have already been characterised in chapter 3. [COOH] / [OH] patterned surfaces with 10 μm wide stripes were fabricated by microcontact printing. [OH] was chosen for the background surfactant, due to its similar wettability, and because it should undergo less specific binding interactions with acid functionalised nanowires.

For comparison, SAMs of [COOH] and [OH] have been formed on planar gold substrates. The XPS spectra for both of these SAMs have already been analysed in chapter 3. Contact angle measurements of these planar SAMs are broadly similar. The [OH] surfaces are reported in the previous section to have advancing and receding contact angles of 40° and 20° respectively. This is in comparison to the [COOH] SAMs, that show advancing and receding contact angles of 24° and 16°, larger than similar previously reported measurements of 15° and 8°.[5, 14] To determine the concentration of the constituent thiols in [OH] / [COOH] patterned SAMs these surfaces were also characterized by XPS, Figure 4.8.

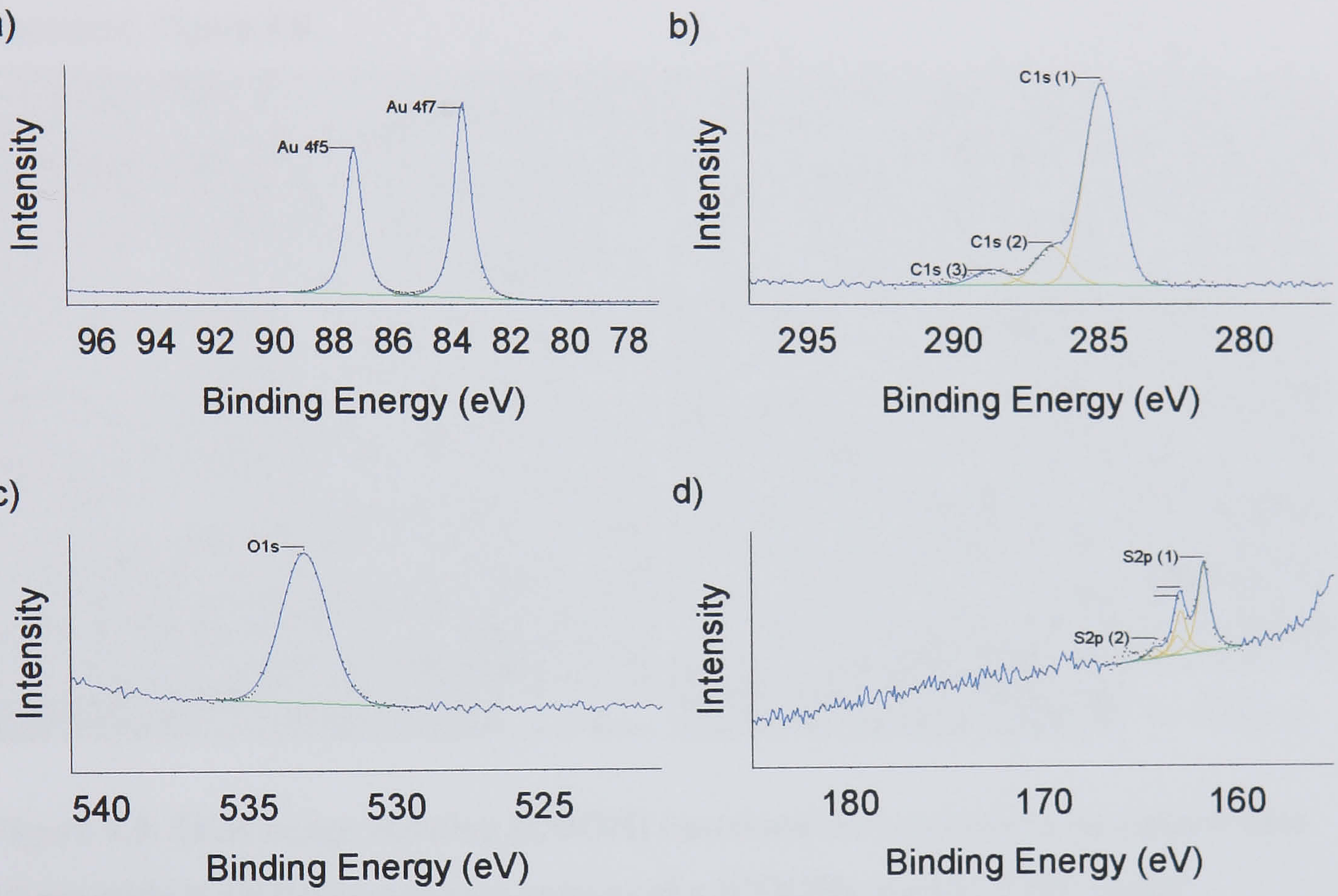

Figure 4.8. XPS spectra for a [COOH] / [OH] patterned SAM with 10 μm wide stripes on gold including high resolution scans of the a) gold 4f, b) carbon 1s, c) oxygen 1s and d) sulphur 2p regions

The XPS spectra show peaks which can be attributed to both of the constituent molecules, previously detected by the characterisation of planar SAMs. The only significant difference between those SAMs formed in solution, and this patterned SAM fabricated by microcontact printing, is the sulphur S2p (1) to gold ratio. The surface concentration of the bound thiolate, S2p (1), is 4.4 % of the total gold measured, equivalent to the value expected for a complete well-formed monolayer. In addition, the surface concentration of unbound thiol, S2p (2), is lower, and accounts for only 20 % of the total sulphur observed. The relative size of the peaks C1s (2) and C1s (3), associated with the COH of

mercapto-1-undecanol, and the [COOH] of mercaptoundecanoic acid respectively, yields the ratio of these two species comprising the patterned SAM. Following this methodology, the patterned SAM can be determined to be 70 % in [OH] and 30 % in [COOH].

Mercaptoundecanoic acid functionalised nanowires were allowed to precipitate, from methanol, onto these surfaces which were then washed with methanol, dried under nitrogen and imaged with scanning electron microscopy. Assembly due to hydrogen bonding between carboxylic acid terminated nanowires and surfaces causes selective placement, Figure 4.9.

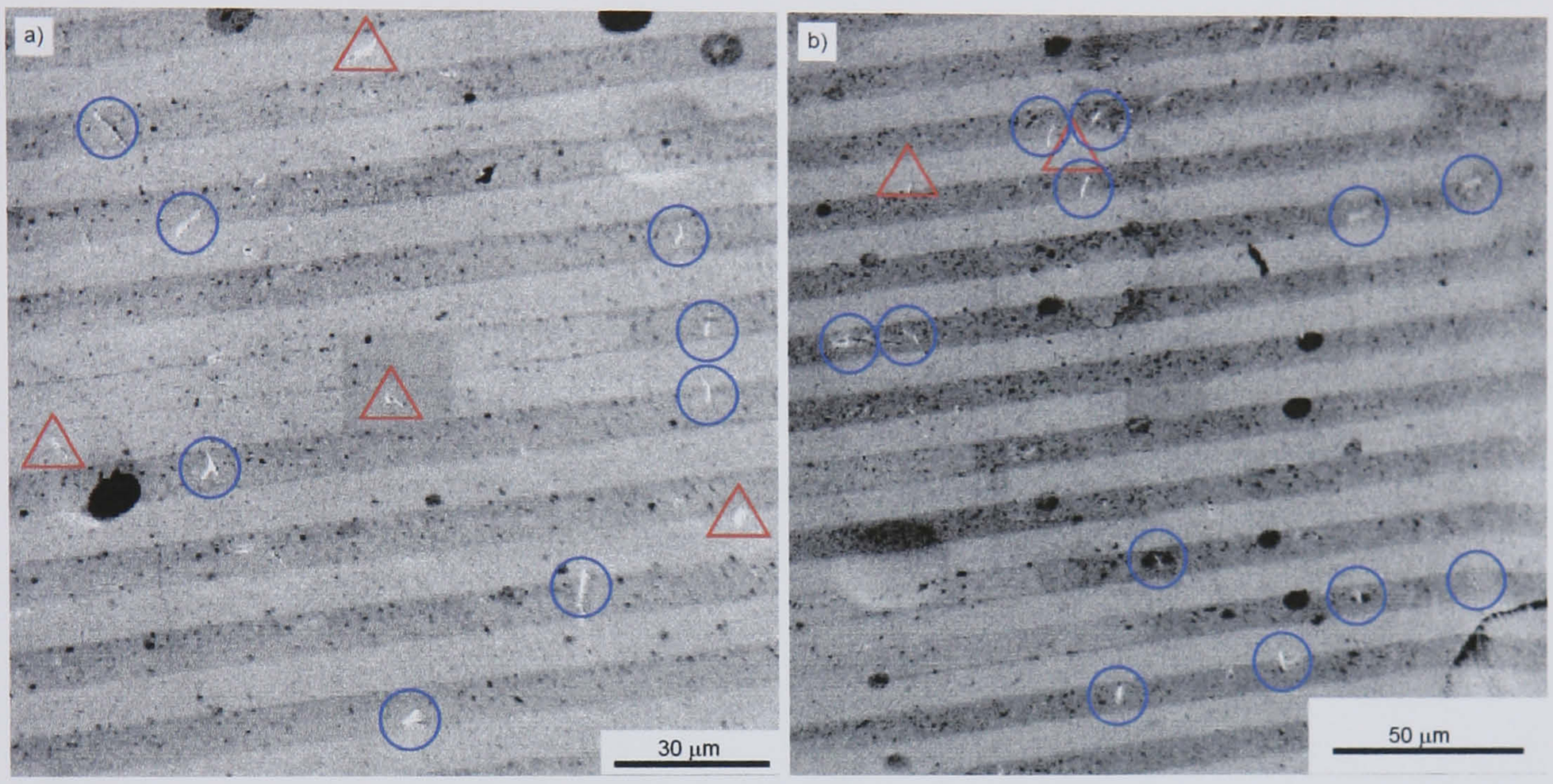

Figure 4.9. SEM image showing [COOH] functionalized nanowires assembled onto 10 µm wide [COOH] terminated regions of a [COOH] (dark) / [OH] (light) patterned surface attached by hydrogen bonding

Darker stripes are the [COOH] regions whilst lighter areas are [OH]. As can be seen, the width of the [COOH] and [OH] stripes on the surface are approximately equal. However, XPS has revealed that the chemical composition of these surfaces is typically 30 % [COOH] and 70 % [OH]. These surfaces were patterned by printing the [COOH] stripes, and backfilling with [OH], to reduce the incorporation of [COOH] in the [OH] regions. It is believed that [COOH] was printed at a relatively low density, and [OH] may have been incorporated into these regions during immersion in the second thiol solution. Whereas the contamination of [OH] in [COOH] regions is expected to be high, the incorporation of [COOH] in [OH] stripes is believed to be low and should not significantly increase binding interactions in these areas. The wires assembled by hydrogen bonding onto the [COOH] regions in Figure 4.9 are circled, whilst those on the [OH] regions are

highlighted with a triangle. Nanowires assembled by hydrogen bonding constitute 77 % of those sampled.

4.4: Nanowire Attachment by Carboxylate Salt Formation

The formation of a carboxylate salt between carboxylic acid terminal groups has also been investigated as a mechanism to bind mercaptoundecanoic acid nanowires and surfaces. [COOH] / [OH] patterned surfaces with 10 μm wide stripes were fabricated by microcontact printing, identical to surfaces used in the previous section. The [COOH] regions of the patterned surface were functionalised with cadmium by immersion into a 1 mM aqueous solution of $CdCl_2$. The salt formation was observed by X-ray photoelectron spectroscopy, Figure 4.10.

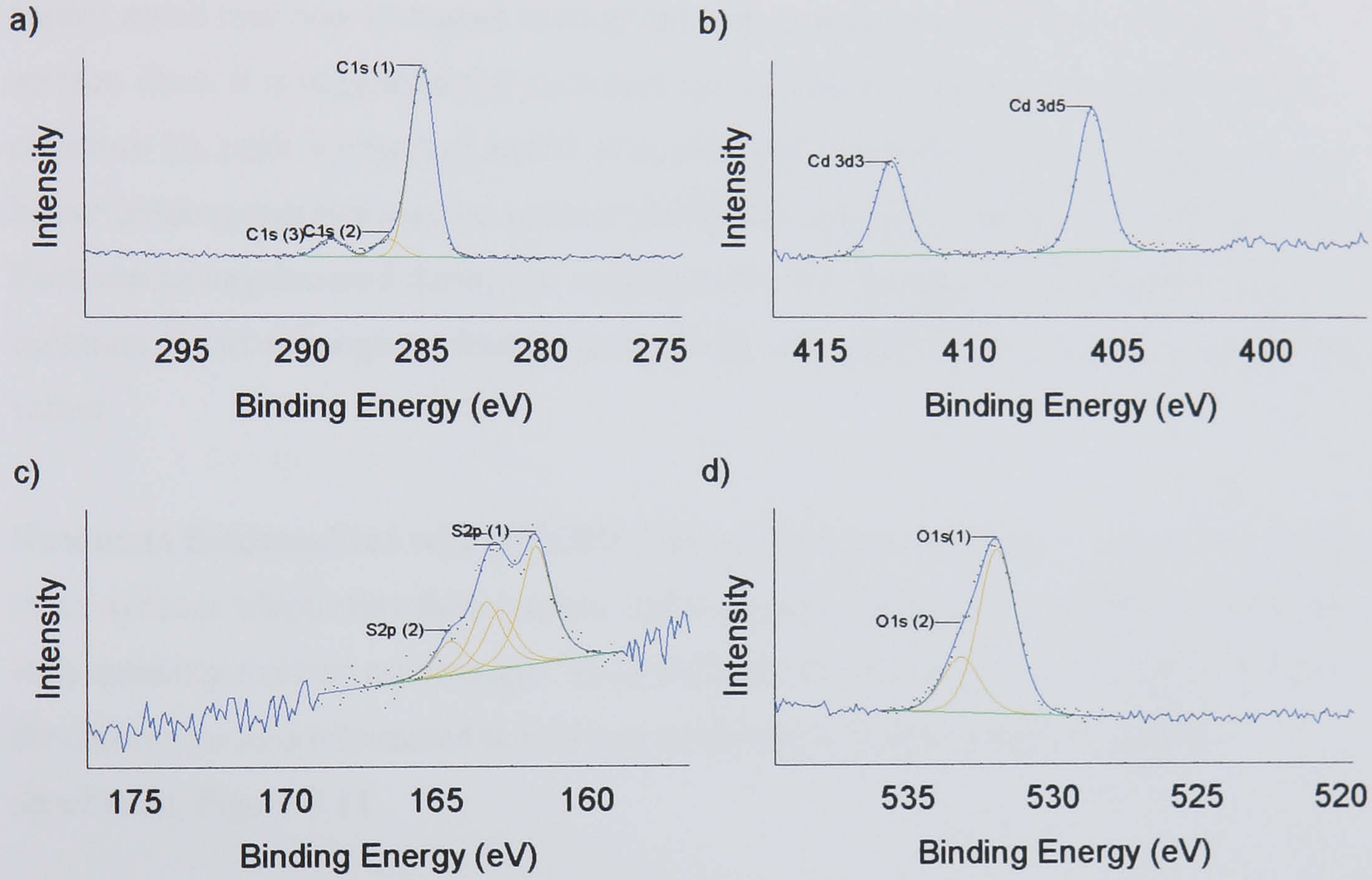

Figure 4.10. XPS characterisation of a [COOH] SAM after exposure to Cd^{2+} ions in aqueous solution, showing high resolution a) carbon 1s, b) cadmium 3d, c) sulphur 2p, and d) oxygen 1s spectra

The carboxylic acid converts from [COOH] to COO^- upon salt formation[15], evident in the C1s spectra. Peak 3 of the carbon spectrum is now observed to be positioned at 288.4eV, shifted 0.9 eV lower than for the acid, and is now associated with the carboxalate.[16] No remaining intensity can be seen at higher binding energies, indicating that all the free acids have been converted. However, the presence of peak 2 at 286.4eV, commonly associated with a COH moiety, is not understood. The O1s spectrum characteristic of

carboxylic acid has a doublet with peaks at 532.6 and 533.8, figure 3.32d. After exposure to cadmium in solution the oxygen peak still requires a doublet to be fit adequately, with peaks at 532.4 eV and 533.8 eV. The ratio of these two peaks changes from O1s (1) / (2) from 1.4 for the acid to 2.9 after exposure to Cadmium. Compared to figure 3.33e the sulphur spectrum has a similar structure and the gold / sulphur ratio is maintained. This suggests exposure to the cadmium salt solution does not degrade the monolayer. The presence of cadmium in the results, figure 4.10b, is thought to be bound to as a metal-carboxylate salt at the terminal group, as has been previously demonstrated.[17] This is supported by the ratio of total sulphur S2p (1+2) to cadmium present on the surface equal to 1.2. Previous studies of the attachment of copper ions to carboxylic acid terminated monolayers have shown a Cu : S2p a ratio of ~2.5.[14, 15] These studies concluded that the copper metal ions may be bound to neighbouring carboxylate pairs at the monolayer surface. Here, it is suggested that cadmium ions are bound to single carboxylates. The cadmium $3d_5$ peak is observed at 405.9eV, although it was expected at 405.1eV. The higher binding energies may be associated with the ionisation state of the cadmium ions. Photoelectrons generated during the measurement will change the ionisation state of cadmium,[14] and although no doublet is observed, this may explain the shift from expected values.

Nanowires functionalised with [COOH] were allowed to precipitate, from methanol, onto these surfaces which were then washed with methanol, dried under nitrogen and imaged with scanning electron microscopy. The formation of a carboxylate salt bridge between the carboxylic acid terminated nanowires and surfaces caused selective nanowire attachment, Figure 4.11.

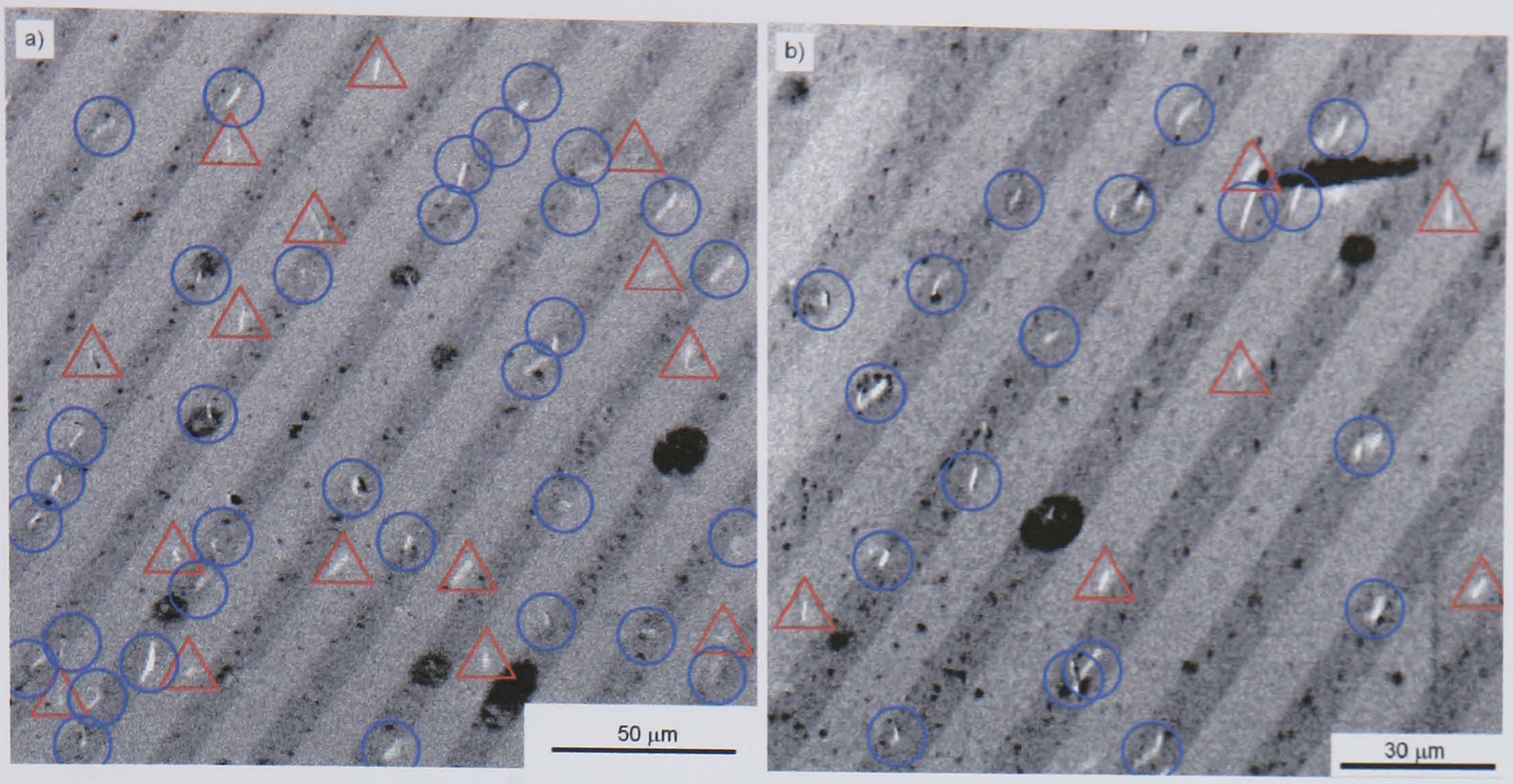

Figure 4.11. SEM image showing [COOH] functionalized nanowires assembled onto 10 μm wide [COOH] terminated regions of a [COOH] (dark) / [OH] (light) patterned surface attached by a cadmium ion linker.

Darker stripes are [COOH] regions whilst lighter areas are [OH]. Nanowires positioned on the [COOH] regions in figure 4.11 are circled, whilst those on the [OH] regions are highlighted with a triangle. Nanowires assembled onto the [COOH] regions constitute 71 % of those sampled.

The chemical attachment of nanowires to reactive surfaces is a simple surface-nanowire binding process, without any long-range assembly forces. Nanowires precipitate at random onto the patterned surface and unbound or weakly bound wires are removed during the washing process. Those wires that remain attached to the reactive regions are said to be assembled. A stronger binding process would be expected to improve the ratio of assembled nanowires. The results presented in figures 4.11 and 4.9 show a broadly similar percentage of assembled nanowires, and the number of sampled nanowires is not great enough determine a statistically meaningful determination of the relative interaction strength.

Nanowires appear aligned parallel to the pattern direction for the carboxylic salt binding experiment, Figure 4.11, whereas those observed on Figure 4.9Figure 4.10 show no preferential orientation. Alignment may arise after adsorption, for example during the washing or drying procedures, where the behaviour of the clean solvent on the surface may introduce order to precipitated nanowires. From the results presented in section 4.2 it is speculated that nanowires are oriented perpendicular to the edge of a receding droplet.

After formation of the cadmium carboxylate salt the wettability of the surface may be expected to change, although this has not been measured. If patterned wettability is introduced this could cause a similar de-wetting behaviour to the hydrophilic / hydrophobic patterned surface shown in Figure 4.4. This would act to align nanowires parallel with the orientation of the striped patterned surface.

4.5: Nanowire Assembly with a Streptavidin / Biotin Linker

Stronger binding interactions between nanowires and surfaces are expected to improve nanowire assembly. Consequentially, the strongest non-covalent binding mechanism, that of the biotin-streptavidin bond, has been investigated as a method to attach bintinylated nanowires to complementary regions of patterned surfaces. These interactions have a free energy of binding which is comparable to that of a covalent bond[9], see chapter 2. SAMS of biotin and the mixed biotin / [OH] thiol on planar gold substrates have already been characterised in chapter 3. The binding of the protein streptavidin to the surface of these mixed monolayers was undertaken in a phosphate buffer, pH 7.4, with a streptavidin concentration of 30 mg ml^{-1}. One hour was allowed for binding to complete. The substances were then removed, washed with milli-Q water and dried in a stream of N_2. Previous studies have observed streptavidin attachment by an increase in surface roughness measured with an AFM.[9] Here the attachment of streptavidin is observed by XPS characterisation, figure 4.12.

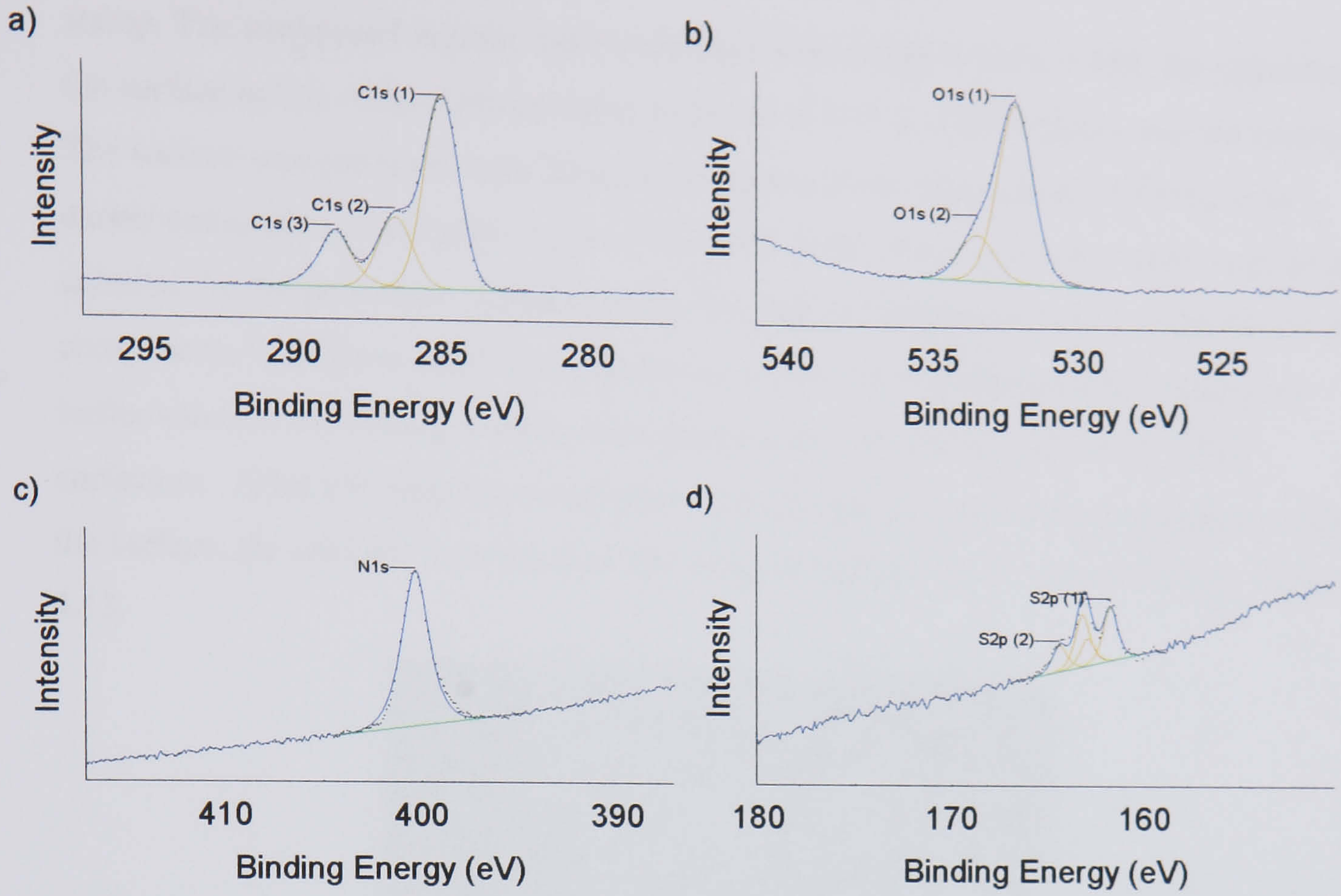

Figure 4.12. XPS spectra for a mixed monolayer of [OH] and biotin on gold activated with streptavidin, including high resolution scans of the a) carbon 1s, b) oxygen 1s, c) nitrogen 1s and d) sulphur 2p regions.

Due to the complexity of the protein, the XPS data for streptavidin has not been modelled with specific moieties in mind. Simply, the presence of streptavidin is noted by the increase of certain molecular combinations in the XPS spectra. The gold / sulphur ratio was consistent with the mixed SAM before exposure to streptavidin, and the total sulphur S2p (1+2) is used as a benchmark against which other species can be compared. The carbon 1s spectrum was fitted with three peaks, their positions show good agreement with figure 3.36a, but the total carbon component C1s (1+2+3) / S2p (1+2) increased from 0.7 to 1. The greater carbon signal was predominantly due to the increase in peaks 2 and 3. The total oxygen O1s (1+2) / S2p (1+2) increased from 0.1 to 0.2, and contains has a shoulder fitted with a new peak at 533.5 eV. The most dramatic change was observed in the nitrogen 1s peak, where the total area ratio for N1s / S2p (1+2) increased from 0.3 to 2.3.

4.5.1 Nanowire attachment to surfaces with a streptavidin linker

Biotin functionalised nanowires were allowed to interact with streptavidin functionalised surfaces. Patterned biotin surfaces were generated by microcontact printing on gold substrates. The mixed biotin / [OH] thiol was stamped first, with a PDMS chequerboard

stamp. The unexposed regions were backfilled with a 100 % [OH] SAM. By patterning the surface in this order contamination of biotin in 100 % [OH] regions was minimised. The surface was patterned with 30 micron squares of the mixed biotin / [OH], with a darker colouration, and lighter squares of 100 % [OH]. After exposure to the streptavidin solution, by the procedure outlined above, the contrast difference between the two surface components was increased. These patterned surfaces were transferred to a phosphate buffer solution containing nanowires functionalised with the mixed biotin / [OH] surfactant. After allowing the nanowires to precipitate from solution, and interact with the surface, the samples were cleaned and imaged with the low-resolution SEM, Figure 4.13.

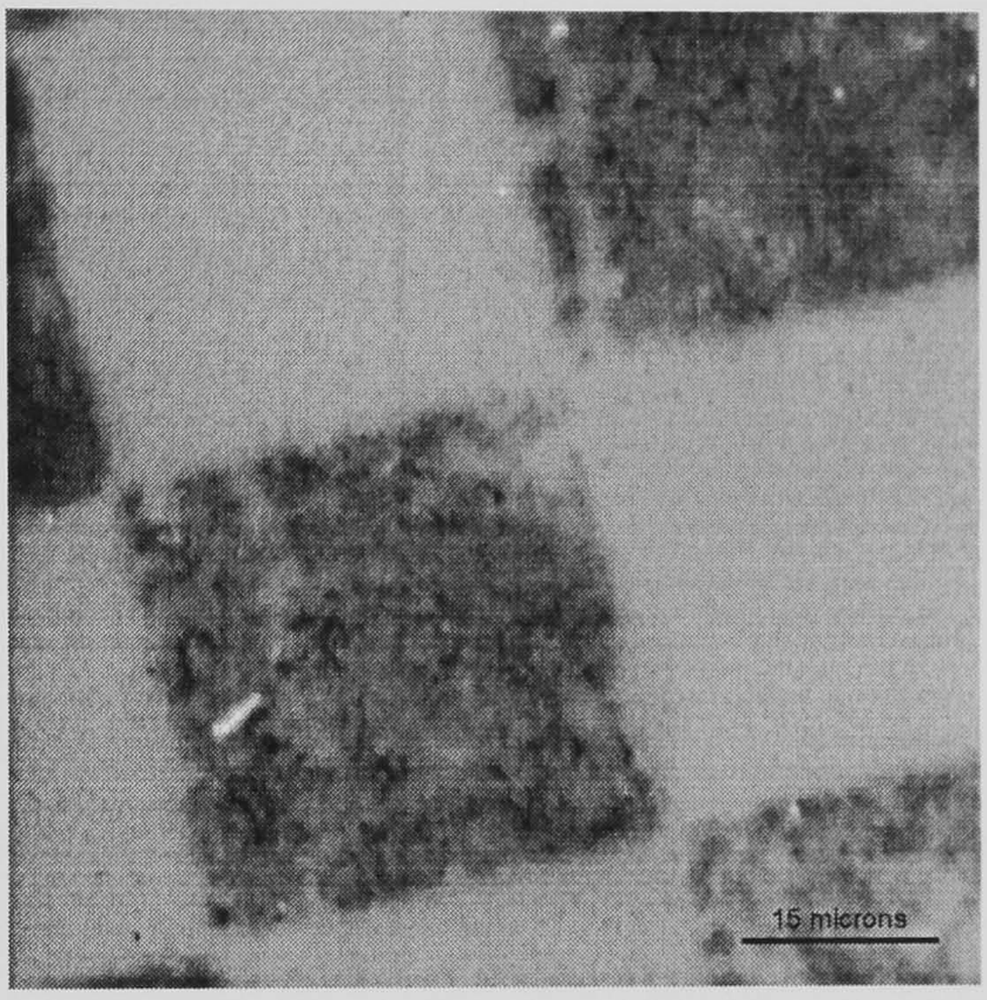

Figure 4.13. SEM of a biotin-streptavidin / [OH] patterned surface after assembly of biotin functionalised nanowires.

The density of nanowires observed across the surface was very low, and nanowires were not necessarily positioned on the darker biotin binding regions. Figure 4.13 shows an image of a single nanowire, positioned on one of the biotin-streptavidin regions of the surface. The streptavidin-biotin binding process was expected to bind biotinylated nanowires to streptavidin functionalised surface regions. The washing process was intended to remove unbound nanowires on the 100 % [OH] regions. A variety of cleaning procedures were used in an attempt to observe nanowire assembly, but nanowire density remained low and conclusive evidence for biotin-streptavidin binding was not observed. The explanation for the lack of bound nanowires is not fully understood. However, a possible flaw of the procedure outline above is discussed at the end of the following section, for reasons that will become apparent.

4.5.2 Nanowire aggregation in solution caused by biotin-streptavidin bonds

Nanowires were functionalised with the mixed biotin / [OH] surfactant in a variety of ways. In addition to the complete coverage produced by the exposure of nanowires to the biotin / [OH] solution, chapter 3, nanowires have also been exposed to the mixed surfactant whilst embedded in the template host. This has allowed the biotin functionality to be added to one or both ends of the nanowire, by the exposure of one or both sides of filled templates. The sides of the nanowire were believed to be protected by the template host. Pilot experiments using XPS characterisation of SAMs on planar gold substrates have shown that the mixed biotin / [OH] surfaces are stable during the sodium hydroxide etch procedure, although any streptavidin is removed. However, these SAMs were considerably degraded by exposure to 70 wt % nitric acid, used to remove the silver electrode. Consequently, the silver electrode was removed from filled templates prior to exposure of the nanowires within. The electrochemical cell, figure 2.8, allowed exposure of only one side of the template (one end of the nanowires) to the surfactant solution. The membranes were etched in 1 M NaOH to release the nanowires, and they were transferred to milli-Q water by the centrifuge procedure. After cleaning, nanowires were transferred to the phosphate buffer solution, and then exposed to streptavidin. Streptavidin was added at 30 mg ml^{-1} concentrations, and solution was left overnight. Nanowires were again transferred back to clean phosphate buffer solution by the centrifuging procedure. Aggregation of nanowires in solution was not observed for either the nanowires with full surfactant coverage, or those with one or both ends coated with surfactant. Neither was any aggregation observed when these samples were dropcast onto silicon surfaces. Aggregation due to biotin-streptavidin binding interactions may not be expected, since all available biotin sites may already have bound streptavidin, blocking the binding process. To test these binding interactions, nanowire solutions functionalised with streptavidin were mixed with identical nanowires that had not been exposed to streptavidin. These nanowires were obtained by splitting the nanowire solutions prior to streptavidin exposure. After reintroduction, the concentration of nanowires with and without bound streptavidin should be approximately 1:1. No aggregation in solution was observed, and similarly, no binding interactions were observed for these mixed nanowire solutions when dropcast on silicon surfaces.

Despite the failure of experiments designed to bind nanowires to surfaces, discussed in section 4.5.1, nanowires with a full coverage of the mixed biotin surfactant were observed

to aggregate in solution after the patterned substrate was withdrawn. Nanowire solutions appeared dispersed immediately after removing the patterned substrate, but aggregation occurred when the sample was left undisturbed for several days. Such was the strength of the interaction that solution particulates aggregated into a single mass. To reproduce these results, nanowires with one end, both ends, and complete coverage of the mixed biotin surfactant, were exposed to streptavidin activated patterned biotin surfaces. After removal of the substrate, nanowires in each solution were observed to aggregate. These solutions were sonicated for 20 s each, to partially disperse the nanowires, and dropcast onto silicon substrates for observation with the low resolution SEM. The results for nanowires with a single end, both ends, and their complete surface exposed to the mixed biotin surfactant are present in figures 4.14, 4.15 and 4.16 respectively. For comparison, nanowires dropcast from the mixed nanowire solutions are also shown in the same figures.

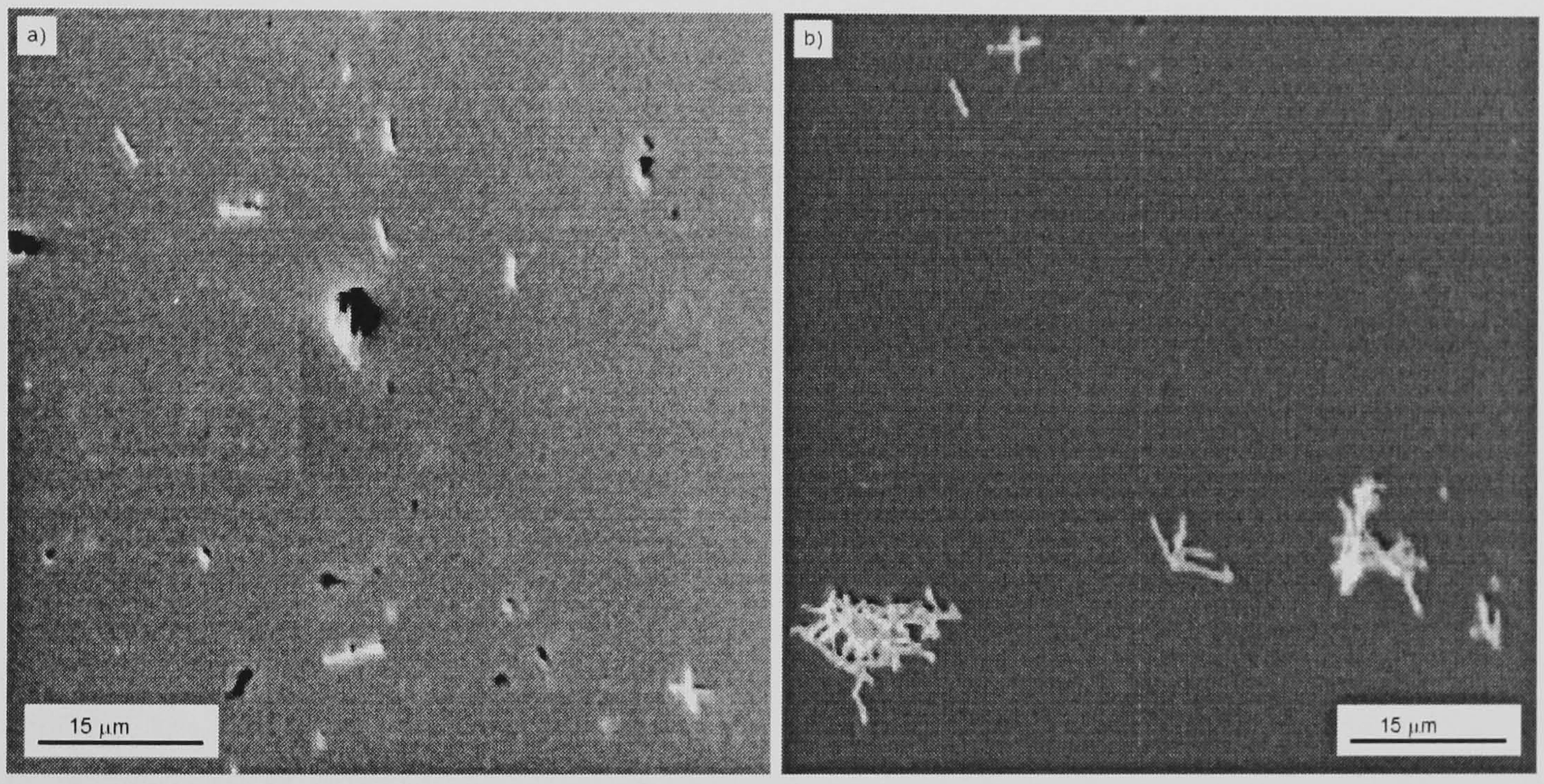

Figure 4.14. Nanowires with biotin / [OH] thiol at a single end dropcast on silicon; a) after mixing streptavidin functionalised wires and bare biotin / [OH] wires in solution, b) after being exposed to a patterned biotin surface functionalised with streptavidin

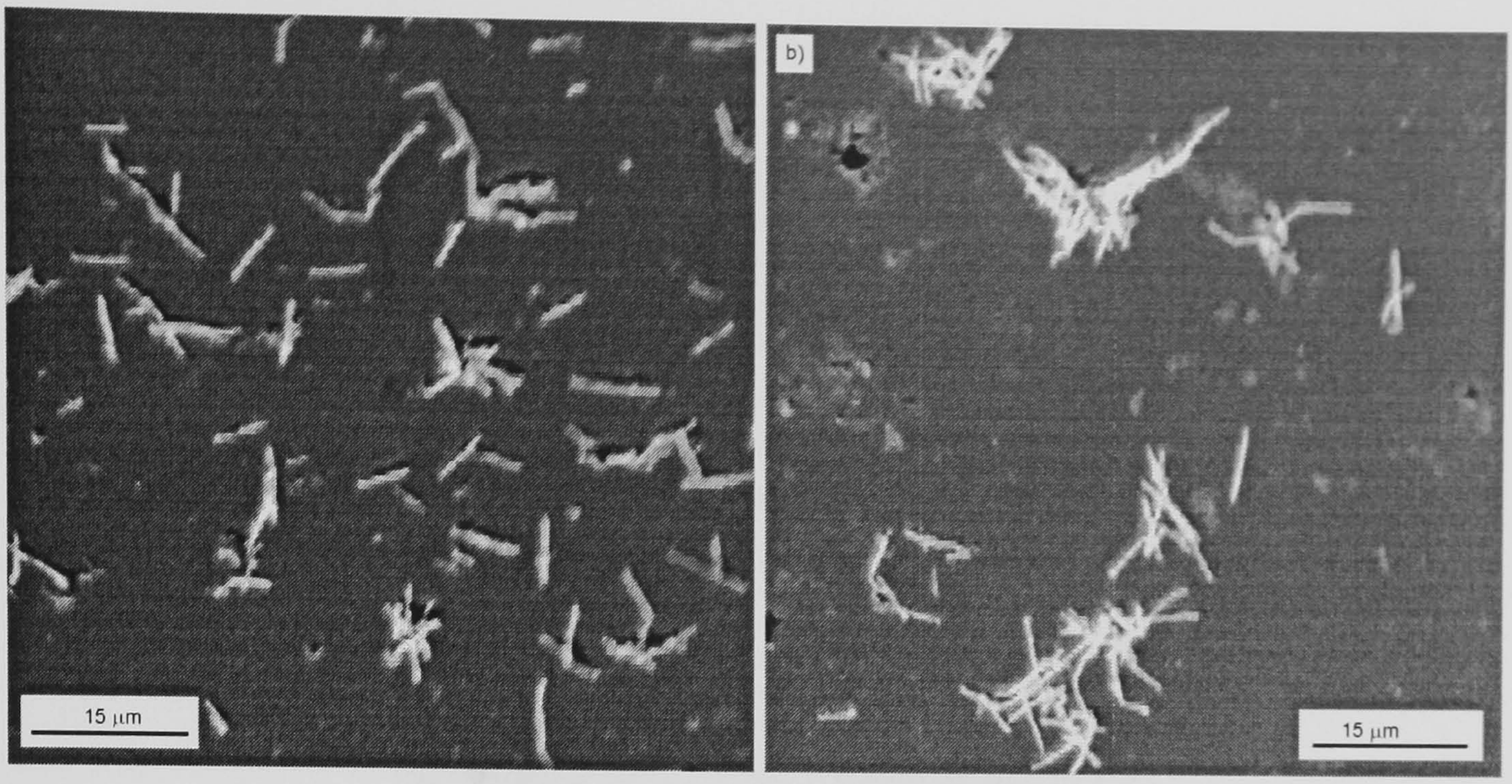

Figure 4.15. Nanowires with biotin / [OH] thiol at both ends dropcast on silicon; a) after mixing streptavidin functionalised wires and bare biotin / [OH] wires in solution, b) after being exposed to a patterned biotin surface functionalised with streptavidin

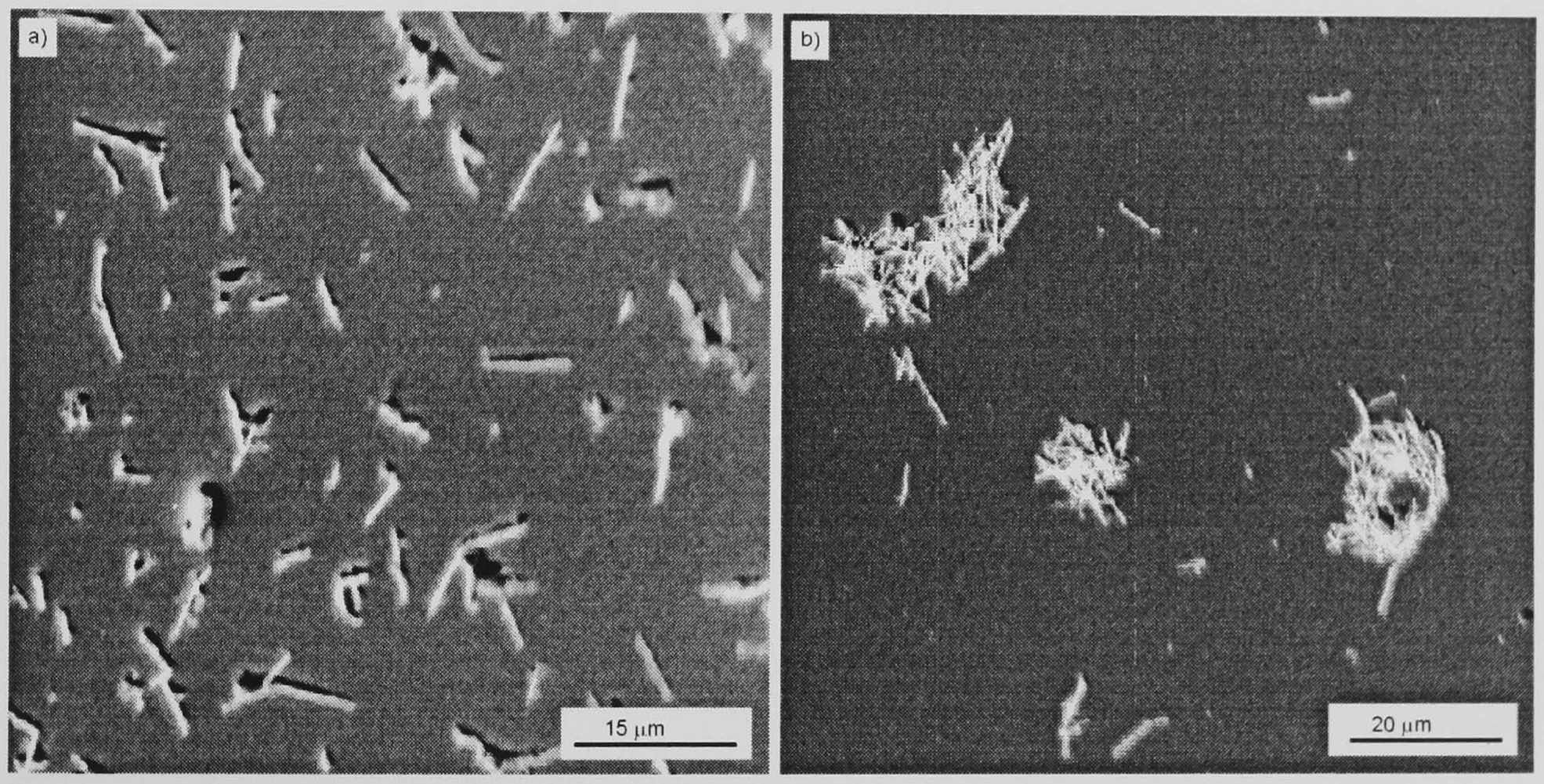

Figure 4.16. Nanowires with complete coverage of the mixed biotin / [OH] thiol; a) a) after mixing streptavidin functionalised wires and bare biotin / [OH] wires in solution, b) after being exposed to a patterned biotin surface functionalised with streptavidin

As previously mentioned, none of the nanowire solutions created by mixing streptavidin activated nanowires with biotinylated nanowires without streptavidin, show any aggregation. In comparison, aggregation is observed for all the nanowires exposed to streptavidin activated surfaces. Furthermore, the size and density of these aggregates increase with increasing surfactant coverage, suggesting that the procedure for selectively

exposing different areas of the nanowires has been successful. Figures 4.14b and 4.15b demonstrate specific binding at the ends of nanowires, with either one or both ends of the nanowires connected in the corresponding samples, as would be expected. With further sonication, nanowire aggregates in solution continued to break down. Figure 4.17 shows the doubled-ended nanowire sample dropcast on silicon after sonication for 1 minute.

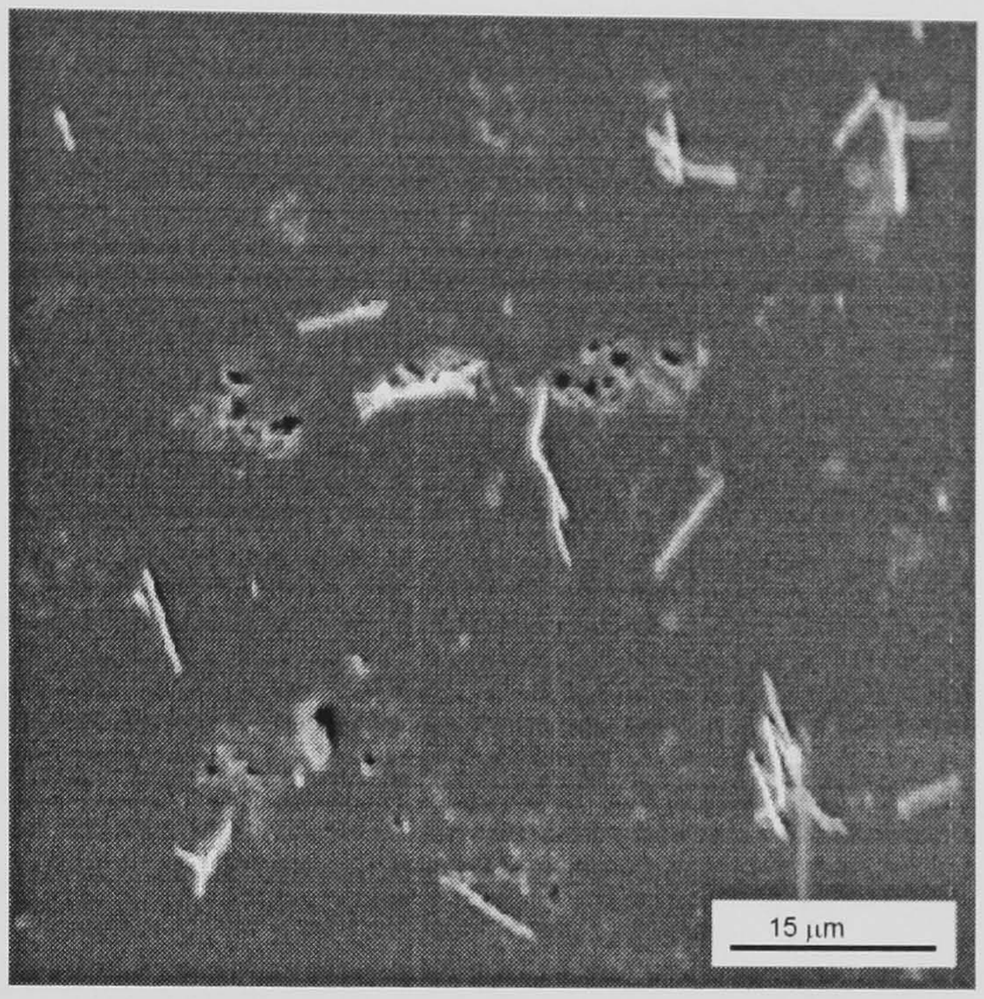

Figure 4.17. Nanowires with both ends functionalised with the mixed biotin surfactant, and exposed to patterned streptavidin activated surfaces, after sonication for 1 minute.

The large aggregations of figure 4.15b are no longer observed, instead, small collections of nanowires are seen, typically in chain-like formations, presumably due to the functionality at the ends of the nanowires. After leaving the nanowire solutions undisturbed for several days, the large-scale aggregations returned.

These results suggest that nanowires exposed to streptavidin in solution are saturated with streptavidin, blocking binding interactions between wires. The attachment of free streptavidin to a biotin site is kinetically favourable to the binding of a two nanowires with a single streptavidin linker. Similarly, solutions of these nanowires mixed with active biotin nanowires do not demonstrate binding interactions, presumably due to excess streptavidin remaining in solution. However, after exposure of biotin nanowires to streptavidin activated surfaces, it appears as though a small quantity of streptavidin is leached from the surface and this causes aggregation of nanowires, after precipitation from solution.

The desorption of streptavidin from biotin-streptavidin surfaces has previously been reported in the presence of solutions containing free biotin.[18] For mixed biotin / alkanethiol SAMs complete desorption of streptavidin molecules was achieved, and faster desorption rates were observed for SAMs with lower surface concentration of biotin.[18] Additionally, the attachment of streptavidin to biotin surfaces does not necessarily form a streptavidin monolayer. Streptavidin absorption is not uniform, and aggregates of streptavidin molecules have been observed on biotin surfaces that are between two and eight protein molecules thick.[19] Excess streptavidin on our patterned biotin surfaces, and leaching of bound streptavidin, provides a mechanism for the transferral of streptavidin from the patterned surfaces to nanowires in solution.

Despite repeated attempts to clean nanowires exposed to streptavidin in solution (to remove excess streptavidin) no aggregation was observed when these were mixed with biotin functionalised nanowires. The leaching of streptavidin from surfaces is the only way that low concentrations of streptavidin in the nanowire solutions have been achieved. These low concentrations are required to prevent excess streptavidin blocking all active biotin sites, and breakdown of attachments between nanowires by desorpition of the biotin-streptavidin link with kinetically favourable streptavidin, or biotin, present in solution. These binding interactions could be broken by sonication of the nanowire solution, but reformed after nanowires had once again precipitated.

4.6: Nanowire Assembly Directed by Electrostatic Surfactant Interactions

Finally, the capability of electrostatic interactions between nanowires and surfaces to drive assembly has been investigated. Electrostatic forces are derived from the use of surfactants on both the nanowires and patterned surfaces that can be protonated or deprotonated by changing the pH of the solvent. The surfactants used were [COOH], aminothiophenol [ATP], and $NH_2(CH_2)_2(OCH_2CH_2)_8NHC{=}OCH_2CH_2SH$ [NH_2]. SAMs of these surfactants have been formed on planar gold substrates, and characterised with XPS. The results for mercaptoundecanoic acid have already been characterised in the previous chapter. The results for [ATP] and [NH2] are shown in figures 4.18 and 4.19, respectively.

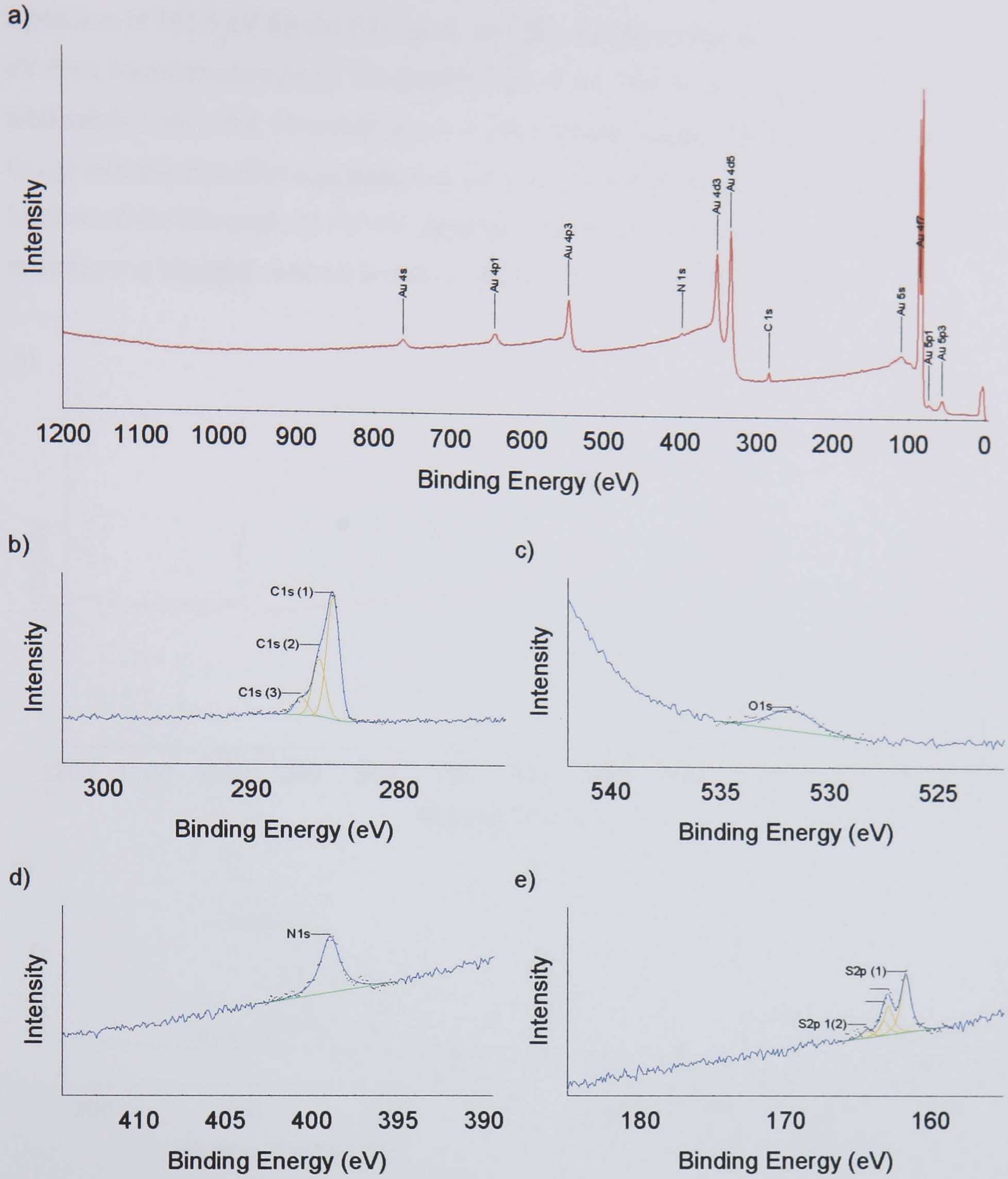

Figure 4.18. XPS spectra for a SAM of [ATP] on gold including a) survey spectra, and high resolution scans of the b) carbon 1s, c) oxygen 1s, d) nitrogen 1s and e) sulphur 2p regions

The XPS spectra reveal all the expected constituents for a monolayer of [ATP] ($NH_2C_6H_4SH$). The carbon 1s spectrum shows 3 peaks, (1), (2) and (3), which have binding energies of 284.5 eV, 285.5 eV and 286.7 eV respectively. This spectrum is consistent with results presented by Lukkari[20], who assigns peak 1 to the aromatic C-C and C_{arom}-S carbon species, peak 2 to C_{arom}-N, and C_{arom}-SO_3. Previous studies of aminothiophenol monolayers have shown a considerable sulfonate species in the sulphur spectrum.[20, 21] The sulphur spectrum shown here displays two doublets, where S2p (1) has

a position of 161.5 eV for the $S2p_3$ peak, and S2p (2) has a binding energy raised by 1.6 eV from bound thiolate peak. The contribution of the S2p (2) doublet is only 20 % of the total sulphur observed. However, figure 4.18e does not display a sulfonate peak, and this brings into question their assignment of the C1s (2) peak with a C_{arom}-SO_3 moiety. The location of the N1s peak, at 402 eV, suggests that the nitrogen terminal group of the monolayer is charged. A small oxygen peak, at 532.6 eV, is also observed.

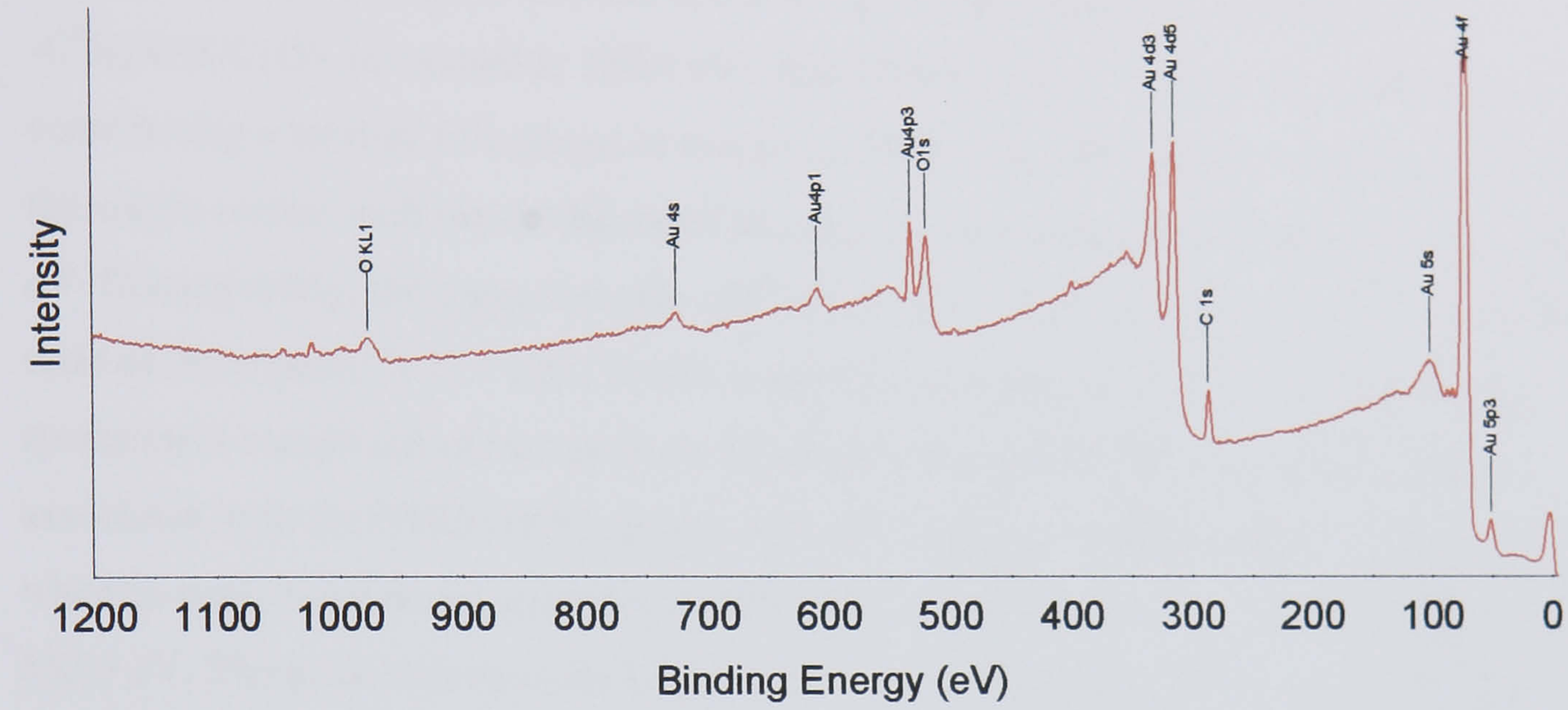

Figure 4.19. XPS spectra for a SAM of [NH2] on gold including a) survey spectra, and high resolution scans of the b) carbon 1s, c) oxygen 1s, d) nitrogen 1s and e) sulphur 2p regions.

The XPS spectra reveal all the expected constituents of the [NH2] monolayer $NH_2(CH_2)_2(OCH_2CH_2)_8NHC(O)CH_2CH_2SH$. The structure of the thiol molecule is exposed by observation of the carbon 1s, oxygen 1s and nitrogen 1s spectra. The familiar saturated hydrocarbon peak (1) at 284.7 eV, is associated with the two hydrocarbons at the thiolated end of the molecule. The proximity of the C(O) bond increases the binding energy of one of these hydrocarbons by ~0.4 eV. There are two additional peaks composed entirely of more complex carbon combinations. Peak 2, at 286.7 eV, can be associated with the starred carbons of the $-C^*H_2OC^*H_2-$ (expected at 286.3 eV), $-C^*H_2NHCC(O)-$ (expected at 286.0 eV), and $-NH_2C^*H_2CH_2-$ (expected at 285.9 eV), contributing a total of 18 carbons to this peak. Peak 3, at 288.7 eV can be associated with the single carbon with the double bond to oxygen, with an expected binding energy 288.0 eV. Consequently, the expected ratio of C1a (1) : (2) : (3) is 11 : 100 : 5.5. The measured ratio of these peaks is 15 : 100 : 8, which is in broad agreement. Similarly, the oxygen spectrum is comprised of two peaks at 531.5 eV (1) and 533.4 eV (2). Peak 1 can be associated with the $NHC(O)CH_2$ group, with an expected binding energy of 531.4 eV, whereas peak 2 can be associated with CH_2OCH_2, expected to have binding energies of 533.5 eV. The peak area ratio for O1s (2) / O1s (1) determined from figure 4.19c is 5, compared with an expected value of 1. Similarly, the nitrogen 1s spectrum is split, with peaks at 398.3 eV (1) and 400.3 eV (2). The two nitrogen combinations in the molecule are expected to have binding energies of 399.8 eV for NH_2 and 399.7 eV for NH, thus the position of peak 1 cannot be explained. The sulphur 2p spectrum is fit with two doublets. The peak position for the $S2p_3$ peak of the S2p (1) doublet is 161.9 eV, and 165.7 eV for S2p (2) doublet. The surface concentration of the S2p (1) peak is 6 % of the total gold measured. Peak 1 is positioned as expected for a gold thiolate bond, but the 3.8 eV separation between peak 1 and 2 is too great for peak 2 to be attributed to a unbound SH thiol. The position of peak 2 is consistent with an oxidised sulphur group present on the surface. The wettability of these surfaces was determined to be 46 and 21 degrees for the advancing and receding contact angles respectively.

4.6.1 Assembly of Nanowires on Patterned Surfaces Using Electrostatic Interactions

Patterned surfaces were incubated with nanowires where both the nanowires and surfaces contained charged regions, under specific solvent conditions. The nanowires were functionalised with [COOH]. Two experiments have been performed; to assemble negatively charged nanowires onto neutral regions of patterned neutral / negatively

charged surfaces, and to assemble negatively charged nanowires onto positively charged regions of patterned positively / negatively charged surfaces.

Patterned surfaces with stripes of [COOH] / [OH] were fabricated by microcontact printing on gold substrates. Nanowires were allowed to interact with such surfaces in pH controlled aqueous solutions. Nanowires precipitate from solution onto the patterned surface, which were then washed with milli-Q 18.2 $M\Omega cm^{-1}$ water and dried under nitrogen.

Electrostatic assembly of nanowires onto mercaptoundecanol / mercaptoundecanoic acid surfaces is reliant on repulsive interaction between the COO^- terminated regions of the surface and COO^- terminated surface of the nanowires. To ensure sufficient deprotonation of the carboxylic acid terminal groups the nanowire solution was adjusted to pH 8 by the addition of NaOH (the pKa value of a mercaptoundecanoic SAMs is ~5.5[22, 23]). After nanowire assembly, the surface was imaged by the SEM, Figure 4.20, which shows the [OH] regions lighter, and [COOH] regions darker.

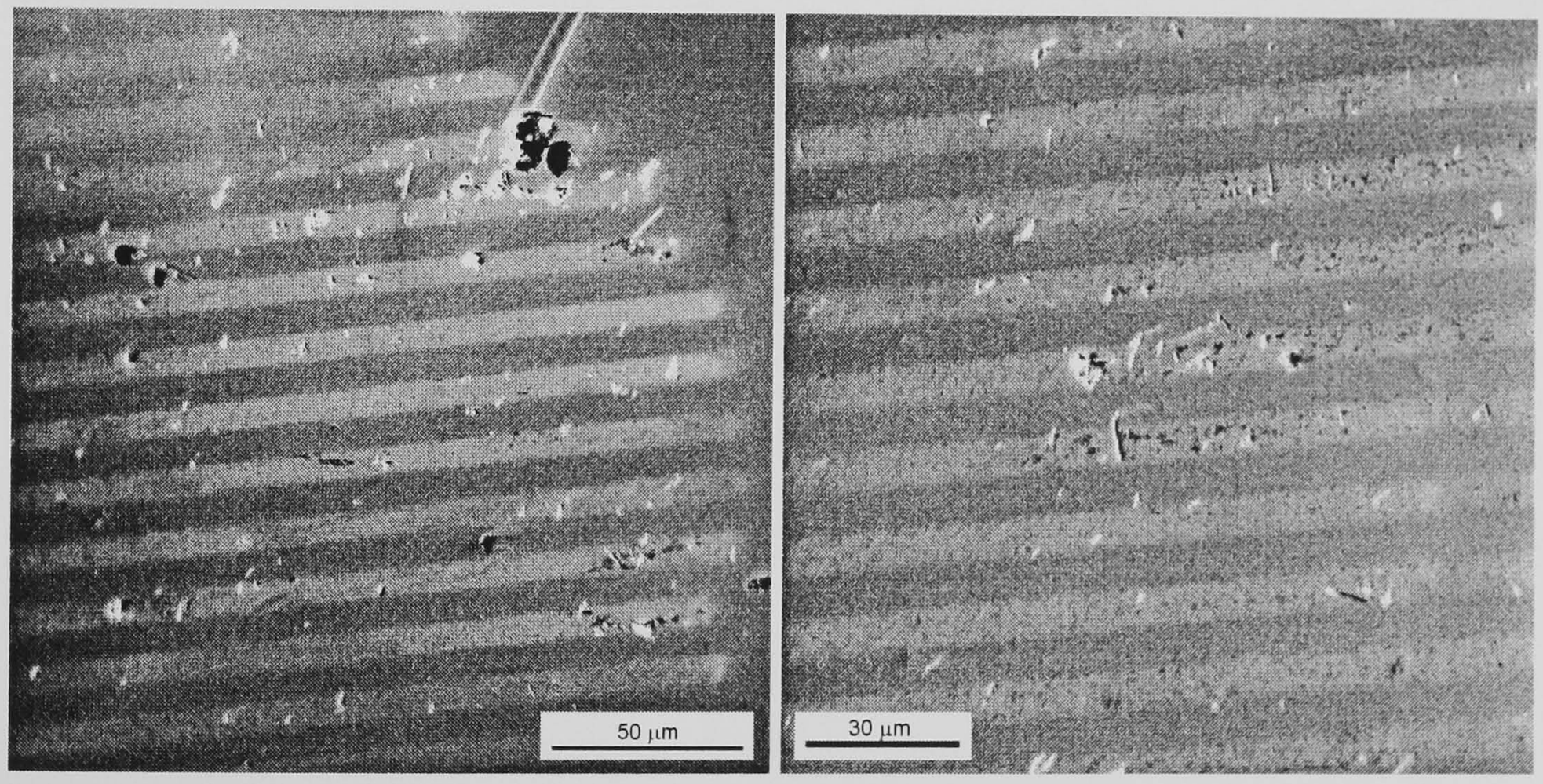

Figure 4.20. SEM images showing COO^- functionalized nanowires assembled onto 10 μm wide [OH] (light) stripes of a [OH] / COO^- (dark) patterned surface from pH 8 NaOH solution.

Electrostatic repulsion causes the nanowires to assemble onto the mercapto-1-undecanol (lighter) regions of the surface, where approximately 85 % of the sampled nanowires were observed. Assembly in solutions with lower pH values was not successful.

The assembly of mercaptoundecanoic acid functionalised nanowires onto [COOH] / [NH2] patterned surfaces is dependent on both repulsive and attractive electrostatic forces, and potentially amide bond formation[24]. It is possible to tailor the pH of the nanowire solution such that NH_2 terminated regions protonate to NH_3^+ and have a net positive charge, whilst the [COOH] surfaces deprotonate to COO^- and have a net negative charge. The pKa of [COOH] and similar [NH2] SAMs has been previously determined so that the range of pH where this applies is approximately ~5.5-7.5[22-25]. The solvent used was 18.2 $M\Omega cm^{-1}$ water, pH ~6.5. After assembly the surface was imaged with a SEM, Figure 4.21, which showed the mercaptoundecanol regions with a lighter coloration, and [NH2] regions as darker.

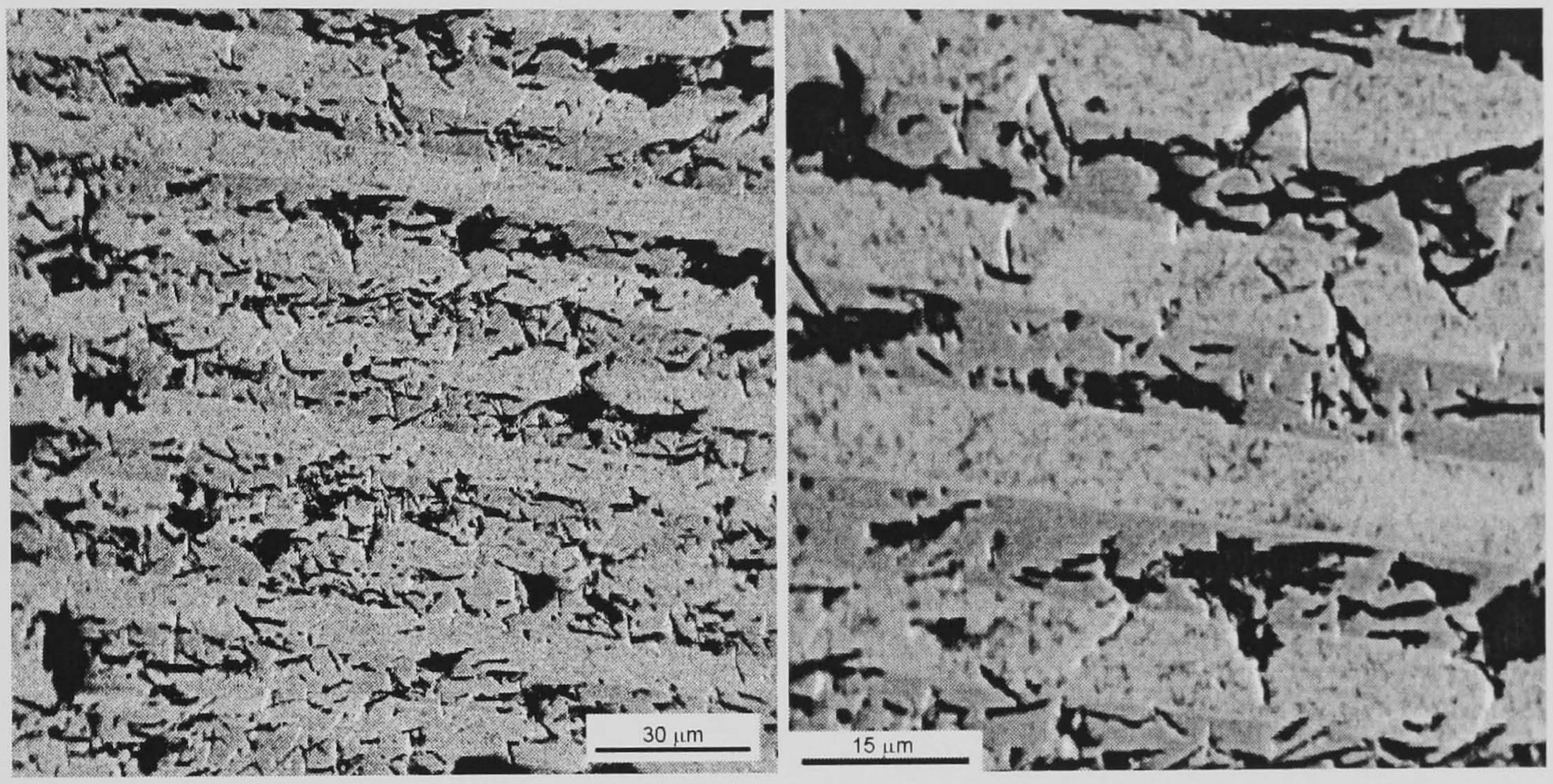

Figure 4.21. SEM image showing COO^- functionalized nanowires assembled onto 5 μm wide NH_3^+ terminated regions of a COO^- (light) / NH_3^+ (dark) patterned surface from water, pH 6.5.

Nanowires have assembled predominantly onto the amine regions, with relatively few wires falling on the acid regions despite the high overall nanowire density. Electrostatic interactions between the nanowires and surfaces provide long-range assembly forces but weak attachment at the surfaces. Although successful assembly is observed on both the surfaces investigated here, no nanowire alignment was observed. Assembly from solutions with different pH values was not successful

4.6.2 Aggregation Nanowires via Mutual Electrostatic Interactions in Solution

Nanowires have been functionalised with [ATP] and [COOH] acid surfactants in a variety of ways. The procedure used to functionalise the ends of nanowires whilst captive in the template membrane, outlined for biotin nanowires, has been used again here. Two similar experiments were performed, in the first case nanowires were functionalised with [COOH] at one end, and [ATP] at the other. In the second experiment, nanowires functionalised with [COOH] at both ends were mixed with a solution of nanowires functionalised at both ends with [ATP]. Pilot experiments (not shown) using XPS characterisation of SAMs on planar gold substrates have shown that [COOH] and [ATP] SAMs were not degraded during the sodium hydroxide etching procedure, used to release the nanowires from the membrane. However, SAMs of these surfactants were considerably degraded by exposure to 70 wt% nitric acid, used to remove the silver electrode. Consequently, prior to exposure of one or both ends to the mixed surfactant solution, the silver electrode was removed. Nanowires with different surfactants at each end were fabricated by exposure of each side to surfactant solutions in the electrochemical cell, figure 2.8. To functionalise both ends of nanowires with the same surfactant, membranes filled with nanowires were immersed in thiol solutions.

Both nanowire samples are expected to display identical behaviour; they should aggregate into nanowire chains or rafts at specific pH ranges in solution. Nanowire aggregation in solution could not be observed at any pH conditions by eye, and certainly not to the extent demonstrated by the biotin functionalised nanowires. However, dropcasting the nanowires from mili-Q water (pH 6) onto a silicon surface did highlight some elements of nanowire aggregation. Slightly better results were observed for nanowires with different functionality at each end, Figure 4.22.

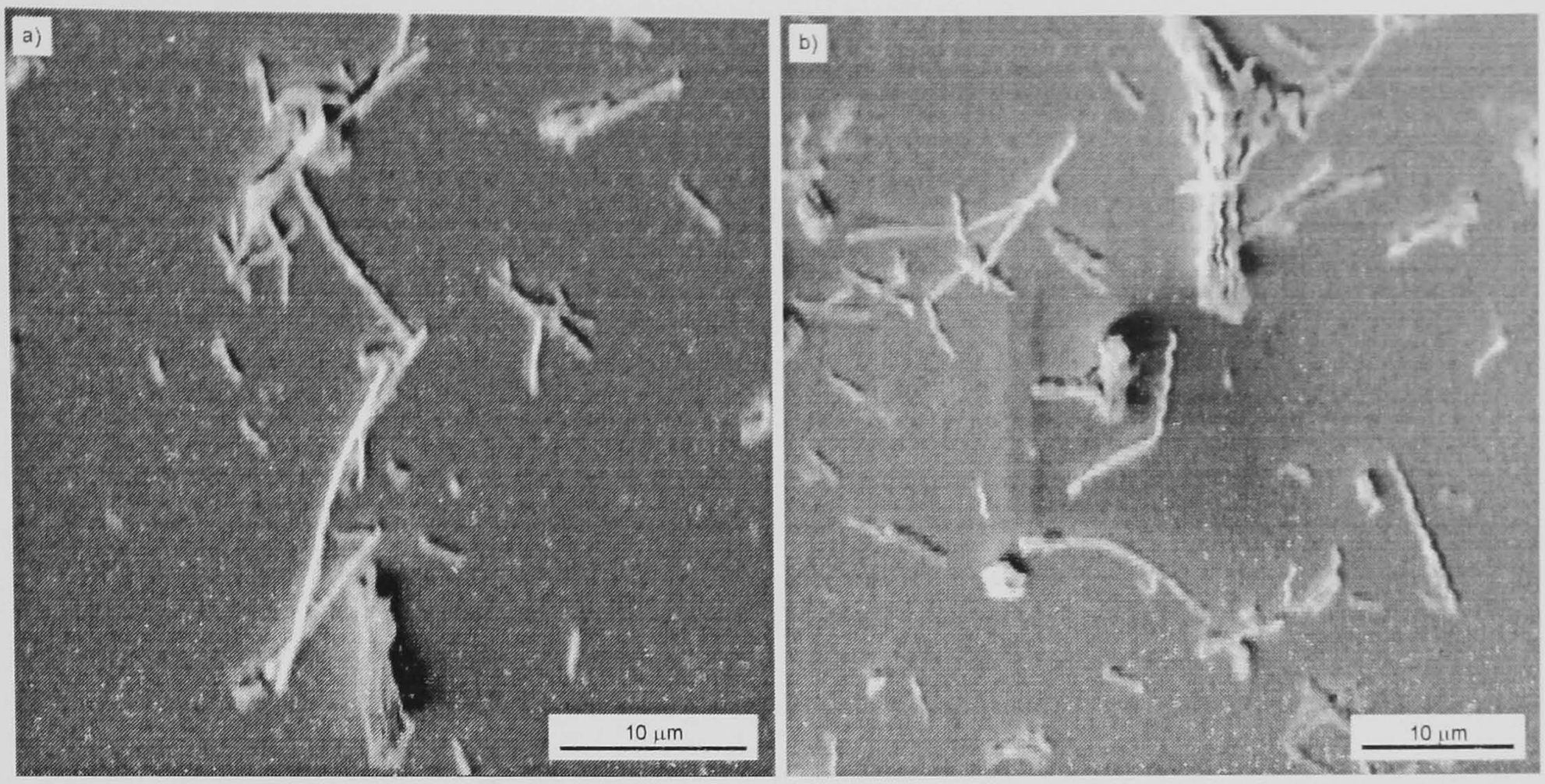

Figure 4.22. SEM images of aggregation of nanowires functionlaised with [ATP] at one end and [COOH] at the other, dropcast from water onto silicon.

Figure 4.22a shows a long chain of nanowires, and smaller groups of nanowires attached end to end. A nanowire 'raft', where nanowires aggregate parallel but are oppositely directed, is shown in figure 4.22b. These expected nanowire assemlies suggested that electrostatic interactions are also capable of driving nanowire aggrsegation in solution.

4.7: References

1. Jiang, X.P.; Ortiz, C.; Hammond, P.T., Langmuir, 2002. **18**(4): p. 1131-1143.
2. vanderVegte, E.W.; Hadziioannou, G., Journal of Physical Chemistry B, 1997. **101**(46): p. 9563-9569.
3. Bain, C.D.; Evall, J.; Whitesides, G.M., Journal of the American Chemical Society, 1989. **111**(18): p. 7155-7164.
4. Martins, M.C.L.; Ratner, B.D.; Barbosa, M.A., Journal of Biomedical Materials Research Part A, 2003. **67A**(1): p. 158-171.
5. Laibinis, P.E.; Whitesides, G.M., Journal of the American Chemical Society, 1992. **114**(6): p. 1990-1995.
6. Nikoobakht, B.; Wang, Z.L.; El-Sayed, M.A., Journal of Physical Chemistry B, 2000. **104**(36): p. 8635-8640.
7. Oliver, S.R.J.; Bowden, N.; Whitesides, G.M., Journal of Colloid and Interface Science, 2000. **224**(2): p. 425-428.
8. Jana, N.R., Angewandte Chemie-International Edition, 2004. **43**(12): p. 1536-1540.
9. Booth, C.; Bushby, R.J.; Cheng, Y.L., et al., Tetrahedron, 2001. **57**(49): p. 9859-9866.
10. Sethuraman, A.; Han, M.; Kane, R.S., et al., Langmuir, 2004. **20**(18): p. 7779-7788.
11. Israelachvili, J.; Pashley, R., Nature, 1982. **300**(5890): p. 341-342.
12. Claesson, P.M.; Christenson, H.K., Journal of Physical Chemistry, 1988. **92**(6): p. 1650-1655.
13. Pashley, R.M.; McGuiggan, P.M.; Ninham, B.W., et al., Science, 1985. **229**(4718): p. 1088-1089.
14. Freeman, T.L.; Evans, S.D.; Ulman, A., Langmuir, 1995. **11**(11): p. 4411-4417.

15. Evans, S.D.; Ulman, A.; Goppertberarducci, K.E., et al., Journal of the American Chemical Society, 1991. **113**(15): p. 5866-5868.

16. Lee, S.J.; Han, S.W.; Choi, H.J., et al., Journal of Physical Chemistry B, 2002. **106**(11): p. 2892-2900.

17. Hai, B.; Wu, J.; Chen, X.F., et al., Langmuir, 2005. **21**(7): p. 3104-3105.

18. Perez-Luna, V.H.; O'Brien, M.J.; Opperman, K.A., et al., Journal of the American Chemical Society, 1999. **121**(27): p. 6469-6478.

19. Haussling, L.; Michel, B.; Ringsdorf, H., et al., Angewandte Chemie-International Edition in English, 1991. **30**(5): p. 569-572.

20. Lukkari, J.; Kleemola, K.; Meretoja, M., et al., Langmuir, 1998. **14**(7): p. 1705-1715.

21. Batz, V.; Schneeweiss, M.A.; Kramer, D., et al., Journal of Electroanalytical Chemistry, 2000. **491**(1-2): p. 55-68.

22. Vezenov, D.V.; Noy, A.; Rozsnyai, L.F., et al., Journal of the American Chemical Society, 1997. **119**(8): p. 2006-2015.

23. vanderVegte, E.W.; Hadziioannou, G., Langmuir, 1997. **13**(16): p. 4357-4368.

24. Giesbers, M.; Kleijn, J.M.; Stuart, M.A.C., Journal of Colloid and Interface Science, 2002. **252**(1): p. 138-148.

25. Zhang, H.; He, H.X.; Wang, J., et al., Applied Physics a-Materials Science & Processing, 1998. **66**: p. S269-S271.

Chapter 5: Dielectrophoretic Assembly and Electrical Characterisation of Nanowires

Nanowires have been manipulated with dielectrophoretic forces to facilitate their assembly between electrodes. This chapter presents results illustrating the assembly of nanowires between electrodes, and the electrical characterisation of nanowires. Specific areas discussed are:

1) The fabrication and characterisation of electrodes.
2) Dielectrophoretic assembly of nanowires between electrodes.
3) Transport measurements of nanowires assembled between electrodes.

5.1: Electrodes

During the course of this work, a variety of electrodes have been used. Preliminary experiments used 4-probe aluminium electrodes on silicon dioxide, received from Haoli Zhang, at Lanzhou University. Subsequent experiments used electrodes made from gold, on glass substrates. These are discussed in more detail below.

5.1.1 Aluminium Electrodes

Aluminium electrodes on silicon dioxide were fabricated by the photolithographic lift-off technique, where the aluminium electrode was etched with a strong sodium hydroxide solution. Each electrode had a contact pad of approximately 2 mm^2, for attaching wires and connecting to the external circuitry. Each individual electrode tapered towards the junction region, Figure 5.1, yielding a minimum separation of ~5 μm between adjacent electrodes. Wires were bound to each contact pad with silver paint, and strengthened with epoxy glue anchoring the wire to the substrate. These electrodes were characterised prior to experiments. A low resolution SEM image of the central area of an electrode, and its electrical characterisation made with the transport apparatus outlined in section 2.5.8, is shown in figure 5.1.

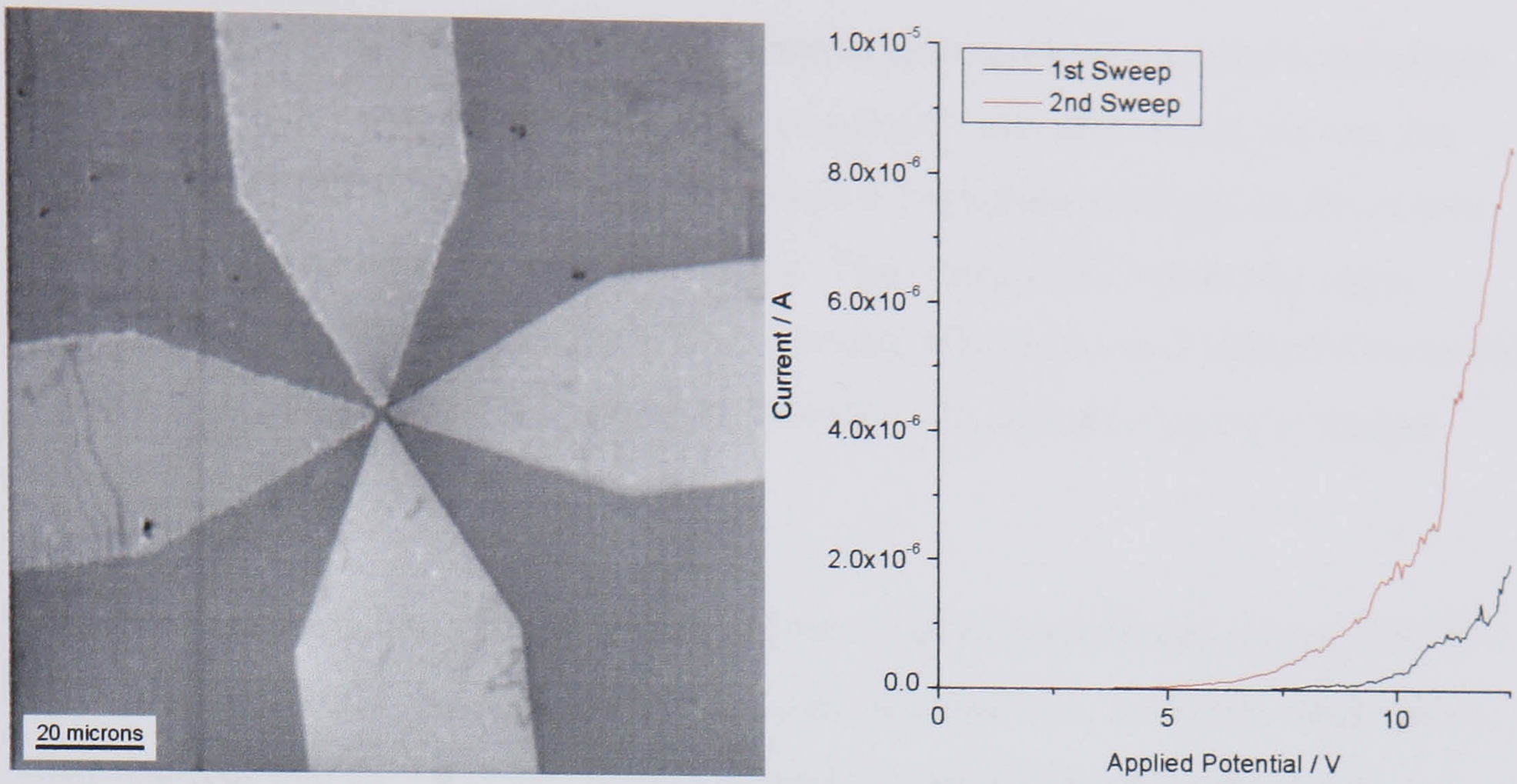

Figure 5.1. SEM image of an aluminium electrode on silicon dioxide, and electrical characteristion between two adjacent contacts

The SEM image in figure 5.1 shows the electrode geometry described above, the lighter areas are the aluminium whilst the darker background is the silicon dioxide substrate. The electrically insulating behaviour of these electrodes is also demonstrated. The voltage between adjacent electrodes was ramped from 0 – 12.5 V. The electrodes insulating properties break down at 7.2 V, and on the subsequent scan at 2.8 V (where the current exceeds 1 nA). The voltage at which this breakdown occurs is too low to be associated with the dielectric between the electrodes, whether through the air or silicon dioxide. It is possible that some aluminium remains on the silicon dioxide surface after etching, and this film can form a conducting pathway at higher voltages. Alternatively, electrical breakdown may occur via ion diffusion of aluminium through the silicon dioxide film. Conducting pathways may form directly between the metallic electrodes, or via the underlying silicon substrate. The change in the voltage at which breakdown occurs would suggest that the process is irreversible once the potential has exceeded 7.2 V.

5.1.2 Gold Electrodes on Glass

The fabrication of gold electrodes on glass substrates was undertaken as described in section 2.3.2.1.1. Further to this description, an additional stage was required. Electron-beam lithography, used to define the central electrode area, was found to be susceptible to charge accumulation on these glass substrates. The resist could be patterned by the electron beam with a variety of procedures, for example, either line by line or section by section. However, whenever the electron beam shifted from one section to the next or one electrode to the opposite one, the accumulated charge offset the position of the electron

beam defining the next section. Written electrode structures were distorted to the extent that electrode pairs were joined and all were completely unusable. To circumvent this problem, the surface of the resist was coated with a 2 nm platinum layer, sputtered onto the surface with an Agar 208HR sputter coater. This overlayer dissipated the excess electrons introduced by the electron beam. Exposure of the resist to the electron beam still resulted in degradation, and was entirely removed by the same developing procedure described in section 2.5.7.2.

Gold was deposited onto glass substrates to form 2 opposing electrodes separated by 3 or 5 μm, although all the results presented used electrodes with the 3 μm gap. Once again, each electrode had a contact pad of approximately 2 mm^2 for attaching wires and connecting to the external circuitry. Scanning electron microscopy and electrical characterisation of these bare electrodes is shown in figure 5.2.

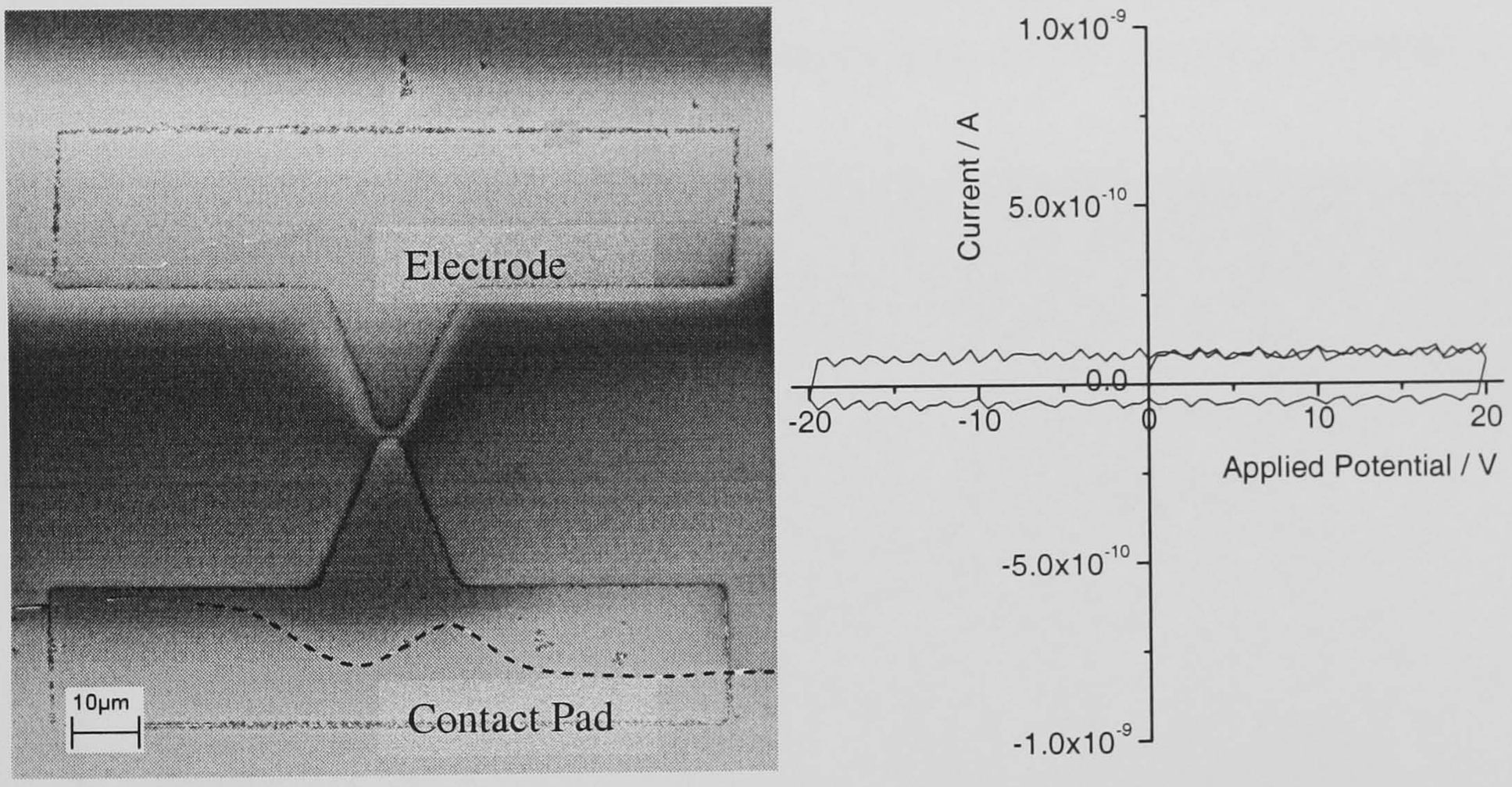

Figure 5.2. SEM image of a gold electrode on glass, and electrical characteristion

The SEM image, figure 5.2, shows the two opposing electrodes, and the entire area patterned by electron beam lithography. The overlaid gold contact pads are 2 mm squares, separated by 75 μm. In the locality of the central electrode area the gap between contact pads is reduced to 50 μm, with a pattern used for alignment of the e-beam and photolithography fabrication stages. One edge of this narrowed region in the contact pads is highlighted with a dashed line in Figure 5.2. The electrode shows insulating behaviour up to 20 V (and indeed 40 V, not shown), with no electrical breakdown observed.

5.2: Dielectrophoretic Assembly of Nanowires

The origin of the dielectrophoretic force has already been discussed in section 2.3.2.1. Nanowires were assembled onto the electrodes described above. A droplet of nanowire solution was placed on the electrode structure, whilst an alternating potential was applied across the electrode gap. After assembly, the electrode was washed with methanol whilst the alternating potential was maintained. After drying under N_2, the electrodes were observed with an SEM. Here, results are presented describing the assembly of nanowires onto both the aluminium electrodes on silicon dioxide and gold electrodes on glass, at a range of assembly conditions.

5.2.1 Dielectrophoretic Assembly onto Aluminium Electrodes

Due to the insulating breakdown of aluminium electrodes, Figure 5.2, the applied potential was generally minimised whilst assembling nanowires onto these electrodes. An SEM image of one typical electrode after assembly of nanowires at a 2 V_{pp} (150 kHz) is shown in Figure 5.3.

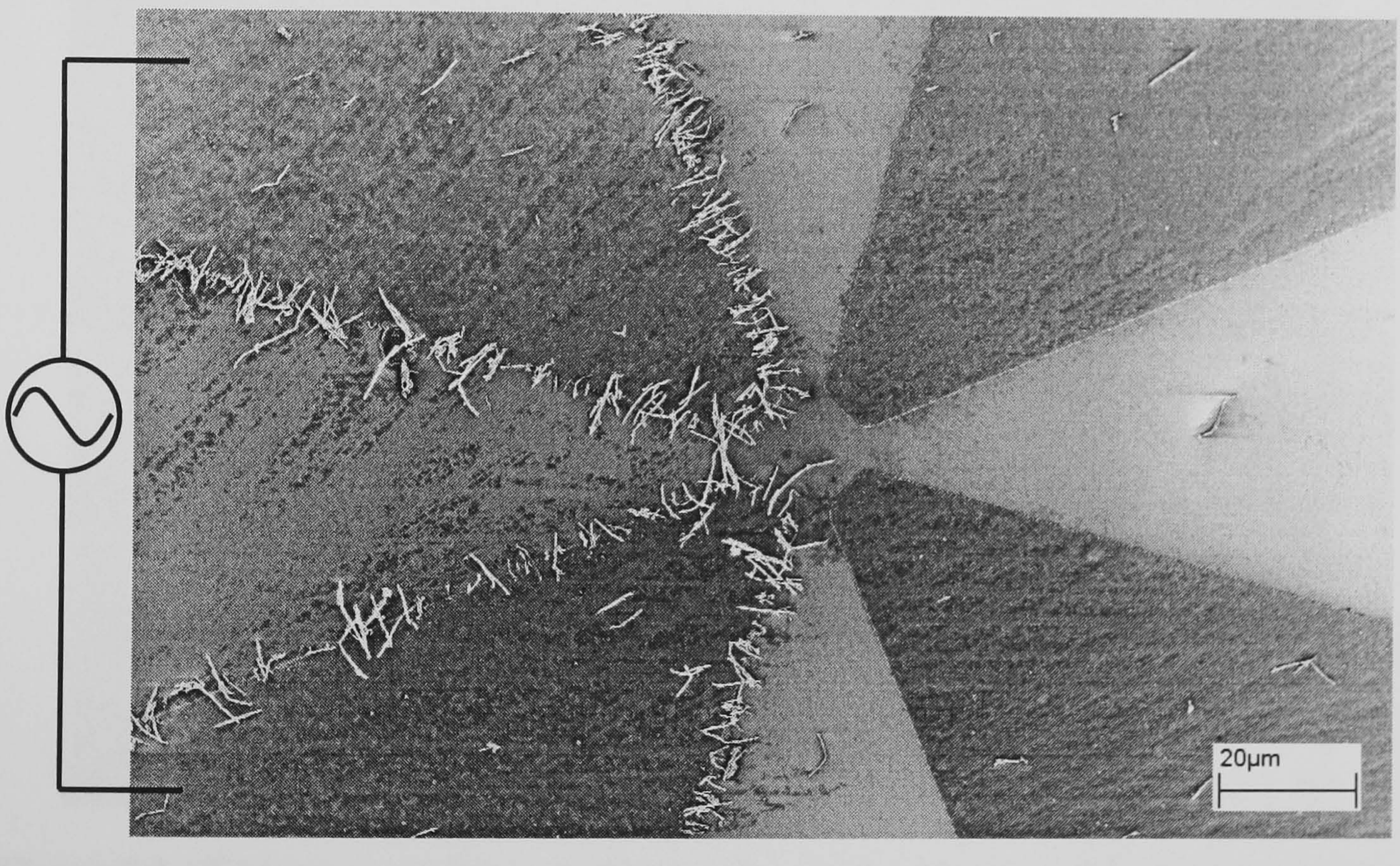

Figure 5.3. Dielectrophoretic assembly of nanowires at 2 Vpp (150 kHz) onto a pair of contacts of an aluminium / silicon dioxide electrode

It should be noted that assembly was observed for all applied potentials above 1 V_{pp}, including potentials significantly higher than the breakdown voltage of these electrodes. At these higher potentials, excess nanowires and other constituents of the solution, i.e. silver flake, were assembled onto the central electrode area. At lower applied potentials, very few nanowires remain on the surface. Generally, the density of assembled nanowires

is related to the local electric field strength, i.e. by the magnitude of the applied potential and the electrode geometry. It would be expected that nanowires assemble at the highest densities where the gap between electrodes is smallest. This is not observed, and nanowires are assembled with a uniform density all around the electrode and contact pad edges. The relationship between the dielectrophoretic conditions and nanowire assembly has been explored in greater detail (both theoretically and experimentally) for gold electrodes.

5.2.2 Dielectrophoretic Assembly onto Gold Electrodes

Dielectrophoretic assembly of nanowires onto gold electrodes shows significantly different behaviour to the assembly of nanowires onto aluminium electrodes. The placement of nanowires still occurs at the edges of the electrodes, but nanowire density is dependent on the local electrode separation (local electric field). An SEM image of nanowires assembled onto a gold electrode with a 2 V_{pp} (150 kHz) alternating potential is shown in Figure 5.4.

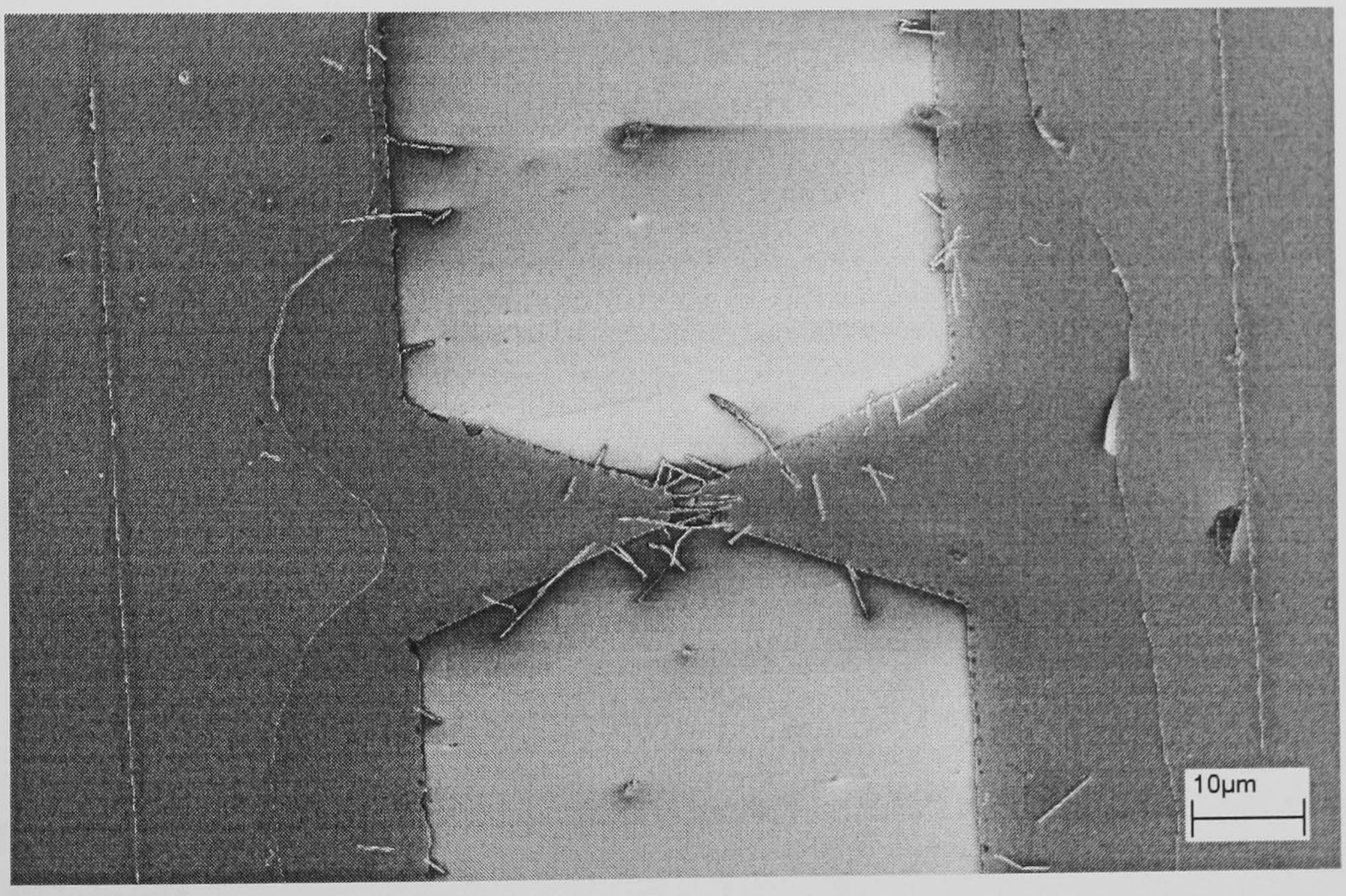

Figure 5.4. SEM image of gold nanowires assembled onto a gold / glass electrode at 2 V_{pp} (150 kHz) for 15 s.

The high local electric field directly between the electrodes acts to assemble wires in greater density here. Once again, applied potentials below 1 V_{pp} show a very low density of assembled nanowires, this is discussed in greater detail later. Pilot experiments to determine the effect of the assembly time have shown this to be of importance as well. Typically, electrodes are exposed to the nanowire solution for 15 s prior to washing with

methanol. However, longer time periods, at identical conditions, show an increase in the number of assembled nanowires. It is thought that precipitation of nanowires within the droplet increases the number of nanowires whose behaviour is significantly modified by dielectrophoretic forces. Therefore, the number of assembled nanowires increases with the time of exposure to the nanowire solution. For consistency, all other results presented here have been exposed to the nanowire solution for 15s.

As mentioned previously, during assembly the current passed between the electrodes was monitored with a digital oscilloscope across a 1 kΩ load resistor, RL figure 5.5. The assembly process was characterised at four distinct stages of assembly; prior to assembly with a dry electrode (Dry), prior to assembly with the electrode exposed to HPLC methanol (Methanol), during assembly where the electrode is exposed to the nanowire solution (Nanowire), and after assembly, washing and drying (Assembled), Figure 5.5.

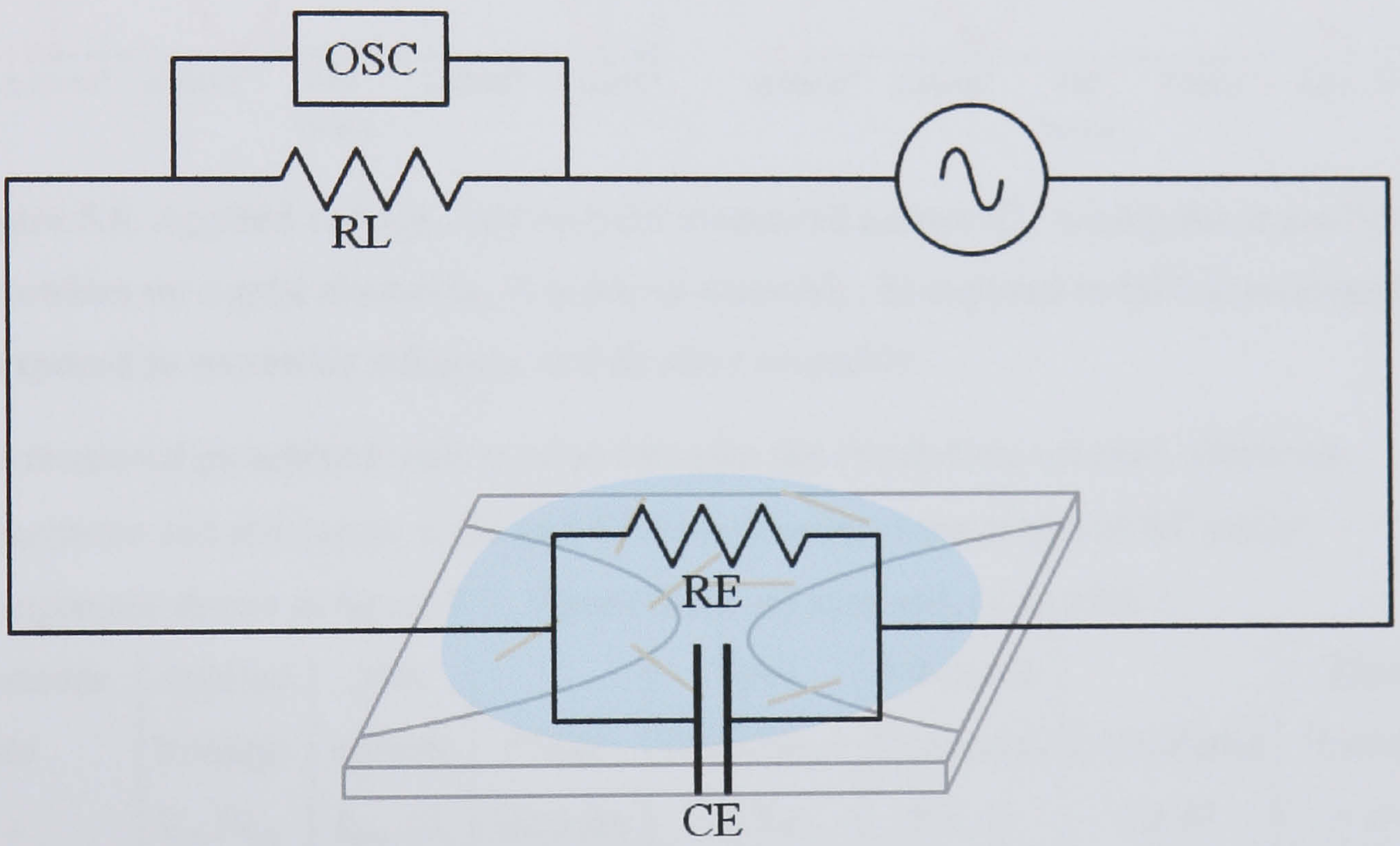

Figure 5.5. Schematic diagram showing how assembly process has been modelled as an RC circuit

During assembly the electrode can be considered to behave as an imperfect capacitor, with parallel contribution from the gap resistance (RE) and electrode capacitance (CE). This circuit may be modelled as a driven RC circuit. The recorded traces, with the voltage measurement across RL converted to current, are shown in Figure 5.6.

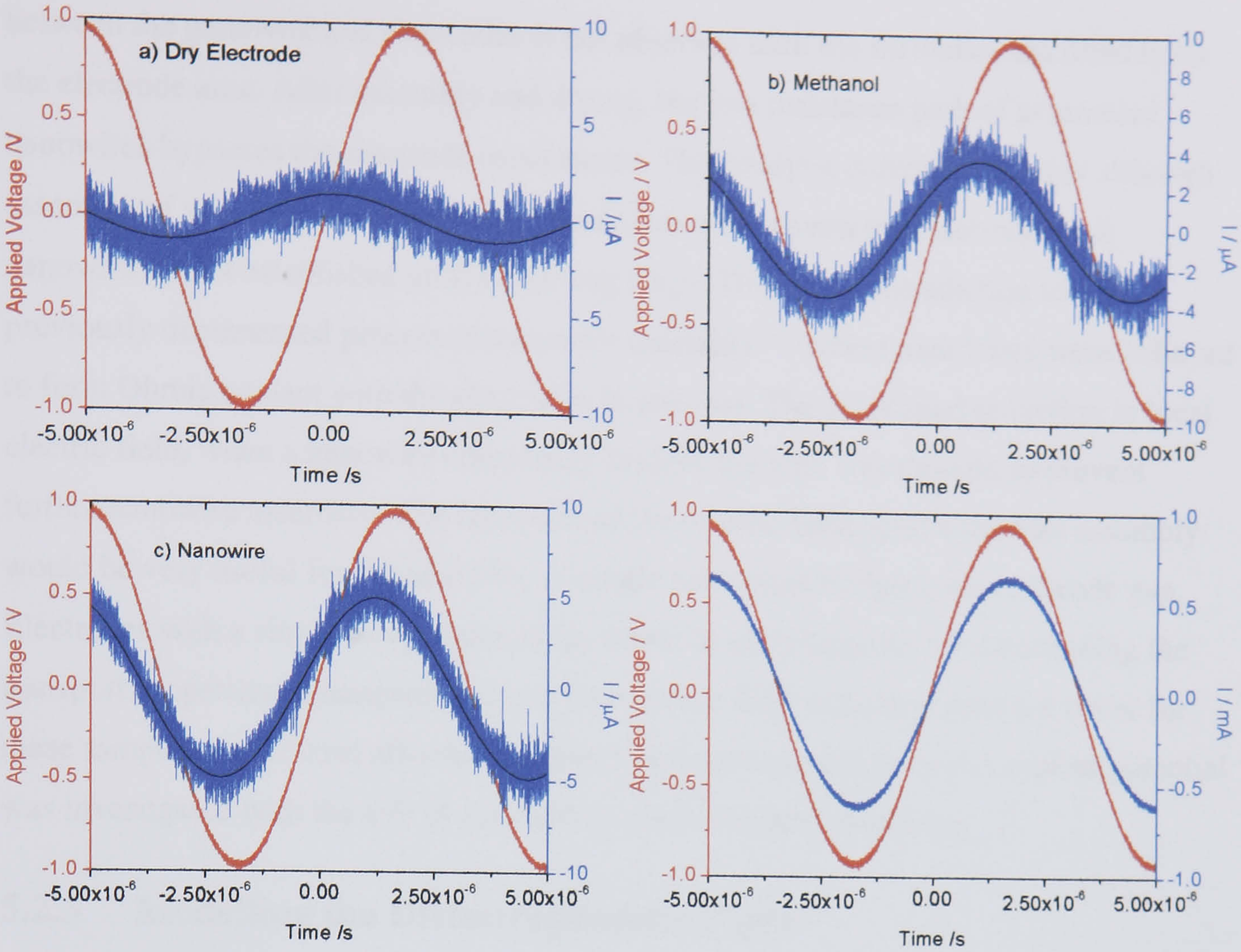

Figure 5.6. Applied voltage, and current measured across RL during the assembly of nanowires on a gold electrode, a) prior to assembly, b) exposed to HPLC methanol, c) exposed to nanowire solution, and d) after assembly

The measured parameters were used to calculate the circuit time constant, electrode capacitance and resistance, τ, CE and RE respectively, of the proposed RC circuit arrangement shown in figure 5.5. These results are summarised in table 1.

Electrode State	Applied Voltage V_A /V_{pp}	Max current I_{max} /A	Phase /degrees	Total Impedance Z /Ω	Electrode Resistance RE /Ω	Capacitance CE /F	Time Const τ /s
Dry	0.97	$1.5x10^{-6}$	80	$6.5x10^{5}$	$3.9x10^{6}$	$1.66x10^{-12}$	$1.6x10^{-9}$
Methanol	0.97	$3.5x10^{-6}$	37	$2.8x10^{5}$	$3.5\ x10^{5}$	$2.36x10^{-12}$	$2.3x10^{-9}$
Nanowire	0.97	$4.8x10^{-6}$	21	$2.0\ x10^{5}$	$2.2\ x10^{5}$	$1.96x10^{-12}$	$1.9x10^{-9}$
Assembled	0.94	$6.3x10^{-4}$	-4	$1.5x10^{3}$	500	-	-

Table 5.1. Electrical parameters detailing the progress of dielectrophoretic assembly of nanowires on a gold electrode

Throughout assembly, the capacitance remains approximately constant, despite changes in the permittivity of the dielectric. The progression of assembly is characterised by a reduction in the electrode resistance, from 3.9 MΩ to 500 Ω. Importantly, direct contact

between the nanowire and electrodes is not observed until the methanol has dried from the electrode area. After assembly and drying, the low resistance path of assembled nanowires bypasses the electrode capacitance. This analysis demonstrates that although assembly of wires occurs in solution, Ohmic contact between the electrodes and nanowires is not established until the drying stage. This is in contradiction to the previously documented process of nanowire assembly[1, 2], where nanowires were believed to form Ohmic contact with the electrodes in solution. The associated reduction in local electric field, when a nanowire completely bridged the gap, was thought to prevent further nanowire assembly. The reduction of the electric field upon nanowire assembly would be very useful for the assembly of single nanowires bridging the electrode gap. Electrodes with a single bridged nanowire would be advantageous for determining the transport properties of nanowires. Since this electric field reduction does not occur for these samples, the control afforded to dielectrophoretic assembly by the applied potential was investigated with the aim of assembling single bridged nanowires.

5.2.3 Modelling the Dielectrophoretic Force

A theoretical description of dielectrophoresis has been provided in section 2.3.2.1, in which the relationship between the dielectrophoretic force and the applied potential has been determined. Here, these relationships are applied to the specific case for gold nanowires assembled between the gold electrodes on glass, and the dielectrophoretic force has been modelled.

5.2.3.1 Potential Dependence of the Dielectrophoretic Force

The dielectrophoretic force, F_{DEP}, is dependent on the strength, and gradient, of the local electric field, equation 5.1.

Equation 5.1 $$F_{DEP} = \pi r^2 l \varepsilon_m \,\mathrm{Re}\{K\} \left| \frac{dV_{rms}}{dx} \nabla_x \left(\frac{dV_{rms}}{dx} \right) \right|$$

The force is also proportional to the volume of the nanowire, $\pi r^2 l$, the permittivity of the surrounding medium, ε_m, and the real part of the complex polarisation factor K, given by equation 5.2.

Equation 5.2 $$\mathrm{Re}\{K\} = \frac{\omega^2(\varepsilon_m \varepsilon_p - \varepsilon_m^2) + (\sigma_m \sigma_p - \sigma_m^2)}{e_m^2 \omega^2 + \sigma_m^2}$$

The real part of the complex polarisation factor K is derived from permittivity, ε, and the conductivity, σ, and angular frequency of the applied potential, ω. See section 2.3.2.1 for

further information. The indices *m* and *p* relate to the medium (methanol) and particle (gold) respectively. Finite element modelling of the electrode has been used to determine the spatially averaged electric field, and its gradient, for a specific nanowire location close to the electrode gap (width 150nm, length 4μm). The software used to perform these calculations was QuickField version 5.2, published by Tera Analysis. These calculations were based upon a steady state applied potential, equal to the RMS voltage of the applied field. Typical output from these finite element calculations is shown in figure 5.7, based upon assembly with a 4 V_{pp} applied field.

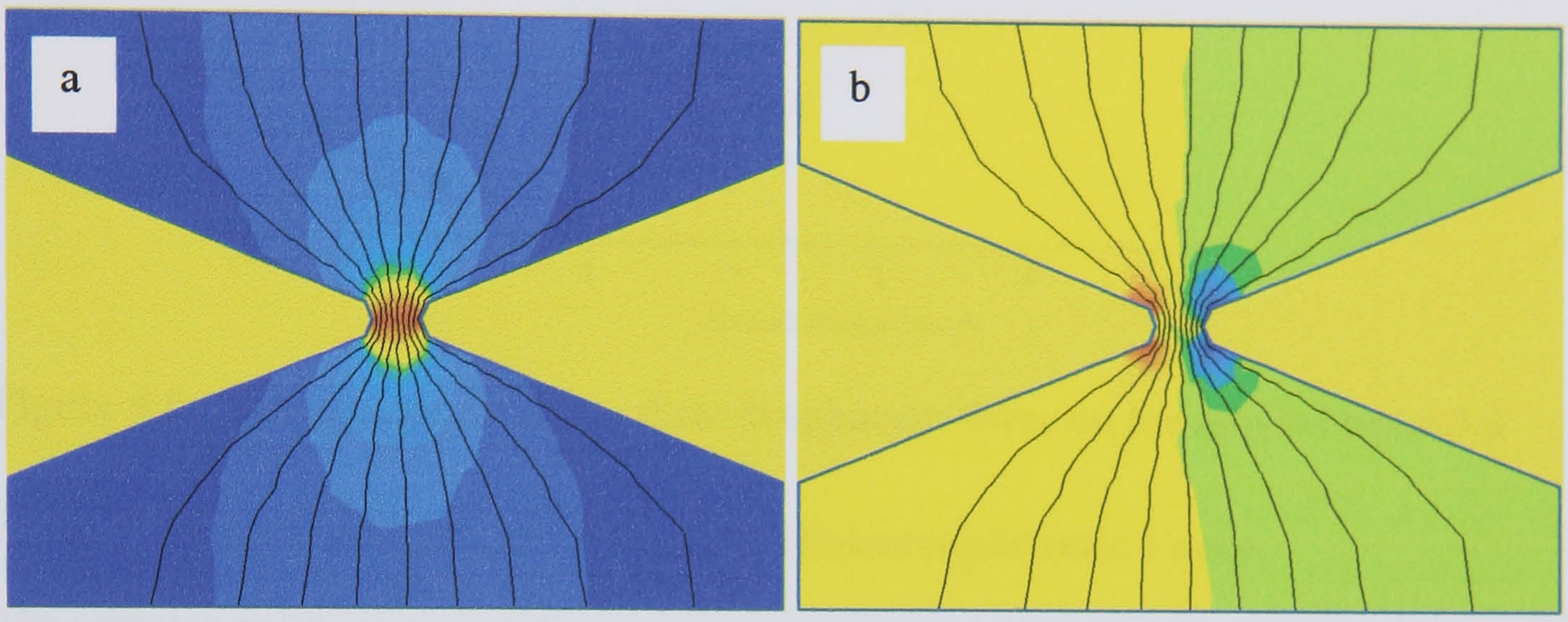

Figure 5.7. Finite element calculations of a) the electric field strength, and b) the electric field gradient shown by colour variation for the gold electrode with a 3 μm gap. The black lines are lines of equipotential.

The geometry of this model is consistent with the gold electrodes on glass, within the confines of meshing constraints. The gold electrodes are coloured in gold, and the width of the model covers the central 50 μm of the electrodes. As such, fixed voltage boundary constraints were applied at the electrode edges, and the left and right hand edges of the modelled area. The only additional data required was the permittivity and conductivity of methanol, values of $\varepsilon_m = 32.6\varepsilon_0$ and $\sigma_m = 2.2 \times 10^{-5}$ Sm^{-1} were used.[3] The images shown in figure 5.7 show the electric field strength and field gradient for the gold electrodes with a 3 μm gap on glass. It should be noted that whilst the electric field strength is at a maximum directly between the electrodes, the electric field gradient is negligible. There is no spread in the electric field strength along the line bisecting both electrodes. Calculations were made for applied potentials between 0 and 5 V_{pp}. In addition to the permittivity and conductivity of methanol, the values for gold of $\varepsilon_p = 6.9\varepsilon_0$ and $\sigma_p = 4.5 \times 10^7$ Sm^{-1} were used for the nanowire component in the complex polarisation factor, equation 5.2.[3] A quadratic dependence of the dielectrophoretic force was observed with

the applied potential, Figure 5.8, which is consistent with expectations and preliminary results suggesting improved nanowire assembly at higher applied potentials.

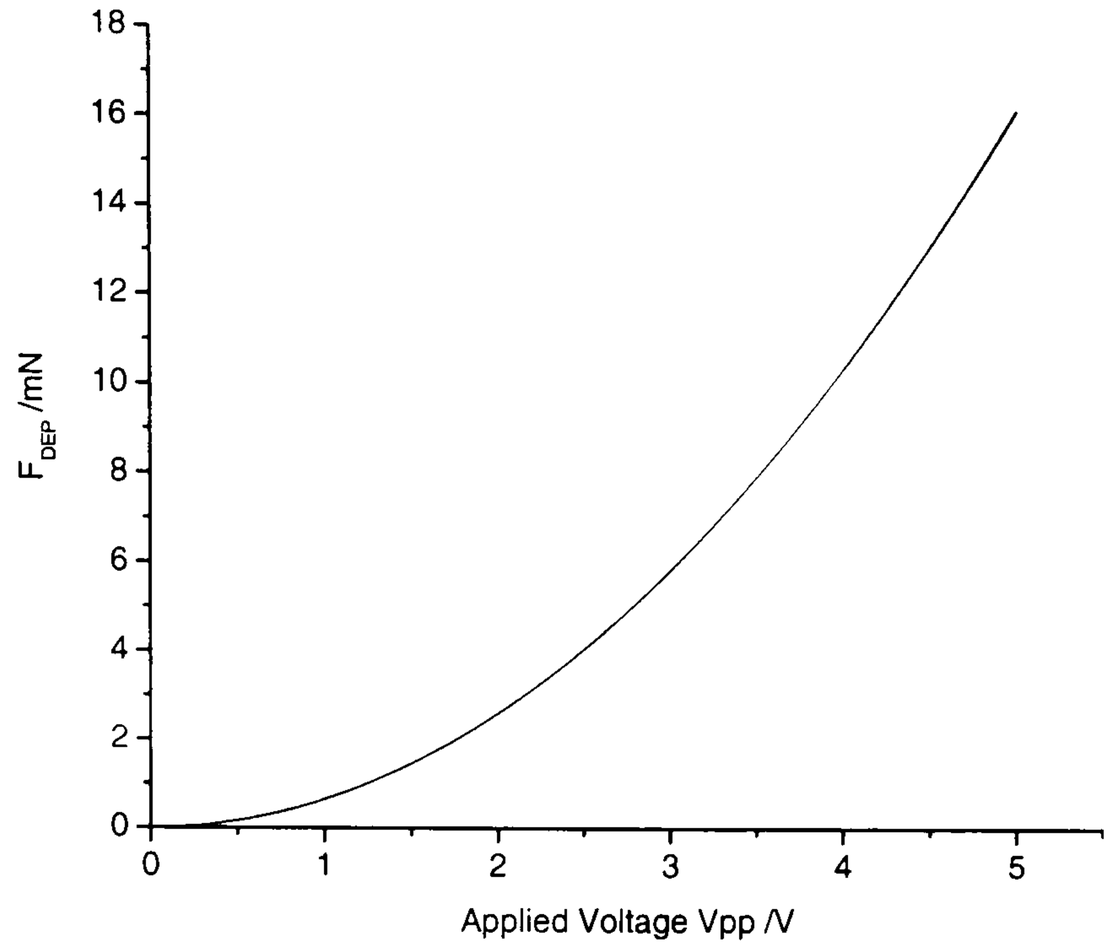

Figure 5.8. The dependence of the dielectrophoretic force on the applied potential

5.2.3.2 Frequency Dependence of the Dielectrophoretic Force

The complex polarisation factor's dependence on the permittivity introduces a relationship between the dielectrophoretic force and frequency of the applied field. Equations 5.3 and 5.4 show the high and low frequency limits respectively [4].

Equation 5.3
$$\mathrm{Re}\{K\} = (\varepsilon_p - \varepsilon_m)/\varepsilon_m \qquad \omega \to \infty$$

Equation 5.4
$$\mathrm{Re}\{K\} = (\sigma_p - \sigma_m)/\sigma_m \qquad \omega \to 0$$

At the low frequency limit the dielectrophoretic force is determined by the relative conductivity of the particle and the medium, whilst at high frequencies the force will be dependent on their relative permittivity. The transition between these two regimes is demonstrated by plotting the dielectrophoretic force against frequency, Figure 5.9. All calculations were performed with an assumed voltage of 2.5 V_{pp}.

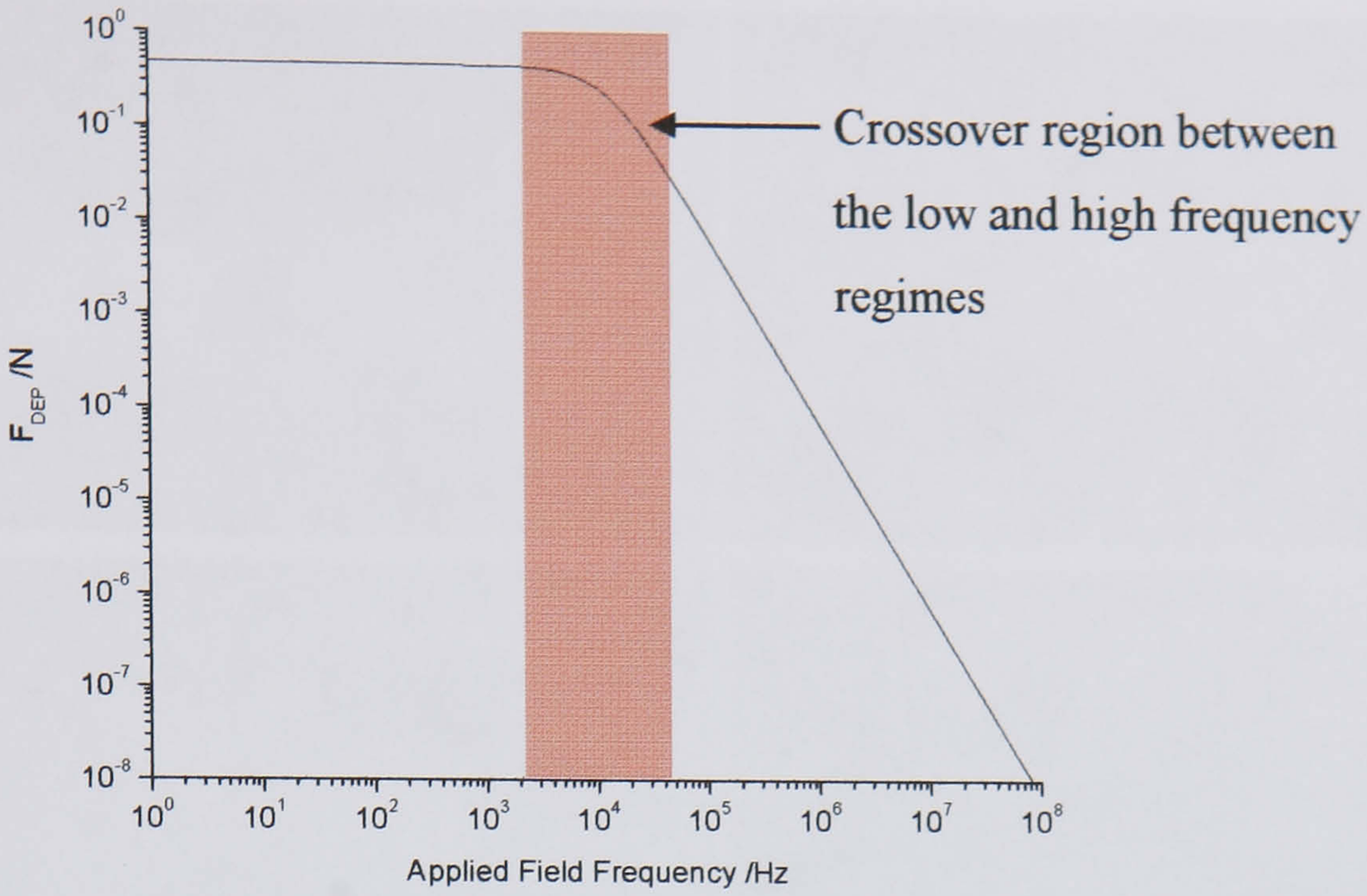

Figure 5.9. The dependence of the dielectrophoretic force on the applied field frequency

Below 10 kHz there is no strong dependence of the dielectrophoretic force on the frequency of the applied field. In this regime the factor Re{K}, equation 5.2, is dominated by the difference between the conductivities of the particle and medium. Above 10 kHz the permittivity component significantly reduces the strength of the dielectrophoretic force. For frequencies above 20 GHz the permittivity component cause the dielectrophoretic force to become negative.

5.2.4 Exploring the Variable Space of Dielectrophoresis

The aim to assemble a single nanowire between electrodes requires greater control of the assembly procedure via optimisation of the electric field. Presented below are results that investigate the variable space of dielectrophoretic assembly, by adjusting both the applied potential and applied field frequency.

5.2.4.1 Variation of the Applied Potential

To test these relationships a series of eight experiments was performed, with nanowires assembled from methanol onto gold electrodes at applied potentials between 0.5 and 4 V_{pp} (150 kHz). Across this range the dielectrophoretic force is expected to increase by a factor of 64. Nanowires were assembled from the same solution in each case, ensuring that the nanowire density remained constant. After assembly, each sample was imaged with SEM, and the results are shown in figures 5.10a-h.

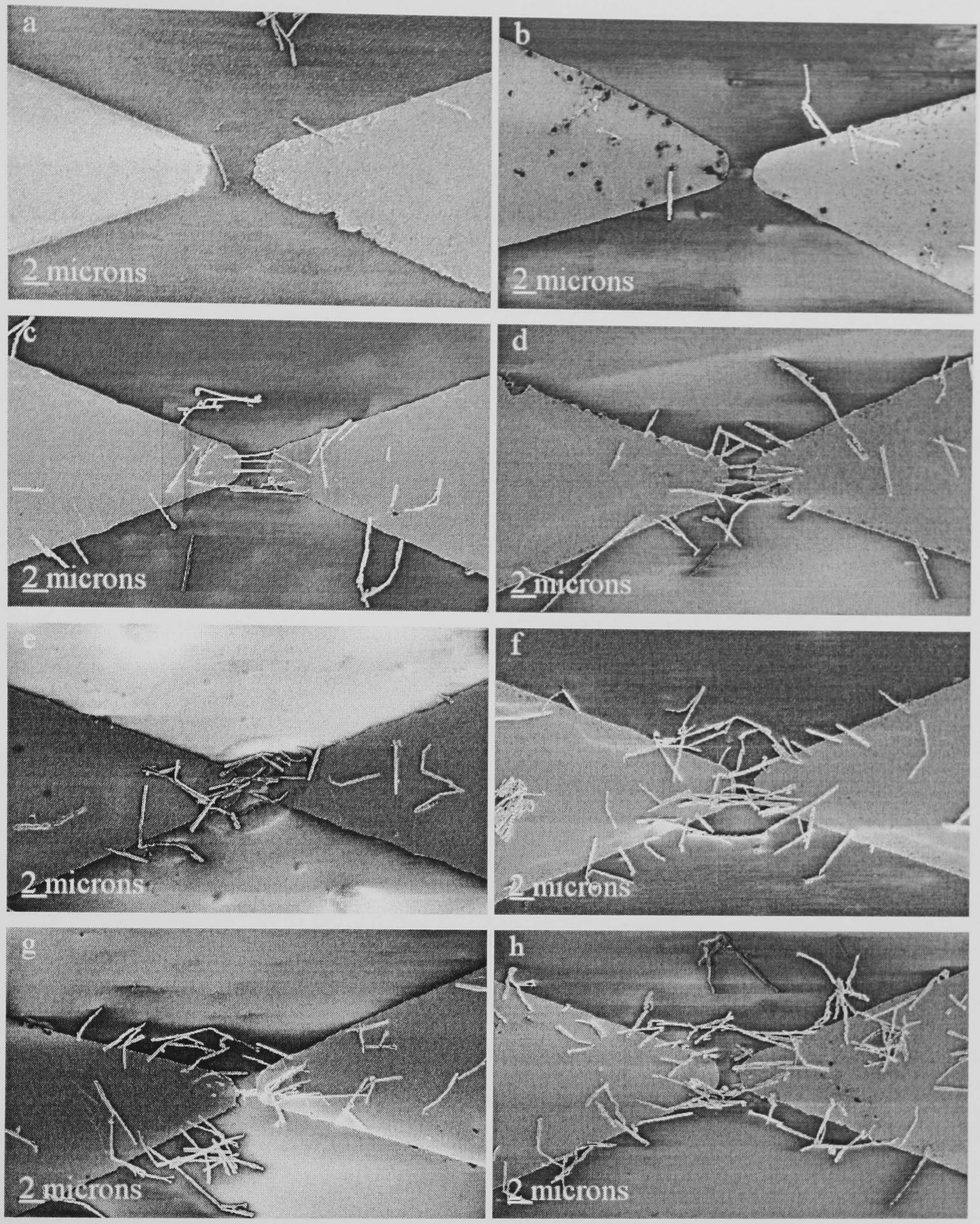

Figure 5.10. The series of scanning electron micrographs showing nanowire assembly between electrodes at different applied potentials: a) 0.5 V_{pp}, b) 1 V_{pp}, c) 1.5 V_{pp}, d) 2 V_{pp}, e) 2.5 V_{pp}, f) 3 V_{pp}, g) 3.5 V_{pp}, h) 4 V_{pp}

The SEM images for 0.5 V_{pp} and 1 V_{pp}, figures 5.10a and 5.10b, show that the assembly of bridged nanowires is not observed under these conditions. The only evidence for dielectrophoretic assembly is a few nanowires captured by one end at the electrode edges, other nanowires can be observed randomly distributed on the electrode surface. These results are consistent with preliminary experiments discussed above.

Between 1.5 and 3 V_{pp}, figures 5.10 c-f, the electrodes are bridged by multiple nanowires. Nanowires are deposited along the edges of the electrode and contact pad, with a much greater density across the electrode gap. The high density of nanowires in this region is a consequence of the fact that an Ohmic contact between the nanowire and electrode is not formed until the drying phase.

Above 3 V_{pp}, figures 5.10g and 5.10h, many nanowires are assembled onto the electrodes both at the electrode gap, and at slightly lower density along other edges of the electrode. Closer inspection reveals structures around the electrode gap that appear to be melted objects or partial nanowires. After assembly at these conditions, currents would be in excess of 2 mA_{rms} and it is quite possible that these currents are capable of melting/evaporating bridged nanowires.

5.2.4.2 Variation of the Applied Field Frequency

An investigation into the frequency sensitivity of dielectrophoretic nanowire assembly was conducted with the applied potential fixed at 2.5 V_{pp}. The frequency was varied between 10 Hz and 100 kHz with experiments performed at each order of magnitude. In addition, an assembly experiment was performed at a constant applied field of 2.5 V_{DC} for comparison. The theoretical results derived above show that below 10 kHz the dielectrophoretic force is dominated by the conductivity of gold, and $\mathrm{Re}\{K\}$ lies within the low frequency regime, equation 5.4. Above 10 kHz, the contribution of particle, and medium's, permittivity is significant. The ratio of the dielectrophoretic forces at 10 Hz : 100 Hz : 1 kHz : 10 kHz : 100 kHz has been calculated to be is 100 : 99.9 : 99.3: 59.5 : 1.4. After assembly, each electrode was imaged with SEM and these results are presented in figure 5.11.

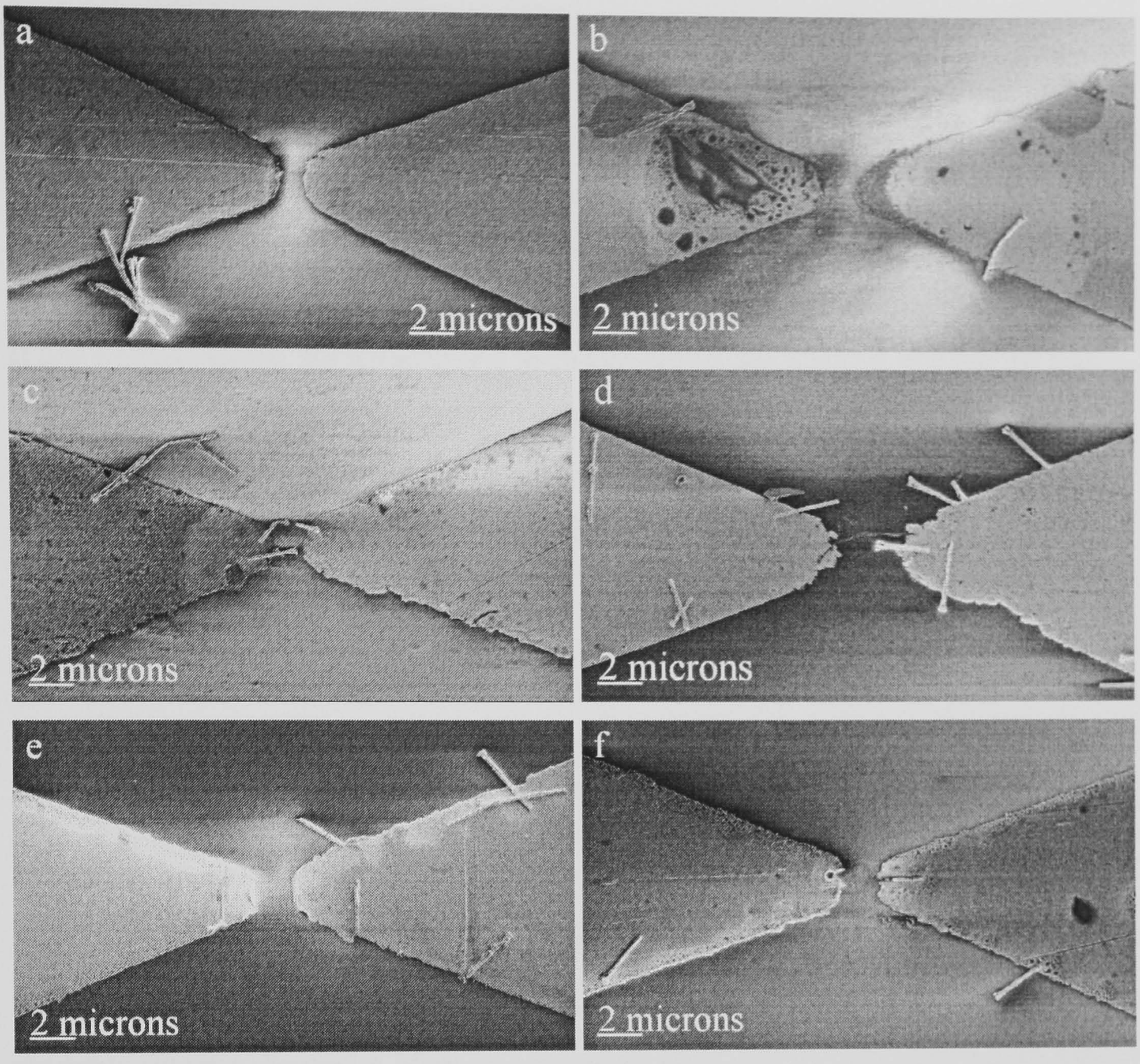

Figure 5.11. The series of scanning electron micrographs showing nanowire assembly between electrodes at different applied field frequencies: a) DC, b) 10 Hz, c) 100 Hz, d) 1 kHz, e) 10 kHz, and f) 100 kHz

These experiments were conducted with a different nanowire solution to that used to observe the voltage dependence. Consequently, they are not directly comparable with the results present in figure 5.10, since the density of nanowires in solution was lower.

The observed assembly behaviour does not completely follow that predicted theoretically. At a frequency of 10 Hz, figure 5.11b, very few assembled nanowires are observed although the dielectrophoretic forces were expected to be at their strongest. At higher frequencies more assembled nanowires are observed. Figures 5.11c and 5.11d, at 100 and 1000 Hz respectively, show an increasing density of nanowires with frequency. The density of assembly nanowires is seen to decrease slightly at 10 kHz, figure 5.11e, and decreases again by 100 kHz, figure 5.11f.

In summary, a decrease in the number of assembled nanowires is observed at higher frequencies, as expected, but assembly at lower frequencies is not as successful as predicted. Although the reason for poor nanowire assembly is not completely understood. it may be associated with frequency of the applied field. The dependence of dielectrophoresis on the electric field strength means that the dielectrophoretic force has the same frequency as the applied potential. The dielectrophoretic force is transient. and at low frequencies the dielectrophoretic force may reduce for significantly long periods such that nanowires may be removed during the washing process. At all the frequencies investigated here the electric field between the electrodes would be expected to drop to zero, since the circuit time determined from table 1 is negligible when compared to the period of the applied field.

From the examples presented in figure 5.11, only one electrode shows the formation of a nanowire bridge, figure 11c. Unexpectedly, this nanowire is clearly broken and appears to have melted. This has occurred at applied potentials 1 V lower than similar bridged nanowires were observed to have melted in figure 5.10.

5.3: Electrical Characterisation of Nanowires

The electrical transport properties of nanowires have been characterised after their assembly between electrodes. Measurements were made with the apparatus described in section 2.5.8. The results, and their intricacies, are presented below.

5.3.1 Electrical Characterisation of Nanowires Assembled on Aluminium Electrodes

Gold nanowires were assembled onto the aluminium / silicon dioxide electrodes at a range of dielectrophoretic conditions, as discussed previously. With regard to the insulating breakdown of these electrodes, figure 5.1, the applied potential during assembly was minimised. It should be noted that at voltages beyond the electrical breakdown of these electrodes assembly was still observed. Nanowire bridges usually contained multiple nanowires, arranged either side-by-side or linked end to end. Figure 5.12 shows a higher resolution image of figure 5.3, detailing the central electrode area and bridged nanowires.

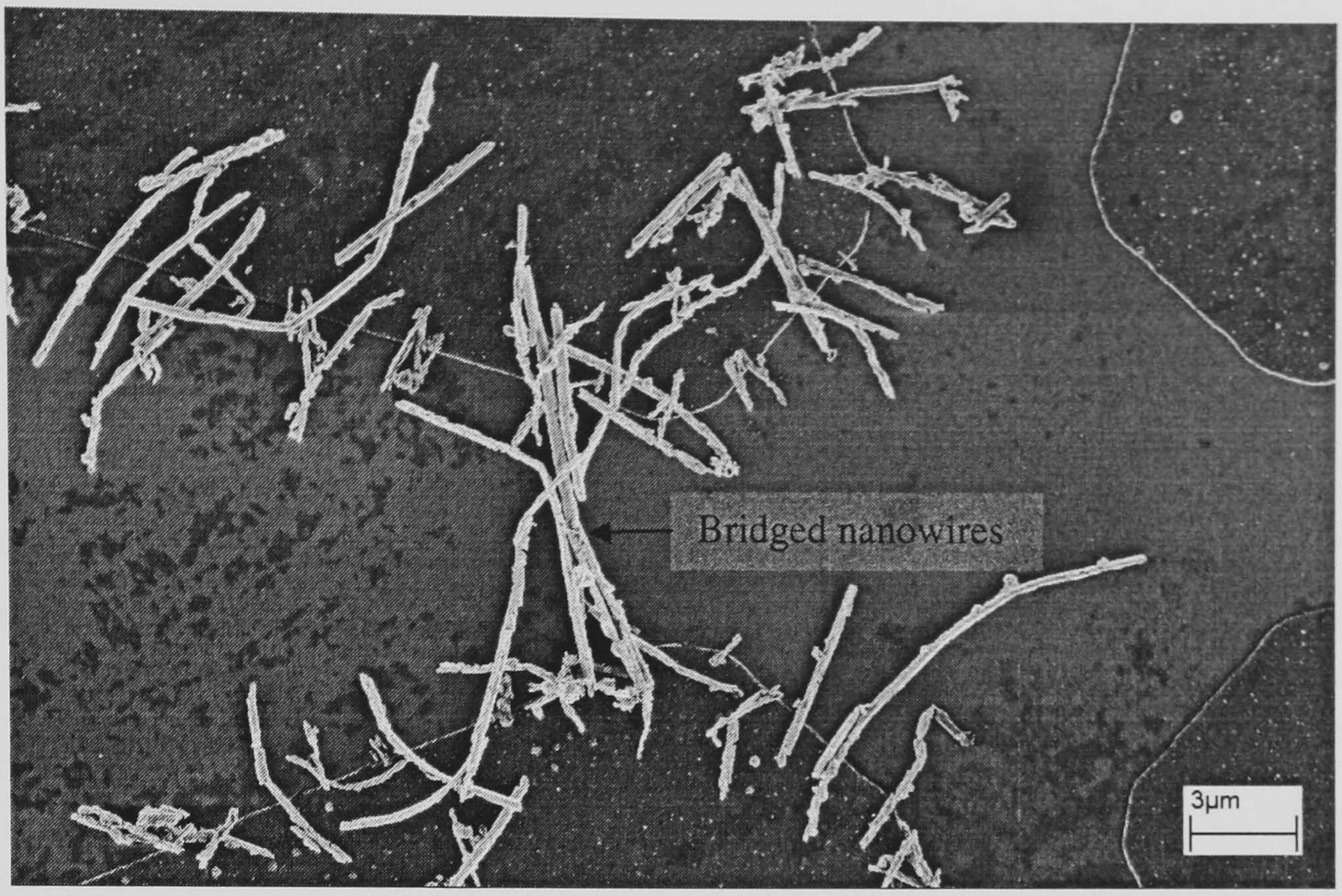

Figure 5.12. Observation of nanowires bridging an aluminium / silicon dioxide electrode after assembly at 2 V_{pp}, 150 kHz

The two electrodes are connected by one main nanowire, with each end attached to different electrodes, and several further interconnected nanowires. It is not known which nanowires will contribute towards conduction across the electrode gap. Transport measurements between the leftmost contacts of figure 5.12 show an Ohmic behaviour with a resistance of 1100 Ω, figure 5.13.

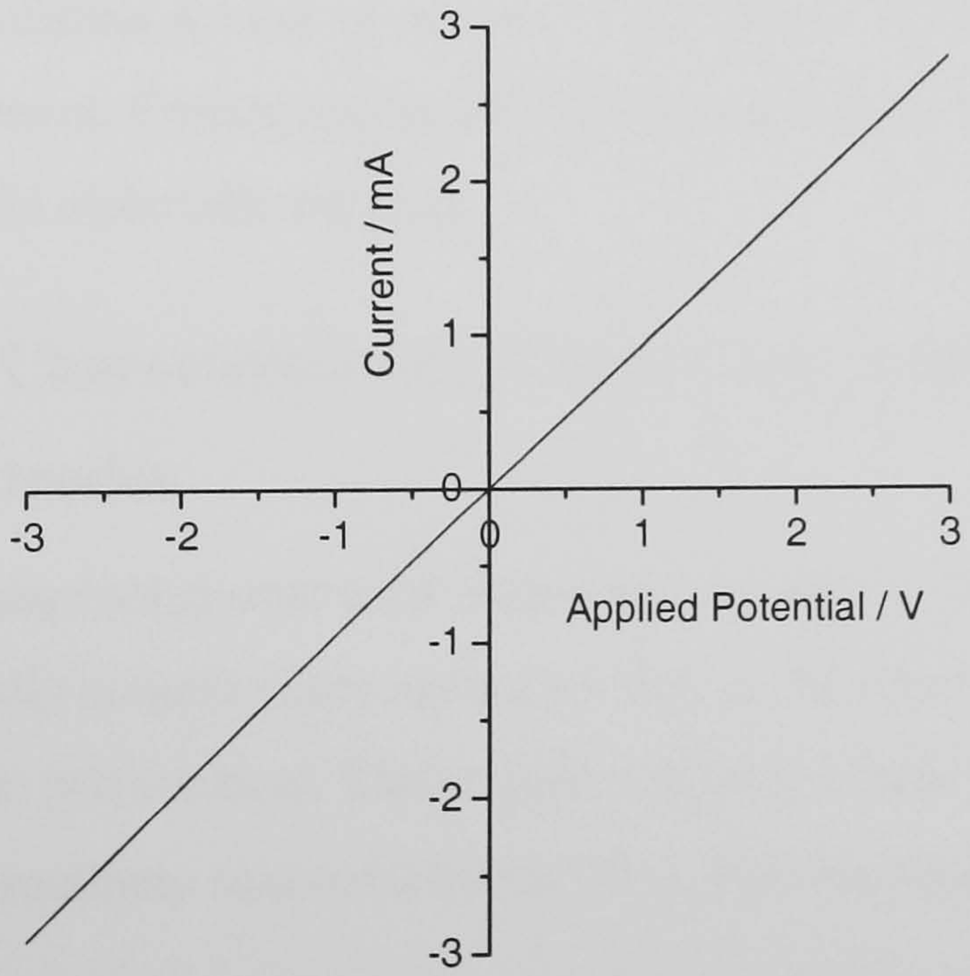

Figure 5.13. Transport properties for the leftmost contacts of the electrode shown in figure 5.12

The expected resistance for a single nanowire bridging this gap is approximately 6 Ω (determined classically using equation 2.12, radius 75 nm, length 5 μm and resistivity 2.2×10^{-8} Ωm. The observed resistance is larger than expected, however, it was highly reproducible and all nanowires assembled between gold electrodes returned consistent measurements. In light of the electrical breakdown of these electrodes, figure 5.1, a control experiment was undertaken. An aluminium electrode was subjected to typical assembly conditions, whilst exposed to HPLC methanol. A potential of 2 V_{pp} (150 kHz) was applied for 5 minutes, consistent with the total time taken for nanowire assembly, and the washing and drying processes. After drying the electrode, the transport characteristics were measured and shown to be identical to figure 5.13 (without any bridged nanowires). Apparently, the dielectrophoretic assembly conditions cause a permanent breakdown of the electrode such that its insulating behaviour is replaced with a ~1 kΩ, resistance. It is thought that conducting pathways form between the electrodes and the silicon substrate.

The potential dropped across the electrode gap is negligible when compared to the potential dropped, in parallel, between the aluminium electrodes and the silicon substrate. The assembly of nanowires was due to an electric field associated with the potential drop between electrode and substrate. As such, the electrode geometry does not significantly influence the local electric field, and the electric field is uniform at the electrode edges. The observation of a constant density of nanowires all around the electrode edges, figure 5.3, supports this argument. Consequently, aluminium electrodes on silicon dioxide have been superseded by gold electrodes on glass.

5.3.2 Electrical Characterisation of Nanowires Assembled on Gold / Glass Electrodes

Nanowires have been assembled onto gold electrodes at a variety of assembly conditions. These structures typically contain many nanowires that could potentially contribute to conduction between the two contacts. They samples display Ohmic transport behaviour, with resistance values routinely measured below 20 Ω. For example, figure 5.14 shows an

electrode assembled at 2 V_{pp}.

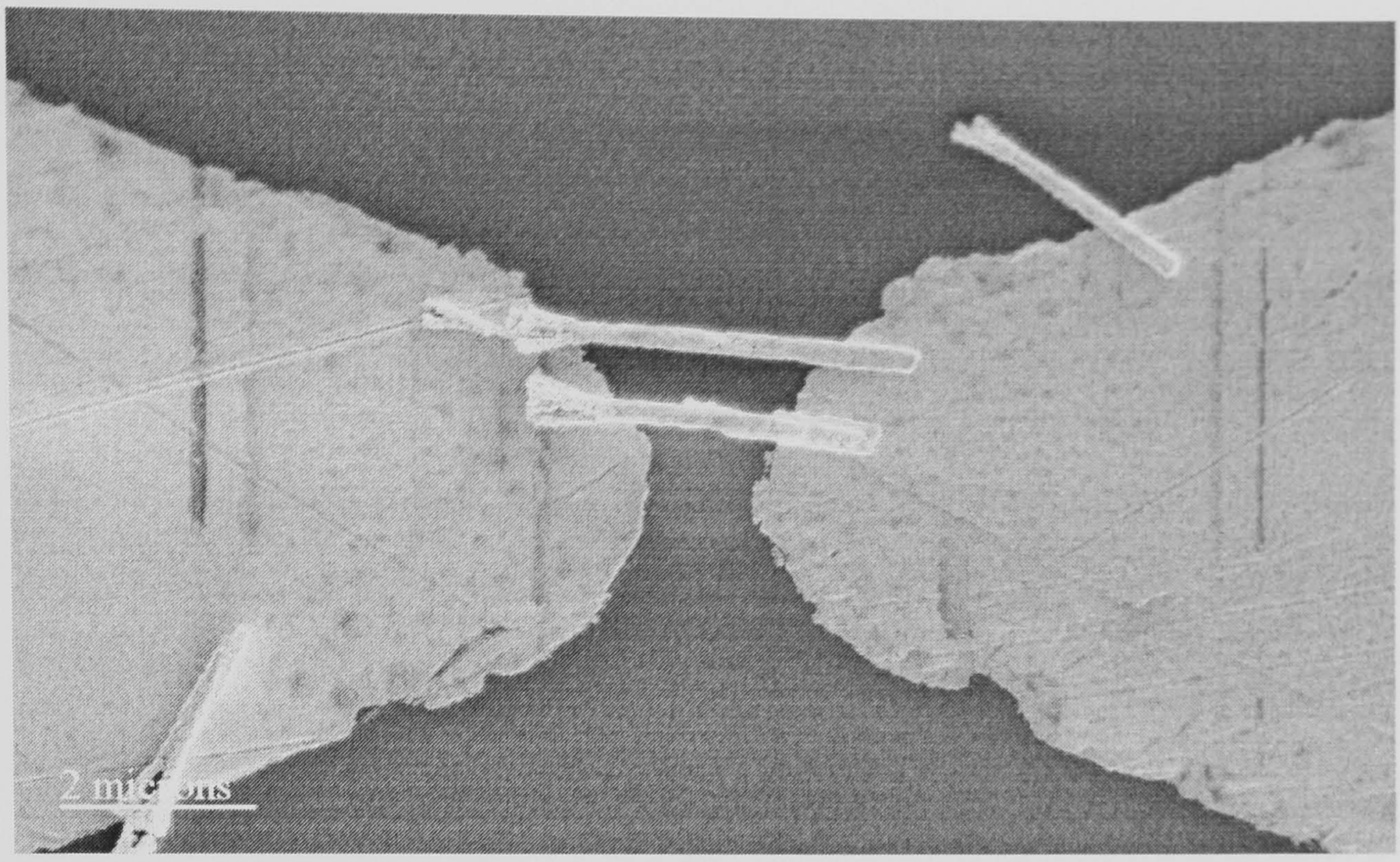

Figure 5.14. SEM image of gold nanowires assembled across a gold / glass electrode at 2 V_{pp} (150kHz)

This electrode has two nanowires clearly bridging the gap, in parallel, with no other nanowires forming a conduction pathway. When the electrical properties of this electrode are tested, an Ohmic 17.5 Ω resistance is observed, figure 5.15.

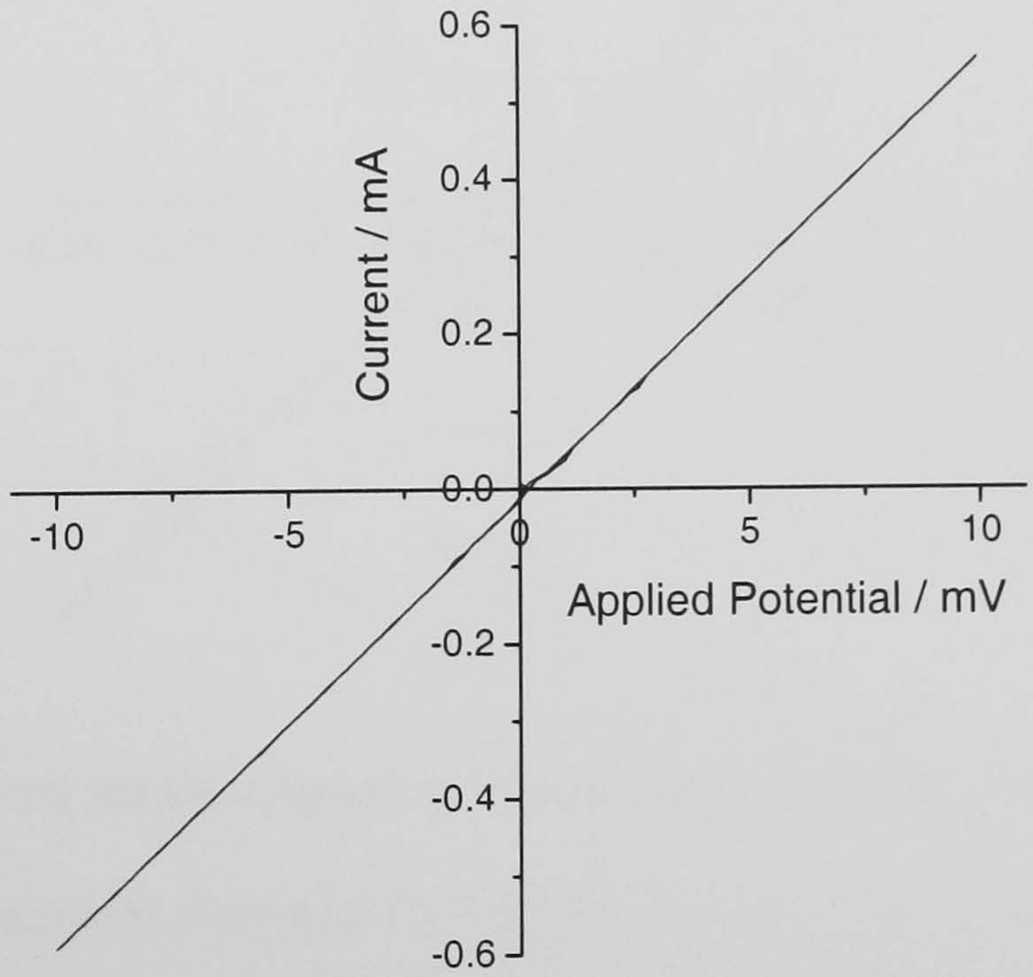

Figure 5.15. Transport measurement of the electrode shown in figure 5.14 showing 20 Ω total resistance

If each nanowire is thought to have an equal contribution to these transport properties, individual nanowire resistance is 35 Ω, although practically this figure represents an

upper limit to the nanowire resistance. Expected resistance values for gold nanowires (radius 75 nm, length 2 μm and resistivity $2.2x10^{-8}$ Ωm) can be determined classically as 2.5 Ω. However, given that the bulk resistivity of gold is $2.2x10^{-8}$ Ωm, the nanowires have an approximate diameter of 150 nm, and the mean free path of conduction electrons in gold is ~40 nm, the resistivity should be increased by a factor of 1.2.[5] An assumption has been made that no electrons are scattered elastically at the surface of the nanowire. but instead suffer a complete loss of their drift velocity. By subtracting the expected nanowire resistance, a value for the contact resistance can be calculated to be 16 Ω. This is significantly lower than contact resistance values reported by Cai at 70 Ω [6] and Evoy at 130 Ω [7] on similar systems.

The presence of contact resistance is thought to be primarily due to the presence of contaminants in solution. Upon drying the electrode, solvent surrounding the nanowires will dry leaving a film of contaminants between the electrode and nanowire. Initially, transport measurements typically returned resistance values of several hundred Ohms, figure 5.16.

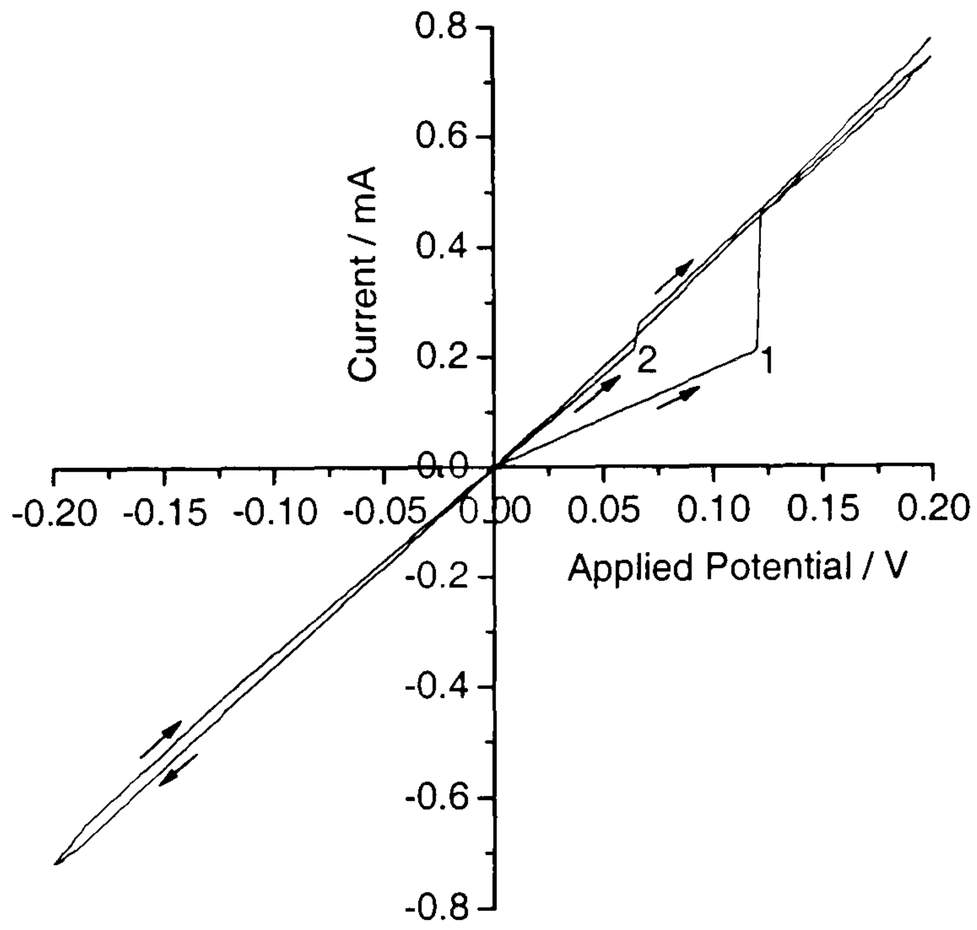

Figure 5.16. Transport measurement of figure 5.10c showing variable resistance.

The resistance measurement shown in figure 5.16, across the electrode shown in figure 5.10c, varies between 580 and 270 Ω. The change is predominantly due to a sequence of jumps during the transport measurement, points 1 and 2 in figure 5.16. These jumps occur on the increasing sweep of the voltage cycle, and affect a permanent change to the electrode resistance. They are presumably associated with significant changes in the

contact resistance contribution to the electrode resistance. These jumps have been observed on electrodes bridged by single and multiple nanowires.

The association between contact resistance and solution contaminants is supported by AFM manipulation of nanowires. AFM was used in an attempt to move a nanowire on the electrode imaged in figure 5.10b, and the results shown in figure 5.17.

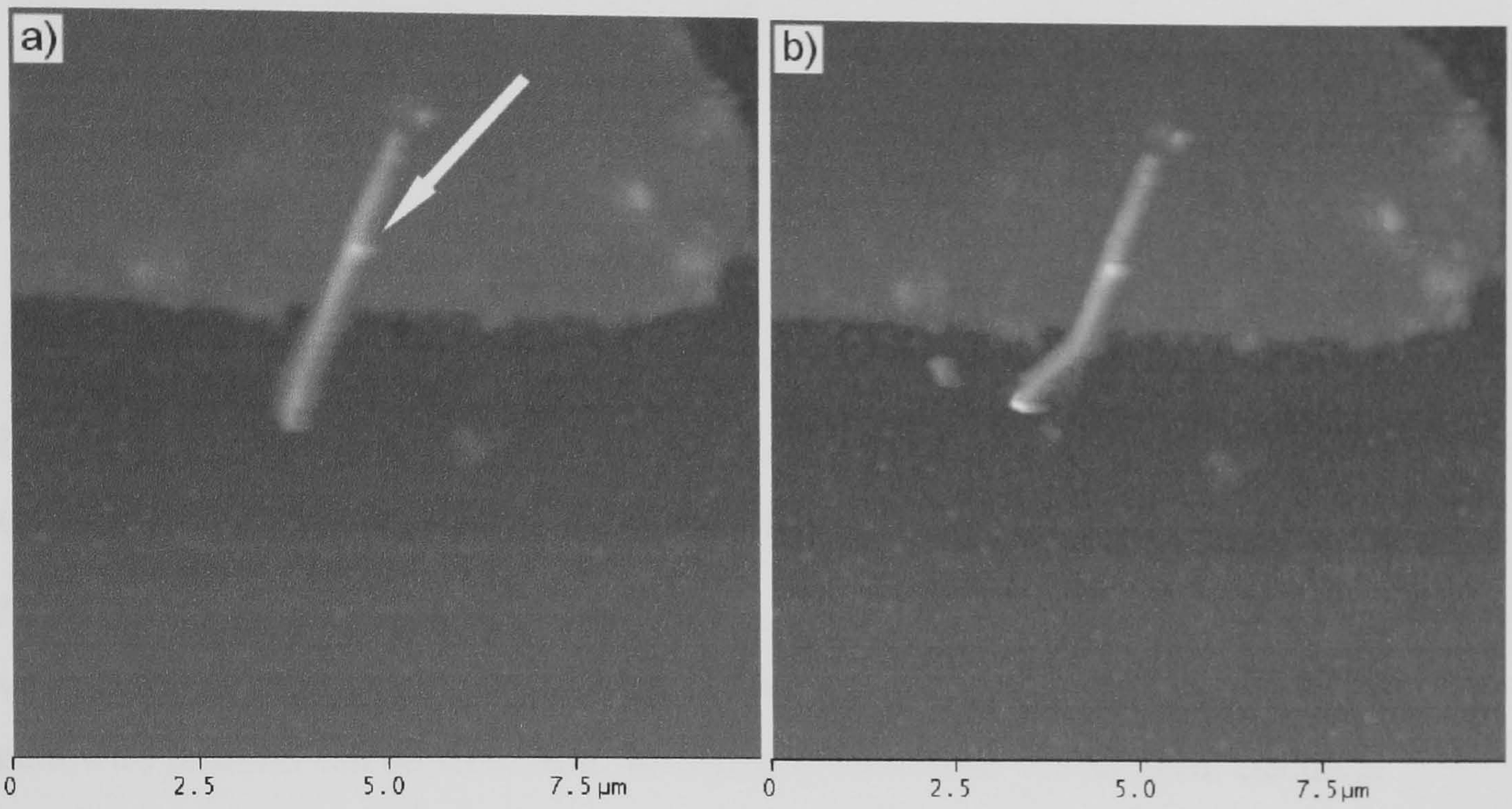

Figure 5.17. AFM images of a nanowire on the surface of the electrode imaged in figure 5.10b a) before and b) after manipulation

The image shows the initial nanowire position at the edge of the electrode. After the AFM image figure 5.17a was recorded the tip was approached to the surface, and moved along the path directed by the white arrow. After manipulation, the bulk of the nanowire has not moved, rather the end protruding from the electrode has bent. A 'shadow' of the original nanowire position can still be seen in figure 5.17b, it is believed that this artefact is surface contamination dried from solution underneath the nanowire. To remove these signs of surface contamination additional cleaning of the nanowires in solution was required. The nanowire solution was filtered through a Whatman 'Cyclopore' membrane filter, and captured nanowires were washed and resuspended in methanol. After this additional cleaning stage the AFM manipulation experiment was repeated, figure 5.18.

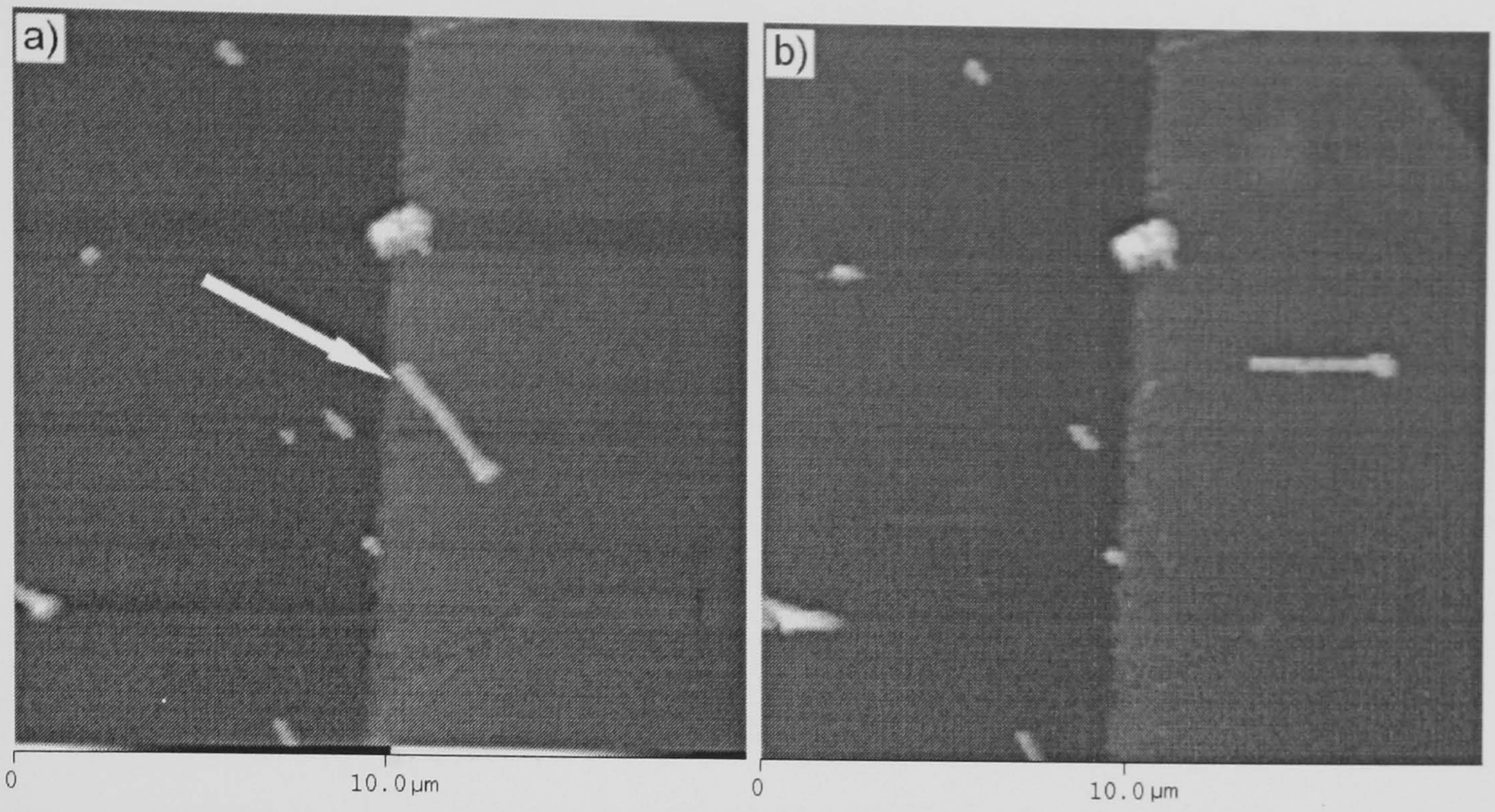

Figure 5.18. AFM images of gold nanowires assembled onto an electrode at 1.5 V_{pp} (150 kHz) a) before and b) after manipulation

Now, the nanowires attachment to the surface is much weaker and upon manipulation with the AFM the wire completely detaches. In figure 5.18b no outline of the previous nanowire position can be seen. After the filtering procedure was adopted, electrical characterisation of nanowires assembled between electrodes consistently returned resistance values of approximately 20 Ω.

It has been hypothesised that certain assembly conditions drive currents through bridged nanowires sufficient to melt them. To determine the current required to melt a nanowire, the electrode shown in figure 5.10c was subjected to repeated transport measurements over increasing larger voltage ranges, with the potential ramped at 0.01 Vs^{-1}. During this series of experiments, of which figure 5.16 is one measurement, the resistance between the two electrodes varied from 500 to 60 Ω. During the final transport measurement, where the potential was ramped to 0.6V, the electrode gap once again became insulating, figure 5.19.

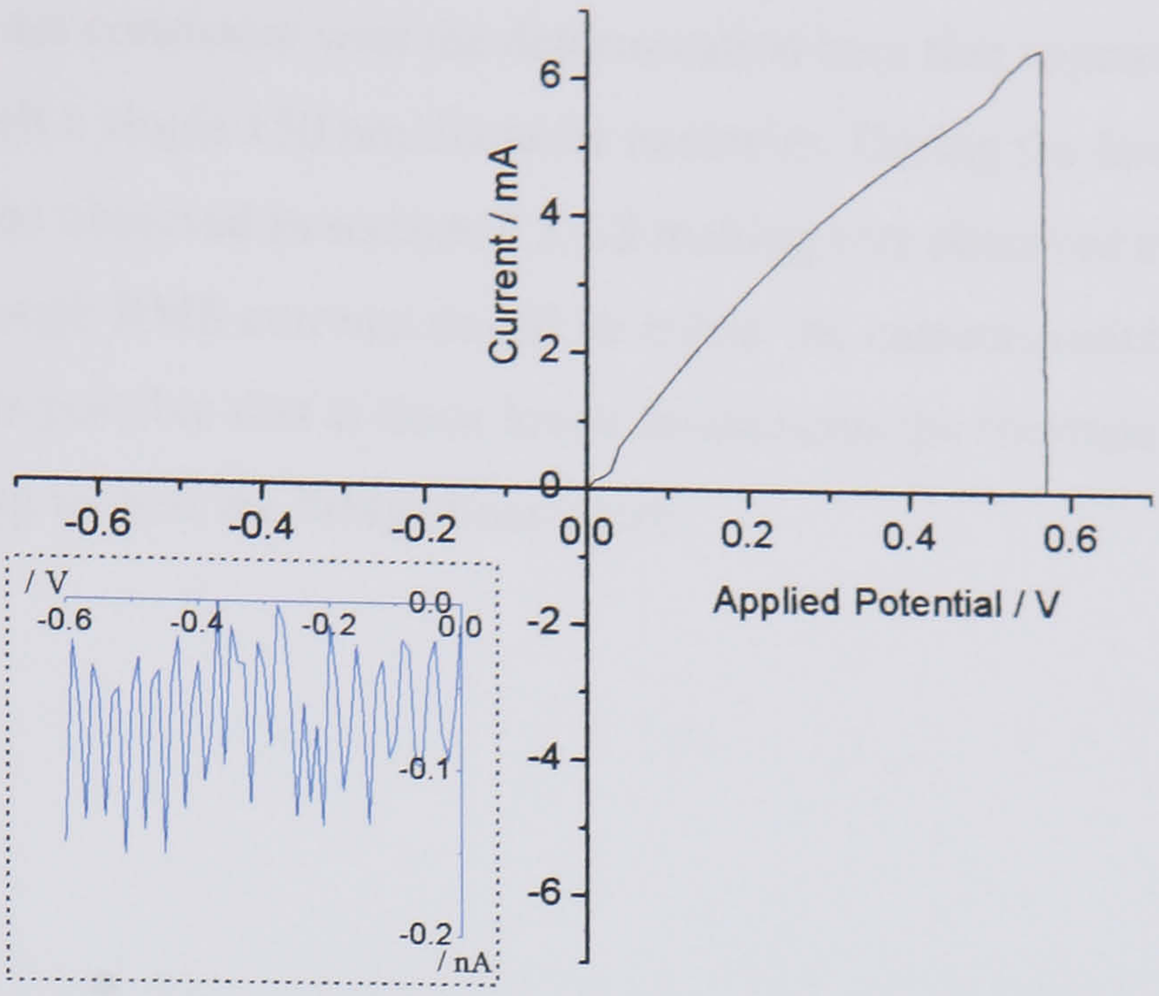

Figure 5.19. Transport properties of the electrodes shown in figure 5.10c, with the voltage range increased until the electrode became insulating

The electrode became insulating at 0.57 V with a current of 6.5 mA. The voltage cycle continued up to 0.6V before returning to 0V and through a negative potential sweep during which currents remained ~10^{-10}A, shown in blue. Immediately after this experiment the electrode was imaged with high resolution SEM, figure 5.20 shows before and after images showing the state of the electrode.

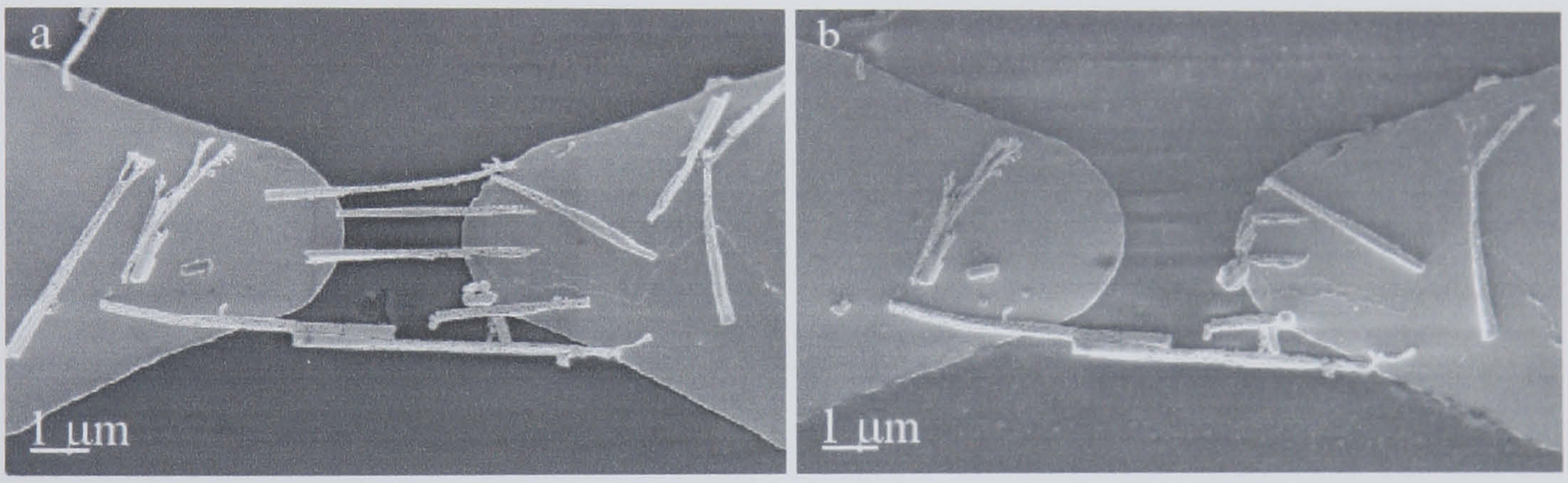

Figure 5.20. SEM image of nanowires assembled at 1.5 V (150 kHz) (a) before and (b) after melting.

After the electrode becomes insulating, the three main nanowires bridging the electrodes have been removed. Additional nanowires on the surface of the electrode are altered or removed, but noticeably the two nanowires that bridge the gap end-to-end remain intact. Apparently, these nanowires do not contribute to conduction between the two contacts. The structures observed are consistent with what one would expect for melted nanowires. In addition, figure 5.20b displays ~100 nm particulate on the electrode surface, which is presumably remnants of nanowires that once bridged the electrodes. Experimental observations of melted nanowire bridges, figure 5.10, occur at applied potentials above 3

V_{pp}. These results are consistent with the determination here that approximately 2.2 mA_{rms} was required to melt a single 150 nm diameter nanowire. During the low frequency assembly conditions observed in section 5.2.4.2 melting was observed at 2.5 V_{pp} (100Hz), figure 5.11c. Although RMS currents would be below the currents required for melting measured here, it is possible that at these lower frequencies the transient current is higher for sufficiently long to melt the bridged nanowire.

5.4: References

1. Kratochvilova, I.; Kocirik, M.; Zambova, A., et al., Journal of Materials Chemistry, 2002. **12**(10): p. 2927-2930.
2. Smith, P.A.; Nordquist, C.D.; Jackson, T.N., et al., Applied Physics Letters. 2000. **77**(9): p. 1399-1401.
3. *Handbook of Chemistry and Physics*. 82 ed, ed. Lide, D.R. 2001: Chapman & Hall/CRC.
4. Dimaki, M.; Boggild, P., Nanotechnology, 2004. **15**(8): p. 1095-1102.
5. Sondheimer, E.H., Advances in Physics, 2001. **50**(6): p. 499-537.
6. Cai, L.T.; Skulason, H.; Kushmerick, J.G., et al., Journal of Physical Chemistry B, 2004. **108**(9): p. 2827-2832.
7. Evoy, S.; DiLello, N.; Deshpande, V., et al., Microelectronic Engineering, 2004. **75**(1): p. 31-42.

Chapter 6: Conclusions and Further Work

The work presented in this thesis has considered the formation, assembly and characterisation of gold nanowires.

The template synthesis of nanowires has been undertaken by both electroless and electrochemical deposition in a variety of template materials. The first results chapter (chapter 3) includes a discussion concerning the variety of template materials used, the deposition procedures undertaken, and characterisation of the nanowires produced. Three types of template have been used; electrochemically formed porous alumina, and Whatman 'Anodisc' and 'Cyclopore' filtration membranes. Deposition was successfully achieved in all these materials, although the bulk of results presented in this thesis used nanowires derived from the Whatman 'Anodisc' membranes. Important to the deposition procedures was the wettability of pores in the template. The polycarbonate from which 'Cyclopore' membranes are produced is hydrophilic, which allowed complete filling of pores with electrolyte solutions. Although naturally hydrophilic, having contact angles with water as low as 5°, alumina is known to absorb hydrocarbon contamination which increases its hyrophobicity. Potentially, the contact angles of alumina contaminated with hydrocarbons from the atmosphere increases to greater than 80°.[1, 2] Deposition was unsuccessful in certain batches of 'Anodisc' membranes, and it is believed that failure was due to the decreased wettability of contaminated membranes. After deposition, nanowires could be removed from each of these templates by a range of simple chemical procedures. XPS characterisation of gold nanowires from the filtration membranes showed the presence of silver in solution, originating from the electrode used for deposition into 'Anodisc' and 'Cyclopore' membranes. Nanowires were successfully functionalised with a range of thiol surfactants, both whilst contained in the template and suspended in solution.

In comparison to studies of colloid or carbon nanotube self-assembly, there is relatively little work published on the assembly of metallic nanowires onto surfaces. In the second results chapter (chapter 4) a discussion concerning the surfactant mediated self-assembly of nanowires has been presented. Nanowires were assembled via nanowire-nanowire, nanowire-surface, and nanowire-fluid interactions. Specific functionality was imparted to the nanowires with a range of thiol based surfactants, which determined the assembly

process. Nanowires assembly was successfully achieved on surfaces, and in solution. Typically, the surfaces used were patterned with thiol surfactants by microcontact printing, such that they contained regions of different functionality. A summary of the nanowire self-assembly techniques used are shown in table 6.1, and results of particular interest are commented on below.

Hydrophobic functionalised nanowires	Nanowires aggregated into fern-like anisotropic structures, where component nanowires were aligned parallel.
Nanowire assembly onto surfaces with patterned wettability	Nanowires assembled onto hydrophilic surface stripes, preferentially aligned parallel to these stripes.
Nanowire attachment by hydrogen bonding	[COOH] functionalised nanowires bound preferentially to [COOH] regions of patterned [OH] / [COOH] surfaces, due to formation of an acid dimer.
Nanowire attachment by carboxylate salt formation	[COOH] nanowires assembled onto carboxylate regions of patterned [OH] / [COOH] surfaces, functionalised with cadmium ions, bound via a carboxylate salt.
Nanowire assembly with a streptavidin / biotin linker	Attachment of nanowires to surfaces was unsuccessful. Aggregation of biotinylated nanowires in solution was observed if the streptavidin concentration was limited.
Nanowire assembly directed by electrostatic interactions	Charged nanowires could be directed onto charged surfaces by electrostatic interactions, but alignment of nanowires was not observed. Similarly, charged nanowires in solution may be encouraged to aggregate.

Table 6.1. Summary of nanowire self-assembly from the various surfactant based systems presented in chapter 4.

The self-assembly of nanowires has the potential to create complex structures[3]. For example, nanowires possess several advantages over spherical colloids as components for nanoscale circuitry; they are better suited to replicating wire based structures[4], forming nanoscale interconnects[5], and can be used to assemble complex devices themselves[6-10]. However, added complications are also introduced when manipulating anisotropic components, including the requirement to control both their placement and orientation. To date, there are only two studies known that have demonstrated the assembly of metallic nanowires with both a specific placement and orientation of nanowires on

surfaces[11, 12]. These studies have used complementary surfactant based interactions to bind nanowires at selected regions of a patterned surface, in addition to either fluid flow[11], or an external magnetic fields[12], to control their alignment. The assembly of nanowires onto surfaces with patterned wettability was an entirely self-contained process, and both nanowire placement and alignment are successfully derived solely from the surface-fluid interaction.

It has been shown that chemical reactions between functionalised nanowires and surfaces are capable of selectively binding nanowires to reactive surface regions, whilst unbound or weakly bound nanowires were washed away. The exception to this is the attachment of biotinylated nanowires to patterned streptavidin surfaces. Here, binding of excess streptavidin to nanowires in solution was thought to kinetically more favourable than the formation of a bond between the surface and nanowire. Although it was not possibly here to demonstrate the biotin binding of nanowires to surfaces, it has been done so previously in the literature.[12] Interestingly, biotinylated nanowires were shown to aggregate strongly in solution after exposure to these surfaces.

Negatively charged nanowires assembled onto neutral regions of a COO^- / [OH] patterned surfaces, due to electrostatic repulsion between the deprotonated surfactants. This result should be compared with nanowire attachment to patterned surfaces via hydrogen bonding, where [COOH] functionalised nanowires bound preferentially to [COOH] regions on [COOH] / [OH] surfaces. Both experiments used identical surfaces and nanowires, whilst different assembly mechanisms were utilized by tailoring the solvent. With electrostatic interactions the nanowires assemble onto [OH] regions of the surface, whilst hydrogen bonding caused the nanowires to attach to the [COOH] regions.

In the third results chapter (chapter 5) a discussion relating to the directed assembly of nanowires by dielectrophoretic forces has been presented. Subsequently, the transport properties of nanowires assembled between electrodes has been characterised. Theoretical modelling and experimental results were used to characterise the dielectrophoretic forces a nanowire was subjected to during assembly. Consequently, optimum assembly conditions could be approximated. To maximise the dielectrophoretic force, at any given potential, the frequency of the applied field should be minimised. However, a certain threshold frequency is required such that the dielectrophoretic force is sufficiently stable to the prevent removal of nanowires during washing. For the assembly procedure

developed during the course of this work, frequencies below 100 Hz should be avoided. However, since variations in the dielectrophoretic force below 1 kHz are negligible, it is suggested that 1 kHz frequencies are used. In addition, the applied potential, and load resistor, should be optimised to maximise the dielectrophoretic force, but prevent excess current upon assembly. For the purpose of assembling single nanowires bridging the electrodes the applied potential should be minimised, whilst ensuring that the dielectrophoretic force is sufficient to prevent the removal of nanowires during the washing stage. The time the electrodes were incubated with the nanowires, and the density of nanowires in solution, were also deemed important factors.

Once assembled, the electrical characterisation of nanowires was possible. Transport measurements are believed to be dominated by contact resistance between the electrode and nanowires. The contact resistance was minimised by filtering contaminants from the nanowire solution, causing the resistance of electrodes with bridged nanowires to fall from several hundred Ohms to ~20 Ω. The maximum contribution of a single nanowire to these structures is less than 35 Ω, including contact resistance. The intrinsic resistance of these nanowires is thought to approximately 1.5 Ω/μm, showing that a contact resistance per nanowire of ~16 Ω is still present. However, these measurements have significantly lower contact resistance than 70 Ω [13] and the 130 Ω [14] values previously reported for similar systems. In addition it was shown that these nanowires melt when approximately 2.2 mA is passed through them.

6.1: Further Work

The initial aims of this project broadly followed the three results chapters presented in this thesis. The goals were to fabricate gold nanowires, and to devise a technique capable of directing their assembly between electrodes. It was initially thought that the technique developed for the assembly of nanowires between electrodes would be based upon thiol surfactants. A variety of techniques were to be investigated, from simple binding mechanisms, to interactions that directed the positioning and / or alignment of nanowires across the electrode gap. Preliminary experiments were undertaken on patterned planar substrates, a selection of which is presented in chapter 3. However, the control afforded by dielectrophoresis superseded these surfactant based techniques, and was adopted.

In addition, it was hoped that the research could be extended to characterise the transport properties of gold nanowires by alternative methods. There are two specific experiments

that it has not been possible to complete, discussed below, that will hopefully be addressed in the future.

The first has already been alluded to; nanowires may be manipulated on surfaces with SPM probes, initial results are shown in figures 5.17 and 5.18. The presence of contact resistance is thought to be due to solution contaminants condensing around, and underneath, the nanowire. Once deposited, it was planned that individual nanowires could be manipulated with an AFM tip to move them from their original position to one that bridges the electrode gap. In so doing, surface contaminants on the nanowire would be abraded away, and the electrode should be free from contaminants. It was of interest to see what resistance values could be obtained by this process. Following from this was the idea to create a 'nano-switch'. By manipulating one end of a bridged nanowire on and off the electrode, the current could be turned on and off. Initial problems were associated with significant adhesion of nanowires to the surface by contaminants. Rather than move, the nanowire would bend or break, figure 5.17. After reducing the quantity of contaminants in solution, nanowires were significantly easier to manipulate, but problems exist with nanowires adhering to the AFM tip, or being flicked large distances across the surface.

The second was to perform 4-probe transport measurements of nanowires, by addressing a single nanowire with 4 STM tips. As such, the contact resistance present during measurements on electrodes (and between the tips and nanowires) would be negated. An Omicron 4-probe STM is now is place that is capable of such measurements. Each STM tip may be individually controlled and addressed, whilst the tips and sample below are monitored simultaneously with a LEO FEGSEM, figure 6.1.

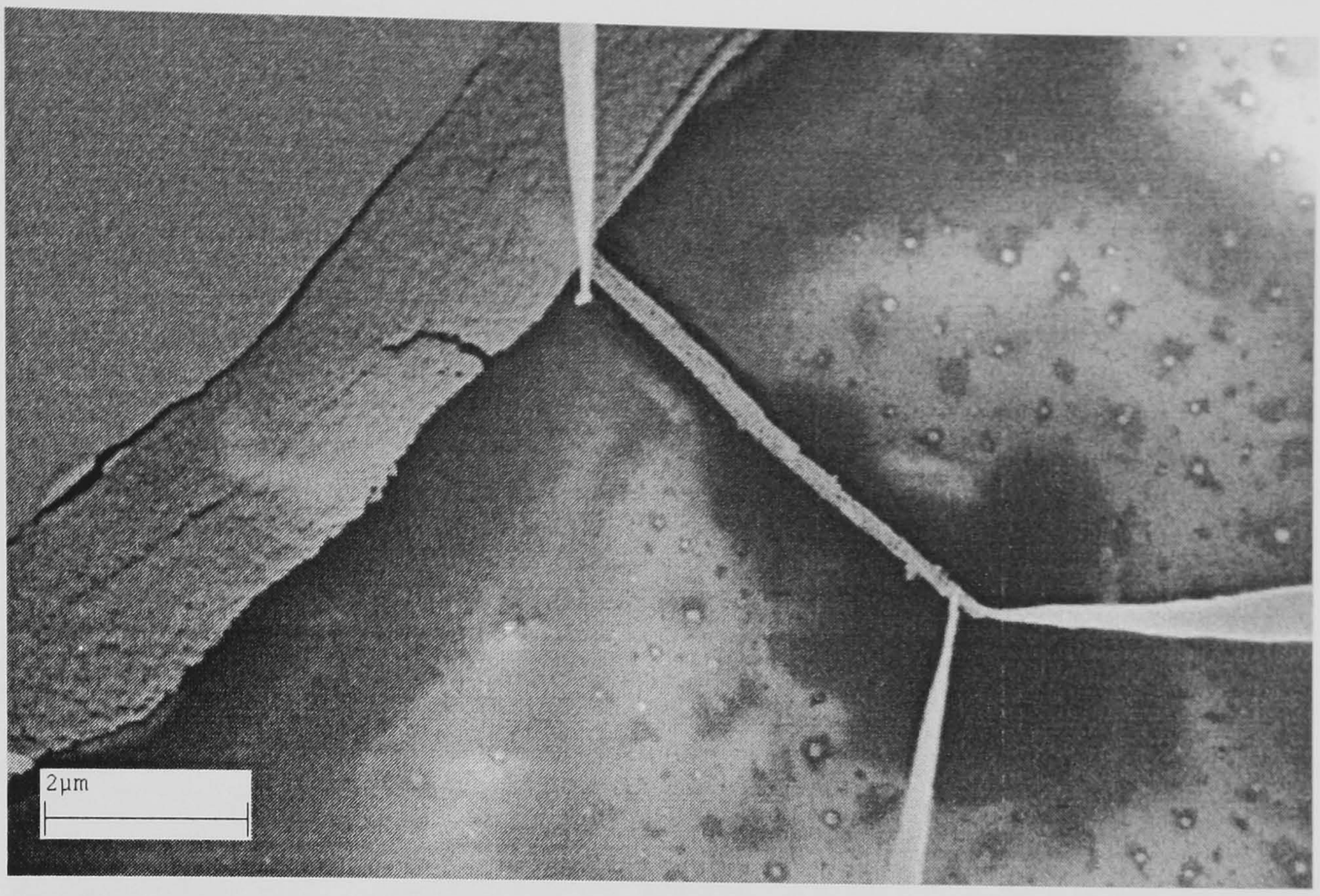

Figure 6.1. SEM image of a gold nanowire positioned perpendicularly at an electrode edge, being addressed with three STM tips.

Preliminary experiments have demonstrated the capability to position the STM tips at different locations along the nanowire. However, problems remain when supplying current or monitoring voltages with these tips. Continued work with this instrumentation is expected to produce interesting and original results.

The development of 4-probe STM measurements would also allow accurate characterisation of more complex structures. Template fabrication of nanowires allows the incorporation of different elements along the length of the nanowire. These may be metal[15-17], semi-conductor[18], or organic stripes[13, 19, 20]. However, electronic characterisation of these structures and devices has generally been performed by 2-probe techniques. The most closely related example to work presented in this thesis was published by Cai *et al.*[13] Here, monolayer junctions were embedded within gold nanowires by a 5 stage growth procedure. Although only a low yield of non-defective nanowires were achieved, they managed to assemble some of the intact nanowires between electrodes by dielectrophoresis. They measured resistance values of 60 MΩ for a single nanowire, attributed to an incorporated C_{12} monolayer. Originally it was hoped that our research would yield nanowires containing molecular junctions and multilayers. A procedure to develop nanowires containing a monolayer junction was developed. In our work, the nanowires were formed by an initial electrodeposition phase, adsorption of a dithiol monolayer, and the attachment of gold nanoparticles which catalysed a final stage

of electroless gold deposition. Some nanowires have been produced by this method, figure 6.2.

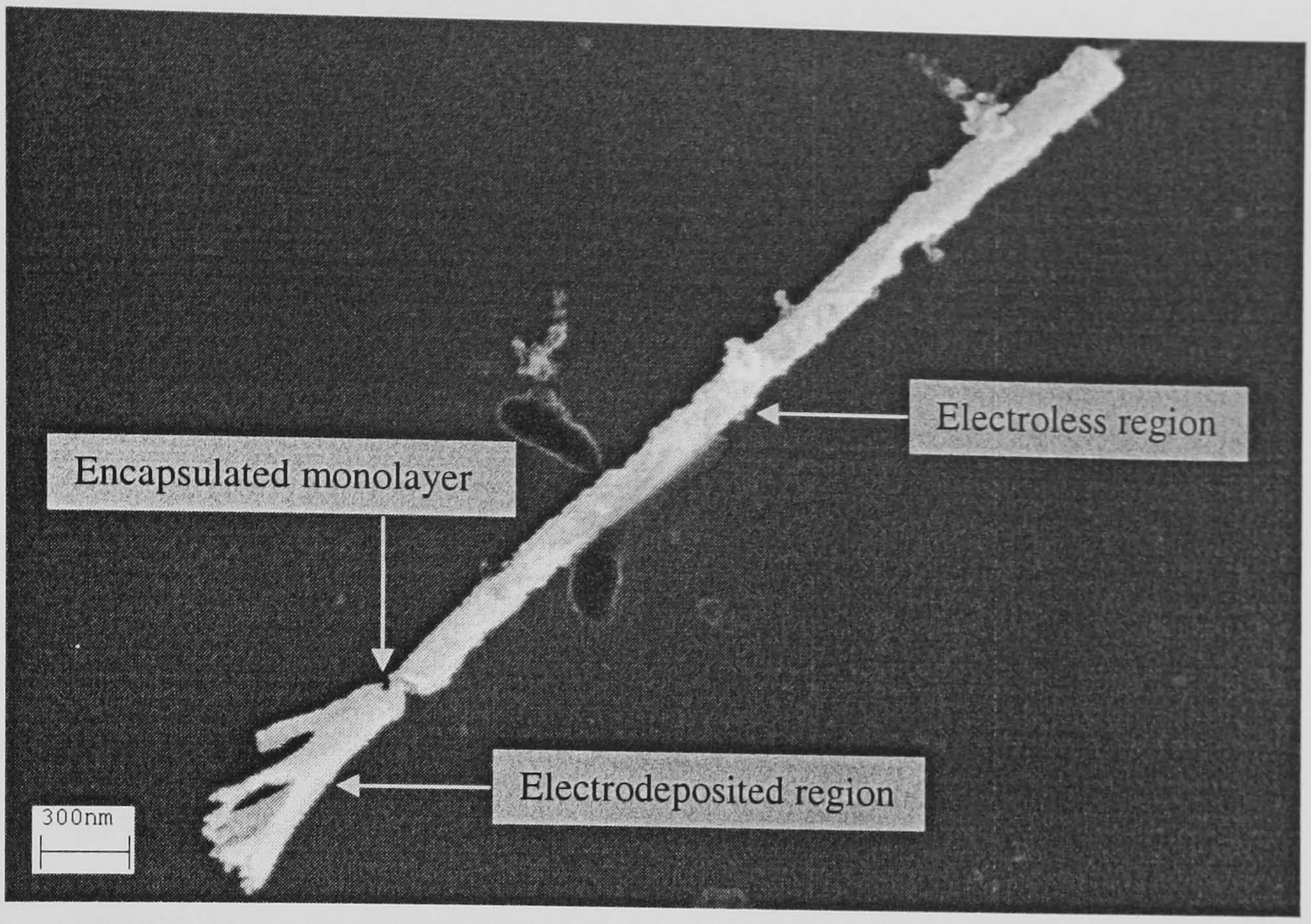

Figure 6.2. Nanowire with a sequence of electrodeposited gold, nonanedithiol monolayer, gold nanoparticles and electroless gold.

The initial electrodeposition stage was formed at 1 V_{pp} for 1 minute from the HCl electrolyte. Comparison with figure 3.23 shows that this section should be ~300 nm long. The narrowing in the nanowire is presumed to be due to the monolayer junction, where growth continued from only a few gold nanoparticles bound to this monolayer. The electrical characterisation of these nanowires, with reference to bulk gold nanowires, is the best way to determine their structure. Unfortunately, the yield of potentially successfully formed nanowires has been too low for their assembly between electrodes with dielectrophoretic forces. The development of the alternative methods for electrical characterisation has not been fast enough to characterise these nanowires. Although the encapsulation of organic layers in gold nanowires has already been demonstrated[13, 19, 20] (with similar problem of low yield) it was intended to extend the fabrication procedure to produce nanowires with multilayer surfactant-nanoparticle multilayers within the nanowire. In addition, 4-probe measurements would be able to plot the voltage drop along the length of the nanowire, and locate the position of any incorporated devices.

6.2: References

1. Paula-Santos, F.; Campos, E.; Costa, M., et al., Materials Research, 2003. **6**(3): p. 353.
2. M.R. Alexander, T.L., G.E. Thompson, E. McAlpine and A.J. Roberts, *Changes in the Al Surface upon Exposure to Ambient Conditions*. 2000, Kratos.
3. Whitesides, G.M.; Boncheva, M., Proceedings of the National Academy of Sciences of the United States of America, 2002. **99**(8): p. 4769-4774.
4. Melosh, N.A.; Boukai, A.; Diana, F., et al., Science, 2003. **300**(5616): p. 112-115.
5. Li, C.; Zhang, D.H.; Liu, X.L., et al., Applied Physics Letters, 2003. **82**(4): p. 645-647.
6. Fuhrer, M.S.; Nygard, J.; Shih, L., et al., Science, 2000. **288**(5465): p. 494-497.
7. Keren, K.; Berman, R.S.; Buchstab, E., et al., Science, 2003. **302**(5649): p. 1380-1382.
8. Bachtold, A.; Hadley, P.; Nakanishi, T., et al., Science, 2001. **294**(5545): p. 1317-1320.
9. Rueckes, T.; Kim, K.; Joselevich, E., et al., Science, 2000. **289**(5476): p. 94-97.
10. Huang, Y.; Duan, X.F.; Cui, Y., et al., Science, 2001. **294**(5545): p. 1313-1317.
11. Huang, Y.; Duan, X.F.; Wei, Q.Q., et al., Science, 2001. **291**(5504): p. 630-633.
12. Salem, A.K.; Chao, J.; Leong, K.W., et al., Advanced Materials, 2004. **16**(3): p. 268-+.
13. Cai, L.T.; Skulason, H.; Kushmerick, J.G., et al., Journal of Physical Chemistry B, 2004. **108**(9): p. 2827-2832.
14. Evoy, S.; DiLello, N.; Deshpande, V., et al., Microelectronic Engineering, 2004. **75**(1): p. 31-42.

15. Wang, J.G.; Tian, M.L.; Mallouk, T.E., et al., Nano Letters, 2004. **4**(7): p. 1313-1318.

16. Nicewarner-Pena, S.R.; Carado, A.J.; Shale, K.E., et al., Journal of Physical Chemistry B, 2003. **107**(30): p. 7360-7367.

17. Keating, C.D.; Natan, M.J., Advanced Materials, 2003. **15**(5): p. 451-454.

18. Bjork, M.T.; Ohlsson, B.J.; Sass, T., et al., Applied Physics Letters, 2002. **80**(6): p. 1058-1060.

19. Kratochvilova, I.; Kocirik, M.; Zambova, A., et al., Journal of Materials Chemistry, 2002. **12**(10): p. 2927-2930.

20. Kovtyukhova, N.I.; Martin, B.R.; Mbindyo, J.K.N., et al., Journal of Physical Chemistry B, 2001. **105**(37): p. 8762-8769.